

Development of a Conformation-Sensitive Assay for the Detection of Inter-Domain Interactions Mediated by Allosteric Akt Inhibitors

Dissertation

zur Erlangung des akademischen Grades

Doctor rerum naturalium

(Dr. rer. nat.)

der Fakultät Chemie der Technischen Universität Dortmund

vorgelegt von

Dipl.-Ing. Zhizhou Fang

aus Peking (China)

Dekan: Prof. Dr. Roland Winter

1. Gutachter: Prof. Dr. Daniel Rauh

2. Gutachter: Prof. Dr. Herbert Waldmann

Datum der Abgabe: 05.06.2013

Datum der Disputation: 22.08.2013

Die vorliegende Arbeit wurde unter der Leitung von Herrn Prof. Dr. Daniel Rauh in der Zeit vom 07.09.2009 bis 31.12.2010 am Chemical Genomics Centre der Max-Planck-Gesellschaft in Dortmund und vom 01.01.2011 bis 30.04.2013 im Fachbereich Chemische Biologie der Fakultät Chemie der Technischen Universität Dortmund angefertigt. Im Rahmen dieser Arbeit sind folgende Publikationen entstanden:

Z. Fang, C. Grütter & D. Rauh. Strategies for the Selective Regulation of Kinases with Allosteric Modulators: Exploiting Exclusive Structural Features. *ACS Chem. Biol.*, **2013**, 8, 58-70.

R. Schneider, A. Gohla, J. R. Simard, D. B. Yadav, Z. Fang, W. A. L. van Otterlo & D. Rauh. Overcoming compound fluorescence in the FLiK screening assay with red-shifted fluorophores. *J. Am. Chem. Soc.*, **2013**, 135, 8400-8408.

Z. Fang, J. R. Simard, H. D. Nguyen, T. Phan & D. Rauh. Development of fluorescently labelled kinases for screening of inhibitors targeting inter-domain communications. *European Patent Office*, EP 13 17 0412.4.

Z. Fang, J. R. Simard, D. Plenker, H. D. Nguyen, T. Phan, P. Wolle, S. Baumeister, R. K. Thomas & D. Rauh. Discovery of Inter-Domain Stabilizers - A Novel Assay System for Allosteric Akt Inhibitors. *Nat. Chem. Biol.*, **2013**, eingereicht.

Teile dieser Arbeit wurden bereits in den oben genannten Publikationen veröffentlicht.

Sperrvermerk

Die vorliegende Dissertation beinhaltet vertrauliche Informationen. Die Weitergabe des Inhalts der Arbeit im Gesamten oder in Teilen ist grundsätzlich untersagt. Es dürfen keinerlei Kopien oder Abschriften - auch in digitaler Form - angefertigt werden. Ausnahmen bedürfen der schriftlichen Genehmigung des Autors.

Hiermit versichere ich an Eides statt, dass ich die vorliegende Arbeit selbstständig und nur mit den angegebenen Hilfsmitteln angefertigt habe.

Dortmund, 05.06.2013



.....

Hinweis der Universitätsbibliothek der TU Dortmund zum Sperrvermerk

Die Dissertation wurde am 26. 8. 2013 zur Veröffentlichung auf dem Repository der TU Dortmund eingereicht und der Bibliothek der TU Dortmund ein nicht-ausschließliches Veröffentlichungsrecht eingeräumt. Damit ist der Sperrvermerk widerrufen. Dies wurde durch den Autor am 27.8.2013 per Mail bestätigt.

Daniela Scholz, 27.8.2013

Acknowledgments

First of all, I would like to thank the many people who have supported me through the project and made this entire endeavour possible:

Prof. Dr. Daniel Rauh for the opportunity to carry out my project in his group under his supervision, the interesting topic and his guidance throughout my PhD. Prof. Dr. Herbert Waldmann for giving access to his department and accepting the role as second referee.

The entire Rauh group, their current and former members, for providing a very enjoyable and productive work atmosphere. In particular André Richters for all his good advice and partnership, especially with KinEASE issues. Dr. Haridas Rode, Dr. Matthäus Getlik and Dr. Vijaykumar Pawar for their advice on chemistry questions. Dr. Jeffrey Simard for his support with assay development. Dr. Hoang Duc Nguyen, Dr. Trang Phan and Svenja Mayer-Wrangowski for teaching me to work with insect cells. Dr. Ralf Schneider, Simone Eppmann and Christian Becker for their advice on biochemistry questions. Dr. Christian Grütter for his support in crystallography. And my students Stefan Baumeister, Patrik Wolle and Luis Bering for helping out in the lab.

All the colleagues in the Chemical Genomics Centre, MPI Dortmund and TU Dortmund for their support. Dr. Björn Over, Philipp Thiel, Dr. Hernan Grecco and Dr. Qiang Li for their help on computational tools. Dr. Rolf Rose for teaching me how to use Biacore, and Dr. Anne Kuhlee for NanoTemper. Sandra Bergbrede, Anna Schäfer, Sabine Wohlgemuth, as well as Tim Bergbrede, Astrid Sander, Tina Rogowski from the DPF for their support on insect cell expression. Dr. Andrey Antonchick, Dr. Christian Hedberg, Prof. Dr. Markus Kaiser and Prof. Dr. Frank Schulz for their advice on synthetic problems. Dr. Sven Müller for his help on microscopes. Dr. Nadine Weikart and Dr. Sabine Möcklinghoff for their advice with EPL. Dr. Reiner Große for his help with dielectric constants, and Dr. Rebecca Meyer with fluorescence lifetimes.

The International Max Planck Research School in Chemical Biology, and in particular Prof. Dr. Martin Engelhard, Dr. Waltraud Goody-Hofmann and Christa Hornemann for providing inter-departmental communication and financial support for conferences.

The people from the Lead Discovery Center for the fruitful discussions. Dr. Jan Eickhoff, Dr. Axel Choidas and Carsten Degenhart for their support with screening technology and logistics. Dr. Carsten Schulz-Fademrecht for his advice on synthesis questions. Dr. Uwe Koch for teaching me cheminformatics. Dr. Bert Klebl, Dr. Peter Nussbaumer and Dr. Michael Hamacher for their collaboration.

Our collaboration partners at Merck KgaA for their support. Dr. Stefan Jäkel, Dr. Mark Schütte, Dr. Dirk Müller-Pompalla, Dr. Ansgar Wegener and Kerstin Leiding for providing viruses and help on insect cell expression. Dr. Dieter Dorsch and Claudio-Winfried Ritzert their advice on purification problems.

Prof. Willem van Otterlo from Stellenbosch University, South Africa, and Prof. Dr. Roman Thomas from the University of Cologne for our collaborative projects. Dennis Plenker and Dr. Johannes Heuckmann for performing the cellular experiments. Dr. Klaus Suhling from King's College London, United Kingdom, for his help on fluorescence questions.

Dr. Wolf Hiller and his team from the NMR department for taking and processing my NMR spectra. Dr. Petra Janning and Dr. Andreas Brockmeier for their help on MS issues. Ralf Maserki, Holger Konopka and Thomas Blöß for the technical implementation of my wild ideas.

André Richters, Laura Dietrich, Grant Klimaytys, Dr. Liana Allen, Svenja Mayer-Wrangowski and Julian Engel for proof-reading my thesis.

And finally, my parents for supporting and believing in me throughout my life, regardless of what I decided to do. And special thanks to my girlfriend Laura and all my friends for their moral and mental support.

Abstract



In addition to the catalytically active kinase domain, many kinases feature regulatory domains that govern their activity. Modulating and interfering with these inter-domain interactions presents a major opportunity for understanding biological systems and developing innovative therapeutics. Therefore, small molecule inhibitors that target these interactions with an allosteric mode of action have great value and higher intrinsic selectivity, as these interactions are often unique for a single kinase or kinase family. Protein Kinase B (PKB, also known as Akt) is such a multi-domain kinase and represents an important target in cancer research. A number of allosteric inhibitors have been reported for Akt over the last years, with one of them currently in clinical phase II trials. Their mode of action requires the presence of a regulatory PH domain as they bind at the PH/kinase domain interface, locking Akt into an inactive conformation. This unique binding site enables an extraordinary high selectivity and therefore low off-target toxicity. However, all known inter-domain inhibitors so far are based on the same scaffold, and the discovery of new chemical entities is hampered by the lack of methods to identify such inhibitors in high-throughput screens. This thesis describes the development of iFLiK (interface-FLiK), a fluorescence-based assay that can monitor such inter-domain interactions. Guided by X-ray crystal structures, the assay was designed to sense the conformational changes of the protein associated with these interactions by attaching an environmentally sensitive fluorophore to a suitable site. In order to establish the assay, a series of probe molecules were synthesised and tested for their inhibitory activity in *in vitro* and cellular assays. Furthermore, the proteins required for iFLiK were expressed in insect cells and labelled with various fluorophores, systematically assessing their suitability to report on protein conformations. iFLiK could easily distinguish allosteric from classic ATP-competitive inhibitors, thereby providing a proof of principle that solvatochromic fluorophores are capable to monitor protein-protein interactions when attaching the sensor to the correct position. After extensive and careful assay optimisation and validation with orthogonal assay systems, an in-house library was screened with iFLiK. Novel compounds with a scaffold that was previously not described as allosteric Akt inhibitors were identified.

Zusammenfassung



Die Aktivität vieler Proteinkinasen wird durch das Zusammenspiel der Kinasedomäne mit zusätzlichen regulatorischen Domänen gesteuert. Daher besitzen niedermolekulare Verbindungen, die solche Interdomänen-Interaktionen allosterisch adressieren und modulieren können, einen großen Wert in der chemischen Biologie und der Pharmaforschung, da diese Interaktionen oft spezifisch für bestimmte Kinasen bzw. Kinasefamilien sind, und somit im Gegensatz zu klassischen ATP-kompetitiven Inhibitoren eine höhere Selektivität versprechen. Die Proteinkinase B (PKB, auch genannt Akt) ist eine solche Multidomänen-Kinase und stellt ein wichtiges Zielprotein in der Krebsforschung dar. Im Hochdurchsatzscreening wurden in den letzten Jahren eine neue Familie von allosterischen Akt Inhibitoren entdeckt, deren Wirkmechanismus die Anwesenheit einer regulatorischen PH Domäne voraussetzt, da sie in einer Bindungstasche an der Grenzfläche zwischen der Kinase- und PH Domäne binden und dadurch Akt in einer inaktiven Konformation arretieren. Diese einzigartige Bindetasche führt zu einer außergewöhnlich hohen Selektivität und somit *in vivo* potenziell niedrigen Toxizität durch Reduktion unerwünschter Arzneimittelwirkungen. Allerdings basieren alle bisher bekannten Interdomänen-Inhibitoren auf demselben chemischen Grundgerüst, und die Identifizierung von neuartigen Leitstrukturen wird durch den Mangel an geeigneten Hochdurchsatzmethoden ausgebremst. In der vorliegenden Arbeit wird die Entwicklung von iFLiK (*interface-FLiK*) beschrieben, einem Fluoreszenz-basierten Assay, der solche Interdomänen-Interaktionen detektieren kann. Die für iFLiK benötigten Proteine wurden anhand kristallographischer Informationen konzipiert, in Insektenzellen exprimiert und schließlich mit verschiedenen Fluorophoren gekuppelt, um ihre Eignung als Sensoren für Proteinkonformationen systematisch zu untersuchen. Zur Etablierung des Assays wurden zudem eine Reihe von Sondenmolekülen synthetisiert und auf ihre biologische Aktivität *in vitro* und in BT474 Zellen untersucht. Mit iFLiK konnten allosterische Inhibitoren von ATP-kompetitiven unterschieden und somit ein Machbarkeitsbeweis erbracht werden, dass solvatochrome Fluorophore zur Detektion von Protein-Protein-Interaktionen geeignet sind, wenn der Fluorophor an der korrekten Stelle angebracht ist. Nach sorgsamer und eingehender Assayoptimierung sowie Validierung mit orthogonalen Assaysystemen wurde eine interne Substanzbibliothek mit iFLiK durchmustert. Dadurch konnten Verbindungen mit einem neuartigen Grundgerüst gefunden werden, die vorher nicht als allosterische Akt Inhibitoren bekannt waren.

Table of Contents

TABLE OF ABBREVIATIONS.....	V
LIST OF FREQUENTLY USED COMPOUNDS	XI
LIST OF FREQUENTLY USED PROTEINS.....	XII
1 INTRODUCTION.....	1
1.1 PROTEIN KINASES	1
1.1.1 Kinase Structure and Regulation	2
1.1.2 Kinase Inhibitors	6
1.2 AKT	12
1.2.1 Activation mechanism	13
1.2.2 Akt inhibitors	16
1.2.3 Allosteric Inter-Domain Akt Inhibitors	19
1.3 FLUORESCENCE.....	23
1.3.1 Solvatochromic Fluorophores	24
1.3.2 Förster Resonance Energy Transfer.....	25
1.4 ASSAY TECHNOLOGIES	27
1.4.1 KinEASE.....	28
1.4.2 Fluorescent Labels in Kinases (FLiK)	29
1.4.3 NanoTemper	30
1.4.4 Biacore	31
2 AIMS AND OBJECTIVES	33
3 RESULTS AND DISCUSSION	35
3.1 ASSAY DESIGN	35
3.2 PROTEIN PRODUCTION	37
3.2.1 Protein Expression in Insect Cells	37

3.2.2	Protein Purification <i>via</i> FPLC	40
3.3	SYNTHESIS OF PROBE COMPOUNDS	47
3.4	BIOLOGICAL ACTIVITY OF PROBE COMPOUNDS	52
3.4.1	<i>in vitro</i> Activity	52
3.4.2	Cellular Activity	56
3.5	iFLiK ASSAY DEVELOPMENT	59
3.5.1	Selecting Appropriate Reporter Fluorophore	59
3.5.2	Determining the Optimal Enzyme Construct	67
3.5.3	Optimisation of Assay Conditions	71
3.5.4	Validation with NanoTemper Assay	81
3.5.5	Validation with Biacore Assay	93
3.6	HIGH-THROUGHPUT SCREENING	95
3.6.1	Primary Screen of RL Library	95
3.6.2	Primary Screen of Waldmann Library	97
3.6.3	Secondary Screen	102
3.7	CRYSTALLISATION	108
3.8	SUMMARY AND CONCLUSION	110
3.9	FUTURE WORK	113
4	EXPERIMENTAL	115
4.1	GENERAL EXPERIMENTAL	115
4.1.1	Instruments	115
4.1.2	Materials and Consumables	115
4.2	PROTEIN PRODUCTION	116
4.2.1	Expression	116
4.2.2	Purification	120
4.3	BIOCHEMICAL ASSAYS	121
4.3.1	KinEASE	121

4.3.2	iFLiK.....	122
4.3.3	NanoTemper	123
4.3.4	Biacore	124
4.3.5	Tryptic Digest	124
4.3.6	Mass Spectrometry.....	125
4.4	CELLULAR EXPERIMENTS	126
4.5	PROTEIN CRYSTALLISATION	126
4.6	MOLECULAR DOCKING	126
4.7	COMPOUND SYNTHESIS	127
4.7.1	<i>tert</i> -Butyl 2-chloropyridin-4-ylcarbamate (55)	127
4.7.2	<i>tert</i> -Butyl 2-chloro-3-formylpyridin-4-ylcarbamate (56).....	128
4.7.3	2-Chloro-3-formylpyridin-4-amine (57)	129
4.7.4	4-(1,3-Dioxolan-2-yl)benzotrile (59)	129
4.7.5	1-(4-(1,3-Dioxolan-2-yl)phenyl)-2-phenylethanone (60).....	129
4.7.6	2-(4-(1,3-Dioxolan-2-yl)phenyl)-5-chloro-3-phenyl-1,6-naphthyridine (61)	130
4.7.7	4-(5-Oxo-3-phenyl-5,6-dihydro-1,6-naphthyridin-2-yl)benzaldehyde (62).....	130
4.7.8	2-(4-((4-(2-Oxo-2,3-dihydro-1 <i>H</i> -benzo[<i>d</i>]imidazol-1-yl)piperidin-1-yl)methyl)phenyl)-3-phenyl-1,6-naphthyridin-5(6 <i>H</i>)-one (63a)	131
4.7.9	2-(4-((4-(5-Chloro-2-oxo-2,3-dihydro-1 <i>H</i> -benzo[<i>d</i>]imidazol-1-yl)piperidin-1-yl)methyl)phenyl)-3-phenyl-1,6-naphthyridin-5(6 <i>H</i>)-one (63b)	132
4.7.10	2-(4-((3,4-Dihydroisoquinolin-2(1 <i>H</i>)-yl)methyl)phenyl)-3-phenyl-1,6-naphthyridin-5(6 <i>H</i>)-one (63c)	132
4.7.11	Methyl 1-(4-(5-oxo-3-phenyl-5,6-dihydro-1,6-naphthyridin-2-yl)benzyl)piperidine-4-carboxylate (63d).....	133
4.7.12	2-(4-((4-(4-Methoxyphenyl)piperazin-1-yl)methyl)phenyl)-3-phenyl-1,6-naphthyridin-5(6 <i>H</i>)-one (63e)	134
4.7.13	3-Phenyl-2-(4-((4-(pyrimidin-2-yl)piperazin-1-yl)methyl)phenyl)-1,6-naphthyridin-5(6 <i>H</i>)-one (63f)	134

4.7.14	3-Phenyl-2-(4-((4-(tetrahydrofuran-2-carbonyl)piperazin-1-yl)methyl)phenyl)-1,6-naphthyridin-5(6 <i>H</i>)-one (63g).....	135
5	APPENDIX	137
5.1	ESTABLISHING THE KINEASE ASSAY	137
5.2	ESTABLISHING THE BIACORE ASSAY.....	140
5.3	NMR SPECTRA.....	142
	TABLE OF REFERENCES	149

Table of Abbreviations

Å	Ångström, 10^{-10} m
aa	amino acid
Ab	antibody
Abl	Abelson murine leukemia viral oncogene homologue
Ac	acetyl
AC ₅₀	concentration of half-maximal activity
ADP	adenosine-5'-diphosphate
AF568	Alexa Fluor 568
ALK	anaplastic lymphoma kinase
AMP-PNP	adenylyl-imidodiphosphate
anh.	anhydrous
Ar	aryl
ATP	adenosine-5'-triphosphate
AU	arbitrary units
A _x	absorption at wavelength x nm
bar	10^5 N/m ²
βARK	β-adrenergic receptor kinase 1
BCR	breakpoint cluster region
βME	β-mercaptoethanol
Boc	<i>tert</i> -butyloxycarbonyl
BRAF	serine/threonine-protein kinase B-Raf
Brij-35	polyoxyethylen (23) laurylether
BSA	bovine serum albumine
BTK	Bruton's tyrosine kinase
CBB	Coomassie Brilliant Blue
CDK	cyclin-dependent kinases
CHAPS	3-[(3-Cholamidopropyl)dimethylammonio]-1-propanesulfonate
CML	chronic myelogenous leukemia
conc.	concentrated
COSY	correlation spectroscopy
cSrc	cellular sarcoma kinase

d	day, 24 h
Da	Dalton, g/mol
DCM	dichloromethane
ddH ₂ O	Milli-Q grade water (Millipore)
dil.	diluted
DIPEA	<i>N,N</i> -diisopropylethylamine
DMAP	4-dimethylaminopyridine
DMF	<i>N,N</i> -dimethylformamide
DMSO	dimethylsulfoxide
DNA	deoxyribonucleic acid
DNA-PK	DNA-dependent protein kinase
DTT	dithiothreitol
ϵ_x	molar extinction coefficient at x nm
EDC	1-ethyl-3-(3-dimethylaminopropyl)carbodiimide
EDG	electron donating group
EDTA	ethylenediaminetetraacetic acid
EGFP	enhanced green fluorescent protein
EGFR	epidermal growth factor receptor
eq	equivalent
ESI	electrospray ionisation
Et	ethyl
ETK	epithelial and endothelial tyrosine kinase
EWG	electron withdrawing group
FDA	Food and Drug Administration
FPLC	fast protein liquid chromatography
FLiK	fluorescent labels in kinases
fl_x	fluorescence intensity at wavelength x nm
FRB	FKBP12-rapamycin binding
FRET	Förster resonance energy transfer
g	multiples of standard gravitational acceleration, 9.83 m/s ²
GF	gel filtration
GI ₅₀	concentration of half maximal growth inhibition
GIST	gastrointestinal stromal tumor
GndCl	guanidinium chloride

h	hour, 60 min
η	refractive index
HEPES	4-(2-hydroxyethyl)-1-piperazineethanesulfonic acid
HER2	human epidermal growth factor receptor 2
HM	hydrophobic motif
HMBC	heteronuclear multiple-bond correlation spectroscopy
HPLC	high-performance liquid chromatography
HR-MS	high resolution mass spectrometry
HSQC	heteronuclear single quantum coherence
HTRF	homogeneous time-resolved fluorescence
HTS	high-throughput screening
Hz	Hertz, 1/s
IAA	iodoacetamide
IANBD	<i>N</i> -((2-(iodoacetoxy)ethyl)- <i>N</i> -methyl)amino-7-nitrobenz-2-oxa-1,3-diazole
IC ₅₀	half-maximal inhibitory concentration
ID	inter-domain
IEX	ion exchange
IFU	infectious units
IGF-1R	insulin-like growth factor receptor
ILK	integrin-linked kinase
IP ₄	inositol 1,3,4,5-tetrakisphosphate
iPr	<i>iso</i> -propyl
IR	infrared
ITC	isothermal titration calorimetry
ITK	IL2-inducible T-cell kinase
JAK	janus kinase
JNK	c-Jun N-terminal kinases
JIP1	JNK interacting protein 1
K _d	dissociation constant
K _m	Michaelis constant
L	litre, 10 ⁻³ m ³
LC-MS	mass spectrometry-coupled liquid chromatography
LR-MS	low resolution mass spectrometry
M	mol/L

μ	dipol moment
MAPK	mitogen-activated protein kinase
Me	methyl
min	minute, 60 s
MK2	mitogen-activated protein kinase-activated protein kinase 2
MKK4	mitogen-activated protein kinase kinase 4
MKK7	mitogen-activated protein kinase kinase 7
MOI	multiplicity of infection
mRFP	monomeric red fluorescent protein
MS	mass spectrometry
MS/MS	tandem mass spectrometry
MST	microscale thermophoresis
mTOR	mammalian target of rapamycin
mTORC1	mTOR-raptor complex
mTORC2	mTOR-riCTOR complex
mw	microwave
NBD	nitrobenz-2-oxa-1,3-diazole
NSCLC	non-small cell lung cancer
NMR	nuclear magnetic resonance
NOESY	Nuclear Overhauser effect spectroscopy
NP-40	polyethylenglycol(40)-nonylphenolether
NTA	nitrilotriacetic acid
p38 α	mitogen-activated protein kinase 14
PAGE	polyacrylamide gel electrophoresis
PDB	protein data bank
PDGFR	platelet-derived growth factor receptor
PDK1	phosphoinositide-dependent kinase-1
PDK2	phosphoinositide-dependent kinase-2
PI3K	phosphoinositide 3-kinase
PIF	PDK1-interacting fragment
PIKK	phosphatidylinositol 3-kinase related kinase
PIP ₂	phosphatidylinositol (4,5)-bisphosphate
PIP ₃	phosphatidylinositol (3,4,5)-trisphosphate
PBS	phosphate-buffered saline

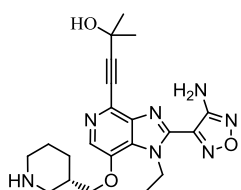
PE	petrol ether
PEG	polyethylene glycol
Ph	phenyl
PH	Pleckstrin homology
pI	isoelectric point
PKA	Protein Kinase A
PKC	Protein Kinase C
PKG	Protein Kinase G
PP2A	Protein Phosphatase 2 α isoform
PPI	protein-protein interaction
ppm	parts per million
Pr	n-propyl
PRK2	Protein Kinase C-related protein kinase-2
PTEN	phosphatase and tensin homolog
PyMPO	4-(5-(4-methoxyphenyl)oxazol-2-yl)pyridinium
Φ	fluorescence quantum yield
R	rest
RLK	resting lymphocyte kinase
RM	reaction mixture
ROCK	Rho-associated protein kinase
RP	reversed-phase
rpm	revolutions per minute
RSK	ribosomal s6 kinase
RT	room temperature
RTK	receptor tyrosine kinase
RU	resonance units
S6K	70 kDa ribosomal protein S6 kinase 1
SAR	structure-activity relationship
SDS	sodium dodecyl sulfate
SGK	serum-and glucocorticoid-induced protein kinase
SH	Src homology
SPR	surface plasmon resonance
STD	saturation transfer difference
SX	size exclusion

TBK1	TANK-binding kinase 1
TBS	Tris-buffered saline
tBu	<i>tert</i> -butyl
tBuLi	<i>tert</i> -butyllithium
TEC	tyrosine kinase expressed in hepatocellular carcinoma
TEV	Tobacco Etch Virus
Th	Thomson, 1 Da/e
THF	tetrahydrofuran
TLC	thin layer chromatography
Tris	tris(hydroxymethyl)aminomethane
Triton X-100	polyethylene glycol <i>p</i> -(1,1,3,3-tetramethylbutyl)-phenyl ether
Ts	tosyl, 4-toluenesulfonyl
Tween-20	polyoxyethylene (20) sorbitan monolaurate
UV	ultra violet
VEGFR	vascular endothelial growth factor receptor
wt	wild type
w/	with
w/o	without
w/v	weight per volume

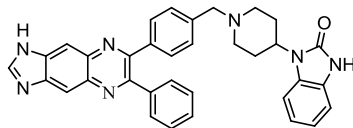
Table 1 Amino acids and their abbreviations.

Amino acid	3-letter code	1-letter code
alanine	Ala	A
arginine	Arg	R
asparagine	Asn	N
aspartic acid	Asp	D
cysteine	Cys	C
glutamic acid	Glu	E
glutamin	Gln	Q
glycine	Gly	G
histidine	His	H
isoleucine	Ile	I
leucine	Leu	L
lysine	Lys	K
methionine	Met	M
phenylalanine	Phe	F
proline	Pro	P
serine	Ser	S
threonine	Thr	T
tryptophan	Trp	W
tyrosine	Tyr	Y
valine	Val	V

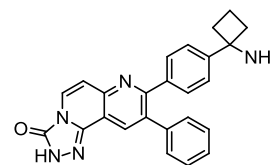
List of Frequently Used Compounds



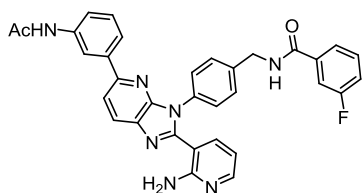
GSK690693
32



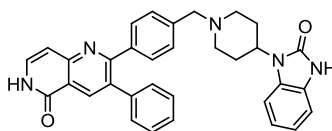
Akti-1/2
49



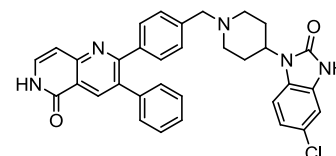
MK-2206
50



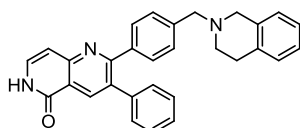
53



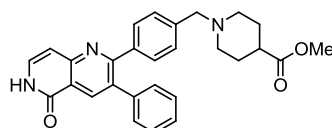
63a



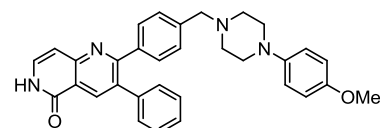
63b



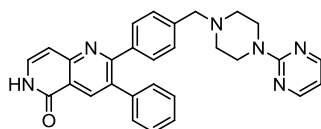
63c



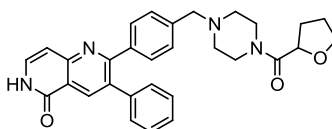
63d



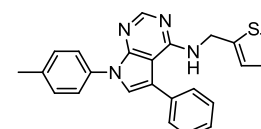
63e



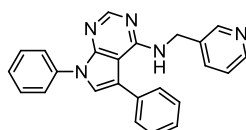
63f



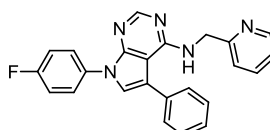
63g



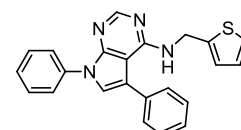
75a



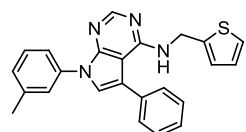
75b



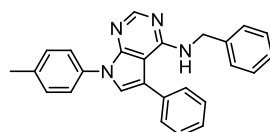
75c



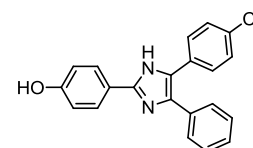
75d



75e



75f



86a

List of Frequently Used Proteins

Akt1 wt

human Akt1 (UniProt entry P31749)

residues 1-480

N-terminal MSFF-His₆-DFDIPTTENLYFQGAMGS

Akt2 wt

human Akt2 (UniProt entry P31751)

residues 1-481

N-terminal MSYY-His₆-DYDIPTTENLYFQGAMGS

ΔPH-Akt1

human Akt1 (UniProt entry P31749)

residues 118-480 (S473D)

N-terminal MSYY-His₆-DYDIPTTENLYFQGAMGSM

de91

human Akt1 (UniProt entry P31749)

residues 2-445 (E49C, C296S, C310S, C344S)

N-terminal MGSTS-His₆-DHITSLYKKAGFENLYFQG

de92

human Akt1 (UniProt entry P31749)

residues 2-480 (E49C, C296S, C310S, C344S)

N-terminal MGSTS-His₆-DHITSLYKKAGFENLYFQG

pHT1023

human Akt1 (UniProt entry P31749)

residues 2-480 (E49C, C296S, C310S, C344S, C460S)

N-terminal MGSTS-His₆-DHITSLYKKAGFENLYFQG

1 Introduction

Second only to cardiovascular failures, cancer is still one of the leading causes of death in the western world, accounting for 13% of all deaths worldwide in 2008.^{1,2} Prognoses for the future project the number of deaths to reach 13.1 million in 2030. The most lethal forms of cancer are breast, prostate, colorectal, lung, cervical, pancreas and stomach cancers.³

Hanahan and Weinberg have summarised the characteristics that define cancer: Tumour cells grow indefinitely, become independent from growth signals, are able to avoid apoptosis, promote increased angiogenesis, possess the ability to invade into foreign tissue, evade immune system responses and reprogramme their energy metabolism.⁴ A variety of therapies have been developed over the years to address these indications, ranging from surgical removal of affected tissue to radiotherapy. Due to the lack of knowledge about the precise mechanisms of cancer in the last century, treating patients with chemotherapy had focussed primarily on prohibiting cell replication altogether by deploying cytostatic agents. While there have been many successful cases of patients recovering from cancer after chemotherapy, it has proven ineffective as a general method to cure cancer. In addition, this unspecific approach to cancer treatment had severe side effects such as nausea, loss of hair, fatigue and anaemia.

Over the course of the last decade, an increasing understanding of the molecular mechanisms that lead to cancer has enabled targeted therapies. Imatinib as a prime example has shown that protein kinase inhibitors can be powerful drugs for the effective long-term treatment of cancer.⁵ This has put kinases into the focus of modern drug discovery and cancer research.

1.1 Protein Kinases

Kinases are enzymes belonging to the class of transferases that catalyse the transfer of the γ -phosphate group of ATP onto a substrate, which is one of the most important classes of post-translational modifications. In the case of protein kinases, these substrates are other proteins and serve as crucial components of signalling pathways. These kinase-catalysed phosphorylations often change the charge or conformation of their substrates, thereby activating or inactivating them, influencing the formation of multi-protein complexes or altering their subcellular localisation. Kinases have complex functions in the regulation of cellular processes such as proliferation, differentiation, metabolism and apoptosis. As their molecular

counterparts, phosphatases catalyse dephosphorylation reactions to counteract kinases. Relatively unspecific by themselves, they gain their selectivity in an ensemble of other proteins by forming multi-component complexes.

Misregulation of kinase activity is the cause for many diseases, ranging from Alzheimer's disease, diabetes mellitus and atherosclerosis to Parkinson's disease, obesity and inflammatory diseases as well as amyotrophic lateral sclerosis and, most prominently, cancers of various kinds. This misregulation can manifest in different forms, e.g. gene amplification or transcriptional changes that lead to overexpression of the protein, altered enzyme activity by mutation or a misregulation of the respective phosphatase antagonist.

1.1.1 Kinase Structure and Regulation

Albeit diverse in their primary amino acid sequence, the 518 genetically encoded human protein kinases are remarkably similar in their three-dimensional structure. The pivotal feature of all kinases is the catalytically active kinase domain, consisting of an N-terminal lobe (N-lobe), usually containing an array of β -sheets, and a C-terminal lobe (C-lobe) dominated by α -helices, both connected *via* the flexible hinge region. The active site is located between these two subdomains, containing the ATP binding pocket, which contacts the hinge region, and the adjacent substrate-binding pocket (Figure 1). An (often sterically demanding) amino acid is located at the N-terminal end of the hinge region, limiting the size of the binding pocket and thusly known as gatekeeper residue. Substrate access to the active site is controlled by a flexible loop, the activation loop (A-loop), starting with the conserved amino acid sequence Asp-Phe-Gly (DFG). The aspartate is crucial in the coordinative network of hydrogen bonds to the phosphate groups of ATP, which is further activated for the catalytic transfer onto the substrate by complexation with Mg^{2+} . In the active state of a protein kinase, this DFG-motif occupies a hydrophobic back pocket adjacent to the ATP binding site next to the α C-helix of the N-lobe. In the inactive state, the DFG-motif can swing out of the hydrophobic back pocket, resulting in an A-loop conformation that partially blocks the ATP and substrate binding site.⁶ In most cases, these conformational changes are the result of phosphorylations of residues located within the activation loop, which are responsible for kinase activation. However, not all kinases are known to be able to adopt such a DFG-out conformation, and the overall regulation of kinases is much more complex and requires additional regulatory elements.

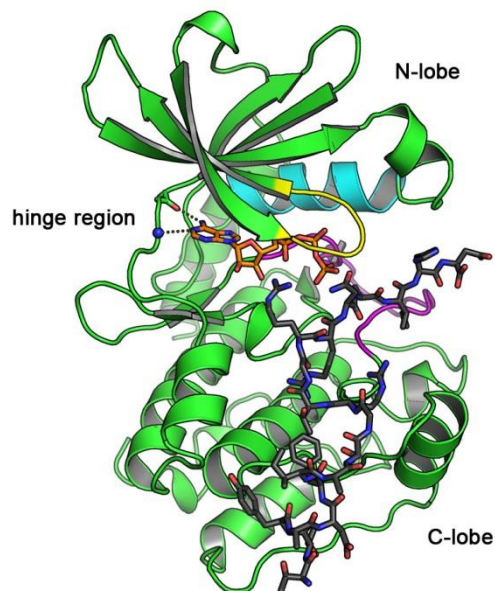


Figure 1 Structural features of a typical kinase domain (co-crystal structure of PKA with AMP-PNP shown here, PDB code 1ATP). The α C-helix is coloured in cyan, activation loop in magenta, glycine-rich loop in yellow and the substrate in dark grey. The ATP analogue AMP-PNP (orange sticks) forms hydrogen bonds to the backbone of amino acids in the hinge region.

While kinase-catalysed phosphorylations affect the activity of their substrates, protein kinases themselves are often regulated in highly intricate sequences. Apart from the canonical kinase domain, in which the aforementioned A-loop phosphorylations determine their catalytic activity, many kinases also feature additional domains which can regulate their activity.

One example of such allosteric regulation *via* regulatory domains is the Abelson murine leukemia viral oncogene homologue (Abl, also known as JTK, p150, Abl1 or c-Abl). Abl is an extensively investigated protein kinase, and involved in signalling pathways regulating cell proliferation, differentiation and apoptosis, and misregulation of Abl has been associated with tumorigenesis.⁷ A prominent example of a malignancy induced by the misregulation of Abl is chronic myelogenous leukemia (CML), which is characterised by an increased growth of myeloid cells in the bone marrow.⁸ It is caused by the translocation of a segment of the breakpoint cluster region (BCR) on chromosome 22 to the Abl gene on chromosome 9, yielding a new, fused BCR-Abl enzyme.⁹ This fusion protein shows tyrosine kinase hyperactivity and is insensitive to native regulatory signals. In addition to the catalytically active kinase domain, Abl possesses an N-terminal cap, two Src homology domains (SH3 and SH2), a DNA-binding domain and an actin-binding domain.¹⁰ The N-terminal cap can be myristoylated, which plays a major role in the auto-inhibition of the Abl phosphorylation activity.¹¹ X-ray crystallography reveals that the myristate moiety is lodged in a deep pocket within the C-lobe of the kinase domain and causes a 90° bend of the α I-helix. This bending of residues 518-530 enables the SH3 and SH2 domains to approach and bind to the kinase domain (PDB entry

1OPL).¹² Mutations of the residues connecting the SH3 and SH2 domain have shown that these two domains interact strongly with each other, thereby acting as a rigid clamp on the kinase domain.¹³ Upon phosphorylation of Tyr245 by Src-family kinases, the SH domains adopt a different association pattern with the kinase domain: The SH2 domain now sits on top of the N-lobe, while the SH3 domain appears to be flexible in solution.¹⁴ In the constitutively active fusion protein BCR-Abl, the regulatory N-terminal cap has been replaced, rendering it incapable of myristoylation-induced auto-inhibition.

Another example is the AGC-family member phosphoinositide-dependent kinase-1 (PDK1), which is considered a master kinase and upstream activator of many other AGC kinases vital for growth factor and insulin signalling such as Akt, S6K, PKC and SGK.¹⁵ PDK1 was first purified and characterised by Alessi *et al.* in 1997,¹⁶ and later validated as a potential anti-cancer drug target.¹⁷ PDK1 features a catalytically active kinase domain with a hydrophobic groove on the N-lobe as well as a PH domain for the recognition of PIP₃ and recruitment to the plasma membrane.¹⁸ However, in contrast to the other family members, PDK1 does not possess the C-terminal hydrophobic motif (HM) which binds intramolecularly to the hydrophobic groove.¹⁹ Instead, the hydrophobic groove in PDK1 serves as a recognition site for the HMs of its substrate kinases.¹⁵ This recruitment mechanism enables PDK1 to phosphorylate the activation loop of the substrate kinase and thereby activating its basal kinase activity.²⁰ After A-loop phosphorylation, the substrate HM is expelled from the PDK1 hydrophobic groove, complements with its own hydrophobic groove and fully activates the substrate kinase. In 1999, Balendran *et al.* discovered that the C-terminus of the Protein Kinase C-related protein kinase-2 (PRK2) interacts with the hydrophobic groove of PDK1, and termed it the PDK1-interacting fragment (PIF).²¹ Hence, the hydrophobic groove became known as the PIF binding pocket. When treated with PIF, the activity of PDK1 increases dramatically.

The c-Jun N-terminal kinases (JNKs), comprising the three isoforms JNK1, JNK2 and JNK3, are a subgroup of the MAP kinase family and are commonly known as stress activated kinases.²² Like many members of the MAP kinase family, the activity of JNKs is regulated by upstream kinases such as MKK4 or MKK7 *via* A-loop phosphorylation.²³ To achieve selectivity in the regulation of MAPKs, their activation is predominantly mediated by scaffolding proteins. Originally identified by Whitmarsh *et al.* in 1998 in yeast two-hybrid cells, the JNK interacting protein 1 (JIP1) was found to selectively bind to JNK1 and its upstream activators MKK7 and MLK3.²⁴ Bringing these enzymes in spatial proximity to each other, JIP1 forms a quaternary complex in which MLK3 can phosphorylate MKK7, which in turn activates JNK1. Although this demonstrated the physiological role of JIP1 in the activation of JNK1, overex-

pression of JIP1 has been found to inhibit JNK1 activity, possibly by retaining the JNK1-JIP1 complex in the cytosol.²⁵ In 2004, Heo *et al.* published the crystal structure of JNK1 in complex with pepJIP1, a 11-mer peptide consisting of the sequence which is essential for the interaction of JIP1 with JNK1 (PDB entry 1UKI).²⁶ The structure showed that pepJIP1 binds to the C-lobe of JNK1 and induces a rotation of the N-lobe against the C-lobe by 15°. This results in a less ordered activation loop, which might render it more accessible for the phosphorylation by MKK7. Recent molecular dynamics simulations suggest that the electrostatic contribution to the free energy of binding of the JNK1-pepJIP1 complex is decisive for its high selectivity.²⁷

Like many receptor tyrosine kinases, the epidermal growth factor receptor (EGFR) forms homo-dimers in an equilibrium. Binding of the native epidermal growth factor to the extracellular receptor domains stabilise the activated dimeric state, leading to an autophosphorylation of the intracellular kinase domains.²⁸ Another receptor tyrosine kinase, the insulin-like growth factor receptor (IGF-1R), consists of two extracellular ligand-binding domains (α -subunits) and two cytoplasmic domains (β -subunits).²⁹ The α -subunits are covalently cross-linked *via* disulfide bridges and form a receptor complex that can bind to its native ligand IGF-1 and insulin. The β -subunits consist of the transmembrane- and the kinase domain. Upon ligand binding, the IGF-1R tetramer undergoes conformational changes, which triggers autophosphorylation of its kinase domain, resulting in a gain of IGF-1R phosphorylation activity and the initiation of MAPK and PI3K signalling pathways.^{30,31}

The activity of cyclin-dependent kinases (CDKs) is dependent on their binding interaction with cyclins, which represents a unique feature throughout the kinome. The various subtypes of cyclins (cyclin A, B, D and E in humans) are regulatory proteins that are expressed at different stages in the cell cycle, each activating individual CDKs.³² CDK2 forms active complexes with cyclins A and E. The crystal structure of the CDK2 in complex with cyclin A solved by Jeffrey *et al.* revealed the specific interactions between these two proteins (PDB entry 1FIN).³³ Cyclin A binds firmly and extensively to the N- and C-lobe of the kinase domain *via* hydrophobic and polar interactions. In particular, it binds to the activation loop and the so-called PSTAIRE-motif on the α C-helix, causing a 90° rotation of the helix, thereby restructuring the ATP binding pocket and stabilising an active conformation. A number of cyclin-interacting proteins are known, such as p21WAF1, p57Kip2, p16INK4a, p18INK6 and p27Kip1, which function as native CDK inhibitors (CDKIs), representing important tumor suppressor proteins. The N-terminal inhibitory domain of the cyclin-dependent kinase inhibitor 1B (p27Kip1 or CDKN1B) was found to bind to the CDK2/cyclin A complex by inter-

acting with the CDK2 N-lobe and the cyclin A cyclin box, preventing the activation of CDK2 by blocking the ATP binding pocket (PDB entry 1JSU).³⁴ Presumably, other CDKs exhibit similar interactions with their respective target CDK/cyclin complex.

The mammalian target of rapamycin (mTOR) is a member of the phosphatidylinositol 3-kinase related kinases (PIKKs) and is involved in the PI3K/Akt/mTOR signalling pathway mentioned above. It can form two different complexes with different sets of proteins, the mTOR complex 1 (mTORC1) with raptor, mLST8 and PRAS40, and the mTOR complex 2 (mTORC2) with rictor, mSIN1 and mLST8, each with distinct biological functions.³⁵ The natural product rapamycin, isolated from the bacterium *Streptomyces hygroscopicus*, inhibits mTORC1 in an allosteric fashion. Mediated by hydrophobic interactions with the 12 kDa FK506-binding protein (FKBP12), it forms a complex that is able to inhibit the activity of mTORC1 by binding to the C-terminus of mTOR, also termed the FKBP12-rapamycin binding (FRB) domain.³⁶ Interestingly, FKBP12 does not seem to interact with mTOR directly, the majority of contacts are formed by rapamycin. Probably, this binding relays conformational changes throughout mTOR and interferes with mTORC1 complex formation.³⁷ However, the exact inhibition mechanism remains unclear.

1.1.2 Kinase Inhibitors

From a pharmacologic perspective, small-molecule kinase inhibitors are ideal reagents for perturbing and investigating kinase function at any stage of cellular development.³⁸ Variations in the kinase inhibitor concentration allow for graded phenotypes and a transient temporal control. Such features are essential for quantifying the flux of information that passes through molecular networks and for elucidating network architecture and dynamics to, for example, assess potentially druggable nodes beyond individual genes and proteins.³⁹

The development of kinase inhibitors traditionally focusses on ATP-competitive small molecules, as all kinases require ATP as a cofactor. However, ATP-competitive inhibitors (or type I inhibitors) are generally troubled by selectivity issues, since the ATP binding pocket is highly conserved across the whole kinome (Figure 2).⁴⁰ One solution is to target the so-called hydrophobic back pocket adjacent to the ATP binding site, which is less conserved and therefore offers better chances of selectivity.⁶ By occupying the back pocket, the conserved DFG motif is pushed out into the ATP binding region, thus blocking the access of ATP to the hinge region, and the activation loop is kept in an inactive conformation, the DFG-out conformation (type III inhibitors). Inhibitors that contact the hinge region but also stretch into the hydrophobic back pocket are thusly categorised as type II inhibitors. Recently, it has been sugges-

ted that the increased potency of type II and III inhibitors arise from the increased drug residence time on the target kinase, as binding such an inhibitor induces and stabilises the inactive conformation, removing it from the equilibrium between the active DFG-in and the inactive DFG-out conformation and thereby shifting it towards the inhibited state.⁴¹ In the inactive conformation, dissociation of the inhibitor from the kinase is decreased, as the dissociation trajectory is blocked by residues of the activation loop.⁴² Finally, type IV inhibitors are compounds which bind at remote sites on the kinase and regulate its activity e.g. by stabilising inactive conformations.⁴³

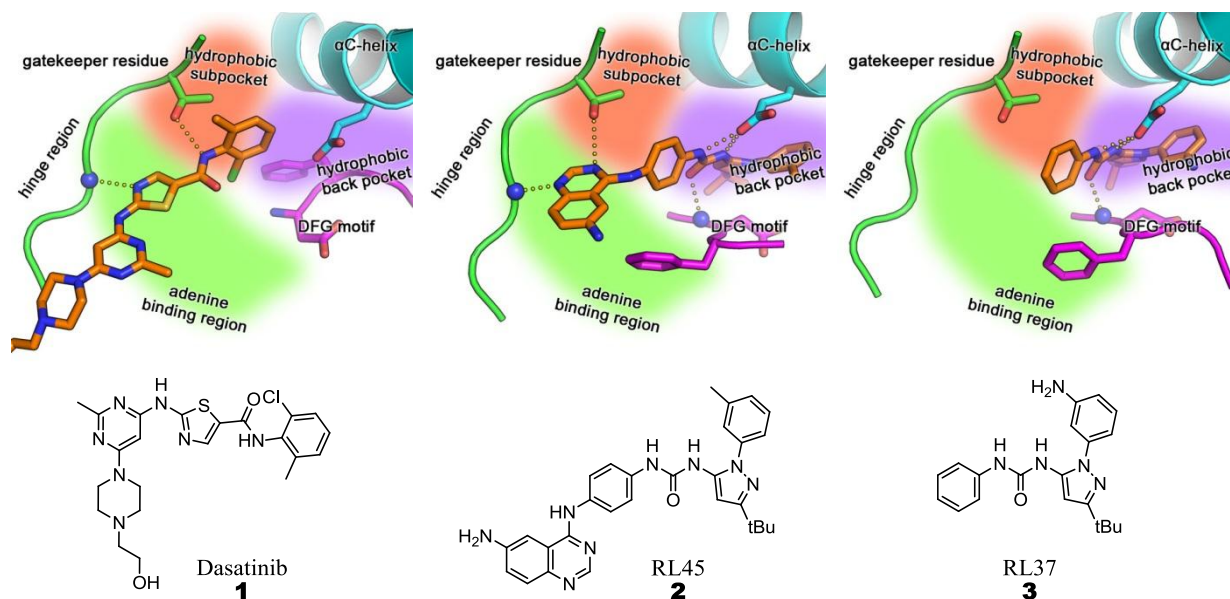


Figure 2 Examples of type I-III kinase inhibitors and their different binding modes in cSrc. Left: Dasatinib (PDB code 3G5D) as an example of a type I kinase, occupying the adenine binding region and forming hydrogen bonds to the gatekeeper and the hinge region. The activation loop is in the DFG-in conformation. Middle: The type II inhibitor RL45 (PDB code 3GCQ) occupies both the adenine binding region and the hydrophobic back pocket, forcing the DFG motif into an inactive DFG-out conformation. Right: The type III inhibitor RL37 (PDB code 3F3U) resides only in the hydrophobic back pocket and inhibits by arresting the DFG motif in the DFG-out conformation, which thereby blocks binding of ATP.

The BCR-Abl inhibitor imatinib is the first clinically approved kinase inhibitor. In a high-throughput screening campaign, compounds of the 2-phenylaminopyrimidine series were identified as hits and were further developed into a successful drug.⁴⁴ This immense success heralded the beginning of extensive clinical development of kinase inhibitors as anti-cancer drugs. As of today, 15 small molecule kinase inhibitors have been approved by the FDA (Table 2 and Figure 3): The multitarget type I inhibitors axitinib (trade name Inlyta by Pfizer), pazopanib (trade name Votrient by GlaxoSmithKline) and sunitinib (trade name Sutent by Pfizer) primarily address VEGFR and PDGFR, and were approved for the treatment of renal cell carcinoma in 2012, 2009 and 2006, respectively. Another type I inhibitor bosutinib (trade name Bosulif by Pfizer) targets the BCR-Abl kinase and was approved in 2012 for CML.

Crizotinib (trade name Xalkori by Pfizer) is a type I EML4-ALK inhibitor and was approved for non-small cell lung cancer in 2011. Dasatinib (trade name Sprycel by Bristol-Myers Squibb) is another type I multitarget inhibitor, that was approved in 2006 for prostate cancer. The type I EGFR inhibitors erlotinib (trade name Tarceva by Roche) and gefitinib (trade name Iressa by AstraZeneca) were approved by the FDA for the treatment of NSCLC in 2005 and 2003, respectively. The first clinically approved kinase inhibitor imatinib (trade name Gleevec by Novartis) inhibits BCR-Abl in a type II fashion, approved in 2001 for the treatment of CML and in 2002 for GIST. The type I inhibitor lapatinib (trade name Tyverb by GlaxoSmithKline, approved in 2007) addresses EGFR and HER2 in breast cancer. In 2007 and 2012, respectively, the type II BCR-Abl inhibitors nilotinib (trade name Tasisign by Novartis) and ponatinib (trade name Iclusig by ARIAD Pharmaceuticals) were approved as second-line treatment for CML. Ruxolitinib (trade name Jakavi by Novartis) was approved in 2011 for the treatment of myelofibrosis by inhibiting JAK. The broadband type II inhibitor sorafenib (trade name Nexavar by Bayer) was approved for renal cancer in 2005 and liver cancer in 2007. The type I inhibitor Vemurafenib (trade name Zelboraf by Roche) targets BRAF and was approved in 2011 for the treatment of melanoma.

Table 2 Summary of current kinase inhibitors approved for cancer treatment by the FDA. RCC = renal cell carcinoma. CML = chronic myeloid leukemia. NSCLC = non-small cell lung cancer. ALL = acute lymphoblastic leukemia. GIST = gastrointestinal stromal tumor.

Inhibitor	Trade name	Company	Mode of action	Target kinases	FDA approval
Axitinib	Inlyta	Pfizer	Type I	VEGFR, PDGFR, cKIT	2012: RCC
Bosutinib	Bosulif	Pfizer	Type I	BCR-Abl	2012: CML
Crizotinib	Xalkori	Pfizer	Type I	EML4-ALK	2011: NSCLC
Dasatinib	Sprycel	BMS	Type I	BCR-Abl, cKIT	2006: CML, ALL
Erlotinib	Tarceva	Roche	Type I	EGFR	2005: NSCLC
Gefitinib	Iressa	AstraZeneca	Type I	EGFR	2003: NSCLC
Imatinib	Gleevec	Novartis	Type II	BCR-Abl	2001: CML 2002: GIST
Lapatinib	Tyverb	GSK	Type I	HER2, EGFR	2007: breast cancer
Nilotinib	Tasisign	Novartis	Type II	BCR-Abl, cKIT, LCK, DDR, PDGFR	2007: CML
Pazopanib	Votrient	GSK	Type I	VEGFR, PDGFR, cKIT	2009: NSCLC
Ruxolitinib	Jakavi	Novartis	Type I	JAK	2011: myelofibrosis
Ponatinib	Iclusig	ARIAD	Type II	BCR-Abl	2012: CML, ALL
Sorafenib	Nexavar	Bayer	Type II	VEGFR, PDGFR	2005: RCC 2007: liver cancer
Sunitinib	Sutent	Pfizer	Type I	VEGFR, PDGFR, cKIT	2006: RCC, GIST
Vemurafenib	Zelboraf	Roche	Type I	BRAF	2011: melanoma

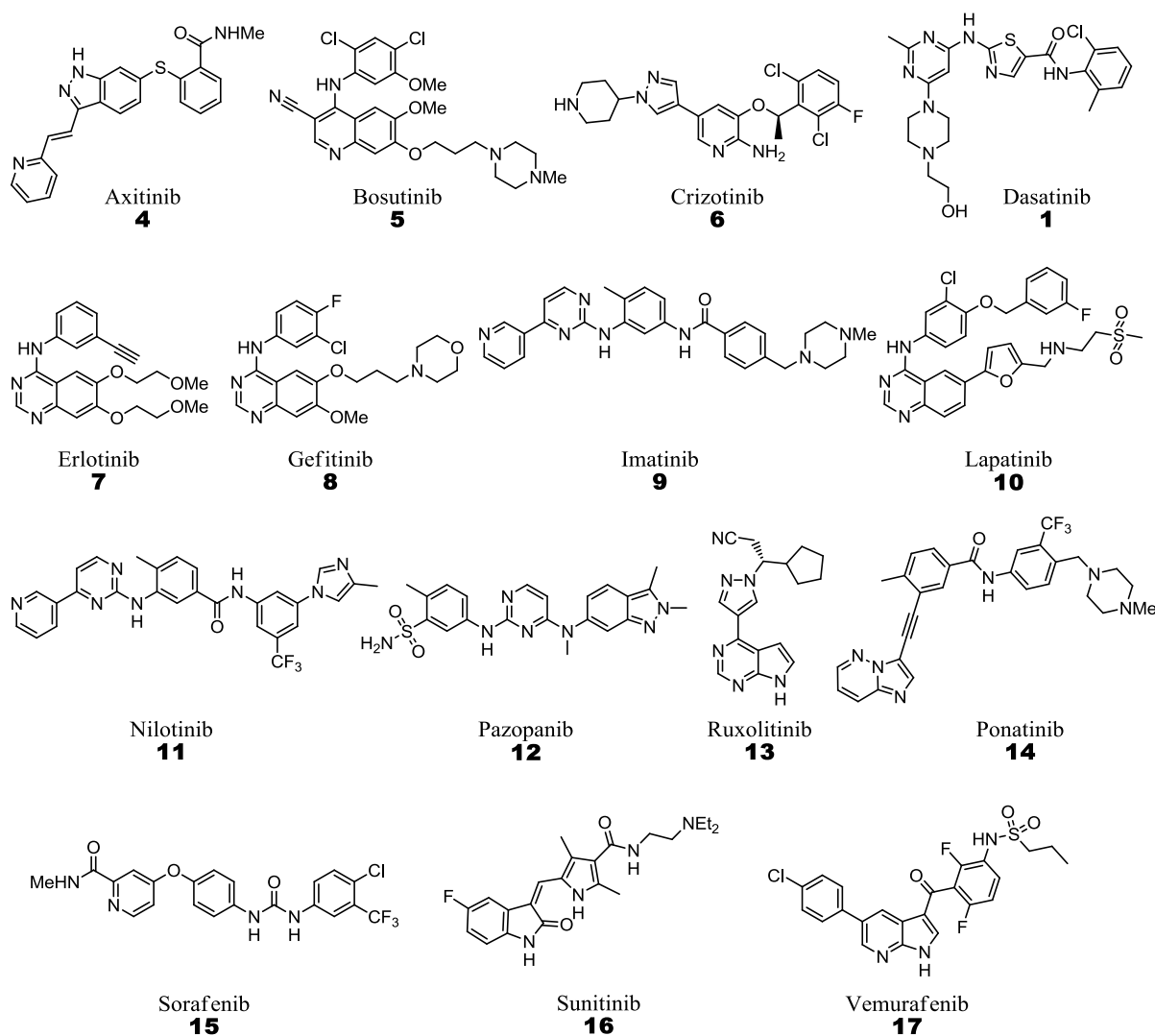


Figure 3 Structures of current kinase inhibitors approved for cancer treatment by the FDA.

While inhibiting multiple kinases has been shown to have therapeutic value in some cases by circumventing feedback loops, selective inhibitors are required to understand the function of single kinases.⁴⁵ Although a few examples of highly selective ATP-competitive kinase inhibitors exist and highlight the power of modern medicinal chemistry research, in the majority of cases, such type I inhibitors are troubled by selectivity issues. Compounds with a purely allosteric mode of action offer distinctive advantages that make them particularly interesting for research. First, they do not have to compete with the high intracellular levels of ATP, thus allowing the identification of weak binders. Additionally, as allosteric binders do not need to interfere with interactions to native ligands, the effect of their binding is not limited to inhibition but can also amplify kinase activity. Understanding the structural details of kinase conformational changes eventually allows for the rational design of innovative type II, type III and type IV inhibitors and next generation activators, to circumvent the current limitations. As regulation of activity can vary greatly among the different kinases, strategies to interfere with

such mechanisms are equally diverse. Some general approaches for activation and inhibition have been employed such as regulating the cellular translocation of kinases, imitating native activators or preventing the formation of active or activated complexes. These regulatory mechanisms and structural characteristics of certain kinases have been exploited by small molecules, which can allosterically modulate that kinase's enzymatic activity. Such compounds offer the possibility of achieving high selectivity as these structural features and the related regulatory mechanisms are often unique and characteristic to a single kinase or kinase family. There exists a great variety in the complex regulation of protein kinase activity due to distinct structural features as discussed in chapter 1.1.1, and individual characteristics can be exploited and addressed by small organic molecules e.g. to gain selectivity based on structural uniqueness (Figure 4).⁴⁶

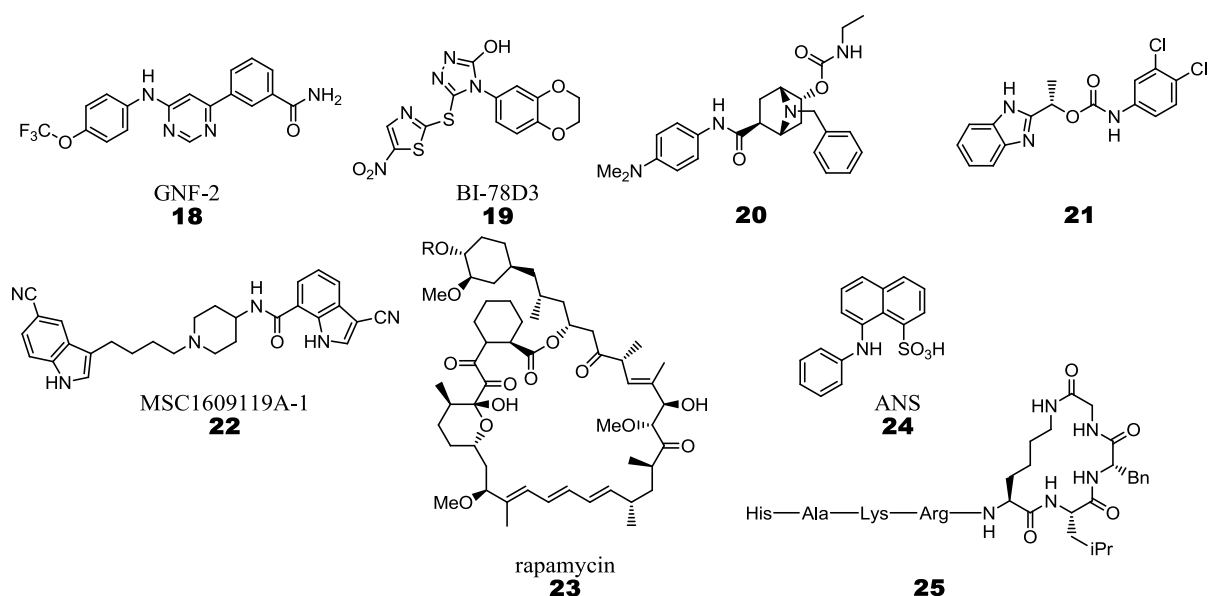


Figure 4 Examples of allosteric type IV inhibitors: GNF-2: Abl inhibitor, myristoyl agonist, facilitates auto-inhibition state of Abl by bending of α I-helix. BI-78D3: JNK1 inhibitor, JIP1 antagonist, stabilises the inactive JNK1 conformation. **20**: PDK1 inhibitor, destabilises active conformation of PDK1. MSC1609119A-1: IGF-1R inhibitor, arrests DFG motif in an inactive conformation, disrupts α C-helix of IGF-1R. Rapamycin: mTOR inhibitor, stabilises mTOR-FKBP12 association, prevents formation of the active complex mTORC1. **21**: Chk1 inhibitor, interferes with the substrate recognition. ANS: CDK2 inhibitor, displaces α C-helix necessary for cyclin A binding. **25**: CDK2 inhibitor, peptidomimetic cyclin antagonist derived from cyclisation of octapeptide HAKRKLFG.

As it was described earlier, the activity of protein kinase Abl is regulated by its SH2 and SH3 domains. In 2006, Adrián *et al.* reported on a series of *N*-phenylpyrimidinamines that specifically inhibited proliferation of BCR-Abl-transformed cell lines.⁴⁷ Biochemical experiments and X-ray co-crystal structures of Abl with the most potent inhibitor GNF-2 (**18**) revealed the myristate pocket as its binding site (PDB entry 3K5V).^{48,49} GNF-2 binding induced Abl auto-inhibition by bending of the α I-helix and resultant conformational fixation of the kinase domain by the SH3 and SH2 domains.

Various scaffolds are known that inhibit Chk1 in a non-ATP-competitive manner (e.g. quinazolinone **21**).^{50,51} Follow-up compound development and co-crystal structure analysis with Chk1 (PDB entries 3F9N, 3JVR and 3JVS) confirmed the allosteric binding site of these inhibitors, forming hydrogen bonds and hydrophobic interactions to the protein surface adjacent to the α D-helix at the start of the C-lobe. This shallow binding pocket has been priorly described as a substrate recognition site, suggesting that these allosteric inhibitors might interfere with the substrate recognition of Chk1.⁵²

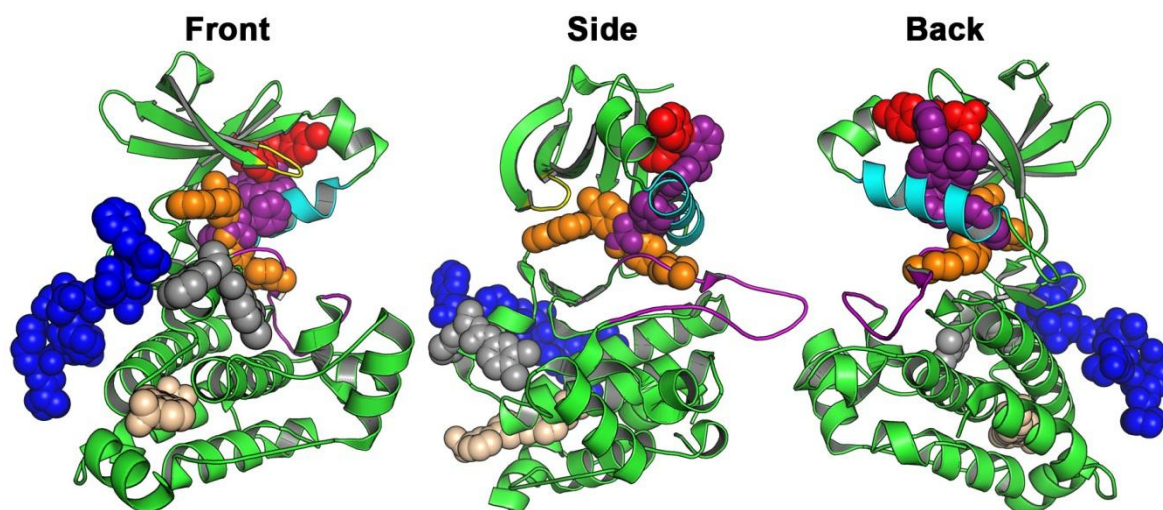


Figure 5 Archetypical kinase domain (green) with α C-helix (cyan), activation loop (magenta), glycin-rich loop (yellow) and ATP binding site (orange spheres) shown in three orientations (front refers to conventional display with N-lobe at the top, C-lobe on the bottom and hinge region left). The binding sites of a few known type IV inhibitors are highlighted: **20** in PDK1 (red), ANS in CDK2 (purple), BI-78D3 in JNK1 (blue), **21** in Chk1 (grey) and GNF-2 in Abl (beige).

1.2 Akt

Protein Kinase B (PKB), also known as v-akt murine thymoma viral oncogene homologue (Akt) or related to A and C kinase (RAC) is a member of the AGC kinase family. First described by Jones *et al.* in 1991, it was quickly identified as an oncogene, and current pharmaceutical research dedicates much efforts to developing small molecule inhibitors for Akt.⁵³

Akt plays a pivotal role in signalling pathways responsible for cell survival, proliferation and apoptosis, regulating these processes *via* its downstream targets such as FoxO1, MDM2, p21, p27, CREB, GSK-3, Bad and procaspase-9.⁵⁴⁻⁵⁶ It is most prominently known as key player in the PI3K/Akt/mTOR pathway. The biological role of its three isoforms PKB α /Akt1, PKB β /Akt2 and PKB γ /Akt3 has been examined in knockout mice studies: Knockout of Akt1 resulted in size reduction of all organs and overall growth, heart defects and general decrease of cell proliferation.⁵⁷ Additionally, Akt1^{-/-} mice exhibited a shortened overall lifespan and increased susceptibility towards both induced and spontaneous apoptosis.⁵⁸ Akt2-deficient knockout mice displayed a diabetic phenotype, unable to regulate blood glucose levels.⁵⁹ In the case of Akt3 knockout, attenuated mTOR signalling in the brain and a reduced brain size due to a decrease of white matter fibre could be observed.^{60,61} While Akt3 is primarily expressed in brain cells, Akt1 and Akt2 are ubiquitously found in all cell types.⁶² An overexpression of all isoforms of Akt has been detected in many cancers such as breast, gastric, pancreatic, thyroid, colorectal, ovarian, prostate and melanoma.⁶³⁻⁶⁸ In addition, it has been demonstrated that cells overexpressing Akt showed resistance against death signals such as TRAIL (tumor necrosis factor-related apoptosis-inducing ligand), whereas a knockdown of Akt restored their apoptotic capability.⁶⁹ Since Akt activity suppresses proapoptotic signals by e.g. FoxO, Bad or caspases, it can cause resistances in cancer cells.⁷⁰ Tumour cells with overactive Akt showed resistance to treatment by radiotherapy as well as chemotherapy.^{71,72} Furthermore, in cells exhibiting high levels of Akt in the G1 and G2 stages such as Cdk1AS, it has been found that inhibition of Akt led to a restoration of Chk1 activity and damage processing capacities by G2 cell arrest.⁷³ This shows that hyperactive Akt signalling is capable of overriding damage regulation by apoptosis and supports increased proliferation of misregulated cells.

The molecular structure of the Akt kinase is complex (Figure 10A). In addition to the catalytically active kinase domain, a domain conserved in overall conformation shared among all protein kinases, Akt possesses an N-terminal pleckstrin homology (PH) domain, and a C-terminal hydrophobic motif. The hydrophobic motif is located at the C-terminus of the protein and has a regulatory role for the phosphorylation activity of Akt.

Named after pleckstrin, a protein found in platelets, Haslam *et al.* have identified a number of proteins that possess segments which exhibited a protein fold resembling pleckstrin.⁷⁴ The thusly termed pleckstrin homology domain can be found in some other kinases as well, usually in proteins which interact with the cell membrane, namely the Protein Kinase C mu type (PKC μ), Bruton's tyrosine kinase (BTK), the IL2-inducible T-cell kinase (ITK), the β -adrenergic receptor kinase 1 (β ARK/BARK/GRK2/ARBK1/ADRBK1), the tyrosine kinase expressed in hepatocellular carcinoma (TEC), the epithelial and endothelial tyrosine kinase (ETK/BMX), the resting lymphocyte kinase (RLK/TXK), the Rho-associated protein kinase (ROCK) and the phosphoinositide-dependent kinase-1 PDK1. *Via* its PH domain, Akt binds to phosphatidylinositol lipids and is thereby recruited to the membrane. Until recently, it was unclear how the domains interacted with each other due to the lack of a crystal structure of the full length Akt. Using molecular modelling techniques, surface properties of the two domains like electrostatic potential, hydrophobicity and acidity were calculated to predict how they might interact with each other.⁷⁵ A few amino acids were thusly identified as crucial for the inter-domain interaction. By expressing Akt with an N-terminal EGFP as donor and a C-terminal mRFP as acceptor, they could carry out FRET experiments which afforded information on the spatial proximity of the PH and kinase domain towards each other. In subsequent mutagenesis studies, they could determine that the exchange of the amino acids identified *in silico* did indeed impede the association of the two domains. In 2010, Wu *et al.* published an X-ray crystal structure (PDB entry 3O96), allowing for great insight into the structural characteristics of Akt caused by the interplay of the different domains.⁷⁶

1.2.1 Activation mechanism

This particular composition of subunits defines the complex regulation mechanism of Akt, which is characterised by a multi-step conformational change to gain its phosphorylation activity. In its inactive state, the so-called PH-in or closed conformation, the PH domain forms tight interactions with the kinase domain *via* a salt bridge between Glu17/Arg273 and hydrogen bonds between Asn53/Asn269, Asn54/Val271, Thr81/Asp292, Thr82/Lys179, Lys39/Asp325 and Arg25/Glu322/Asp323/Asn324. In this closed conformation, the PH

domain not only buries the access to the ATP binding pocket, but also displaces the α C-helix from the side of the allosteric pocket, and locks the activation loop in the inactive DFG-out conformation. The hydrophobic motif (and in particular the amino acids Phe469 and Phe472) rests in the so-called hydrophobic groove, formed by the residues Ile186, Val187, Val192, Leu196, Asn199, Phe217, Leu223 and Phe225 on the N-lobe.

The signalling cascade is initiated by the activation of the phosphoinositide 3-kinase (PI3K), which can be stimulated by external growth factors such as EGF, VEGF, IGF-1 or PDGF (Figure 6).⁷⁷⁻⁸⁰ PI3K phosphorylates the second messenger phosphatidylinositol (4,5)-bisphosphate (PIP₂) to phosphatidylinositol (3,4,5)-trisphosphate (PIP₃), which binds to the PH domain of Akt. The PIP₃ binding pocket of Akt is a groove consisting of the positively charged residues Lys14, Arg23, Arg25, Asn53 and Arg86, which form electrostatic interactions with the negatively charged phosphate moieties of PIP₃.⁸¹ Upon coordination to PIP₃, the overall positive charge of the binding pocket is reversed, causing an electrostatic repulsion towards the negatively charged residues on the kinase domain, and, as a result, dissociates from it. The kinase changes into the PH-out or open conformation, in which the activation loop now lies exposed. Consecutively, Thr308 on the activation loop can be phosphorylated by PDK1, an upstream kinase of Akt.¹⁶ Upon phosphorylation, the activation loop moves from the inactive DFG-out to the active DFG-in conformation, opening up the ATP binding pocket and effectively initiating the kinase activity of Akt. Further phosphorylation of Ser473 in the hydrophobic motif by PDK2 increases this activity by a factor of up to 1000. Yang *et al.* observed a 20° rotation of the N-lobe and the C-lobe against each other upon Ser473 phosphorylation.⁸² It was proposed that this alignment stabilises the protein and augments its phosphorylation activity. Ser473 by itself, however, is not sufficient to induce the kinase activity of Akt. This has been proven by Vincent *et al.* in cell studies, in which no downstream targets of Akt were found phosphorylated when only Ser473 was phosphorylated, but not Thr308.⁸³

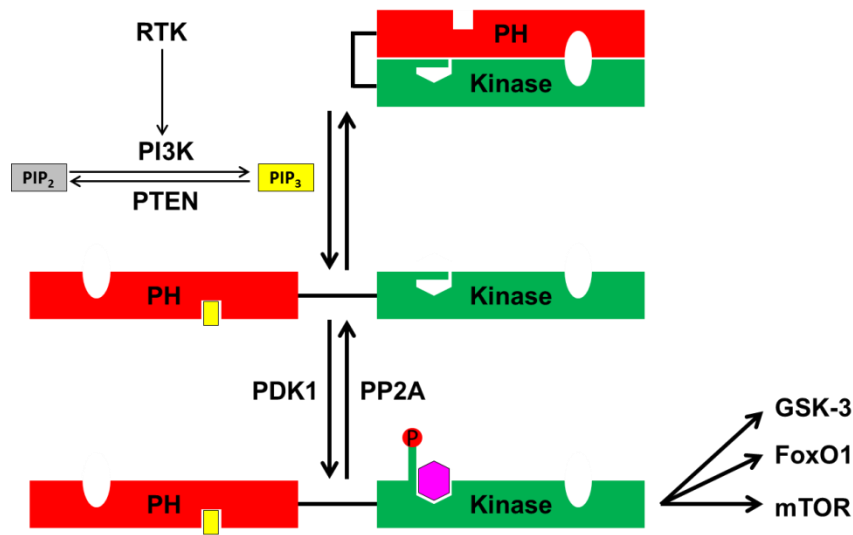


Figure 6 Simplified schematic representation of the PI3K/Akt/mTOR signalling pathway: Receptor tyrosine kinases (RTK) activate PI3K, which phosphorylates PIP₂ (grey box) to PIP₃ (yellow box). This messenger facilitates the dissociation of the two Akt domains, thereby revealing the activation loop (green bar), which can be phosphorylated (red sphere) by PDK1. This activation induces an opening of the ATP binding pocket and enables the access of ATP (purple hexagon), leading to subsequent phosphorylation of downstream kinases such as GSK-3, FoxO or mTOR.

To date, the identity of PDK2 is still under debate. Various kinases are being discussed as candidates for PDK2, each with supporting evidence. In a screening initiative conducted by Chua *et al.* in 2009 employing RNA interference in breast cancer cell lines, over 90 kinases have been found to cause Ser473 phosphorylation.⁸⁴ The rictor-mTOR complex (mTORC2),⁸⁵ the DNA-dependent protein kinase (DNA-PK),⁸⁶ the integrin-linked kinase (ILK)⁸⁷ and the mitogen-activated protein kinase-activated protein kinase 2 (MAPKAPK2 or MK2)⁸⁸ are being considered the most likely candidates for PDK2, while the possibility of autophosphorylation has been abandoned.⁸⁹ In recent publications, it has been suggested that the TANK-binding kinase 1 (TBK1) is involved in Akt activation by phosphorylation of both Thr308 and Ser473.^{90,91}

Recent studies show that conformational changes associated with occupation of the ATP binding pocket, either by ATP itself or by ATP-competitive inhibitors, arrange Arg273 and Lys297 to protect Thr308 from access by the phosphatase PP2A, thereby stabilising its phosphorylation.⁹² On the other hand, once the phosphotransfer from ATP onto the substrate has occurred, Thr308 is rapidly dephosphorylated due to the low affinity of the resulting ADP for the binding pocket. This would suggest that Akt activity is tightly regulated, only allowing one catalytic cycle at a time for each activation event, once again demonstrating the physiological importance of Akt activity.⁹³

Both Akt and its upstream kinase PDK1 are usually located in the cytosol and the nucleus. Upon increase of the basal PIP₃ concentration from 50 nM to 5-200 μM, both kinases are recruited to the membrane, where PDK1 activates Akt.⁹⁴ With the aid of cellular fluorescence imaging, Yoshizaki *et al.* determined that Akt is already closely associated to PDK1 in the cytosol without being phosphorylated.⁹⁵ This shows that PIP₃ does not only serve as a second messenger to bring these two kinases together, as mere spatial proximity between PDK1 and Akt is not sufficient to cause Akt activation, but is vital to cause a structural change of Akt necessary for its activation. This was confirmed separately by Calleja *et al.* via FRET experiments in cells.⁹⁶

In 2007, a somatic mutation of Akt was found in breast, colorectal and ovarian cancers, where the Glu17 residue on the PH domain of Akt was mutated to a lysine.⁹⁷ Since this mutation is located near the PIP₃ binding pocket, the binding affinity towards phosphatidylinositols should be affected. Indeed, *in vitro* experiments showed that the exchange of the negatively charged glutamate to a positively charged lysine increased the affinity of Akt towards PIP₂ as well. Therefore, no prior activation by PI3K was required anymore for a conformational change from the inactive Akt PH-in to the active PH-out conformation. In fact, these E17K mutants were found concentrated at the plasma membrane, exhibited higher activity in cells and induced leukaemia in mouse models.⁹⁸

1.2.2 Akt inhibitors

Over the years, a number of ATP-competitive Akt inhibitors have been developed.⁹⁹⁻¹⁰¹ Due to the high sequence identity in the ATP binding pocket among the AGC kinases, many of these inhibitors are derived from previously known PKA and PKC inhibitors (Figure 7). For example, the nanomolar PKA inhibitor H-89 displayed low micromolar activity against Akt as well. Subsequent optimisation yielded a series of Akt-focussed inhibitors based on this quinoline scaffold (e.g. NL-71-101 with a 2.4-fold selectivity against PKA). Docking experiments of PKA inhibitor derivatives afforded a few pyrimidine derivatives that were predicted to bind to the Akt ATP pocket.^{102,103} A selection were tested for their biological activity, either in LNCaP cells (derived from human prostate adenocarcinoma cells) or in prostate mouse tumour models. From a high-throughput screening campaign, a series of pyridinyl-indazoles were discovered as Akt inhibitors and co-crystallised with a PKA-Akt hybrid.¹⁰⁴ Subsequent optimisation resulted in the inhibitor A-443654 that was shown to induce apoptosis in MiaPaCa-2 cells.¹⁰⁵ However, all ATP-competitive Akt inhibitors so far suffer from poor selectivity, particularly against other kinases of the AGC family. GlaxoSmithKline were

able to bring such an inhibitor (GSK690693) through the preclinical development by optimizing CCT128930, but failed to pass phase I clinical trials, presumably due to off-target activity and hence toxic side effects.^{106,107} By addressing issues like low bioavailability and oral exposure, Array BioPharma followed up in 2012 with GDC-0068, which is currently in phase I trials.¹⁰⁸

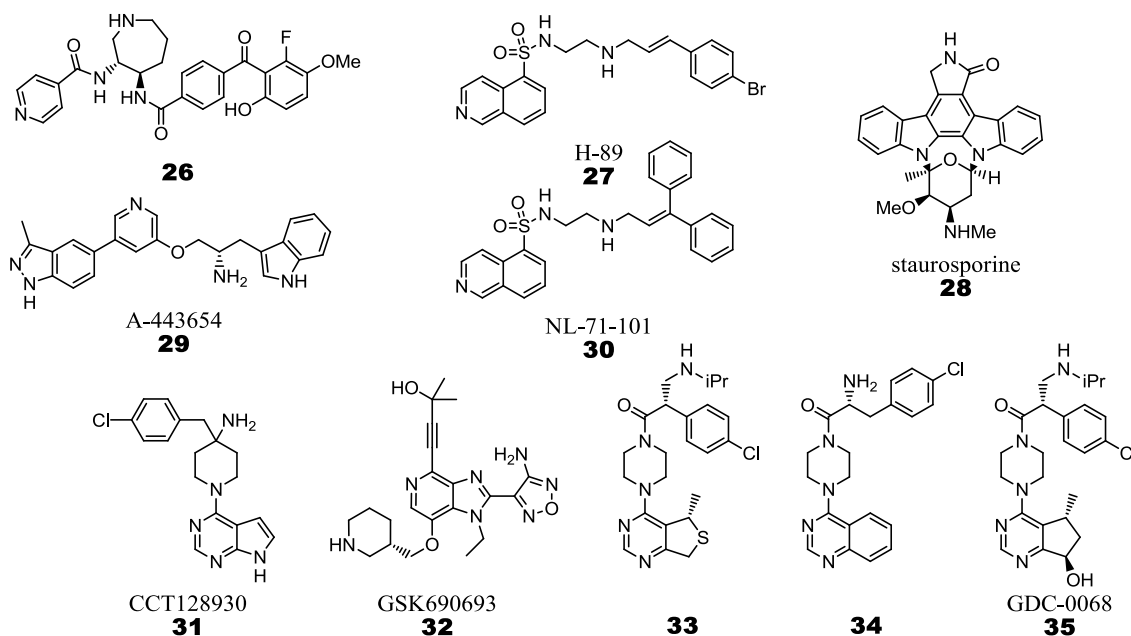


Figure 7 A selection of classical, ATP-competitive Akt inhibitors.

Although much effort has been put into the development of ATP-competitive Akt inhibitors by pharmaceutical companies, their development has been discontinued due to toxicity issues.¹⁰⁹ Owing to its unique activation mechanism, different methods for the inhibition of Akt were pursued.

An alternative strategy to inhibit Akt activity is to prevent its activation by PIP₃. Meuillet *et al.* showed that D-3-deoxy-phosphatidyl-myo-inositols such as DPIEL (**36**) bind specifically to the PH domain of Akt with a high affinity and prevent Akt activity in both biochemical and cell assays.¹¹⁰ They also showed that sulfonamides such as **37** were also able to compete with PIP₃ and inhibit Akt activation in cells.¹¹¹ There are a number of further allosteric inhibitors known such as API-1,¹¹² PIA23,¹¹³ and perifosine,¹¹⁴ whose inhibition strategy is mimicking PIP₃ without effecting an opening of the Akt conformation. All these inhibitors mainly suffer from low solubility, aggregation and adverse pharmacokinetic properties.¹¹⁵

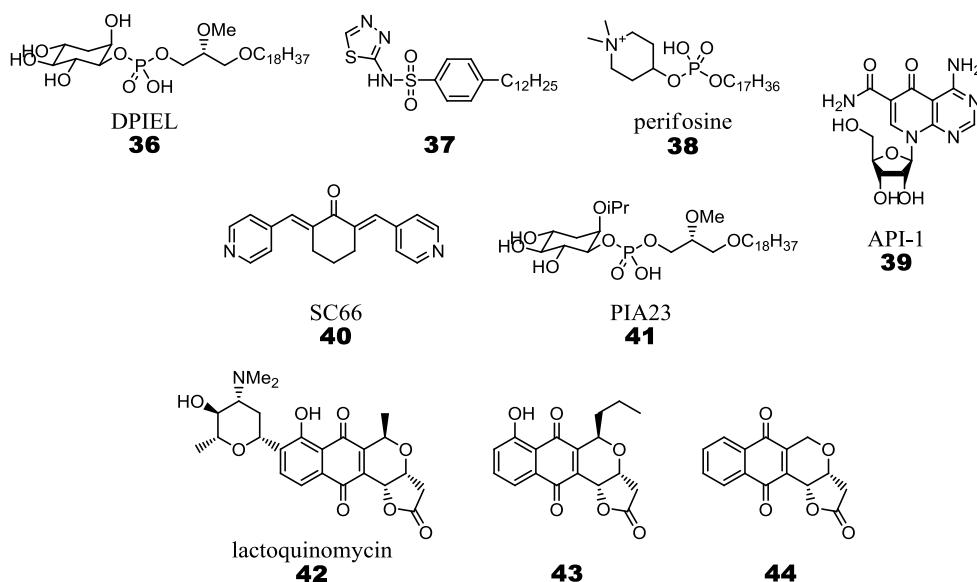


Figure 8 Allosteric Akt inhibitors, either interacting with the PH domain or with the activation loop.

Recently, Jo *et al.* have reported another allosteric Akt inhibitor with a new scaffold and an entirely different mode of action.¹¹⁶ SC66 (**40**) and a group of similar compounds were found to prevent activation of Akt by PIP₃ and translocation to the cell membrane. Instead, SC66 primed Akt for ubiquitination and thereby proteosomal degradation in the pericentrosomal region. This is in conflict with findings that ubiquitination of Akt *via* Lys63 was detected in cases of breast and colon cancer, where it facilitated its activation.¹¹⁷ Interestingly, co-treatment with another allosteric inhibitor reduced the degradation of Akt. The exact binding mode of SC66, however, is unknown so far.

During a high-throughput screening, Toral-Barza *et al.* have discovered that pyranonaphthoquinones (PNQs) such as the antibiotic lactoquinomycin (**42**) are potent inhibitors of Akt with a high selectivity against the related PKA and PKC kinases.¹¹⁸ Based on a novel scaffold, it exhibited a non-ATP-competitive, time-dependent mode of inhibition. By employing C296A, C310A and C29A/C310A mutants of Akt, they determined a dependence on the presence of Cys296 and Cys310 in the activation loop, as the PNQs only showed weak inhibition on the single mutants and no inhibition on the double mutant. As the time dependency implied an irreversible alkylation of the thiol residues *via* lactone opening, they later verified the addition of the PNQ to Cys310 by UV/Vis spectroscopy and mass spectrometry after tryptic digest.¹¹⁹ It was reasoned, that the inhibitory activity of the PNQs might stem from either interfering with the substrate binding or facilitating an inactive conformation.

1.2.3 Allosteric Inter-Domain Akt Inhibitors

In 2005, Lindsley *et al.* reported on the discovery of an Akt inhibitor with a novel scaffold from a high throughput screen (compound **45**, from now on referred to as inter-domain or ID inhibitors).¹²⁰ Unlike previous, ATP-competitive Akt inhibitors, this quinoxaline exhibited high selectivity against other closely related kinases of the AGC family such as Protein Kinase A (PKA), Protein Kinase C (PKC), Protein Kinase G (PKG), the serum-and glucocorticoid-induced protein kinase (SGK), PDK1, 70 kDa ribosomal protein S6 kinase 1 (S6K) and the ribosomal s6 kinase (RSK). Furthermore, it is the first Akt inhibitor, that displayed selectivity against the three Akt isozymes (IC₅₀ Akt1: 3.4 μM, Akt2: 23 μM, Akt3: >50 μM). Remarkably, **45** only showed inhibitory activity against the full length kinase and no activity on the Akt kinase domain alone. This led to the assumption that the inhibitor might interact with structural features only present when PH and kinase domain come together. However at that time, no crystal structure of the full length protein had been published, so the interactions of the domains with each other and of the inhibitor-complex remained unknown.

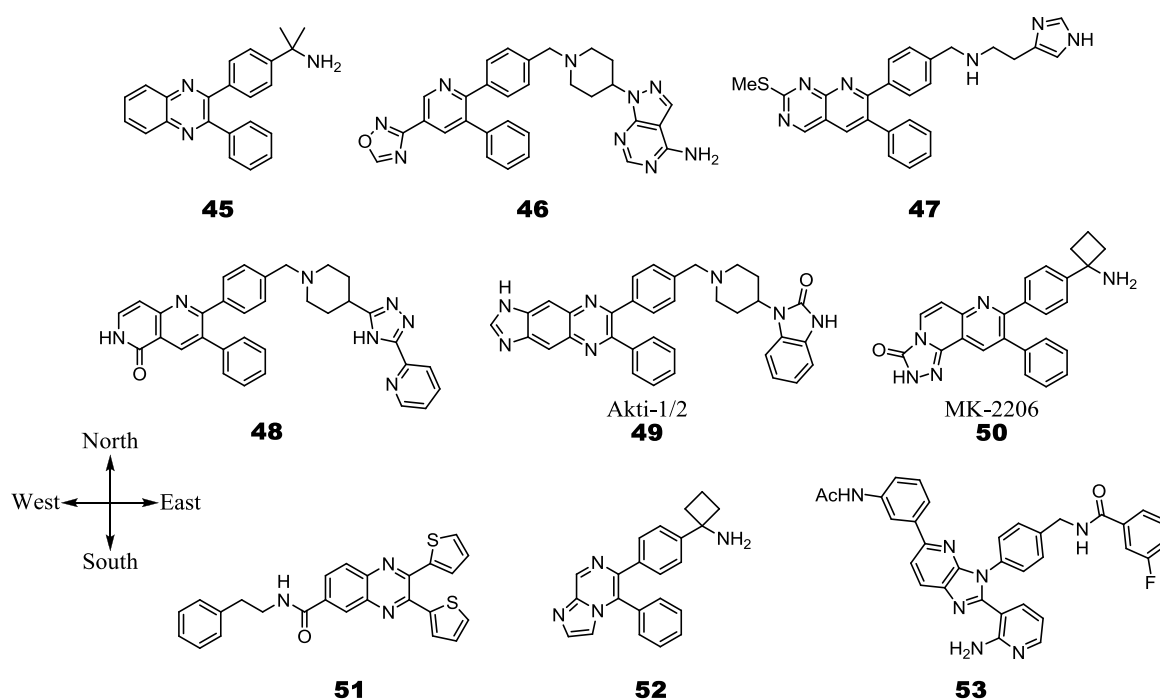


Figure 9 A selection of previously developed ID inhibitors. The nomenclature of the substituents' orientation is indicated on the left.

In the following years, a number of inhibitors based on the initial hit have been synthesised in an attempt to establish an SAR and increase their activity, isozyme selectivity, solubility and bioavailability, leading to a number of inhibitor patents (Figure 9).¹²¹⁻¹²⁵ The northern ring nitrogen of the central scaffold was quickly determined to be crucial for the inhibitory activity, as well as a methylene-bridged amine at the northern phenyl ring. Furthermore, extensive central aromatic rings exhibited better activity than a single heterocycle. As a wide range of groups transpired to be tolerated at both the western and the eastern ends, it soon led to the theory that the allosteric binding pocket might be open to both sides. The PIF binding pocket of Akt was speculated as possible binding pocket, with the two phenyl groups imitating Phe469 and Phe472 of the Akt C-terminus. In light of the tight patent space, efforts were made to find alternative solutions. ImClone Systems had some success in exchanging the crucial phenyl groups against bioisosteric thiophene and furane rings.¹²⁶ Due to the high hydrophobicity of the inter-domain pocket, all inhibitors have suffered from severe solubility issues. With this particular goal in mind, alternative scaffolds were explored by Kettle *et al.* and specifically tested for their solubility in aqueous solutions.¹²⁷ And indeed, some of these heterocycles showed improved solubility while retaining some affinity for the allosteric pocket.

Based on these SAR data and mutagenesis studies, evidence for the possible binding mode of these ID inhibitors was mounting.^{128,129} In 2009, Calleja *et al.* used molecular dynamics experiments to calculate how the PH and kinase domain would interact with each other in the full length Akt.¹³⁰ Their simulations predicted the induction of a 9 Å wide cavity in the kinase domain near the hydrophobic groove by Trp80 in the PH domain, which was previously already identified to be vital for the binding of ID inhibitors to Akt. Docking of Akti-1/2 (**49**), one of the most used ID inhibitors at that time, indeed placed the inhibitor firmly inside the predicted cavity. In 2010, however, the publication of an X-ray crystal structure of full length Akt in complex with Akti-1/2 showed that, in fact, when the two domains came together, major reorganisation of the PH domain not predicted by the MD simulations enabled the formation of a new binding pocket at the domain interface (Figure 10).⁷⁶ The ID inhibitor was sandwiched in between, forming π - π -interactions with Trp80 and hydrogen bonds to both domains, thereby stabilising a closed conformation, in which the ATP binding pocket is both inaccessible and disordered. In the co-crystal structure of Akt with an inter-domain inhibitor based on another scaffold, this arrangement of the domains in the full-length Akt was confirmed by Ashwell *et al.*¹³¹

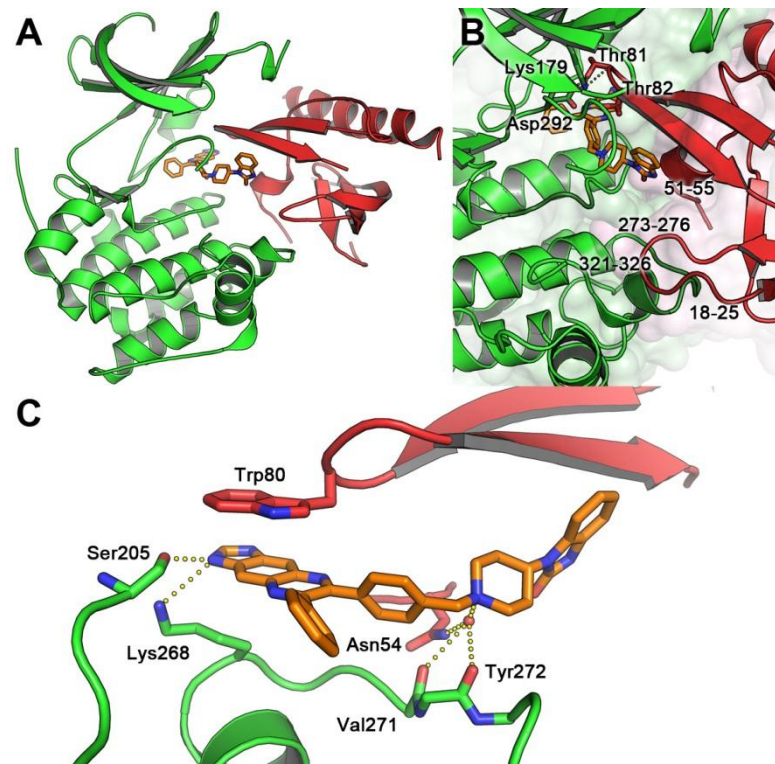


Figure 10 A) X-ray crystal structure of the full length Akt in its closed conformation, co-crystallised with Akti-1/2 (PH domain red, kinase domain green, Akti-1/2 orange, PDB entry 3O96). B) Magnification of the domain interface. Important interactions are highlighted and marked in the respective darker colour. C) Allosteric inhibitor occupying unique binding pocket at the interface of the Akt PH and kinase domain, forming π - π -interactions with Trp80 and hydrogen bonds with Asn54, Ser205, Lys268, Val271 and Trp272.

As these inhibitors were isoform-selective Akt inhibitors, they finally enabled assessment of the role of the three isozymes and the physiological effect when inhibited individually. It was found that inhibiting both Akt1 and Akt2 had a higher apoptotic effect than inhibiting either of these isozymes alone.¹²⁰ The induced apoptosis by inhibiting Akt1 and Akt2 could not be compensated by an upregulation of Akt3.¹³²

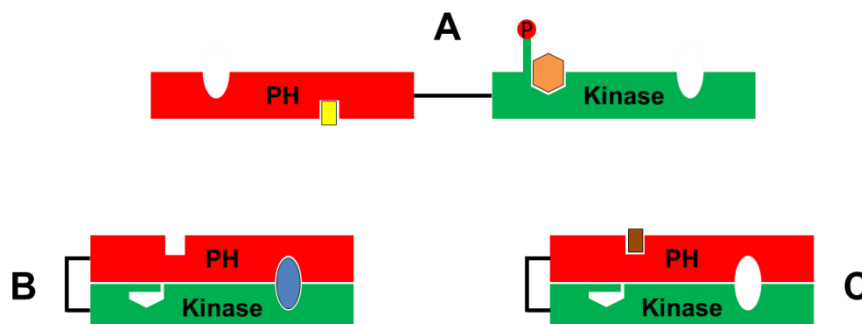


Figure 11 Overview of different inhibition modes of Akt: A) Classical ATP-competitive inhibitors (orange hexagon) occupies ATP binding pocket. B) Allosteric ID inhibitors (blue circle) bind into a unique pocket at the domain interface, locking them in a closed conformation. C) PIP₃ antagonists (brown box) bind into the phosphate pocket at the PH domain and prevent the activation by PIP₃.

In 2009, one of these ID inhibitors, the orally available MK-2206 (**50**), entered clinical phase I trials.¹³³ So far, this drug showed good efficacies in treating tumours.¹³⁴ A combined treatment of non-small cell lung cancer with MK-2206 and erlotinib even showed promising effects in patient populations with resistances.¹³⁵ MK-2206 entered phase II in April 2011 for the treatment of various cancers. In comparison to preceding Akt inhibitors, which all failed in the clinic, it exhibits superior selectivity, good pharmacodynamic properties, and is well tolerated in clinical studies.¹³⁶ These favourable characteristics are owed to its allosteric mode of action by occupying the unique pocket at the domain interface of PH and kinase domain.

1.3 Fluorescence

Fluorescence describes the emission of electromagnetic particles at a longer wavelength than the excitation wavelength, traditionally in the human visible range of the electromagnetic spectrum. It occurs predominantly in more rigid compounds, as the energy cannot be easily dissipated *via* radiationless thermal relaxation. Upon excitation, electrons are promoted from the S_0 to the S_1 state, where vibrational relaxation leads to loss of energy (usually within picoseconds) before returning back to the S_0 ground state. This energy difference between excitation and emission is called the Stokes shift. A special case of fluorescence is phosphorescence, in which the S_1 and T_1 states overlap to some degree, so that excited electrons undergo a inter-system crossing from the singlet to triplet state. Since the direct relaxation from $T_1 \rightarrow S_0$ is a spin-forbidden process, the lifetime of this T_1 state can last up to seconds, whereas fluorescence typically occurs on a nanosecond time scale.¹³⁷

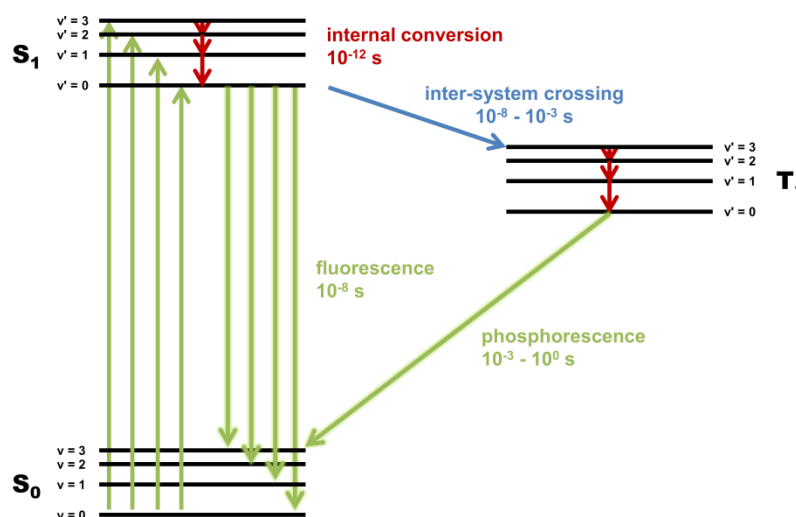


Figure 12 Jablonski scheme for explaining fluorescence: Absorption from S_0 ground state followed by rapid radiationless vibrational relaxation (internal conversion) and subsequent relaxation accompanied by emission of photons. Inter-system crossing from singlet S_1 to triplet T_1 state leads to a spin-forbidden T_1 -to- S_0 and hence slow relaxation.

Depending on the experimental setup, competition with background luminescence signals can be eliminated, enabling the detection of fluorescence with a very high sensitivity and at much lower intensities than mere absorption. Measuring fluorescent signals can be quick and easy, and does not require elaborate instruments or meticulous safety precautions. Therefore, it has become the favourite analytical tool in the biological sciences.

1.3.1 Solvatochromic Fluorophores

Fluorescence is a highly dynamic phenomenon that can be sensitive to environmental influences. For example, some fluorophores are sensitive to the solvent pH, as protonation changes conformation and electronic distribution, and therefore the fluorescence properties of the molecule. Fluorescein, the best known pH-sensitive fluorophore, loses its fluorescent capability below pH 4.2 as its carboxylate group gets protonated, hence disrupting the conjugation of π -electrons.¹³⁸ Other fluorophores can quantitatively detect the presence of inorganic salts such as Ca^{2+} and Cl^- by measuring the quenching kinetics.¹³⁹ These probes often feature a recognition site for the respective analyte and can be specific to a particular binding partner.

As a more general principle, the polarity of the solvent can be detected by fluorophores that exhibit a different dipole moment in the excited state than in the ground state. Following excitation and vibrational relaxation, the surrounding solvent molecules have to adapt to the new electric energy field (usually in the range of around 40 ns). This reorientation requires an energy transfer from the fluorophore to the surrounding molecules, resulting in a change of the energy levels (termed S_1^* and S_0^*). Usually, the energy gap between S_1^* and S_0^* states reduces with higher solvent polarity, leading to a bathochromic shift (red-shift), also called positive solvatochromism. However, the opposite, negative solvatochromism, i.e. a hypsochromic shift (blue-shift) upon polarity increase, has been observed as well. By accounting for molecular volume, solvent polarity and refractivity, Lippert and Mataga have derived a formula to calculate the excited dipole moment (equation (1)).¹⁴⁰ In the resultant Lippert plot, a linear dependence of the Stokes shift and the solvent polarity can be observed.

$$\Delta\bar{\nu} = \frac{2(\mu_E - \mu_G)^2}{h \cdot c \cdot V} \left(\frac{D - 1}{2D + 1} - \frac{\eta^2 - 1}{2\eta^2 + 1} \right) \quad (1)$$

$\Delta\nu$ = difference in wavenumbers between excited and ground state

μ_E = dipole moment of fluorophore excited state μ_G = dipole moment of fluorophore ground state

c = light speed = 299792458 m/s

h = Planck constant = $6.626 \cdot 10^{-34}$ Js

η = solvent refractive index

D = solvent dielectric constant

V = fluorophore volume

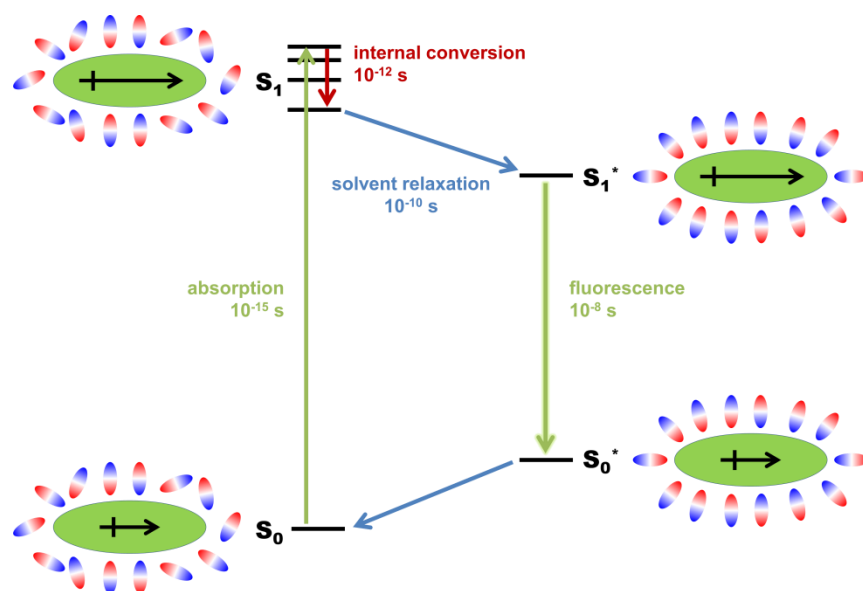


Figure 13 Effect of solvent reorientation on the fluorescence energy states, leading to the S_1^* state, which relaxes to S_0^* before returning to S_0 after solvent reorientation.

In addition to the general polarity, fluorophores can also form specific solvent interactions.¹⁴¹ 2-Anilinonaphthalene, for example, experiences a 30 nm shift of its emission spectrum upon addition of 3% EtOH into an aqueous solution. While this amount of ethanol is insufficient to change the bulk polarity of the solution, the EtOH molecules associate with the fluorophore, thereby stabilising either the ground or excited state. In these cases, the Lippert plot of these fluorophore-solvent pairs will give misleading results.

1.3.2 Förster Resonance Energy Transfer

Förster Resonance Energy Transfer (FRET), also known as Fluorescence Resonance Energy Transfer, can occur when the emission spectrum of one fluorophore (the donor) overlaps with the excitation of another (the acceptor) and are sufficiently close together.¹⁴² In consequence, excitation of the donor leads to an emission of the acceptor. The rate of transfer is proportional to the spectral overlap of donor emission and acceptor excitation (also determined by the donor fluorescence quantum yield and acceptor extinction coefficient), and the orientation and distance between donor and acceptor. Hence, the Förster radius, which is the distance of half-maximal energy transfer, can be calculated with equation (2). The orientation factor κ can only be reliably determined *via* X-ray crystallography or NMR.¹⁴³ In practice, κ^2 is assumed $2/3$ as a temporal mean value due to random motion of the fluorophores, and $\eta = 1.4$ for aqueous solutions.

$$R_0^6 = \frac{9000(\ln 10)\kappa^2 \cdot \Phi_D}{128\pi^5 \cdot N \cdot \eta^4} \cdot \int_0^\infty F_D(\lambda)\varepsilon_A(\lambda)\lambda^4 d\lambda \quad (2)$$

R_0 = Förster radius

κ = orientation factor

N = Avogadro constant = $6.022 \cdot 10^{23} \text{ mol}^{-1}$

η = solvent refractive index

Φ_D = donor fluorescence quantum yield

ε_A = acceptor extinction coefficient

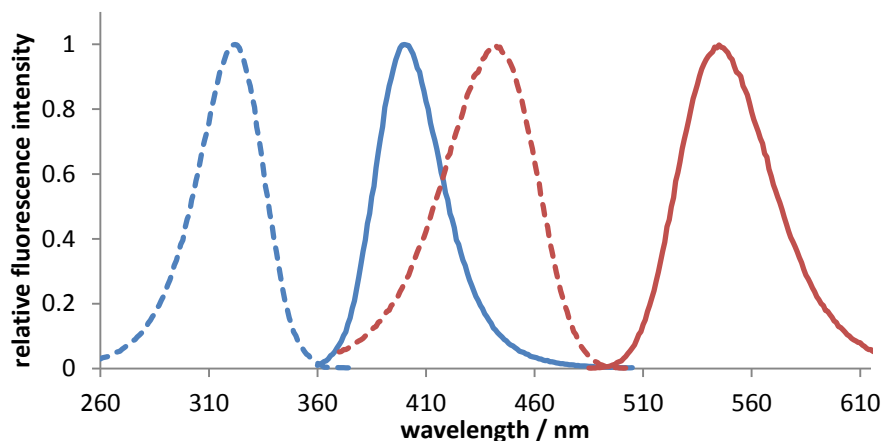


Figure 14 For the occurrence of Förster resonance energy transfer, the emission spectrum of the donor (solid blue line) has to overlap with the acceptor excitation spectrum (dotted red line).

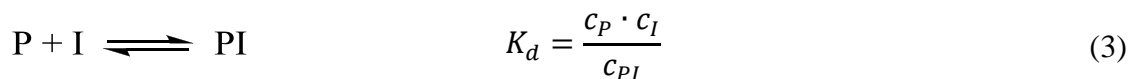
As it becomes apparent from the equation above, the FRET efficiency is strongly dependent on the distance between the fluorophore pair and decays quickly at a rate to the power of 6. When selecting the donor-acceptor pairs accordingly, this steep efficiency-distance correlation can be utilised as a molecular ruler that is able to provide very precise readings. In the biological sciences, however, the FRET phenomenon is mostly employed to detect whether two fluorescently labelled partners are in proximity or not. For simplification, the Förster radius is usually considered as the cutoff distance for the occurrence of FRET.

Radiationless FRET is one of the main causes of fluorescence quenching, as it does not require the direct contact between the fluorophore and quencher like in the case of collisional quenching.

1.4 Assay Technologies

The effect of an analyte on a biological system is the fundamental question that guides research in chemical biology and drug discovery. Studies on the whole target organism are often low throughput and are plagued by considerable complexity and unpredictability. Therefore, simplified models are required for the earlier stages of research (e.g. preclinical phases in the case of drug development). In order to reduce their complexity, biological systems need to be broken down into smaller increments to answer questions about specific interactions within the entire complex network. While these simplifications represent an abstraction of the actual biological problem, these minimal interactions can still viably offer answers about the whole system. As a result, biochemical *in vitro* assays can still provide meaningful results when designed correctly, and can be a powerful tool for obtaining biologically relevant data.

In the context of molecular biology, protein-ligand interactions are one of the key aspects of interest. They are characterised by parameters such as the dissociation constant, which is defined in equation (3) and describes the strength of a particular receptor-ligand complex, i.e. the binding affinity of a ligand for its receptor. For inhibitors, the concentration of half-maximal inhibition (IC_{50}) denotes the inhibitory potency of a compound and is a phenotypical yet standard parameter.



c_P = concentration of free protein

c_I = concentration of free inhibitor

c_{PI} = concentration of protein-inhibitor complex

The reliability and reproducibility of assays are often described by the Z-factor, which is a parameter based on the variation and relative differences of the assay's minimal and maximal responses. This is achieved by including appropriate positive and negative controls to induce each response. Thus, the Z-factor characterises the capacity of an assay to react to changes in the desired biological system of interest. Assuming a normal Gaussian distribution of results, values are considered significant when exceeding 3 times standard deviation of the same sample. Therefore, the Z-factor is described by equation (4). A Z'-factor between 0.5 and 1 is generally considered ideal for high-throughput screening.¹⁴⁴ While the Z-factor is a feature size describing the absolute capacity of an assay, the deductive Z'-factor is calculated from the positive and negative controls in each round of a screening scenario.

$$Z = 1 - 3 \frac{\sigma_p + \sigma_n}{|\mu_p - \mu_n|} \quad (4)$$

μ_p = mean positive controls

μ_n = mean negative controls

σ_p = standard deviation positive controls

σ_n = standard deviation negative controls

1.4.1 KinEASE

There are a variety of methods to measure kinase activity, such as the radioactive EasyTides assay by PerkinElmer¹⁴⁵ or the LanthaScreen,¹⁴⁶ Adapta,¹⁴⁷ Omnia¹⁴⁸ and Z'-LYTE¹⁴⁹ assays marketed by Life Technologies. One of the most commonly employed assays is the KinEASE assay by Cisbio based on the HTRF (homogeneous time-resolved fluorescence) technology.^{150,151} KinEASE is a universally applicable method that indirectly measures the phosphorylation of promiscuously binding, biotin-labelled substrate peptides, either carrying a tyrosine (TK) or serine and threonine (STK1, STK2 and STK3). After incubation with the protein, ATP and MgCl₂, the reaction is quenched by complexation of Mg²⁺ with EDTA, and visualised by incubation with a solution of streptavidine conjugated to the fluorophore XL665 and an anti-phospho-tyrosine or anti-phospho-serine/phospho-threonine antibody conjugated to a europium cryptate fluorophore (Figure 15). If the peptide is phosphorylated, the two fluorophores are in close proximity (in this case within 90 Å) to each other, so that excitation of the donor europium at 317 nm leads to an emission of the acceptor XL665 at 665 nm *via* FRET. The ratio of fluorescence intensities at 665 nm (XL665) and 620 nm (europium cryptate) is equivalent to the degree of substrate phosphorylation and therefore kinase activity. Due to shielding of the f-electrons from oxygen quenching by the cryptate ligand, low extinction coefficients and spin-forbidden f-f-transitions, lanthanide fluorescence has a remarkably long lifetime of about 150 μs.¹⁵² Measuring the fluorescence after a delay of at least 40 μs, therefore, is instrumental to avoid extrinsic fluorescence by the analyte or buffer ingredients, and hence minimises background fluorescence.

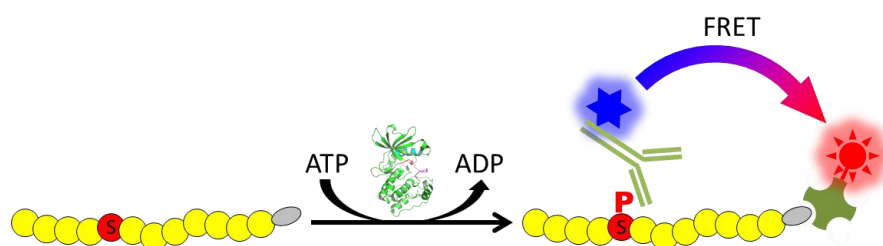


Figure 15 Assay principle of KinEASE: Using ATP as co-factor, the respective kinase transfers a phosphate (red) onto an artificial substrate peptide (yellow) with an N-terminal biotin tag (grey). After the phosphorylation reaction, the donor fluorophore (blue) conjugated to a phospho-specific antibody transfers energy onto the acceptor fluorophore (red) attached to streptavidin.

1.4.2 Fluorescent Labels in Kinases (FLiK)

Kinase regulation is inevitably linked to conformational changes of structural elements particularly in the ATP binding pocket. In the FLiK assay, developed by Jeffrey Simard in our group, the solvatochromic fluorophore Acrylodan is introduced *via* Michael addition onto a cysteine to detect changes in its environment.¹⁵³ In order to attach Acrylodan to the desired position and to avoid multi-labelling, all surface-exposed cysteines were mutated to serine, while a cysteine mutation was introduced to the position of interest. FLiK reports on conformational changes induced by the binding of specific types of ligands and does not require kinase activity.¹⁵⁴ In using the inactive form of the kinase, weak binders are more sensitively identified than in activity-based assays. To date, FLiK has been used to successfully monitor conformational changes of the A-loop and the glycin-rich loop associated with the slow binding of DFG-out binders as well as a method for identifying more selective allosteric ligands (type IV), including assays for the MAP insert pocket of p38 α as well as the myristate pocket of Abl kinase.^{155,156} Recently, we were able to show that the same principle are applicable to phosphatases as well by detecting the binding of inhibitors against the protein tyrosine phosphatase 1B (PTP1B) with the FLiP assay (Fluorescent Labels in Phosphatases).¹⁵⁷

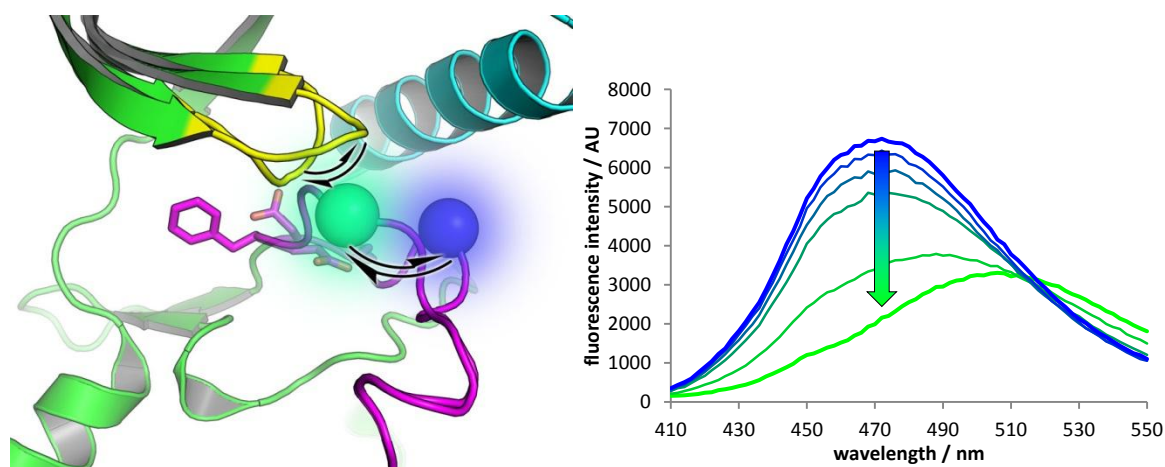


Figure 16 Assay principle of the FLiK assay: Binding of ligands into the ATP binding pocket induce conformational changes, which can be picked up by attaching the environment-sensitive fluorophore Acrylodan to either the glycin-rich loop (yellow) or the activation loop (magenta). Both loops undergo major reorientations upon ligand binding, often accompanied by a transition from DFG-in to DFG-out. This causes a dose-dependent change in the Acrylodan emission spectrum.

1.4.3 NanoTemper

In a temperature gradient, molecules migrate from the warm to the cold region due to an increased Brownian motion.¹⁵⁸ This phenomenon is known as thermophoresis, and the diffusion velocity is dependent on the molecules' hydrodynamic properties, mainly determined by their charge, hydrodynamic radius, shape and hydrational state. As these properties generally change upon binding of a ligand, the different diffusion velocities can be utilised to determine the binding state of a protein-inhibitor complex. With a steepening of the temperature gradient, these differences in velocity become more distinct. However, to avoid damage to the sensitive proteins, the temperature must not be so high as to induce thermal degradation of the proteins of interest. Consequently, in the NanoTemper assay by NanoTemper Technologies, this temperature gradient is produced by an IR laser, which produces a temperature difference of about 8 K over a distance of 150 μm inside a capillary (Figure 17).¹⁵⁹ This microscale thermophoresis (MST) allows for a steep gradient under mild conditions. In order to selectively track its movement the protein of interest is previously labelled unspecifically with a fluorophore, and the depletion of protein from the heat source can be followed by a decrease in fluorescence intensity.

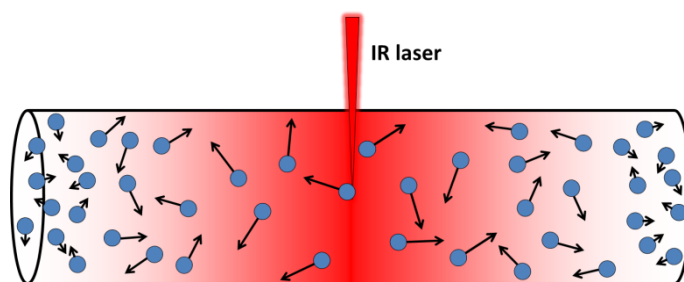


Figure 17 Assay principle of the NanoTemper assay: A protein solution in a capillary is heated up with an IR laser, creating a steep temperature gradient. Due to increased Brownian motion, the protein diffuse from the warm to the cold region. Their depletion can be followed selectively by fluorescence.

1.4.4 Biacore

Surface plasmon resonance (SPR) is able to detect changes on a surface (e.g. thickness, roughness or composition), as these modulate the propagation of plasmons across a metal surface layer and therefore the refractive properties of that particular surface to incoming electromagnetic waves.¹⁶⁰ In the Biacore assay by GE Healthcare, this phenomenon is utilised to detect ligand binding to a receptor by immobilising the protein onto a gold chip and monitor the refraction intensity of a laser at a fixed angle. As the inhibitors bind to the protein, the increase in mass is detected in real time, providing kinetic information on the association and dissociation from the protein-inhibitor complex.¹⁶¹ One drawback of this method is the protein immobilisation, as this can potentially interfere with ligand binding and therefore lead to false results.

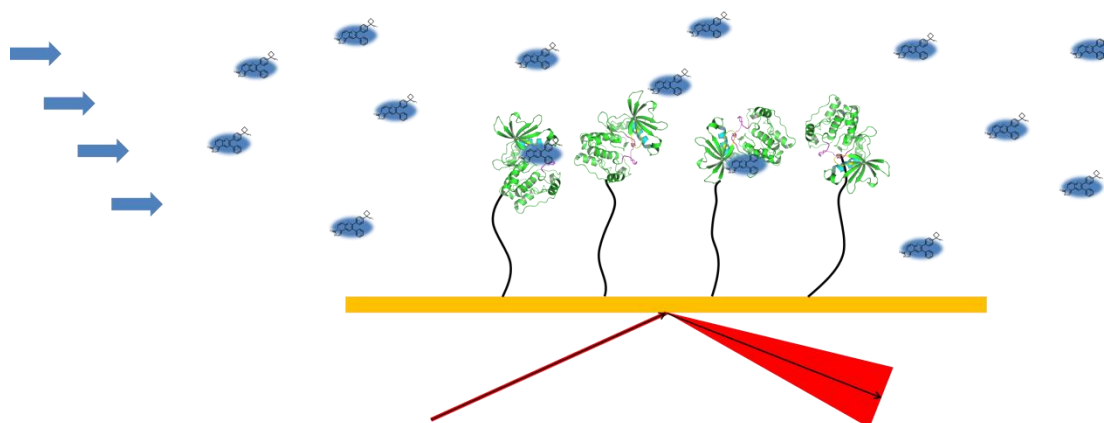


Figure 18 Assay principle of the Biacore assay: Ligand molecules (blue) dissolved in a buffer are passed in a laminar flow over a gold-coated surface (orange), binding to proteins (green) immobilised on this surface. This binding event and resultant mass increase changes the resonance of surface plasmons, thereby altering the refraction properties of an incoming laser (red). This can be detected by a signal increase at a fixed detector angle.

2 Aims and Objectives

As it was demonstrated in the introduction, protein kinases are an attractive target for drug development (chapter 1.1). Many kinases are regulated *via* complex interactions with other proteins or low-molecular-weight ligands. Such interactions are often unique for a particular kinase or kinase family, which offers a chance of selectively modulating these kinases by addressing these characteristics with small molecules (chapter 1.1.1).

One such example is the kinase Akt, which represents an important target in oncology and is known to be addressable by allosteric inhibitors (chapter 1.2). The clinical success of the candidate compound MK-2206 suggests a high therapeutic window for the inhibition of Akt with allosteric ID inhibitors (chapter 1.2.3). All known allosteric Akt inhibitors to this day, however, are based on the hit compound **45**, that was discovered by chance in a high-throughput screening campaign, in which it only inhibited full length Akt. The parallel screening of compounds against both full length Akt and the Akt kinase domain in activity-based assays has remained the only method so far to reliably identify ID inhibitors. Recent studies indicate that allosteric inhibitors have a lower affinity and slow binding kinetics towards the active Akt.¹⁶² Activity-based assays are therefore prone to missing weak binders. In summary, there is currently no assay system that allows the selective screening for allosteric Akt inhibitors.

In order to identify even low-potency compounds in a facile way, a novel assay system is needed that can report on the binding of ligands directly and that does not require the activated Akt. The aim of this thesis is to develop such an assay, that can detect the conformational changes within Akt and interactions between its regulatory PH domain and its catalytically active kinase domain, which are associated with the binding of allosteric ID inhibitors. This rationally designed assay will enable the targeted search for inter-domain inhibitors with novel scaffolds in the high-throughput screen of large libraries. To this end, the following steps have to be taken in the process:

-
1. Structure-guided assay design: As the assay should exploit the conformational changes of Akt, the assay design will be based on structural information about Akt.
 2. Protein expression and purification: On the one hand, the assay will require proteins bespoke engineered for detecting the conformational changes of Akt. These proteins will be expressed in insect cells and purified.
 3. Synthesis of probe molecules: On the other hand, reference compounds will be needed in order to validate the assay. Therefore, a focussed library of small molecules based on scaffolds of known inhibitors will be synthesised to be used as tool compounds.
 4. Assay development and optimisation: With the necessary components in hand (proteins and probe compounds), proof-of-concept experiments will show whether this assay principle is able to provide the desired readout on the biological phenomenon of interest, i.e. reporting on the binding of allosteric Akt inhibitors and the resulting conformational changes. Subsequently, the assay will be optimised for future use in high-throughput screens.
 5. Assay validation: In order to validate the results obtained from this novel assay, orthogonal test systems based on different physical principles will be established and employed to measure the probe compounds.
 6. High-throughput screening: Following this assay optimisation and validation, various libraries will be screened for novel inhibitors. The resultant hits will be validated for their biological effect *in vitro*. In subsequent follow-up studies, other derivatives based on this new scaffold will be investigated to gain insight on their SAR and binding mode with Akt.

3 Results and Discussion

3.1 Assay Design

As it was described in the introduction, the activation of Akt is regulated *via* multiple mechanisms. In addition to the more common regulation by phosphorylation and associated conformational changes of the activation loop, the PH domain plays a major regulatory role by covering the kinase domain and thereby obstructing access to the ATP binding pocket. This inactive conformation is stabilised by ID inhibitors which bind into an allosteric pocket at the interface between the two domains, forming a number of interactions to both domains.

For our novel assay, we set out to use environmentally sensitive fluorophores to detect Akt changing from the active open to the inactive closed conformation (Figure 6). In order to achieve the highest possible sensitivity, the reporter fluorophore has to be introduced close to the domain interface without disrupting the inter-domain interactions. At that time, no crystal structure of the full-length Akt had been published. However, through mutagenesis studies and calculations of surface polarity, electrostatic charges and acid-base reactions, Calleja *et al.* have identified residues 17-19, 50-52, 54-56, 58-61, 76 and 85 on the PH domain, and residues 185, 187-190, 320-324, 353-356, 358-359 and 362-363 on the kinase domain to be part of the domain interface (Figure 19).⁹⁶

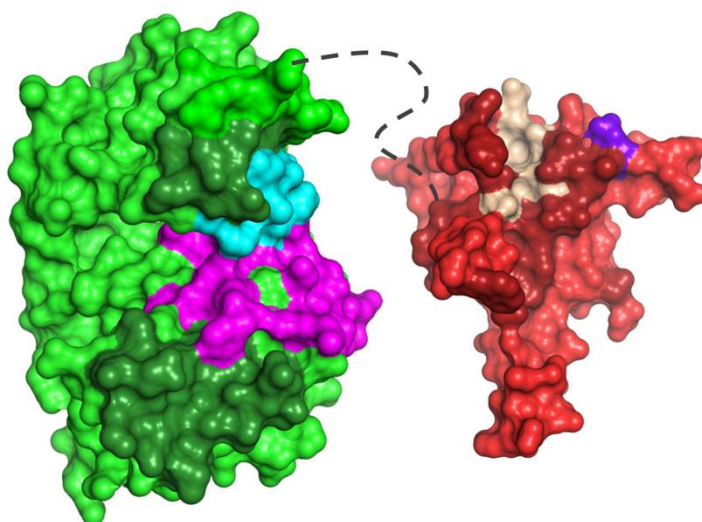


Figure 19 X-ray crystal structures of the PH (red) and kinase domain (green) alone (PDB entries 1UNP and 3CQW, respectively). The α C-helix (cyan), a-loop (magenta) and PIP₃ binding pocket (beige) are highlighted. Amino acid residues known to be involved in the inter-domain interaction are marked in the respective darker colour. The residue Glu49 (purple) close to the domain interface on the PH domain was chosen as labelling position.

Analysing their data on the interaction between PH and kinase domain, we determined Glu49 as a suitable labelling position for the reporter fluorophore. In retrospect, the subsequently published X-ray crystal structures of the full-length Akt (PDB entries 3O96 and 4EJN) confirmed that Glu49 is indeed sufficiently close to the domain interface.^{76,131}

In proteins, cysteine residues are sufficiently reactive and relatively rare, making them the residue of choice to covalently attach the reporter fluorophore. The 480 aa Akt1 protein features 7 native cysteines: Cys60 and Cys77 form a disulphide bridge in the interior of the PH domain, Cys224 is part of the N-lobe and buried as well, whereas Cys296, Cys310, Cys344 and Cys460 are surface exposed, as X-ray crystal structures of the individual domains reveal. For a selective labelling of the reporter fluorophore to the desired position, three kinase constructs were designed for the conformation assay (Figure 20):

- de91 comprises amino acids 1-446 of Akt1. An E49C mutation was introduced into Akt1 and all surface-exposed cysteines were removed (C296S, C310S, C344S) to avoid undesired labelling. Serine was chosen as a replacement for the original cysteine as it resembles it the most in terms of electrostatic and steric properties. This truncated construct lacks the C-terminal hydrophobic motif, which is known to undergo additional conformational changes that might interfere with the reporter fluorophore. Furthermore, it was hypothesised that removing the flexible hydrophobic motif would facilitate crystallisation of the protein.
- pHT1023 encompasses the complete Akt1, also with the artificial E49C mutation and all surface-exposed cysteines removed (C296S, C310S, C344S, C460S).
- de92 also includes the full length sequence of Akt1, differing from pHT1023 by retaining Cys460 in the hydrophobic motif, which is known to have a regulatory function for Akt. Therefore, the strategy with this construct is to keep as close to the wild type sequence as possible.

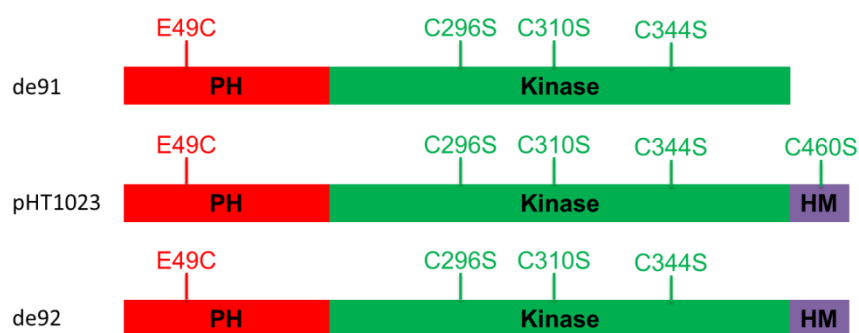


Figure 20 The three constructs designed for the novel conformational assay.

3.2 Protein Production

3.2.1 Protein Expression in Insect Cells

The three constructs described above were cloned into pREN4427-HIS-DEST vectors with an N-terminal His₆-Tag and a recognition sequence for cleavage by the Tobacco Etch Virus (TEV) protease, which were provided by Dr. Mark Schütte from Merck KGaA. In the next step, a baculovirus was generated from this vector by assembling the virus in adherent Sf21 cells. After harvesting the thusly generated virus from the supernatant after centrifugation, the virus was amplified in TriEx Sf9 cells to achieve a higher virus concentration.

For determining the virus titer, the insect cells were grown onto a polymer surface and infected with the respective viruses. After 45 h, the cells were subsequently treated with an anti-gp64 mouse antibody, an anti-mouse antibody/HRP conjugate and finally a Blue Peroxidase substrate. The virus hull protein gp64 is detected in this assay, causing a blue staining of infected cells *via* substrate oxidation (Figure 21). From the proportion of stained to unstained cells, which can be counted under the microscope, the virus titer is calculated: de92 = $5 \cdot 10^7$ IFU/mL; pHT1023 = $1 \cdot 10^7$ IFU/mL; de91 = $6 \cdot 10^7$ IFU/mL.

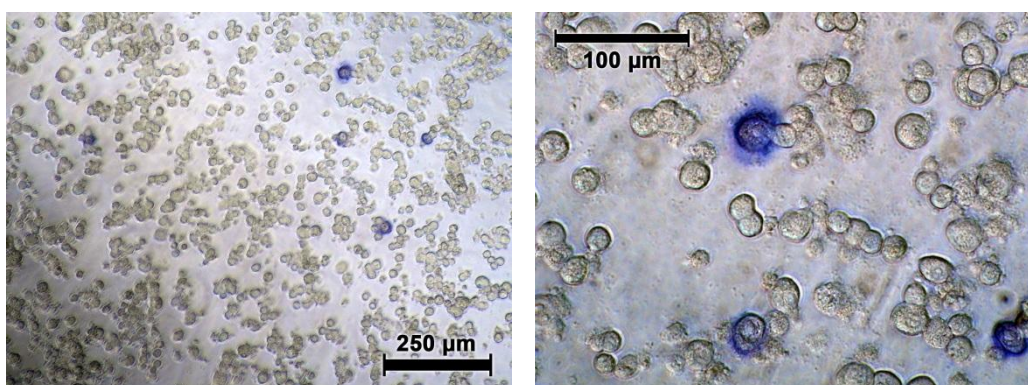


Figure 21 Microscope picture of TriEx Sf9 cells after incubation with a 1/10,000 diluted baculovirus solution for 45 h and immunostained with an anti-gp64 antibody and a Blue Peroxidase substrate, taken at 10x (left) and 40x (right) magnification.

For the virus amplification, a low MOI (multiplicity of infection) and long incubation times are usually preferred to generate the maximum amount of virus from a virus aliquot. However, virus particles in high passages are known to become defective, losing their ability to induce protein expression while still being infectious. Therefore, virus solutions should be amplified from low-passage viruses that were frozen and stored at -80 °C. On the other hand, for the expression of proteins, the optimal conditions to obtain the maximum protein yield have to be found for each virus and cell combination. While it is obvious that a low MOI and short incubation times will not generate much protein, proteins could be lost at a high MOI and long incubation times as the infected cells eventually burst and release the protein into the medium.

In order to optimise expression conditions, test expressions on a 20 mL scale were prepared for each virus. Various permutations of incubation time and MOI were assessed by transfecting TriEx Sf9 cells with different amounts of virus and taking samples at fixed intervals. MOIs were covered over the large range of about 2 orders of magnitude. The samples were analysed for their protein content *via* unspecific Coomassie Brilliant Blue staining and His₅-specific Western Blot, which is specific for the desired protein as no proteins with such a sequence have been detected in the native *Spodoptera frugiperda* proteome so far (Figure 22). From the various small-scale test expressions, the optimal expression conditions were determined to be:

- de92: 48 h at MOI = 3
- pHT1023: 72 h at MOI = 0.5
- de91: 72 h at MOI = 0.3

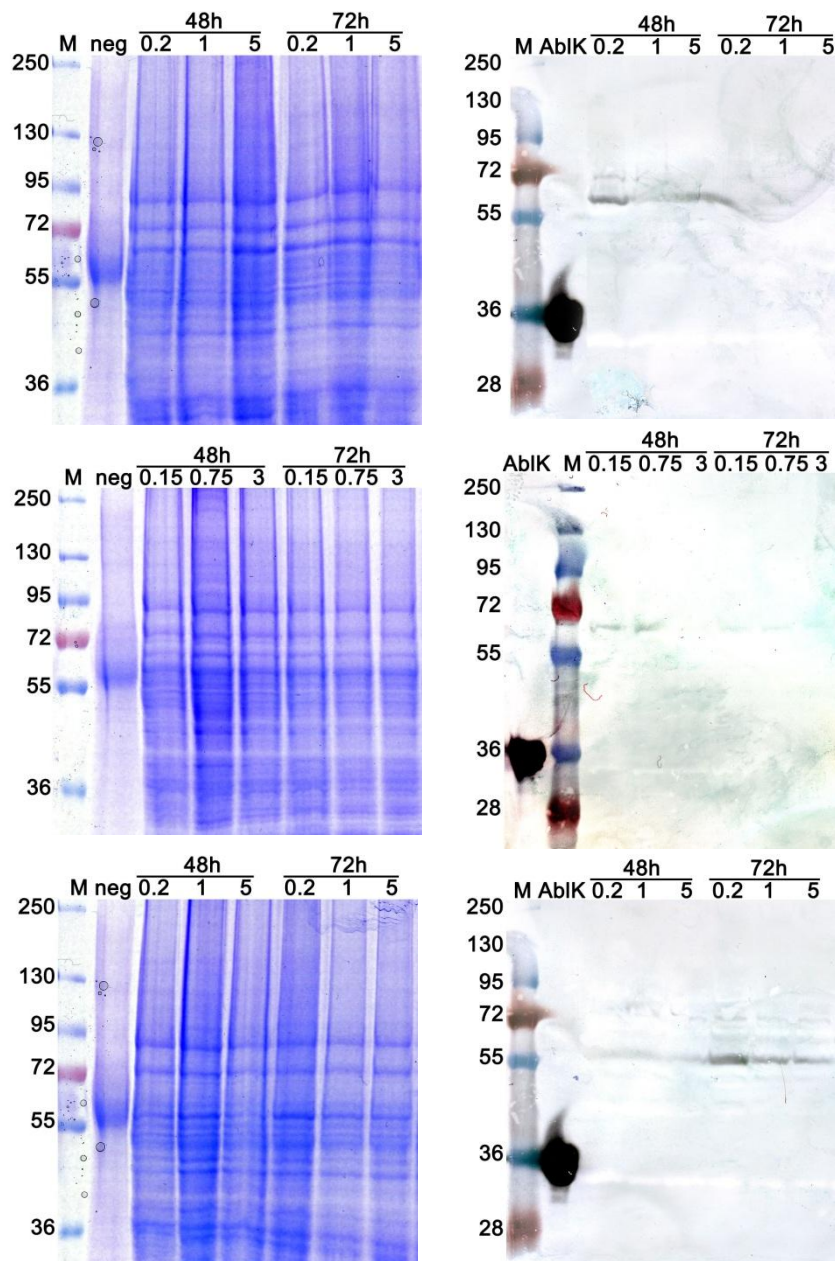


Figure 22 CBB-stained gels (left) and Western Blots (right) with an His₅-specific antibody and a chromogenic substrate of test expressions with de92 (top), pHT1023 (middle) and de91 (bottom) viruses. Bands are separated according to respective MOI and incubation times. PageRuler Plus Prestained by Fermentas was used as marker. Molecular weight is displayed in kDa. The molecule masses of interest are 59 kDa for de92 and pHT1023, and 55 kDa for de91. The lysate from uninfected TriEx Sf9 cells was used as negative control in the CBB-stained gels. An N-terminal His₆-tagged Abl construct was used as positive control for the Western Blot. M = marker; neg = uninfected TriEx Sf9 cells; AbIK = His₆-tagged Abl construct.

In the end, all three constructs were expressed in TriEx Sf9 cells at the conditions described above in 2 L insect cell medium each. The cells were centrifuged, and the cell pellet collected and stored at -80 °C for purification.

3.2.2 Protein Purification *via* FPLC

All three kinase constructs were purified in the same manner: After ultrasonic and pressure-assisted cell lysis, the desired protein was concentrated *via* Ni²⁺ affinity chromatography from the lysate. Competitive elution with a step-wise concentration increase of imidazole provided the target protein in multiple fractions, which was further purified *via* size exclusion chromatography. Using a mixture of reference proteins, the correlation between retention times and molecule size could be roughly estimated. The appropriate fractions for further work-up were identified through SDS-PAGE and CBB-staining after each step.

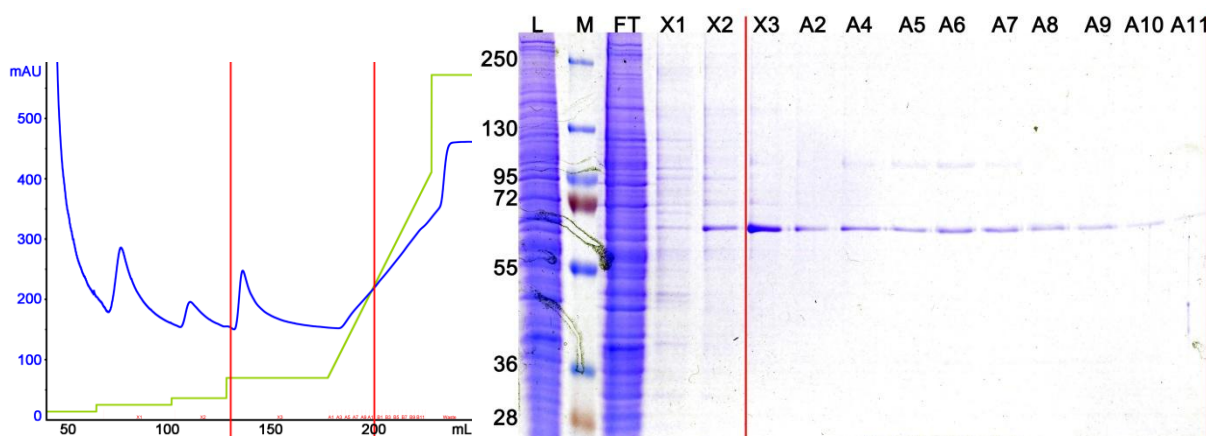


Figure 23 Left: Chromatograms of Ni-NTA chromatography for de92 (blue = UV absorption A_{210} , green = imidazole gradient). Right: Corresponding CBB-stained analytical gel images with PageRuler Plus Prestained by Fermentas used as marker. Molecular weight is displayed in kDa. The target protein has a molecular weight of 59 kDa. L = lysate; M = marker; FT = flowthrough; X1 = 10 mM imidazole; X2 = 20 mM imidazole; X3 = 50 mM imidazole; A2-A11 = 50-500 mM imidazole gradient. Fractions X3-A11 were combined for subsequent SX chromatography.

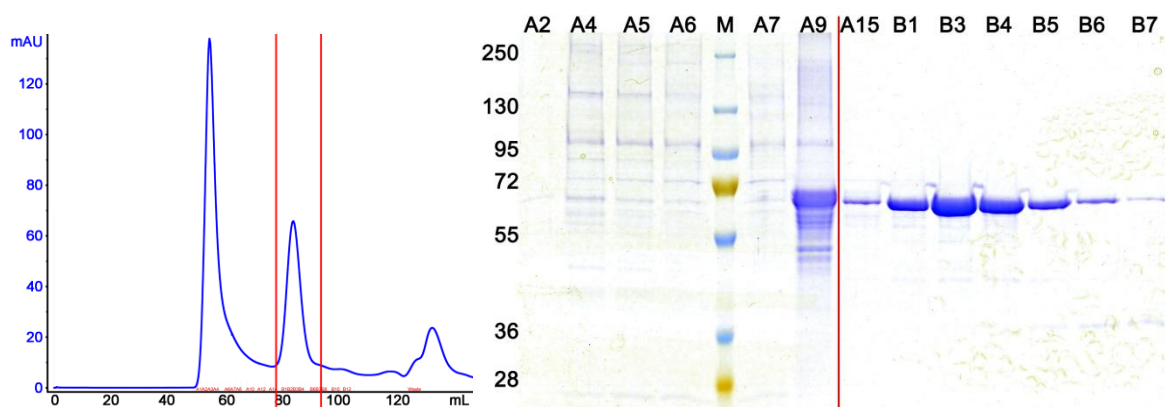


Figure 24 Left: Chromatograms of SX chromatography for de92 (blue = UV absorption A_{210}). Right: Corresponding CBB-stained analytical gel images with PageRuler Plus Prestained by Fermentas used as marker. Molecular weight is displayed in kDa. The target protein has a molecular weight of 59 kDa. Fractions A15-B7 were combined.

For de92, the fractions at 50-200 mM imidazole in the Ni-NTA chromatography were combined. In gel filtration, early fractions containing the exclusion volume and oligomeric proteins were discarded, and only the fractions with protein at the correct mass range of around 59 kDa were collected, combined, concentrated to about 30 μ M, and frozen in liquid nitrogen for storage at -80 $^{\circ}$ C. Protein aliquots after each purification step were taken and analysed in SDS-PAGE (Figure 25). The final protein was analysed with ESI-MS and the corresponding protein mass determined by deconvolution. In the end, a yield of 3.7 mg purified de92 for every litre of expression medium could be obtained.

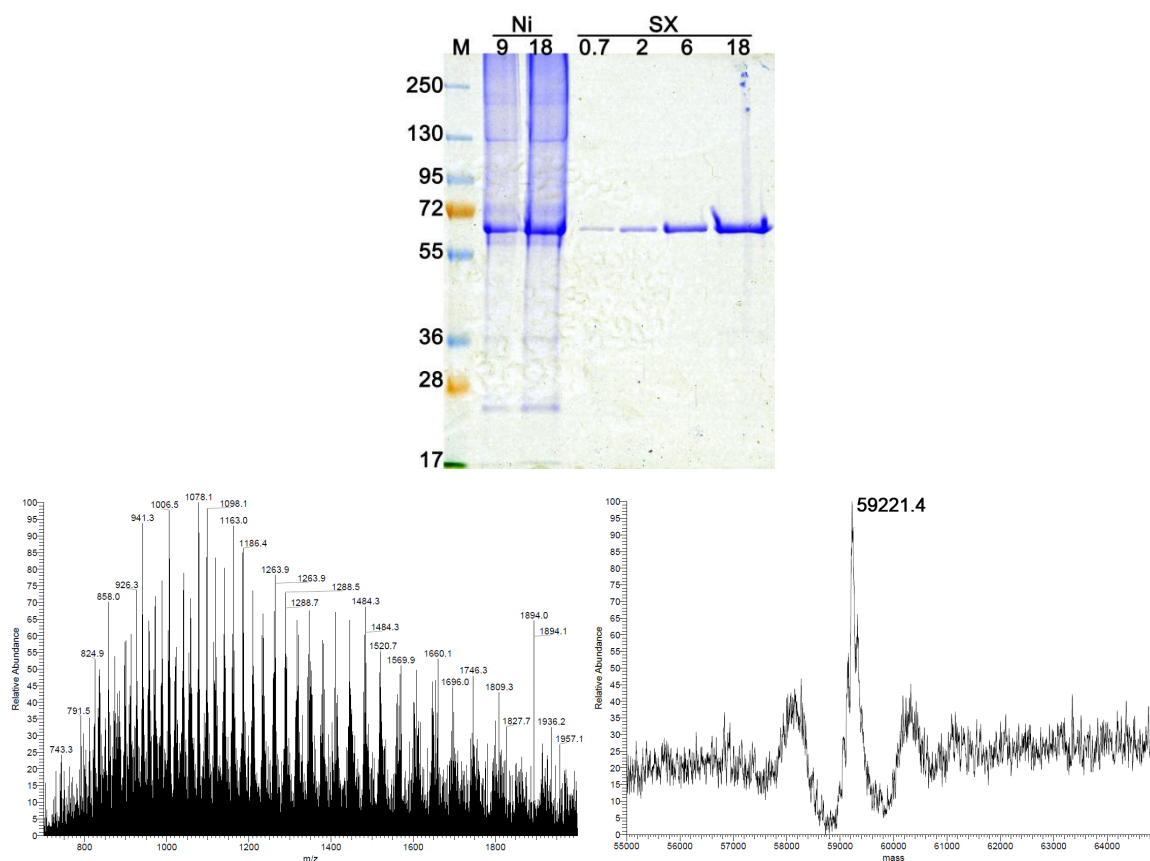
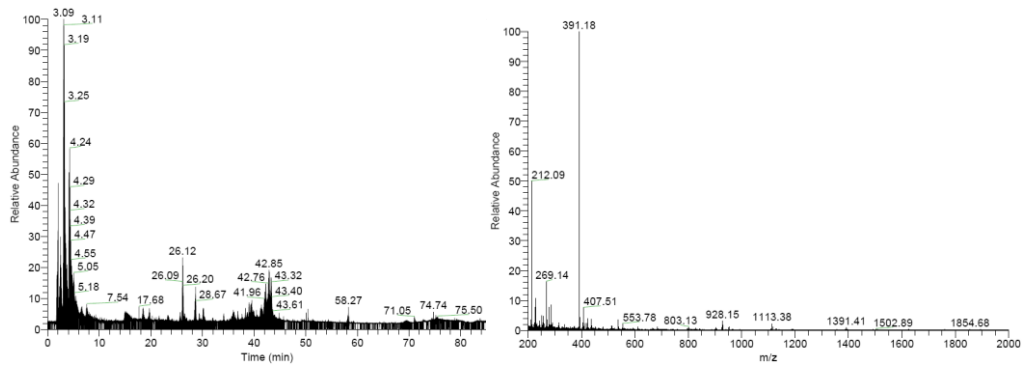


Figure 25 Top: Overview of protein purity after each purification step of de92 with PageRuler Plus Prestained by Fermentas used as marker. Molecular weight is displayed in kDa. M = marker; Ni = Ni-NTA chromatography; SX = SX chromatography. Numbers displayed denote the amount of sample applied to the gel in μ L. Mass determination (right) determined from the deconvolution of ESI-MS data (left).

The CBB-stained SDS-PAGE gel image suggests a very pure protein. The protein mass determined by ESI-MS, however, shows a difference of +240 Da. As the signal intensity indicates a low ion count, the high noise levels might have led to an unusually high instrumental inaccuracy (mass fluctuations of about 0.01% are normally observed on this machine). For a deeper investigation, de92 was digested with trypsin, which proteolyzes after lysines and arginines, and measured *via* HPLC with coupled ESI-MS/MS (Figure 26). Using the

BioWorks Browser by Thermo, most of the expected fragments were identified with very high fidelity (probability score $P < 10^{-4}$). Analysis of the detected fragments show the triple phosphorylation at Ser124, Ser129 and Thr450, which would explain the mass difference. These phosphorylation sites are known in literature and are commonly observed in Akt expressed in insect cells.¹⁷²⁻¹⁷⁵ While their function is not yet elucidated, it is established that they do not determine the basal kinase activity of Akt.



MGSTSHHHHH HDHITSLYKK AGFENLYFQG SDVAIVKEGW LHKRGEYIKT
 WRPRYFLLKN DGTFIGYKER PQDVDQRCAP LNNFSVAQCQ LMKTERPRPN
 TFIIRCLQWT TVIERTFHVE TPEEREWTT AIQTVADGLK KQEEEEEMDFR
 SGSPSDNSGA EEMEVSLAKP KHRVTMNEFE YLKLLGKGTG GKVILVKEKA
 TGRYYAMKIL KKEVIVAKDE VAHTLTENRV LQNSRHPFLT ALKYSFQTHD
 RLCFVMEYAN GGELFFHLSR ERVFSEDRAR FYGAEIVSAL DYLNHSEKNVV
 YRDLKLENLM LDKDGHIKIT DFGLSKEGIK DGATMKTFSG TPEYLAPEVL
 EDNDYGRAVD WWGLGVVMEY MMSGRLPFYN QDHEKLFELI LMEEIRFPRT
 LGPEAKSLLS GLLKDPKQR LGGSEDAKE IMQHRFFAGI VWQHVVYEKKL
 SPPFKPQVTS ETDTRYFDEE FTAQMITITP PDQDDSMCEV DSERRPHFPQ
 FSYSASGTA

Figure 26 Chromatogram and mass spectrum of the trypsinised de92. The expected fragments that were found in ESI-MS/MS are marked in blue.

In the purification of the pHT1023 construct, the 50-100 mM imidazole fractions from the Ni^{2+} affinity chromatography were collected for further SX purification. Again, the fractions with the 59 kDa target protein were concentrated to approximately 30 μM and frozen in liquid nitrogen. This construct, too, proved pure on the analytical SDS-PAGE gel and displayed a mass difference of around 240 Da, which was attributed to the same phosphorylations as in de92. For this construct with the additional C460S mutation when compared to de92, the yield was only 1.7 mg/L.

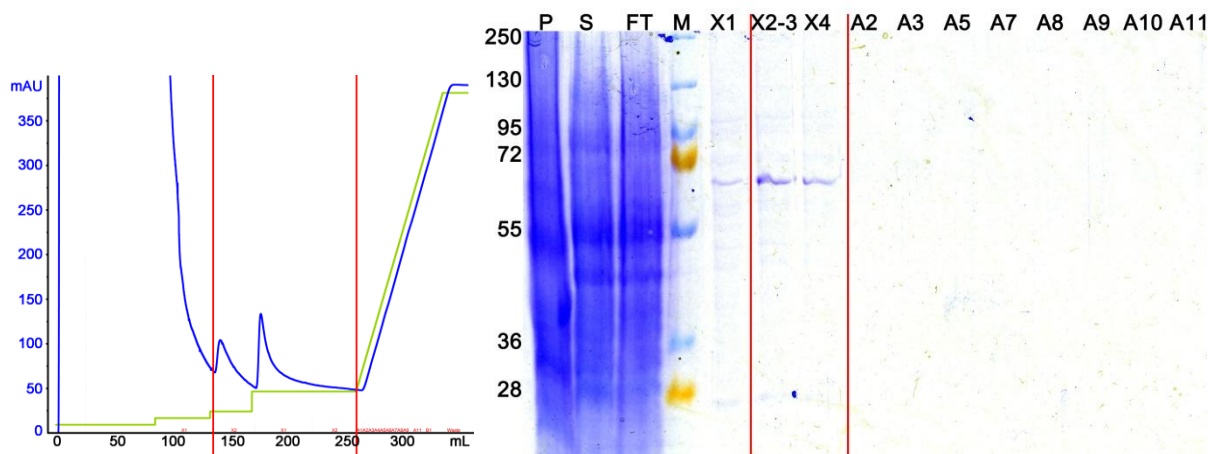


Figure 27 Left: Chromatograms of Ni-NTA chromatography for pHT1023 (blue = UV absorption A_{210} , green = imidazole gradient). Right: Corresponding CBB-stained analytical gel images with PageRuler Plus Prestained by Fermentas used as marker. Molecular weight is displayed in kDa. The target protein has a molecular weight of 59 kDa. P = cell pellet after lysis; S = supernatant after lysis; FT = flowthrough; M = marker; X1 = 10 mM imidazole; X2-3 = 20 mM imidazole; X4 = 50 mM imidazole; A2-A11 = 50-500 mM imidazole gradient. Fractions X2-X4 were combined for subsequent SX chromatography.

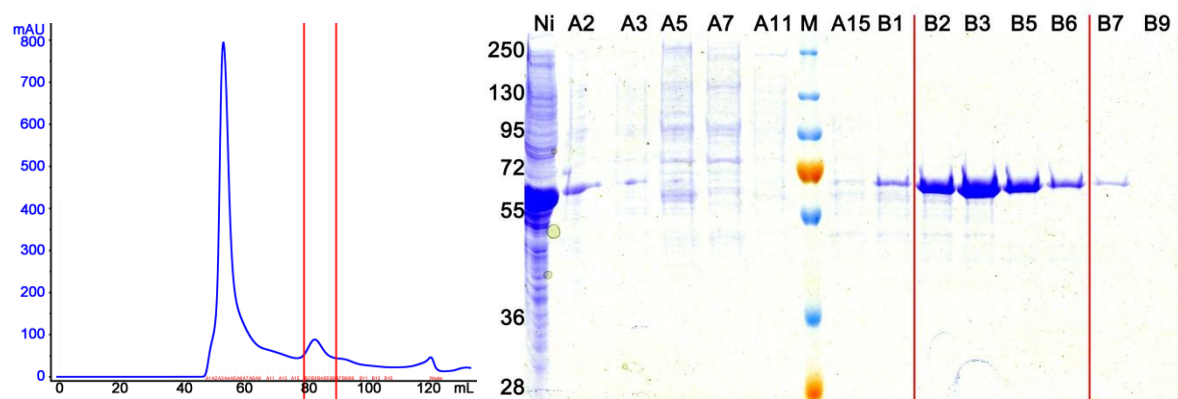


Figure 28 Left: Chromatograms of SX chromatography for pHT1023 (blue = UV absorption A_{210}). Right: Corresponding CBB-stained analytical gel images with PageRuler Plus Prestained by Fermentas used as marker. Molecular weight is displayed in kDa. The target protein has a molecular weight of 59 kDa. Fractions B2-B6 were combined..

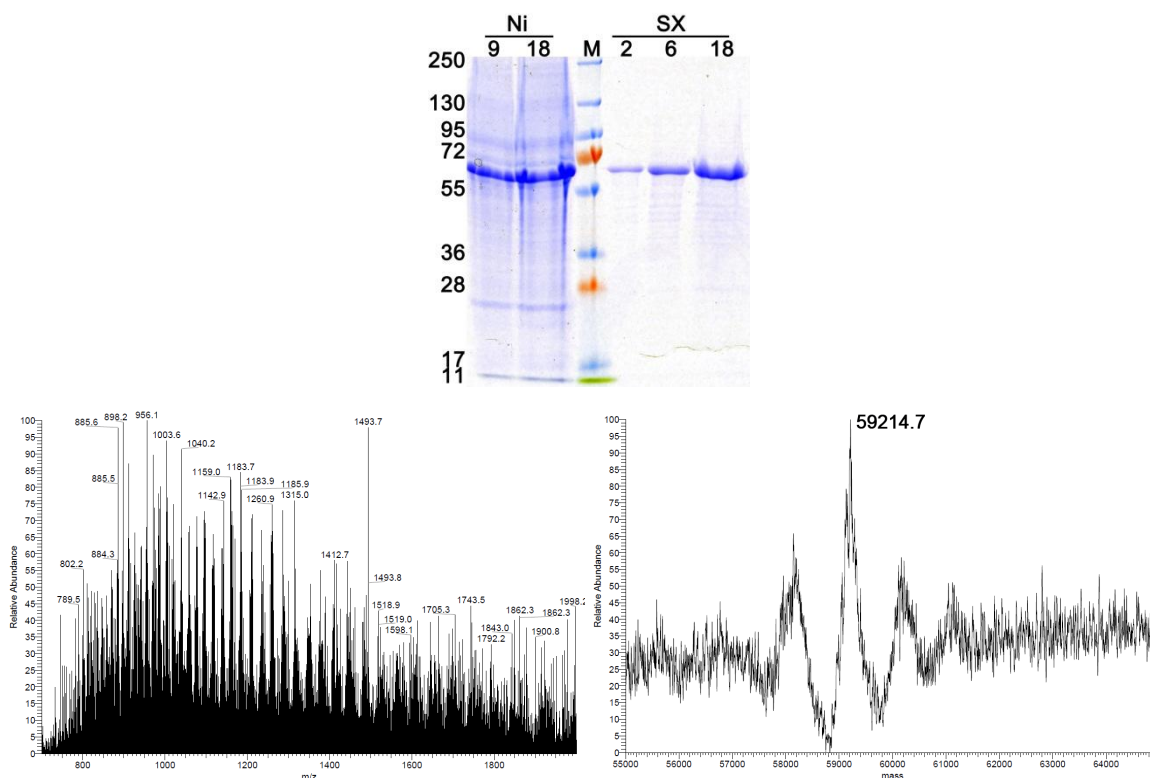


Figure 29 Top: Overview of protein purity after each purification step of pHT1023 with PageRuler Plus Prestained by Fermentas used as marker. Molecular weight is displayed in kDa. Ni = Ni-NTA chromatography; M = marker; SX = SX chromatography. Numbers display denounce the amount of sample applied to the gel in μL . Mass determination (right) determined from the deconvolution of ESI-MS data (left).

The same procedure was repeated for de91, and the 50-100 mM imidazole fractions from the Ni-NTA column were combined for SX chromatography. The 55 kDa protein was collected accordingly, concentrated to roughly 30 μM and frozen in liquid nitrogen. The SDS-PAGE gel confirmed its purity. Interestingly, this protein without the C-terminal hydrophobic motif showed no mass difference that would correspond to a triple phosphorylation. This could suggest that the HM might serve as the recognition site for the upstream kinases responsible for Ser124, Ser129 and Thr450 phosphorylation. This construct lacking the HM had even lower expression rates, accumulating to 0.8 mg/L. SDS-PAGE gels suggest that a large proportion might be misfolded and remains in the insoluble part of the cell pellet after membrane disruption.

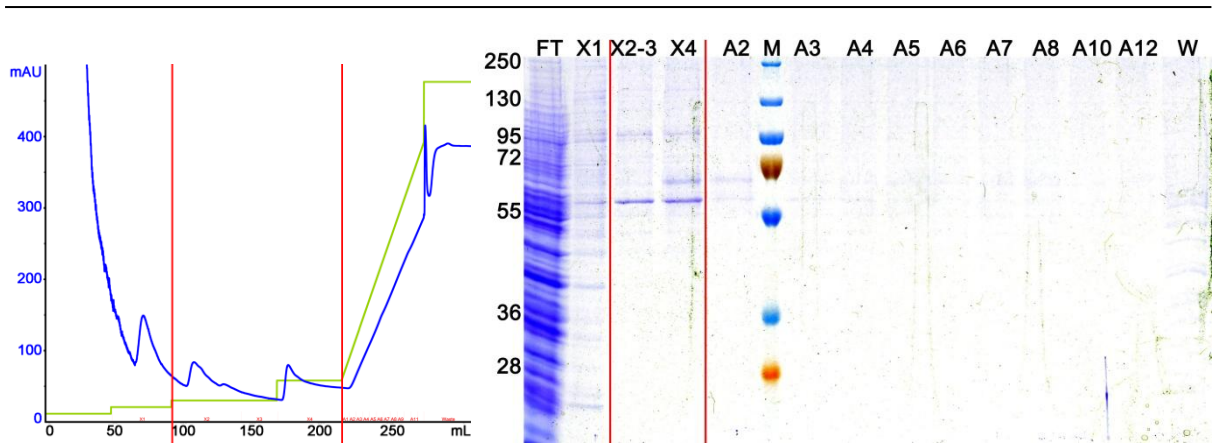


Figure 30 Left: Chromatograms of Ni-NTA chromatography for de91 (blue = UV absorption A_{210} , green = imidazole gradient). Right: Corresponding CBB-stained analytical gel images with PageRuler Plus Prestained by Fermentas used as marker. Molecular weight is displayed in kDa. The target protein has a molecular weight of 55 kDa. FT = flowthrough; X1 = 10 mM imidazole; X2-3 = 20 mM imidazole; X4 = 50 mM imidazole; M = marker; A2-A11 = 50-500 mM imidazole gradient. Fractions X2-X4 were combined for subsequent SX chromatography.

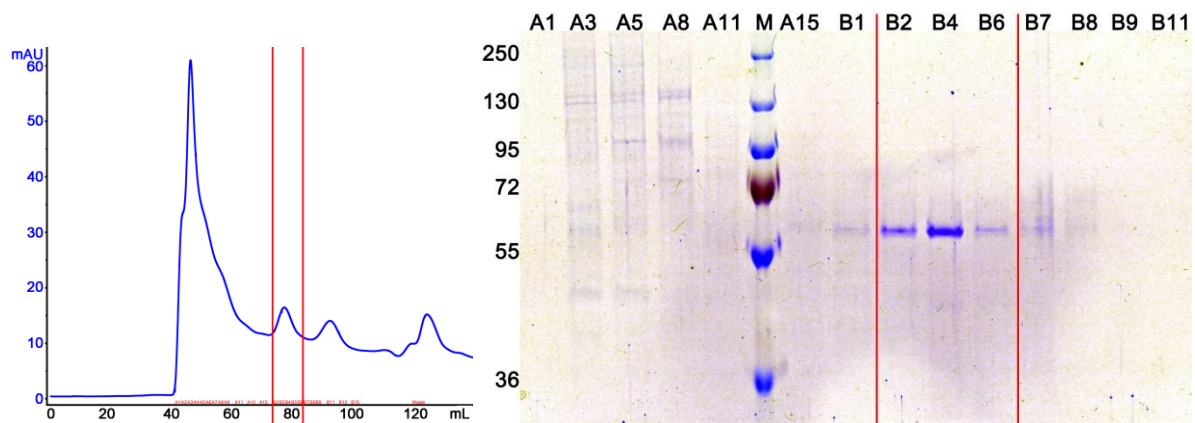


Figure 31 Left: Chromatograms of SX chromatography for de91 (blue = UV absorption A_{210}). Right: Corresponding CBB-stained analytical gel images with PageRuler Plus Prestained by Fermentas used as marker. Molecular weight is displayed in kDa. The target protein has a molecular weight of 55 kDa. Fractions B2-B6 were combined.

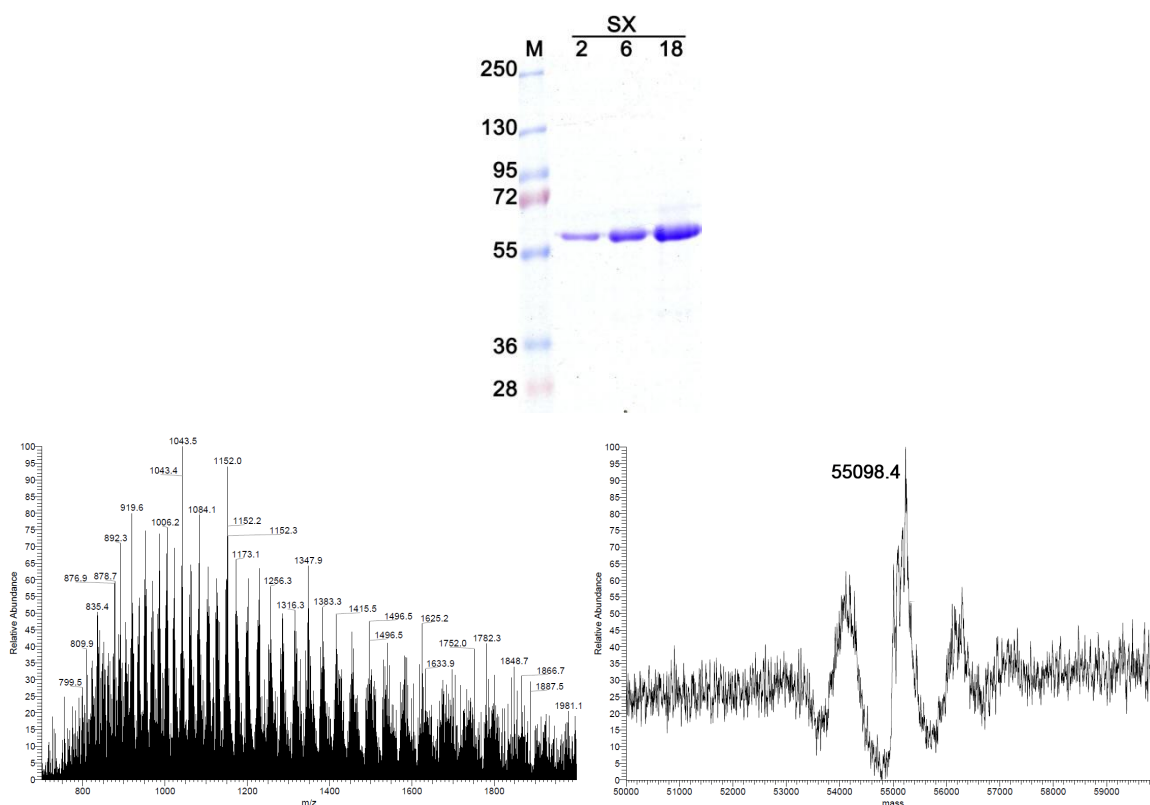


Figure 32 Top: Overview of protein purity after each purification step of de91 with PageRuler Plus Prestained by Fermentas used as marker. Molecular weight is displayed in kDa. M = marker; SX = SX chromatography. Numbers display denounce the amount of sample applied to the gel in μL . Mass determination (right) determined from the deconvolution of ESI-MS data (left).

In summary, 3 different Akt constructs were expressed in insect cells and purified with a yield of 3.7 mg/L, 1.7 mg/L and 0.8 mg/L for de92, pHT1023 and de91, respectively. The highest expression rates, therefore, could be obtained with the construct closest to the wild type. The identity of these three proteins were confirmed by mass spectrometry and tryptic digest, the purity by SDS-PAGE analysis.

Table 3 Summary of the expressed and purified Akt constructs.

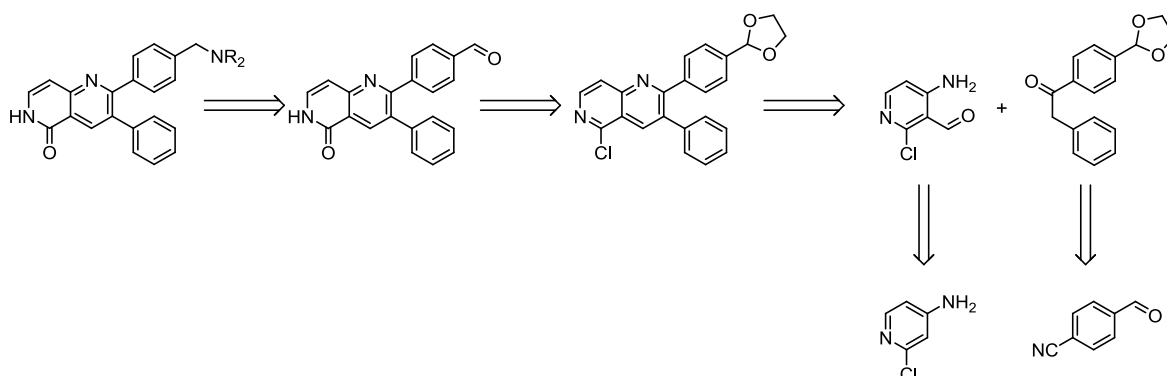
Construct	Yield / mg/L	Calculated mass	Detected mass	Comments
de91	0.8	55098 Da	55098 Da	low solubility
pHT1023	1.7	58965 Da	59215 Da	+240 Da mass difference due to phosphorylation of Ser124, Ser129 and Thr450
de92	3.7	58981 Da	59221 Da	

3.3 Synthesis of Probe Compounds

With the protein in hand, the next step was to obtain allosteric Akt inhibitors, that can be used as reference compounds to establish the assay. Although many allosteric Akt inhibitors have been published and tested (chapter 1.2.3), only Akti-1/2 and the clinical candidate MK-2206 are commercially available. Limited by the number of commercially available allosteric inhibitors as probe molecules to assess the functionality of our future assay, we decided to synthesise a focussed library of ID inhibitors.

Based on the known inhibitors and studying their SAR, the 1,6-naphthyridinone core as scaffold for the western part represented a compromise of high efficacy and reasonable synthetic accessibility (as was seen for compound **48**). As the eastern part has a significant impact on its efficacy as inhibitor, it was decided to introduce diversity at this position, while maintaining the tertiary amine in β -position to the bridging benzyl group.

In order to obtain the desired compounds, a convergent synthesis for the generation of the naphthyridinone core was pursued (Scheme 1): In the final step, the eastern part will be introduced *via* reductive amination with commercially available amines. The 1,6-naphthyridinone will be converted from the corresponding chloro-naphthyridine, which can be obtained easier than the more reactive naphthyridinone. The naphthyridine core in turn will be formed by a Friedländer cyclocondensation of an *ortho*-formylated aminopyridine with a ketone. These building blocks will be synthesised from the starting compounds 2-chloropyridin-4-amine and 4-formylbenzoxantrone, respectively. The benefit of this convergent approach is yield maximisation by reducing linearly dependent synthetic steps, whereas the diversity generating last reaction will provide an easy access to a variety of structurally related compounds.



Scheme 1 Retrosynthesis of the planned naphthyridinone-based inhibitors.

Adapting a protocol by Casiraghi *et al.*, who used a phenol hydroxyl group to direct the formylation by paraformaldehyde into the *ortho* position *via* complexation with transition

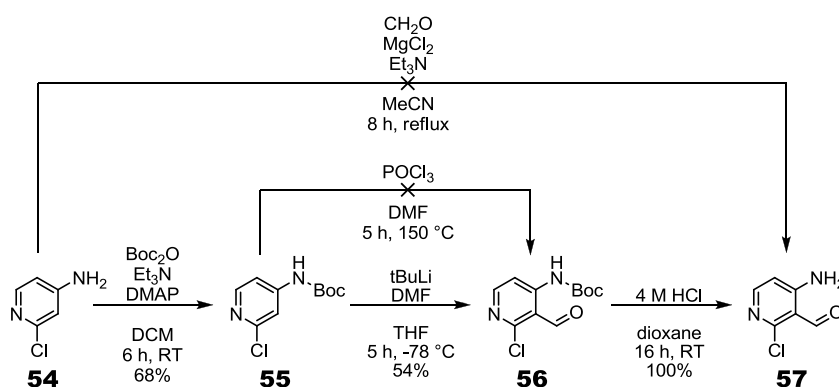
metals, a direct formylation of 2-chloropyridin-4-amine (**54**) with MgCl_2 was attempted (Scheme 2).¹⁶³ Analysis of the reaction mixture with LC-MS, however, did not show the formation of the desired product **57**, demonstrating the need to mask the reactive amine group.

Since introduction of the formyl group in the next step required basic conditions, the acid-labile *tert*-butyloxycarbonyl was chosen as protecting group. Optimising the reaction conditions with respect to solvent, temperature and equivalents of reagents, following observations were made:

- DCM at RT proved to be the best performing solvent.
- Increasing base strength $\text{Et}_3\text{N} < \text{DIPEA} < \text{NaOtBu}$ led to an increase of by-products but not conversion.
- Excess of Boc_2O increased the amount of a double Boc-protected species.
- Adding DMAP increased conversion of **54**.

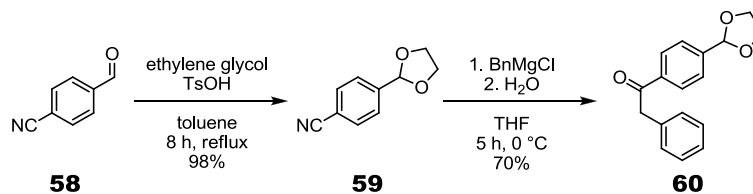
While an excess of Et_3N and Boc_2O gave a complete conversion of **54**, the resulting di-Boc-protected aminopyridine proved to be unreactive in the following *ortho*-formylation, probably due to its steric bulk. For this reason, the amount of DMAP was increased to 0.5 eq while using substoichiometric amounts of Boc_2O . Although conversion was not complete, the proportion of desired product **55** was maximised. Unreacted starting material was recovered in the purification process to be reused for future batches.

Using DMF as formylating agent, the reaction of the mono-Boc-protected reagent to yield **55** was successful with tBuLi as co-reagent but not with POCl_3 . Subsequent deprotection of the Boc group with HCl in anhydrous dioxane gave the desired product **57** as one component of the Friedländer cyclocondensation.



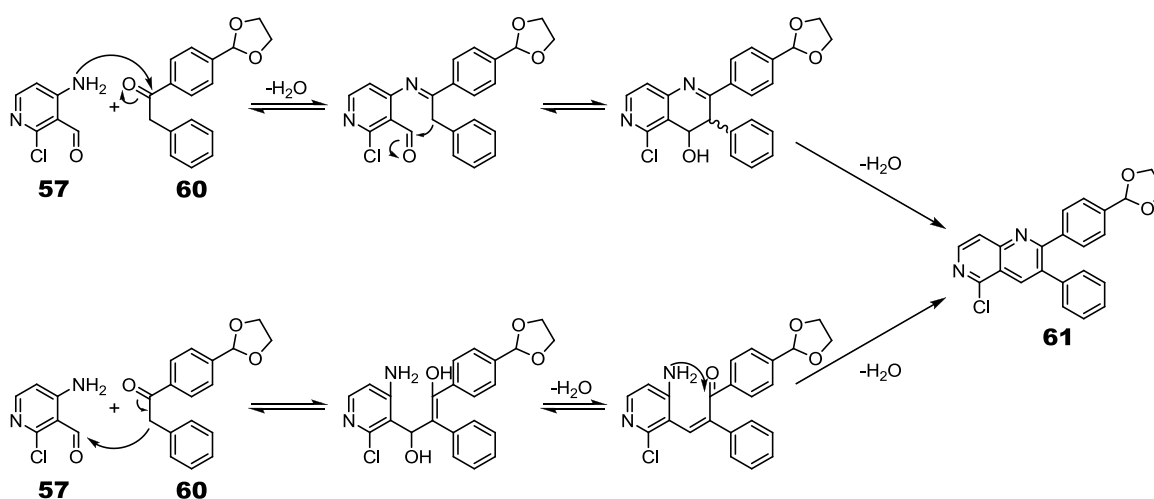
Scheme 2 Attempted and successful formylations of **54** to obtain **57**.

For the other component, the aldehyde **58** was acetal-protected with ethylene glycol under Dean-Stark conditions with near-quantitative yields. The protected nitrile **59** was further reacted with the Grignard reagent benzylmagnesium chloride and hydrolysed *in situ* to produce the desired ketone **60**. All steps went smoothly without major complications (Scheme 3).



Scheme 3 Synthesis of the ketone component **60** for the Friedländer cyclocondensation.

In the literature, a variety of catalysts have been used for Friedländer cyclocondensations. Depending on the substrate, either acids or bases can be more suitable for a particular reaction.¹⁶⁴ Two different mechanisms for acid- or base-catalysis have hence been postulated (Scheme 4):

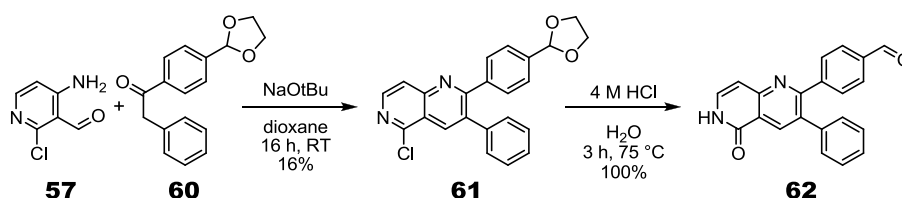


Scheme 4 Two possible mechanisms of the Friedländer cyclocondensation of **57** and **60** to the naphthyridine **61**. The acid-catalysed (upper) and base-catalysed (lower) routes are shown.

Following a protocol by Bilodeau *et al.*, who employed an AcOH-catalysed Friedländer cyclocondensation, only a deprotection of **60** to the corresponding aldehyde was observed, but no formation of the product **61**.¹⁶⁵ Increasing the acidic strength by using TsOH gave the same results.¹⁶⁶ When switching to base catalysis, NaOMe was able to catalyse the cyclocondensation, but also substituted the chloro substituent at the 5-position to methoxy.¹⁶⁷ Therefore, various non-nucleophilic bases such as NaH, Et₃N, DIPEA and NaOtBu were tested for this reaction. None of the nitrogen bases were able to catalyse the cyclisation, whereas NaH was capable of catalysis but also produced a number of by-products. Finally, NaOtBu merged as the most successful catalyst, successfully facilitating the cycloconden-

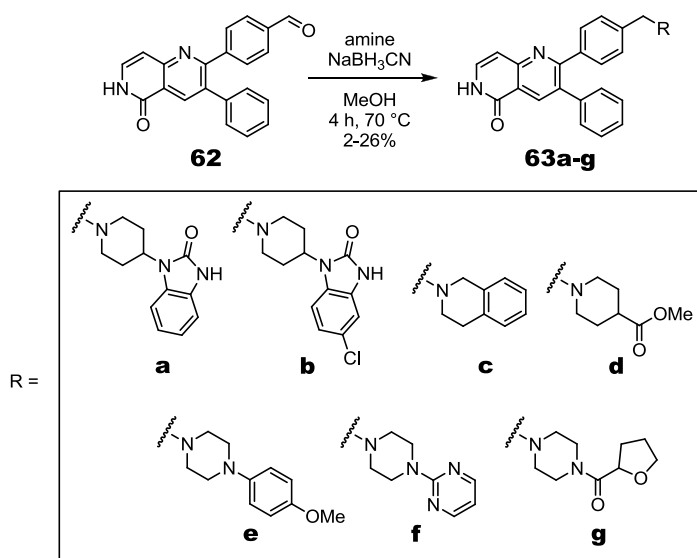
sation with a moderate proportion of side products. Since Friedländer cyclocondensations have been reported using iodine or metals of the lanthanide series as catalysts, we have tested I_2 , $SmCl_3$, $Pr(NO_3)_3$ and $La_2(CO_3)_3$ for the cyclisation of **57** and **60**.^{168,169} However, none of these reagents provoked a reaction of the starting reactants. In the end, it was decided to use NaOtBu as catalyst for the synthesis of **61**.

Deprotection of the acetal and hydrolysis of the chloro substituent to a hydroxy group were combined into one step by heating **61** in aqueous HCl. The resulting phenole moiety of **62** could not be deprotonated at pH 14, but instead was enriched in the aqueous solution when under acidic conditions, which indicates a basic rather than acidic nature of **62**. This reactivity suggests that the tautomerisation of the hydroxypyridine moiety to a lactam structure is indeed the more stable state.



Scheme 5 Formation of the naphthyrindine core *via* Friedländer cyclocondensation and subsequent hydrolysis and deprotection.

For the final diversity-generating step, the deprotected aldehyde **62** was derivatised with various commercially available amines to obtain the final probe molecules **63a-g** *via* reductive amination. Two approaches were investigated, with $NaBH_3CN$ or $NaBHOAc_3$ as reducing agents. While the milder acetate reagent produced fewer side reactions, the conversion of the aldehyde was only marginal. Therefore, using the stronger $NaBH_3CN$ provided complete conversion while maintaining a good selectivity towards the desired product.



Scheme 6 Reductive amination of **62** to give final compounds **63a-g**.

This compound class is known to suffer from low solubilities, possibly due to extensive π - π intermolecular interactions between their aromatic units.¹²⁷ And indeed, from the formation of the naphthyridine core onwards, compound handling became a major issue as these molecules were highly insoluble in any solvent besides DMSO. Purification *via* column chromatography always led to a significant drop in yield, presumably due to the formation of precipitates on the solid phase which cannot be re-dissolved into solution. Purification by precipitation was not a viable alternative, as no solvent combination was able to provoke a precipitation of the compound in significant amounts. Extraction and enrichment in a Soxhlet extractor was not successful either, resulting in loss of the entire product in the Soxhlet capsule. Therefore, the low yields associated with column chromatography had to be accepted. Introduction of the amine for the final compound increased the polarity of the molecule, thus enabling the purification *via* reversed-phase preparative HPLC with still low yields (2-26%).

In summary, the synthesis of the intended probe molecules was successful, providing seven compounds **63a-g** with a naphthyridinone scaffold and various substituents on the eastern part. The identity of all compounds was confirmed by HR-MS, ¹H- and ¹³C-NMR, as well as 2-dimensional COSY, ¹³C-HSQC and ¹³C-HMBC. In addition to their use as probe molecules for the development of the conformational assay, their biological activity *in vitro* and *ex vivo* had to be examined. This will be discussed in chapter 3.4.

3.4 Biological Activity of Probe Compounds

3.4.1 *in vitro* Activity

In order to assess the biological activity of the synthesised probe molecules, their activity against the intended target Akt had to be determined. Two isoforms Akt1 and Akt2, as well as the kinase domain only construct Δ PH-Akt1 were purchased to use them in the activity-based KinEASE assay by CisBio. The KinEASE assay measures the phosphorylation activity of a kinase by FRET between an anti-phospho antibody and an acceptor fluorophore on the substrate (see a more detailed description in chapter 1.4.1). The ratio of the acceptor fluorescence intensity at 665 nm to donor fluorescence at 620 nm (from now on referred to as f_{665}/f_{620}) serves as the assay readout, and correlates directly to the extent of substrate phosphorylation and hence kinase activity. To establish this assay, the optimal reaction parameters for the assay had to be determined experimentally for each kinase and batch, i.e. the kinase's activity, ATP- and substrate- K_m have to be investigated. The process of establishing the KinEASE assay for Akt1, Akt2 and Δ PH-Akt1 is discussed in chapter 5.1.

After these establishing steps, the IC_{50} for a known inhibitor was determined as reference. Even though IC_{50} values are often comparable under controlled conditions, each assay setup still provides different results. Therefore, reference values of known inhibitors have to be established to better range in the results of each particular assay. The clinical candidate MK-2206 was chosen as representative for an allosteric ID inhibitor and H-89 for an ATP-competitive inhibitor. Their IC_{50} s were determined from three independent measurements (Table 4) using the sigmoidal 4-parameter Hill equation (5). The IC_{50} s correlate well with the reported values for Akt1 and Akt2. As expected, the allosteric inhibitor shows no effect on the kinase domain alone, but only on the full-length kinases. In conclusion, the assay was successfully validated with these two reference compounds. Subsequently, other allosteric (Akti-1/2) and ATP-competitive Akt inhibitors (staurosporine, GSK690693 and CCT128930) were evaluated for further reference.

$$f(c_{I,0}) = T + \frac{B}{1 + \left(\frac{c_{I,0}}{IC_{50}}\right)^H} \quad (5)$$

$c_{I,0}$ = total inhibitor concentration

T = top asymptote

B = bottom asymptote

H = Hill coefficient

IC_{50} = concentration of half-maximal inhibition

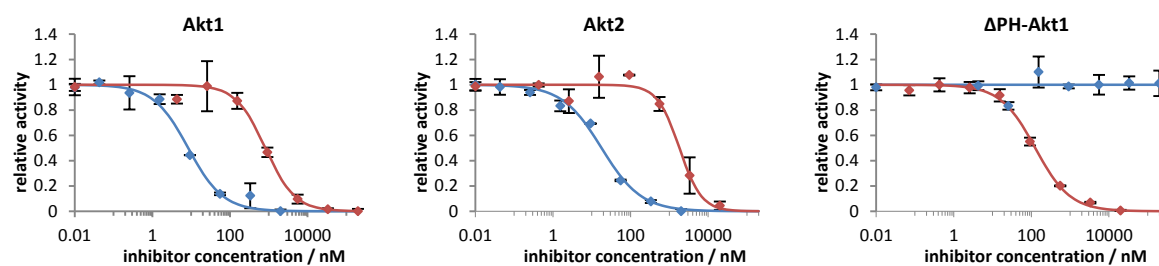


Figure 33 IC₅₀ determination of MK-2206 (blue) and H-89 (red) as reference inhibitors for the validation of the KinEASE assay with Akt1, Akt2 and ΔPH-Akt1.

Table 4 Summary of determined IC₅₀s for various allosteric and ATP-competitive reference inhibitors, including MK-2206 and H-89 for the validation of the Akt1, Akt2 and ΔPH-Akt1 KinEASE assay. n.i. = not inhibiting up to 200 μM.

IC ₅₀ / μM	Akt1		Akt2		ΔPH-Akt1	
	measured	literature	measured	literature	measured	literature
MK-2206	0.006 ± 0.002	0.008	0.020 ± 0.009	0.002	n.i.	n.i.
Akti-1/2	<0.001	0.058	3 ± 1	0.21	n.i.	n.i.
H-89	2 ± 1	1.4	2.1 ± 0.8	1.4	0.14 ± 0.02	1.4
GSK690693	<0.001	0.002	0.004 ± 0.001	0.013	<0.001	0.002
CCT128930	0.029 ± 0.009	0.006	0.20 ± 0.07	0.02	0.030 ± 0.007	0.006
Staurosporine	0.014 ± 0.005	0.011	0.004 ± 0.003	0.011	0.018 ± 0.009	0.011

In summary, the optimal assay parameters were determined to 0.12 nM kinase, 45 min incubation time, 50 μM ATP and 250 nM STK3 substrate for Akt1, 0.51 nM kinase, 17 min incubation time, 65 μM ATP and 300 nM STK3 substrate for Akt2, and 0.06 nM kinase, 20 min incubation time, 65 μM ATP and 300 nM STK3 substrate for ΔPH-Akt1. All KinEASE measurements were conducted with these parameters.

Finally, the synthesised probe molecules **63a-g** as well as **64a-d**, which are allosteric ID inhibitors synthesised by Dr. Abu Taher in the lab of Prof. Willem V. A. van Otterlo, were measured with KinEASE against all three kinase constructs (Table 5). As expected, none of them had an inhibitory effect on ΔPH-Akt1 up to 200 μM, as it lacks the necessary PH domain to form the binding pocket at the domain interface. On the full-length kinases, however, all inhibitors exhibited inhibitory effects with different efficacies. On average, **63a-g** showed a lower potency against Akt2 than Akt1 of about one order of magnitude. This is in congruence with the isoform selectivity known for this class of inhibitors, as Akt2 lacks the Ser205 that is addressed by the carbonyl group of the naphthyridinone scaffold.¹⁷⁰ Within a single isozyme, **63a-g** exhibit the same SAR, with **63a** and **63b** being the most potent inhibitors, and **63e** and **63g** the least.

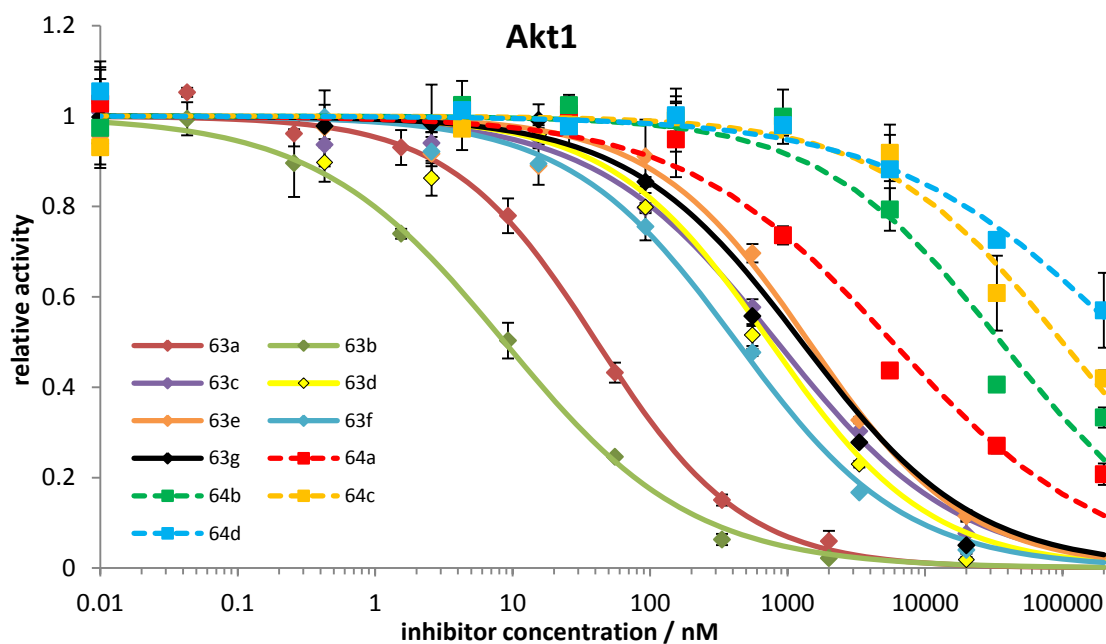
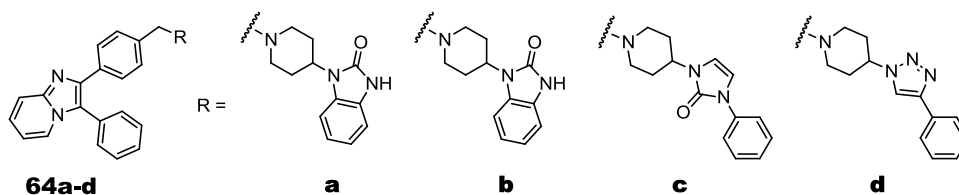


Figure 34 Dose-response curves from IC_{50} determination of **63a-g** and **64a-d** with KinEASE against Akt1.

Table 5 IC_{50} s of synthesised probe molecules. Compounds **64a-d** were provided by the group of Willem V. A. van Otterlo. n.i. = not inhibiting up to 200 μ M.



IC_{50} / μ M	Akt1	Akt2	Δ PH-Akt1
63a	0.033 ± 0.005	0.43 ± 0.02	n.i.
63b	0.010 ± 0.004	0.21 ± 0.04	n.i.
63c	0.8 ± 0.2	7 ± 5	n.i.
63d	0.6 ± 0.1	6 ± 1	n.i.
63e	1.4 ± 0.5	12 ± 1	n.i.
63f	0.40 ± 0.05	8.5 ± 0.6	n.i.
63g	2.1 ± 0.2	24 ± 12	n.i.
64a	3 ± 2	14 ± 4	n.i.
64b	24 ± 13	132 ± 81	n.i.
64c	64 ± 36	681 ± 396	n.i.
64d	144 ± 132	122 ± 28	n.i.

In order to explain the observed SAR, a co-crystal structure of Akt with one of these compounds would provide an unambiguous answer. However, in the absence of an established and functional crystallisation procedure, docking experiments with Glide from the Schrödinger Suite were performed. The crystal structure of the full length Akt1 co-crystallised with Akti-1/2 (PDB code 3O96) was used as template for molecular docking. After pre-processing by adding hydrogens, removing water molecules and correcting bond lengths and angles, a binding pocket of a volume of 5 Å around the original ligand was calculated for the receptor grid. Ligands were prepared by calculating conformers and tautomers at pH 5-9. The thusly prepared ligands and binding pocket were combined in one docking experiment.

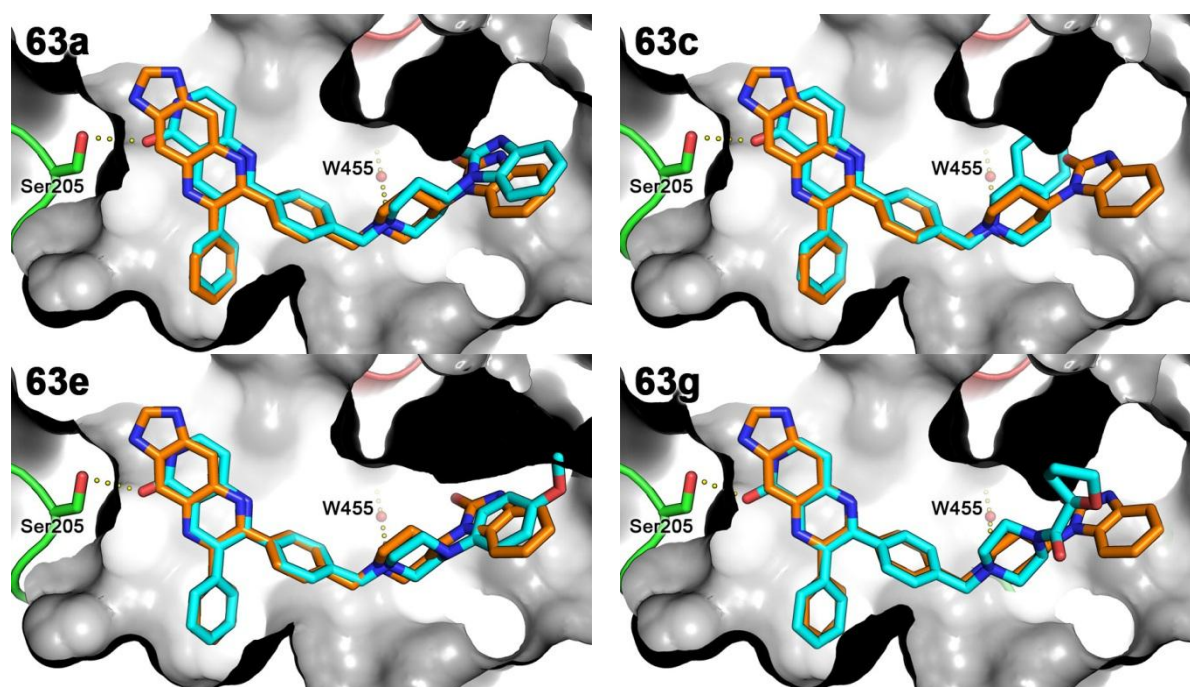


Figure 35 Prediction of the binding mode of synthesised probe molecules (cyan sticks) with Glide, superimposed with the original ligand (orange sticks) in the X-ray crystal structure (PDB code 3O96). **63a** is shown as an example for a potent binder, that fills out the pocket well, **63c** as an example for one that does not fill out the pocket, and **63e** and **63g** as examples for ill-fitting allosteric inhibitors.

The predicted binding mode for **63a**, which possesses the same substituent as Akti-1/2, overlays well with the originally crystallised ligand, giving credit to the validity of the binding poses for this family of inhibitors. The only differences arise from the removal of the water molecule W455 that forms hydrogen bonds between the protein and the piperidine nitrogen. The simulations reveal the reasons for the *in vitro* SAR observed in the KinEASE assay: The most potent **63a** and **63b** nicely fill out the eastern part of the allosteric pocket with their bulky substituents. In contrast, **63c**, **63d** and **63f** are too small and do not fill the pocket completely. On the other hand, **63c** is linear and too long, not fitting well into the pocket. Similarly, the **63c** substituent expands three-dimensionally as compared to the flat

substituents on the other compounds, due to its additional sp³ carbon atoms, which cannot be accommodated into the pocket easily. This order of favourable and unfavourable interactions is in congruence with the KinEASE results and can explain the observed SAR. Therefore, the docking results are likely to represent the actual binding modes of the probe compounds.

In summary, after establishing activity-based *in vitro* assays, the synthesised probe compounds exhibited inhibition of full-length Akt1 and Akt2, but not the kinase domain alone. Docking experiments provided explanations for the SAR. These results suggest that **63a-g** are indeed allosteric Akt inhibitors occupying the allosteric pocket at the interface of PH and kinase domain.

3.4.2 Cellular Activity

Allosteric ID inhibitors are known to exhibit superior selectivity and reduced off-target effects in cells. In collaboration with the group of Prof. Dr. Roman K. Thomas, we investigated the biological effect of **63a-g** on a cellular level to confirm their allosteric mode of action. These experiments were conducted by Dennis Plenker. With the allosteric MK-2206 and the ATP-competitive GSK690693 as reference inhibitors, the breast ductal carcinoma cell line BT474 and the lung adenocarcinoma epithelial cell line H441 were employed as model systems. The effect of the compounds were assessed in dose dependence with the CellTiter-Glo assay, which measures the ATP content of a cell by luciferase luminescence, which gives a quantitative feedback about the cell viability.

When incubated with **63a-g**, MK-2206 and GSK690693, a dose dependent decrease in BT474 cell viability was observed (Figure 36). Mirroring the *in vitro* data, the same order of potency was observable, with **63a** and **63b** exhibiting the strongest effect, and **63e** and **63g** the weakest (Table 6). In contrast, H441 cells showed no significant decrease in viability upon treatment with any of these compounds up to 30 µM. While BT474 is known to be sensitive to Akt inhibition, H441 is resistant to its inhibition, i.e. their survival is not Akt-dependent.¹⁷¹ These results therefore support the hypothesis that Akt is indeed the cellular target which is inhibited by these compounds rather than *via* unspecific toxicity. Interestingly unlike the ID inhibitors, the ATP-competitive GSK690693 is unable to reduce the viability of BT474 cells to zero, indicating a secondary cellular rescue mechanism when inhibiting Akt with ATP-competitive inhibitors.

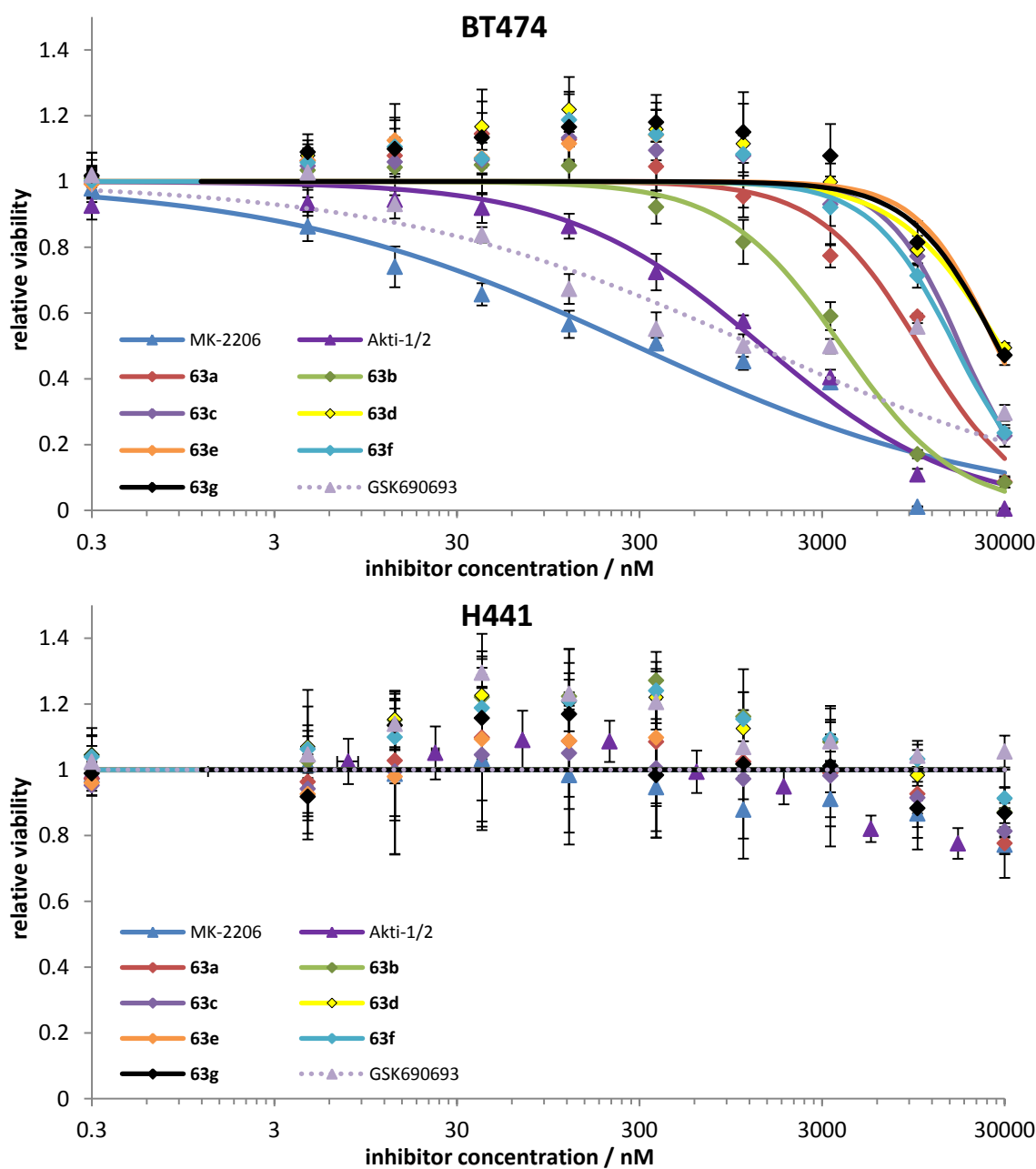


Figure 36 Dose response curves of BT474 and H441 cells upon treatment with **63a-g**, MK-2206, Akti-1/2 and GSK690693. Cell viabilities are expressed relative to DMSO controls.

Table 6 Overview of cellular GI_{50} s of synthesised probe compounds and reference inhibitors against BT474 and H441 cell lines. n.e. = no effect at concentrations up to 30 μ M.

GI_{50} / μ M	BT474	H441
63a	7 ± 2	n.e.
63b	3.2 ± 0.6	n.e.
63c	17 ± 2	n.e.
63d	18 ± 4	n.e.
63e	19 ± 4	n.e.
63f	13 ± 1	n.e.
63g	19 ± 3	n.e.
MK-2206	0.3 ± 0.1	n.e.
Akti-1/2	1.8 ± 0.9	n.e.
GSK690693	0.7 ± 0.2	n.e.

For a more thorough investigation of their effect *ex vivo*, BT474 cells treated with increasing concentrations of MK-2206 and **63b** were harvested and lysed. The lysate was examined by immunostaining *via* Western Blot, using actin-, Akt- and phospho-Akt-specific antibodies. The Western Blots show a dose-dependent decrease of Akt phosphorylation upon treatment with the two compounds, both at the activity-determining Thr308 on the activation loop and the C-terminal Ser473 (Figure 37). Unsurprisingly, the clinical candidate MK-2206 exhibited a higher potency than the synthesised probe molecule **63b**. In comparison, ATP-competitive Akt inhibitors promote hyperphosphorylation of Thr308.⁹² These findings further corroborate **63a-g** as allosteric ID inhibitors.

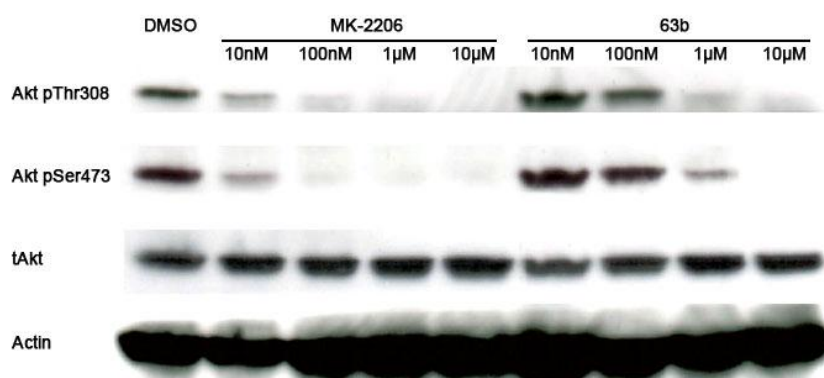


Figure 37 Western Blot of the BT474 cells treated with increasing concentrations of MK-2206 and **63b**. tAkt refers to total Akt, actin serves as loading control.

Interestingly, the sub-nanomolar ATP-competitive Akt inhibitor GSK690693 reduced BT474 viability to about 50% around 0.7 µM, but did not drop further regardless of increasing inhibitor concentration. This upkeep of survival might be attributed to the low selectivity of ATP-competitive Akt inhibitors, leading to stimulation of negative feedback loops by the inhibition of other AGC family kinases, once more demonstrating the benefits of selective Akt inhibition.

3.5 iFLiK Assay Development

3.5.1 Selecting Appropriate Reporter Fluorophore

As described in chapter 1.3.1, fluorophores react differently to changes in their environment. When attached to a protein, their fluorescence properties can be used to report on changes of the microenvironment, i.e. in the direct vicinity of the fluorophore. By labelling residues that are part of the respective binding pocket, the FLiK assay developed in our group was able to detect compounds binding to the ATP-, lipid- or myristate pocket of the respective kinase (for more details see chapter 1.4.2). The current challenge is to investigate whether such environmentally sensitive fluorophores can report on the overall conformational changes of entire proteins by individual domain movements. As these are a direct result of a ligand binding event in the case of ID inhibitors of Akt, this binding would be concluded from such a conformational change. Being a further development of the FLiK assay, the novel assay system will hence be termed iFLiK (interface-FLiK).

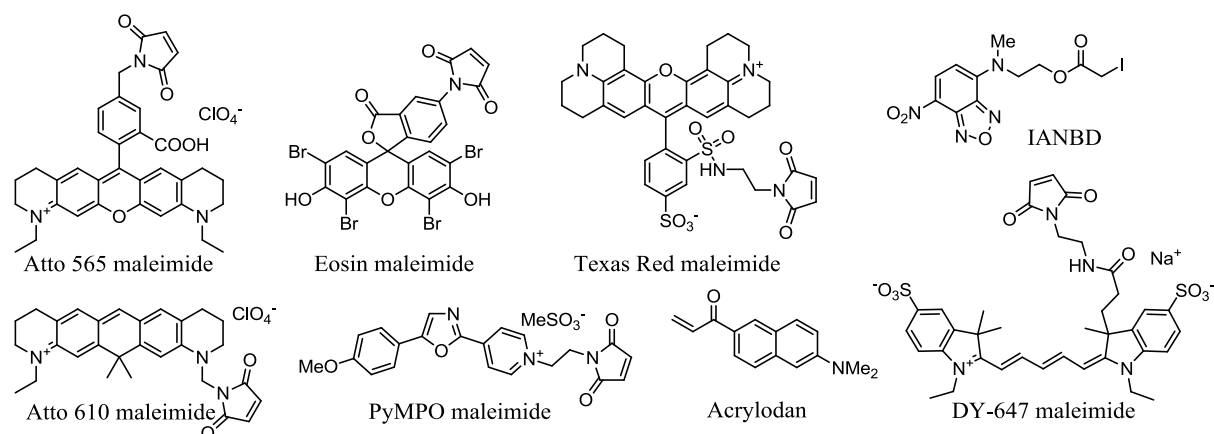


Figure 38 Cysteine-reactive fluorophores tested for iFLiK.

A collection of cysteine-reactive fluorophores were purchased for their use in the iFLiK assay, namely Acrylodan, PyMPO maleimide, DY-647 maleimide, IANBD, Texas Red maleimide, Atto 565 maleimide, Eosin maleimide, Atto 610 maleimide (Figure 38). In order to assess their suitability for the assay, a series of tests with the fluorophores without labelling the protein were conducted to avoid unnecessary protein consumption. To imitate the redox state at the labelled cysteine, each fluorophore was reduced by overnight incubation with 10 eq β -mercaptoethanol for these tests. As the spectral changes of solvatochromic fluorophores are governed by the solvent polarity (see detailed discussion in chapter 1.3.1), the emission spectra of all 8 fluorophores were measured in a variety of solvents with different

polarities (buffer, 20% glycerol in buffer, 20% PEG6000 in buffer, iPrOH, MeCN, DMSO, DMF, acetone and dioxane).

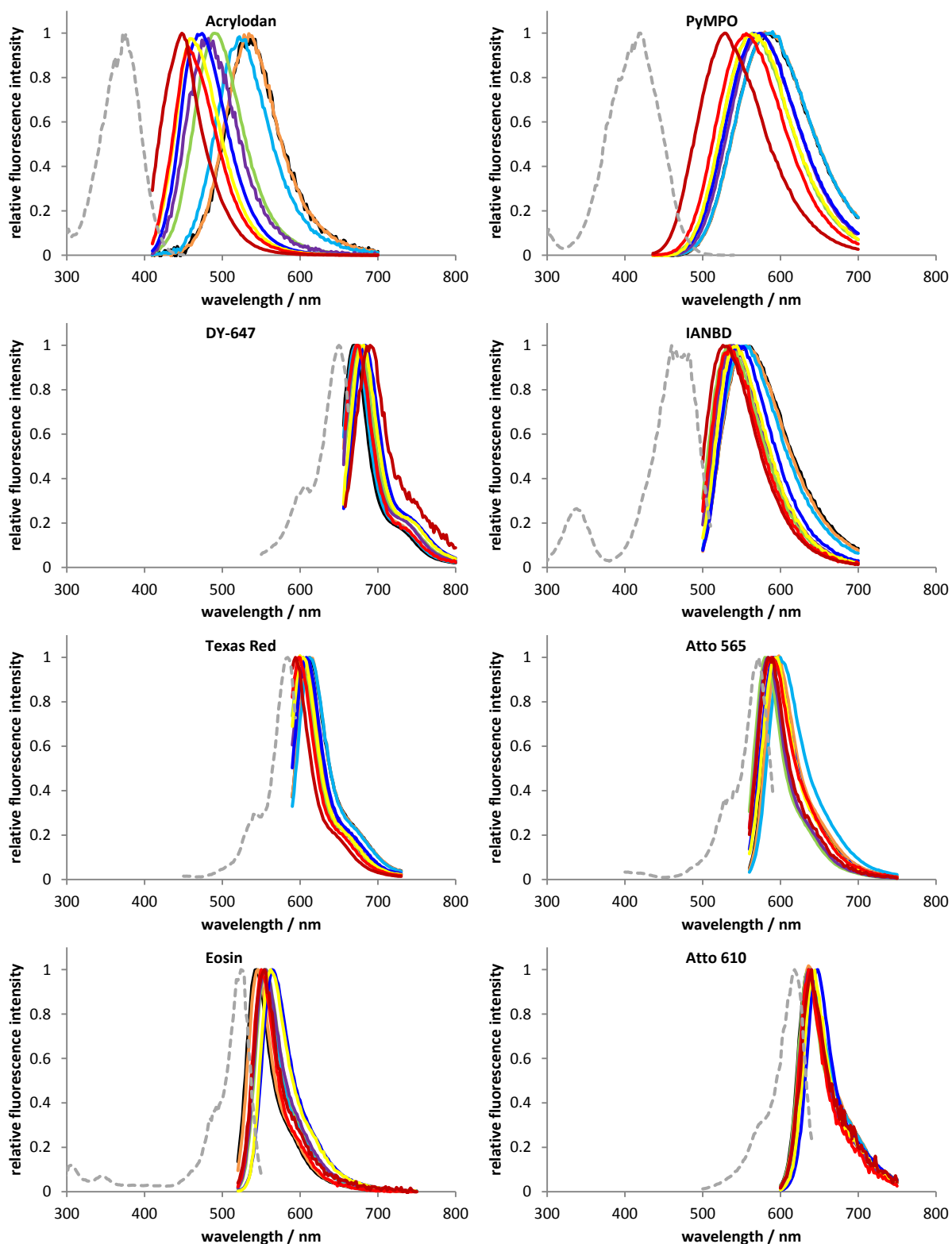


Figure 39 Fluorescence spectra of Acrylodan, PyMPO, DY-647, IANBD, Texas Red, Atto565, Eosin and Atto610 in buffer (black), 20% glycerol in buffer (orange), 20% PEG6000 in buffer (cyan), iPrOH (green), MeCN (violet), DMSO (blue), DMF (yellow), acetone (red) and dioxane (brown). The grey dotted lines mark the excitation spectra.

In these preliminary tests, the fluorophores exhibited different sensitivities towards polarity changes (Figure 39). Acrylodan and PyMPO, which have a strong dipole moment, displayed a bathochromic spectrum shift of up to 88 nm and 56 nm, respectively, with increasing solvent polarity (dioxane to buffer). The highly symmetrical fluorophores Atto 565, Atto 610 and Eosin only showed minor spectrum changes (16 nm, 14 nm and 10 nm). Interestingly, DY-647 responded with a 20 nm hypsochromic spectrum shift towards increasing solvent polarity, leading to negative solvatochromism.

To test how these fluorophores perform as biosensors on Akt, de92 was chosen for these experiments, since it was the best expressing construct. All fluorophores were each incubated individually with de92 over night at 4 °C. To increase the nucleophilicity of the cysteine thiol, the labelling was conducted in the labelling buffer adjusted to pH 7.2. Unreacted fluorophores were removed by size exclusion. Subsequently, these labelled proteins were incubated with various concentrations of the allosteric inhibitor MK-2206 in 384-well plates to observe whether these fluorophores were capable of reporting on the conformational changes associated with the binding of ID inhibitors. For comparison, whether or not the observed effects were selective for this domain movement, the same experiment was conducted in parallel with the ATP-competitive GSK690693, which should not induce these conformational changes (Figure 40). Depending on their structure, the various fluorophores displayed differential responses upon binding of MK-2206, which are summarised in Table 7. Some fluorophores like PyMPO or IANBD exhibited a shift in the emission spectrum and therefore in their fluorescence maximum, whereas an overall intensity increase could be observed with Atto 565 or Eosin. In comparison, no changes in the emission spectra could be observed for any of the labelled Akt when incubated with GSK690693 (apart from fluctuations in the fluorescence intensity of roughly $\pm 10\%$). Furthermore, mixtures of inhibitors with PyMPO-labelled glutathione or β -mercaptoethanol displayed no such effect, confirming that the observed responses are specific to the conformational change of Akt, and not due to interaction with the fluorophores alone. As the binding pocket and labelling site are more than 20 Å apart, an interaction between the ligand and the fluorophore (e.g. *via* resonance energy transfer or direct contact) is highly unlikely. These findings suggest that the observed changes are indeed owed to the conformational changes caused by allosteric inhibitors.

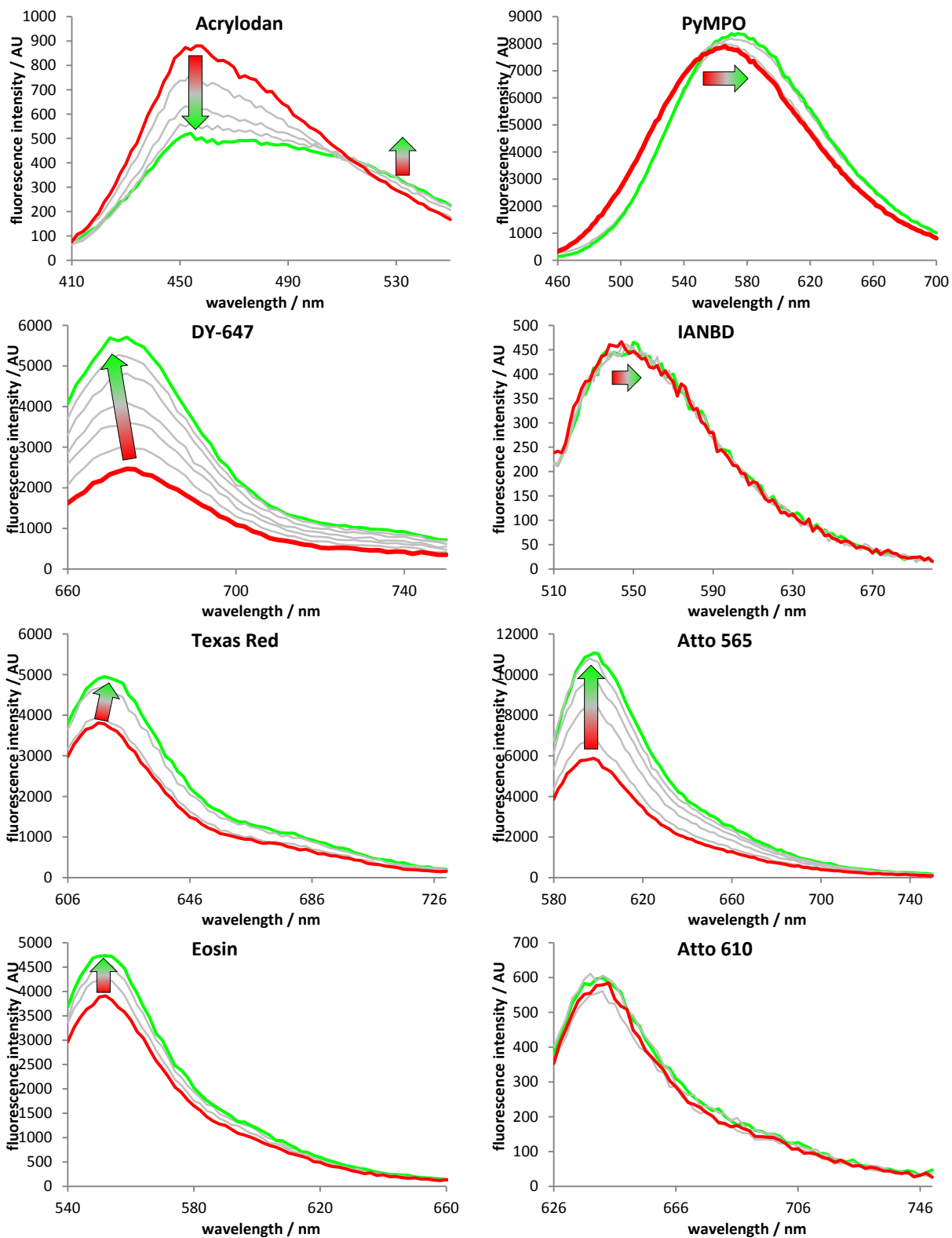


Figure 40 Fluorescence emission spectrum of de92 labelled with Acrylodan, PyMPO, DY-647, IANBD, Texas Red, Atto565, Eosin and Atto610 after incubation with increasing concentrations up to 5 μ M of MK-2206 or **63b** in the case of Acrylodan (red = apo; green = saturated).

Depending on the type of response observed, different assay readouts were used to determine ligand binding affinities. In the case of an intensity change, the fluorescence intensity at the emission maximum was used as the readout. For the quantification of spectrum shifting, the two wavelengths in the emission spectrum with half-maximal emission intensities were recorded, and the ratio of their emission intensities served as the assay readout. By comparing the fluorescence of the kinase incubated with 5 μM MK-2206 to the apo kinase ($n = 6$), signal-to-noise ratios and Z' -factors were calculated for each fluorophore-labelled kinase as descriptors for the assay quality and reproducibility. Additionally, dose-response experiments were performed by incubating the labelled kinases with a dilution series of either MK-2206 or GSK690693 with final concentrations ranging between 0.8 nM and 50 μM . By plotting the respective assay response against the logarithmic inhibitor concentration, the K_d was determined by fitting the data to an asymmetric sigmoidal curve (equation (7)), which was derived from the law of mass action (equation (6)).

$$K_d = \frac{c_I \cdot c_P}{c_{PI}} = \frac{(c_I - c_{PI})(c_P - c_{PI})}{c_{PI}} \quad (6)$$

$$c_{PI}^2 - (c_{P,0} + c_{I,0} + K_d)c_{PI} + c_{P,0} \cdot c_{I,0} = 0$$

$$c_{PI} = \frac{c_{P,0} + c_{I,0} + K_d}{2} - \sqrt{\left(\frac{c_{P,0} + c_{I,0} + K_d}{2}\right)^2 - c_{P,0} \cdot c_{I,0}}$$

$$\frac{c_{PI}}{c_{P,0}} = \theta = \frac{c_{I,0} + K_d}{2} - \sqrt{\left(\frac{c_{I,0} + K_d}{2c_{P,0}} + \frac{1}{2}\right)^2 - \frac{c_{I,0}}{c_{P,0}}} \quad (7)$$

In order to adapt this formula to the binding curves, values for the upper and lower asymptote based on the fractional occupancy were worked in equation (8), as well as the Hill coefficient to account for positive and negative cooperative binding. The resultant asymmetric 5-point Hill function (9) was used for fitting the data.

$$\theta = \frac{f(c_{I,0}) - B}{T - B} \quad (8)$$

$$f(c_{I,0}) = \left(\frac{c_{I,0}^H + K_d^H}{2} - \sqrt{\left(\frac{c_{I,0}^H + K_d^H}{2c_{P,0}} + \frac{1}{2} \right)^2 - \frac{c_{I,0}^H}{c_{P,0}}} \right) (T - B) + B \quad (9)$$

c_I = inhibitor concentration c_P = protein concentration c_{PI} = protein-inhibitor-complex concentration
 $c_{I,0}$ = total inhibitor concentration T = top value B = bottom value θ = fractional occupancy
 $c_{P,0}$ = total protein concentration H = hill coefficient K_d = dissociation constant

Except for Atto 610 and Acrylodan, all fluorophores were able to detect MK-2206 binding to Akt with comparable K_d s but with varying degrees of reliability. The response appeared to be specific to allosteric inhibitors since the labelled kinase was unresponsive to the addition of the ATP-competitive inhibitor GSK690693. In the case of Atto 610, no changes in the fluorescence spectrum could be observed with either inhibitor. For Acrylodan, high levels of MK-2206 auto-fluorescence at the Acrylodan excitation wavelength rendered the measurement with this reference inhibitor impossible. Therefore, experiments were repeated for Acrylodan- and PyMPO-labelled Akt using the less fluorescent **63b**, which evoked the same assay response with PyMPO as MK-2206 did. With Acrylodan, its emission spectrum decreased in intensity and displayed a considerable bathochromic shift by 53 nm, revealing that Acrylodan is also able to report on the conformational changes of Akt induced by allosteric inhibitors.

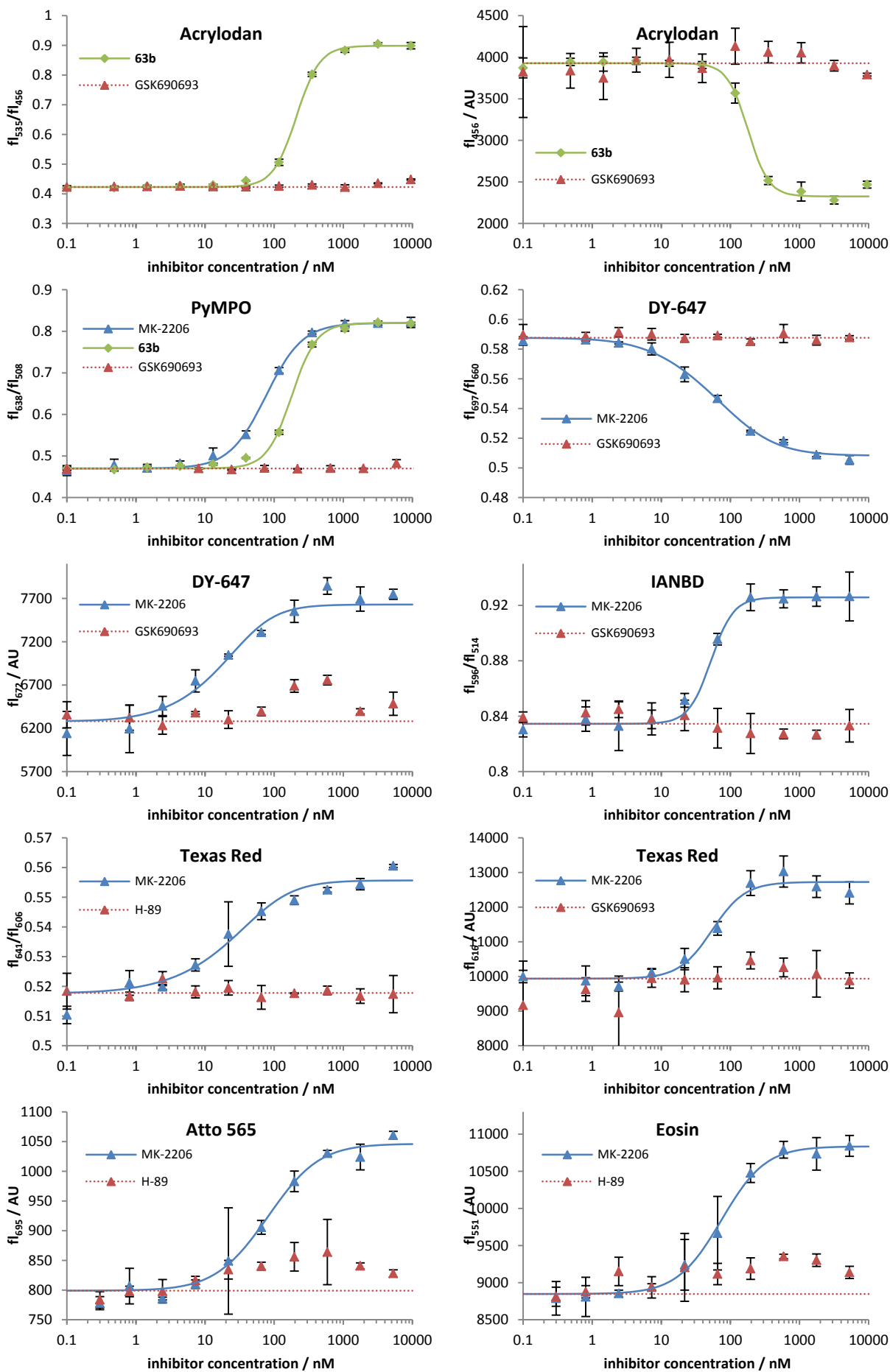


Figure 41 Dose-response curves of the fluorophores tested with MK-2206, **63b** and GSK690693.

Table 7 Overview of fluorophore probes. Structures of reporter fluorophores tested for iFLiK, the observed effects when treated with MK-2206, the chosen assay readouts, Z' -factors, signal-to-noise ratios and determined K_d s for reference inhibitor MK-2206 and **63b** in brackets (n.m. = not measurable due to compound auto-fluorescence).

Fluorophore	Excitation	Effect	Readout	Z'	S/N	K_d MK-2206 (63b)
Acrylodan	386 nm	53 nm red-shift 0.5x signal decrease	535/456 nm 456 nm	0.95 0.69	2.13 1.84	n.m. (207 nM) n.m. (180 nM)
PyMPO	419 nm	16 nm red-shift	638/508 nm	0.90	1.92	96 nM (146nM)
DY-647	640 nm	2 nm blue-shift 2.2x signal increase	697/660 nm 672 nm	0.72 0.56	1.16 2.21	75 nM 63 nM
IANBD	484 nm	5 nm red-shift	596/514 nm	0.38	1.11	85 nM
Texas Red	586 nm	4 nm red-shift 1.3x signal increase	641/606 nm 616 nm	0.42 0.15	1.06 1.25	22 nM 70 nM
Atto 565	559 nm	1.3x signal increase	695 nm	0.23	1.27	63 nM
Eosin	519 nm	1.2x signal increase	551 nm	0.36	1.16	62 nM
Atto 610	606 nm	no changes	-	-	-	-

As expected, fluorophores with high dipole moments were most sensitive towards inhibitor binding, since their Stokes shifts are more susceptible to polarity changes.¹⁴⁰ Indeed, the shifts observed in the assay correlate nicely with the preliminary tests, in which the fluorophores exhibited a hypsochromic (DY-647) or bathochromic (Acrylodan, PyMPO, IANBD, Texas Red) shift in more polar solvents, indicating a transition from a relatively unpolar to a more polar environment upon inhibitor binding (Figure 42). This effect was observed for all fluorophores, suggesting a mechanism in which the reporter fluorophore is localised to the protein surface after labelling, and is displaced by conformational reorganisation of residues around the labelling site upon ligand binding, leading to an increased solvent exposure. Similar observations have been reported by Moreno *et al.* when investigating the effects of labelling human serum albumin with Acrylodan.¹⁷⁶ The observed signal decrease of Acrylodan corroborates this model mechanism, as the energy transfer from the excited fluorophore to the surrounding molecules equals a smaller energy gap between the S_1^* and S_0^* state, resulting in an increased rate of internal conversion and therefore greater degree of radiationless relaxation *via* vibrational modes.¹³⁷ On the other hand, fluorophores with an internal rotor are known to exhibit increased fluorescence in environments of higher viscosity as the rate of rotational relaxation is reduced.¹⁷⁰ Therefore, an increased solvent exposure should lead to a reduced fluorescence quantum yield. In fact with Atto 565, Texas Red, Eosin and DY-647, a fluorescence increase was observed upon inhibitor binding, suggesting a hindered rotation due to their proximity to the protein surface. In comparison to Atto 565, Atto 610 lacks the rotatable *para*-substituted phenyl moiety and hence does not display this emission increase. These intensity changes were marginal and unreliable, however, and might be governed by factors other than rotational relaxation (e.g. rate of quenching, pipetting inaccuracies). This again

demonstrates the limitations of using fluorescence intensity at a single wavelength as an assay readout. Expressing assay readouts as ratios of fluorescence intensities are therefore always preferable as they compensate for such variations in absolute intensities.

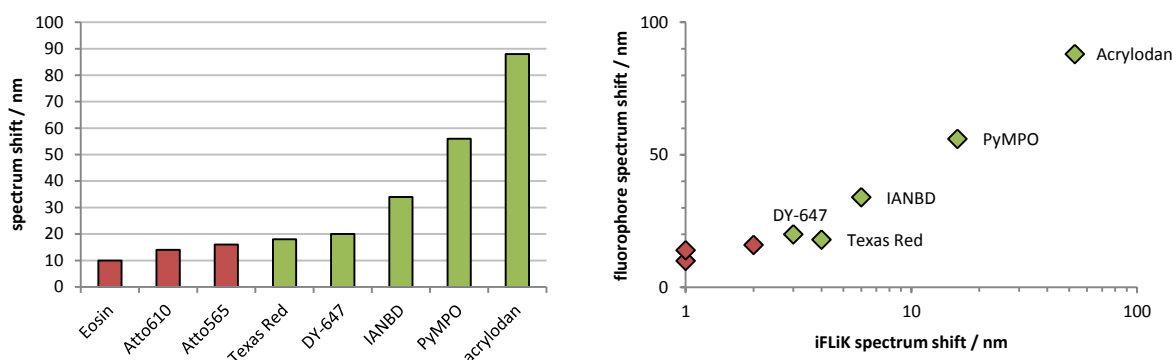


Figure 42 Correlation between protein-free tests of fluorophores and their response in the iFLiK assay. Left: Waterfall plot of emission shifts in pre-tests, coloured according to whether they displayed a significant emission shift in the assay as well (green = observable shift; red = no shift observed). Right: Spectrum shifts observed in pre-test plotted against shifts observed in the iFLiK assay.

In summary, these experiments provided a proof of concept that fluorophores attached to the correct position on Akt were able to selectively report on conformational changes induced by inter-domain binders, and that they can distinguish between such allosteric and classic ATP-competitive inhibitors. This is a major breakthrough by itself, as previous works in the group have shown that the choice of labelling position can be crucial for the feasibility of the entire assay. A variety of fluorophores have been shown to work for iFLiK, but Acrylodan and PyMPO proved to be the best performing probes in terms of reliability. However, in order to avoid inhibitor auto-fluorescence (the difficulties were nicely demonstrated by the strong intrinsic fluorescence of MK-2206), PyMPO was ultimately chosen for future experiments due to its excitation at longer wavelengths.

3.5.2 Determining the Optimal Enzyme Construct

After deciding on PyMPO as the best performing reporter fluorophore, the question of the construct best suited for iFLiK had to be investigated. To this end, the three purified proteins de91, pHT1023 and de92 were labelled with PyMPO maleimide over night and isolated *via* size exclusion. The purified proteins were analysed *via* ESI-MS maleimide (Figure 47), and the protein masses calculated from deconvolution of the differently charged species all exhibited a mass increase of about 376 Da, which is indicative for an addition of a single PyMPO (Table 8).¹⁷⁷

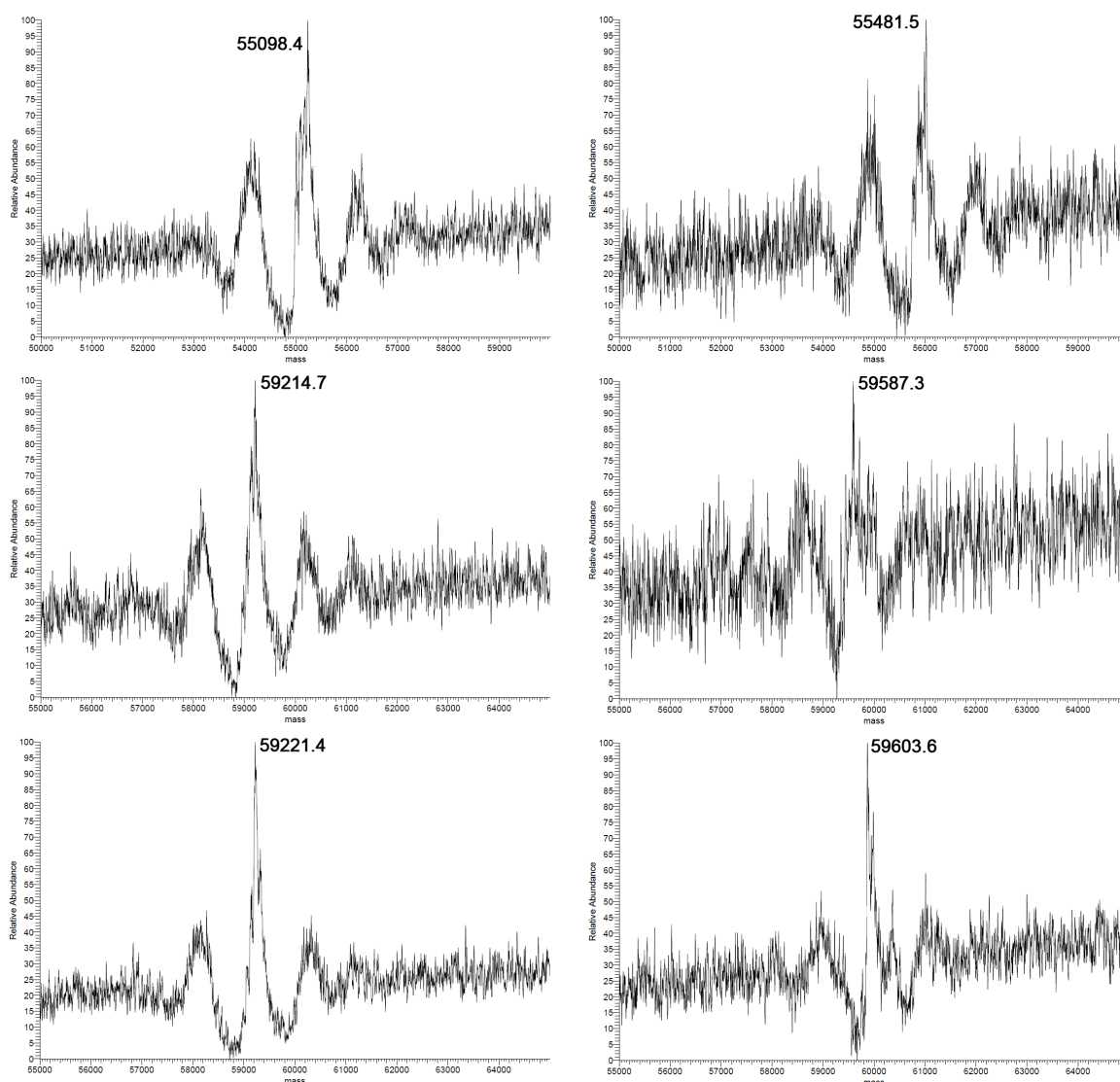


Figure 43 Mass spectrometry results of unlabelled (left) and labelled (right) Akt constructs: de91 (top), pHT1023 (middle) and de92 (bottom).

Table 8 Analytics summary of the PyMPO-labelled Akt constructs. Expected mass difference for PyMPO labelling of cysteine is +376 Da.

Construct	Unlabelled mass	Labelled mass	Mass difference
de91	55098 Da	55482 Da	+384 Da
pHT1023	59215 Da	59587 Da	+372 Da
de92	59221 Da	59604 Da	+383 Da

Each construct was incubated with a dilution series of **63b** and GSK690693. Again, the measured emission spectra of all constructs showed no response to the ATP-competitive GSK690693, but a dose-dependent red-shift with the allosteric inhibitor (Figure 44), which was quantified by calculating the fluorescence ratio of the half-maximum intensities (Table 9).

While the truncated de91 responded with a bathochromic maximum shift from 554 nm to 560 nm, pHT1023 and de92 displayed a shift from 562 nm to 570 nm and 558 nm to 570 nm, re-

spectively. This position towards shorter wavelengths indicates a more hydrophobic (i.e. solvent-protected) environment around the PyMPO sensor in the truncated construct, which matches the susceptibility towards increased aggregation observed during protein purification. The instability of the protein had ultimately resulted in a lower yield, and is the likely reason for the blue-shifted PyMPO fluorescence here. While the determined K_{d} s for **63b** were in the same range for all three Akt1 constructs (70-164 nM), de92 displayed the most pronounced red-shift and (with a Z' -factor of 0.86) was the most reliable protein in the iFLiK assay. As it was also the best expression, it presents itself as the obvious choice for the future experiments.

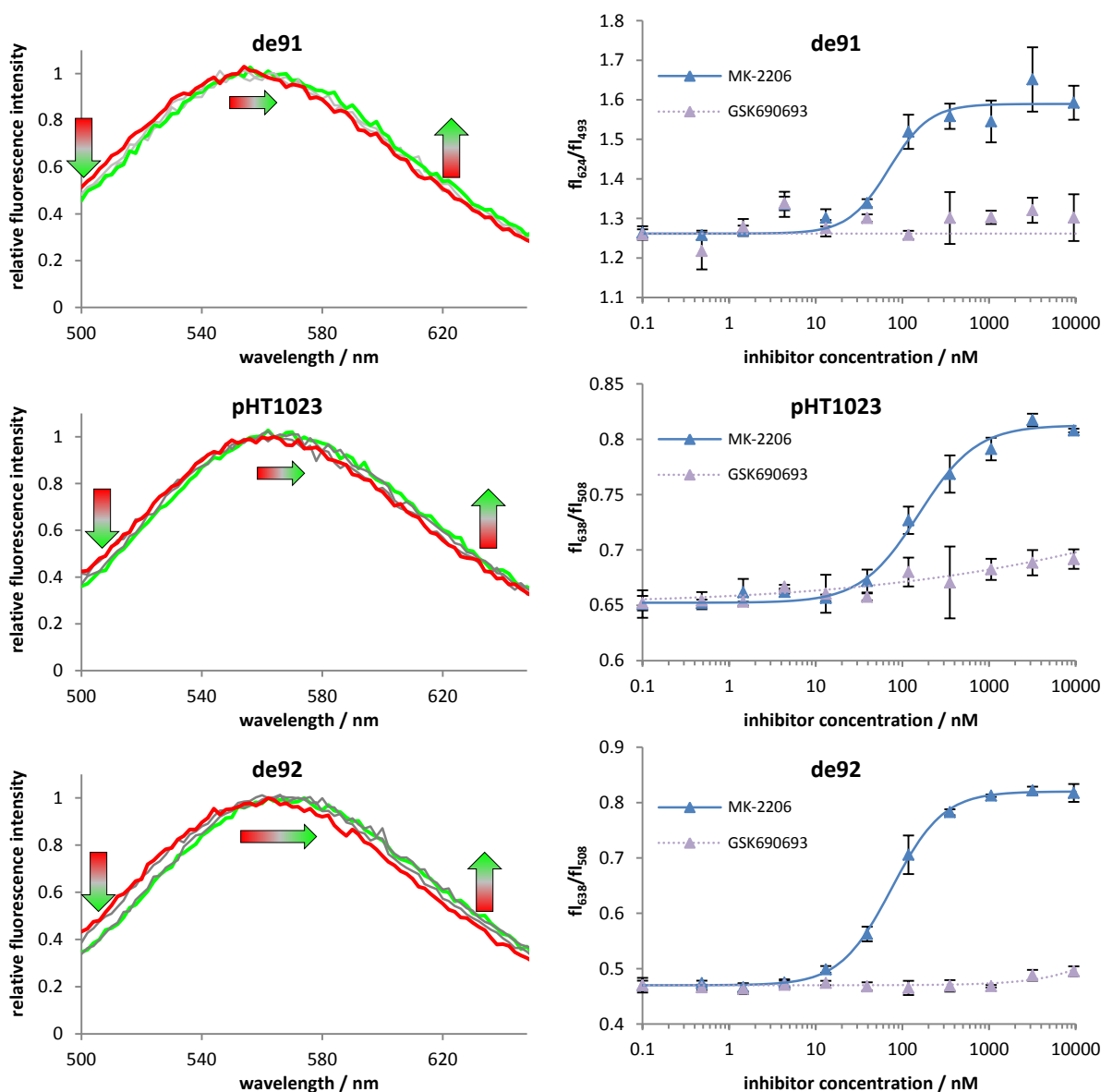


Figure 44 Left: PyMPO fluorescence emission of de91 (top), pHT1023 (middle) and de92 (bottom) upon treatment with increasing concentrations of allosteric inhibitor MK-2206 (red = apo; green = saturated). Right: Dose-response curves of iFLiK constructs with allosteric and ATP-competitive inhibitor.

Table 9 Overview of the iFLiK response for the three Akt1 constructs de91, pHT1023 and de92.

Construct	Maximum shift	Readout	Z'	S/N	K _d 63b
de91	554 nm → 560 nm	fl ₆₂₄ /fl ₄₉₃	0.53	1.26	70 nM
pHT1023	562 nm → 570 nm	fl ₆₃₈ /fl ₅₀₈	0.68	1.19	164 nM
de92	558 nm → 570 nm	fl ₆₃₈ /fl ₅₀₈	0.86	1.43	78 nM

Due to its extra cysteine at the C-terminus, the labelling selectivity in the case of de92 (i.e. the actual labelling positions of PyMPO maleimide) had to be investigated. Despite the additional potential labelling site, the PyMPO fluorescence of de92 was virtually identical to pHT1023, both in shape, position and intensity. To further corroborate this, the labelled de92 was denatured at 90 °C with added DTT, capped with IAA and digested with trypsin. A subsequent analysis with HPLC and coupled ESI-MS/MS revealed that no cysteine in the protein had reacted with the reporter fluorophore other than the desired Cys49 (Figure 45). This is in congruence with the observed 376 Da mass increase of the labelled de92 protein, which also suggests a mono-alkylation with PyMPO.

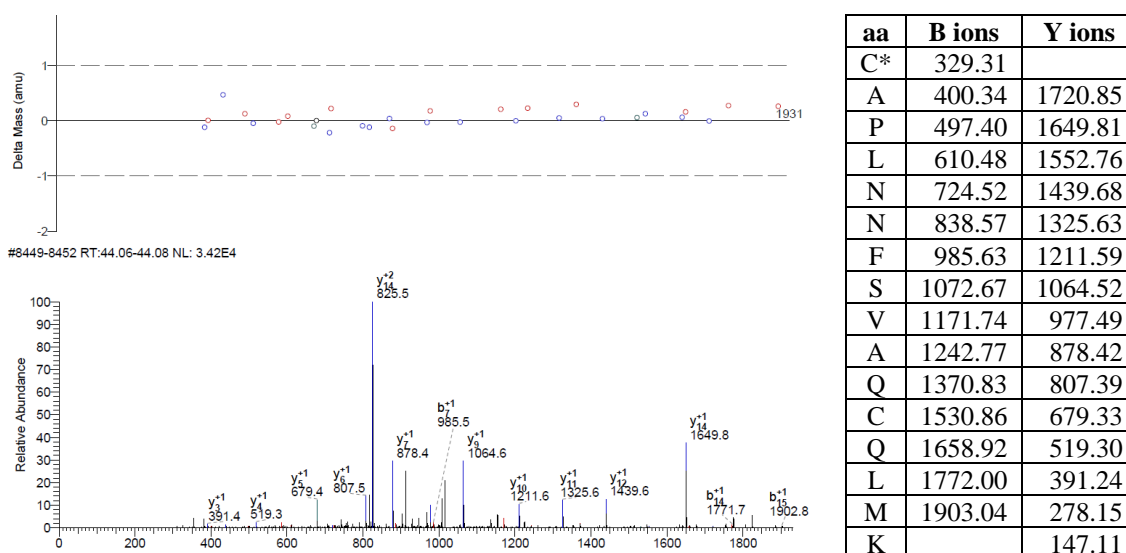


Figure 45 ESI-MS/MS spectrum of the fluorophore-labelled peptide after tryptic digest and mass-to-charge ratios of its resultant fragment ions expressed in Thomson. Precursor ion: 1025.20 Th. Probability score = $6 \cdot 10^{-13}$. C* = labelled cysteine. C = capped cysteine.

In conclusion, de92 was chosen as the optimal construct for the iFLiK assay as it displayed the strongest spectrum shift with the highest Z'-factor and signal-to-noise ratio upon conformational changes induced by allosteric inhibitors and was the best expressing protein from insect cells.

3.5.3 Optimisation of Assay Conditions

After these proof-of-principle experiments, the assay had to be optimised for its use in future high-throughput screens. In the first step, different labelling procedures were investigated by labelling the recombinantly expressed Akt with varying amounts of PyMPO maleimide (0.8 eq, 1.2 eq or 2 eq) and work-up procedure to remove excess fluorophore (quenching with DTT and removal by size exclusion). The experiments show that the addition of DTT had a neither positive nor negative influence on the assay performance. Using an excess of PyMPO maleimide resulted in a reduced assay window, which can be attributed to the unreacted fluorophore that is still present and responsible for a heightened background signal. This excess appears to be unremovable, as it remained with the protein after purification with either FPLC, centricons or dialysis, presumably by tight non-covalent association to the protein. Only in an SDS-PAGE, a separation of the small-sized fluorophore from the denatured protein could be achieved. Furthermore, the SX-subjected proteins showed less stable curves, probably due to the stress put on them in the purification process. Therefore, using substoichiometric amounts of labelling reagent was the procedure of choice, since 0.8 eq of PyMPO provided the best assay window and eliminated the need for removing excess fluorophore as confirmed *via* SX FPLC.

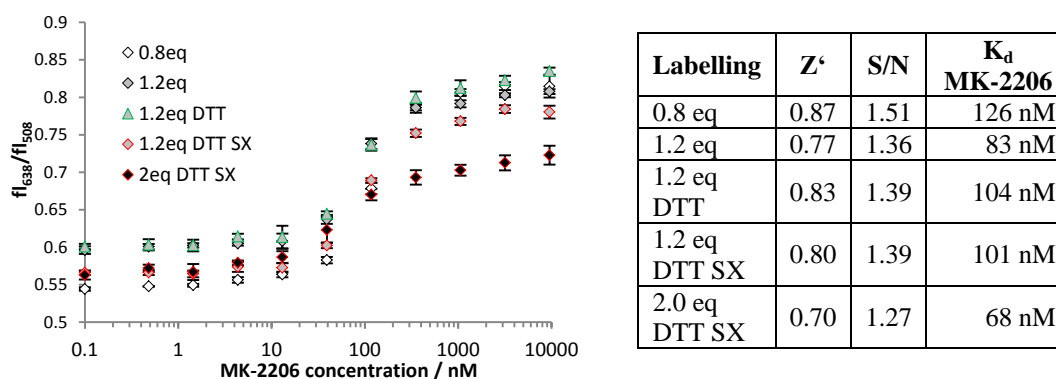


Figure 46 Performance of differently labelled Akt in the iFLiK assay. DTT refers to quenching with 10 eq DTT; SX to purification *via* size exclusion.

Next, the optimal enzyme concentration and reaction volume for the iFLiK assay was determined in order to minimise protein and compound consumption. However, reducing the amount of labelled Akt inevitably lowers signal intensities and hence increases inaccuracies in the measurement. Incubating MK-2206 with 200 nM, 100 nM and 50 nM of PyMPO-labelled de92 in 20 μ L and 10 μ L each confirmed this prognosis. Ultimately, 10 μ L of 200 nM Akt was chosen for the future assay setup, as it provided the most reliable curves with the least waste of material.

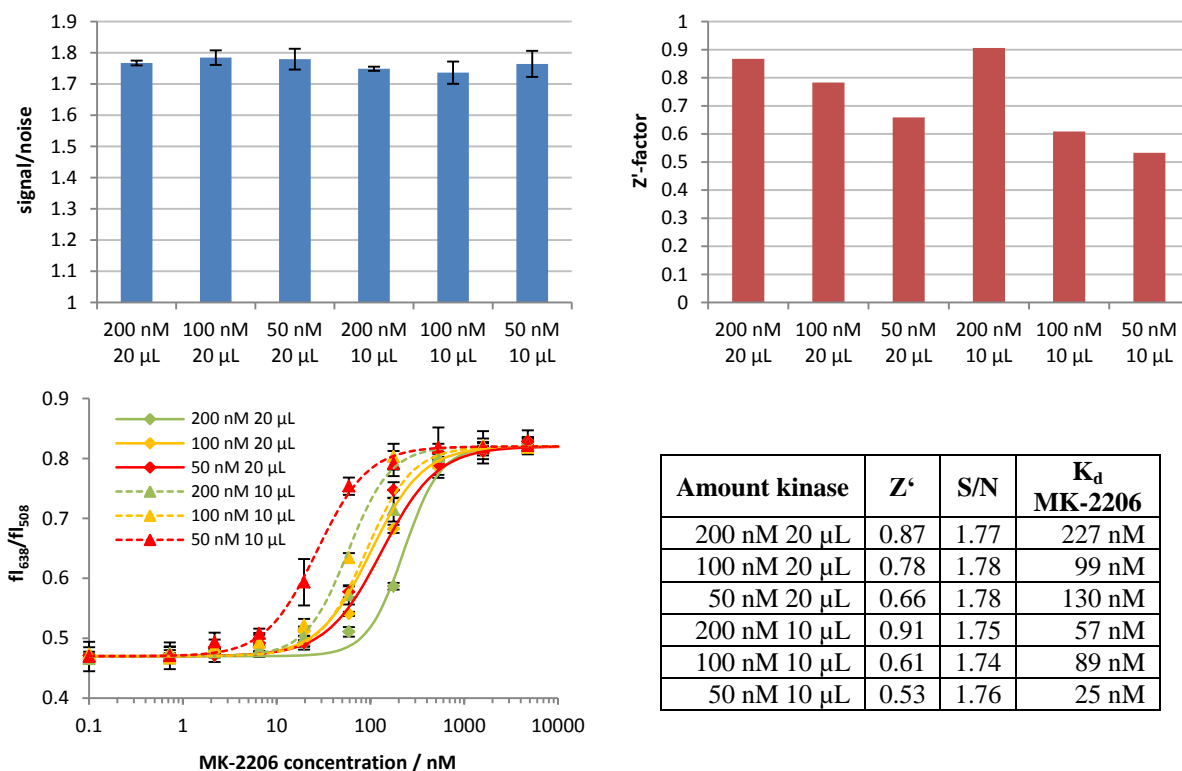


Figure 47 Comparison of different enzyme concentrations and reaction volumes.

Each protein has its own optimal pH range, in which it is most stable. In the context of a conformational assay, protonation states of different residues can alter the minimum-energy protein conformation. Therefore, the pH might influence the assay readout as different protein conformations could be detected, both in the apo and the bound form. In addition, electronic charges around solvatochromic fluorophores influence their fluorescence characteristics, so changing these could lead to a varied assay response. In order to find the optimal pH for iFLiK, Z' and S/N were determined for the pH range 7-8 (experience from prior handling with the protein showed that it is unstable at high pHs, whereas a calculated pI of 6.09 depicts the lower pH limit). Interestingly, all buffers were equally suited for our recombinantly expressed Akt construct across the whole range, although pH 7.4-7.6 provided the best long-term stability of the protein.

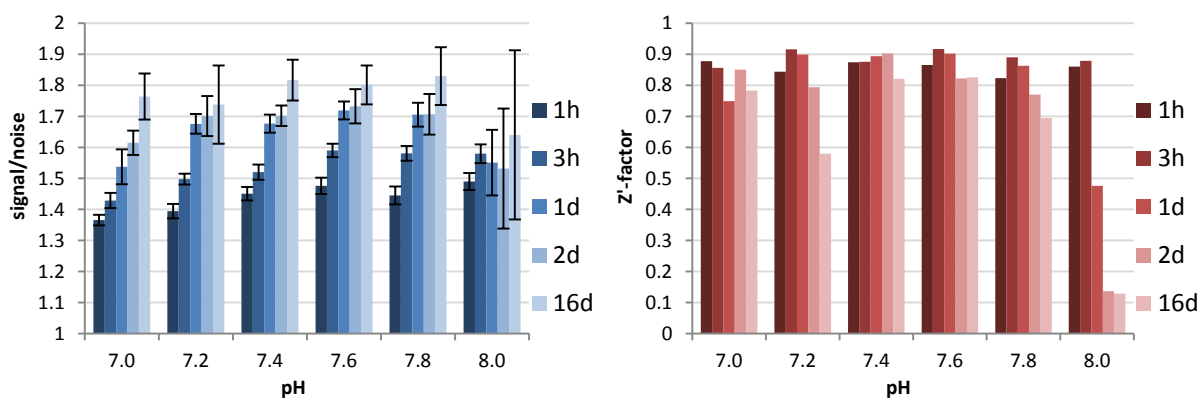


Figure 48 Summary of iFLiK performance at different pHs.

Proteins are known to be sensitive to DMSO, which is usually employed as solvent for stock solutions of small molecules in molecular biology. To investigate this effect on our recombinant Akt construct, the Z' -factor and signal-to-noise ratios were determined by incubating the labelled protein with MK-2206 at different DMSO concentrations. While concentrations between 1-5% did not significantly reduce either Z' or S/N, the values at 0.5% DMSO exhibited high fluctuations in the bound state, presumably owed to bad solubility of the inhibitor. Since the protein was stable even in solutions up to 5% DMSO for longer incubation times, this concentration was chosen for future experiments.

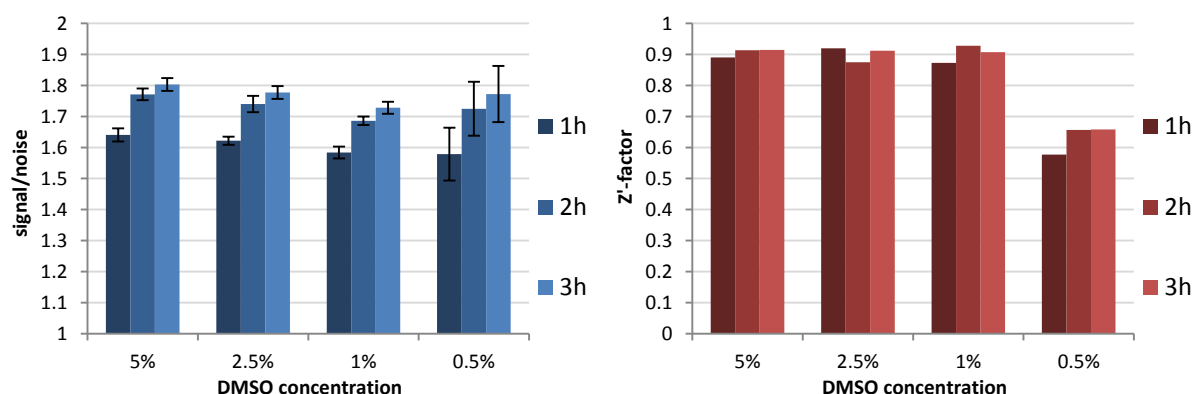


Figure 49 Z' -factor and signal-to-noise ratios of iFLiK in dependence of DMSO present.

In 384-well plates, the shape of the solution in the well is strongly affected by interactions with the polystyrene surface and overlying air due to high surface-to-volume ratios. General experience in high-throughput screening has shown that they tend to adopt irregular shapes, leading to big errors in the fluorescence intensity readouts. This can be ameliorated by the addition of detergents, which mediate interactions at the phase boundaries (both liquid-solid and liquid-air). However, they also have the tendency to destabilise the protein, so minimising the detergent concentration is desirable. Again, the assay was carried out with MK-2206 as positive control in 0.001%, 0.01% and 0.1% of Tween-20, Triton X-100, Brij-35, NP-40 and CHAPS each. As expected, the control wells without detergent exhibited very high

fluctuations resulting in a $Z' < 0$, indicating an unacceptable reliability. In general, signal-to-noise ratios were uniform across all detergents (except with very low concentrations of Triton X-100, Brij-35 and CHAPS). Apart from NP-40, higher detergent concentrations stabilised the assay readout, but also decreased protein stability (higher fluctuations with increasing incubation time). At the lowest concentrations with still good Z' -factor values (i.e. 0.01%), Triton X-100 proved to give the most stable signals, even after 24 h incubation. Therefore, the optimal detergent concentration was appointed to 0.01% Triton X-100. In addition, this experiment (as well as previous ones) showed that the best results could be obtained after an incubation period of 2-3 h at RT.

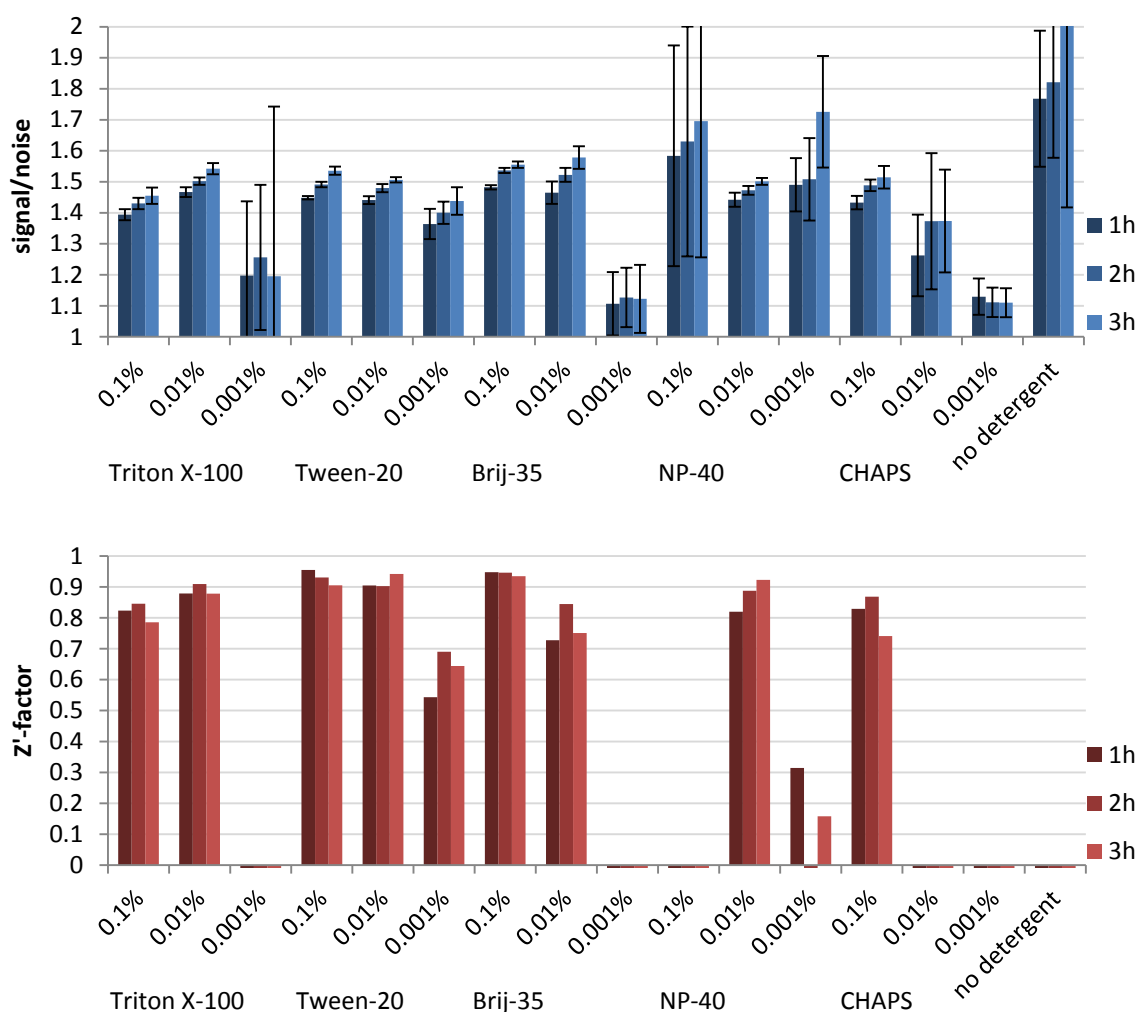


Figure 50 Overview of detergent effect on iFLiK results.

A variety of inorganic salts are regularly used as buffer ingredients fulfilling different purposes. For kinases, magnesium and manganese salts in particular are often added to stabilise the enzyme, since Mg^{2+} is a native co-factor (and Mn^{2+} a magnesium mimic).¹⁷⁸ To examine their effect in iFLiK, apo and MK-2206-incubated Akt was incubated with a combination of $MgCl_2$

and MnCl_2 concentrations between 0-50 mM. These experiments showed that signal-to-noise did not change significantly, regardless of the buffer composition. However, MgCl_2 brought a 40% decrease in fluorescence intensity of the PyMPO label in the apo Akt, but not in the ligand-bound state. In a control experiment with βME -labelled PyMPO in the same buffer, 50 mM of either MgCl_2 or MnCl_2 did not have any effect on the fluorescence, thereby ruling out direct interactions between fluorophore and ions *via* changes in electrostatic charge, ionic strengths or collisional frequency (Figure 51). Instead, a specific interaction of Mg^{2+} with the apo protein has to be assumed. For this reason, the introduction of any unnecessary salts to the system was avoided to maintain the highest possible sensitivity.

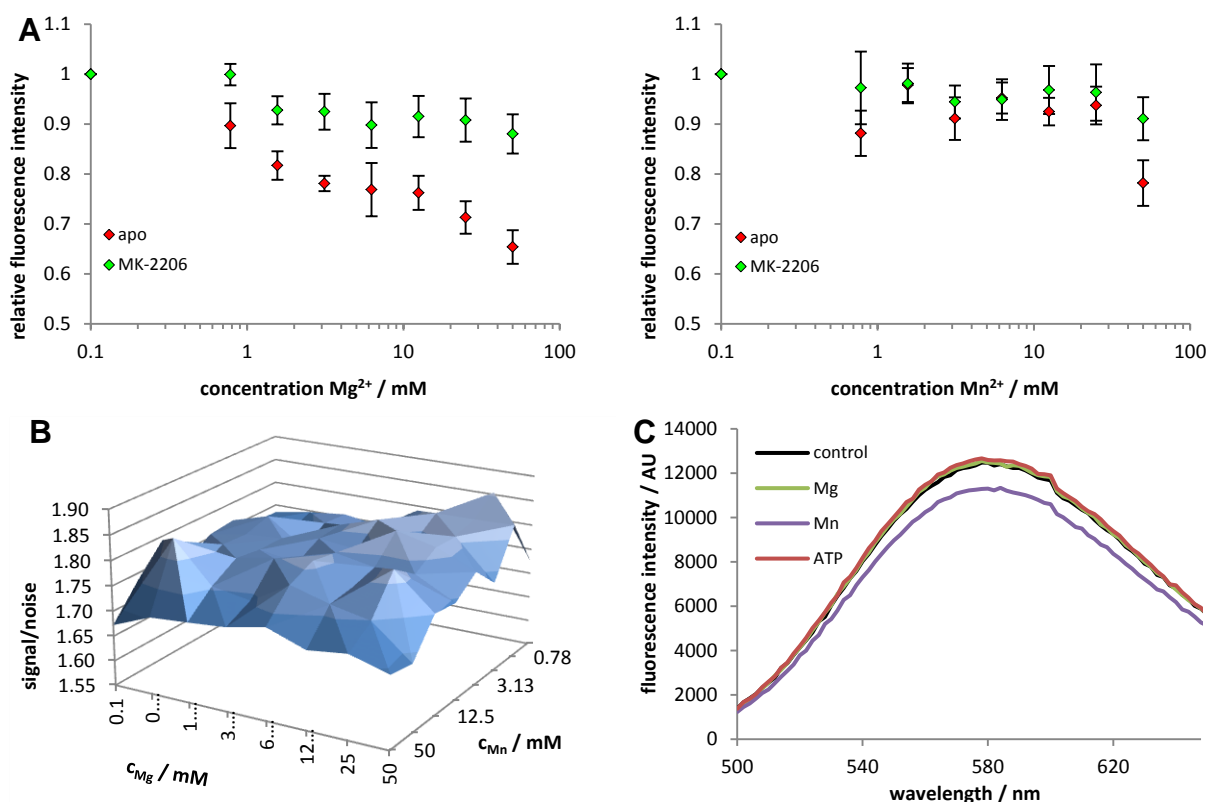


Figure 51 Influence of magnesium and manganese ions in iFLiK. A) PyMPO fluorescence of labelled protein in dependence of MgCl_2 (left) and MnCl_2 (right) concentration. B) Matrix of signal-to-noise ratios in buffers with different Mg^{2+} and Mn^{2+} concentrations. C) Comparison of free PyMPO fluorescence in standard iFLiK buffer, and with 50 mM MgCl_2 and MnCl_2 .

Recombinantly expressed Akt is known to be inactive, i.e. unphosphorylated at Thr308.¹⁷⁹ Therefore, a mixed population of different conformations can be assumed to exist in equilibrium. As iFLiK detects the transition from the open to closed conformation, it was speculated that shifting the equilibrium more to the open conformation prior to adding the ligand could provide an enhanced assay response. For that, PyMPO-labelled de92 was incubated with a concentration series of IP_4 up to 10 μM . In a second experiment, the kinase was pre-incubated with 10 μM IP_4 before carrying out the assay as usual with MK-2206. The

phosphoinositol IP₄ is commonly used as a PIP₃ mimic as it is known to bind in the phosphate pocket of Akt, inducing an opening of the conformation. Therefore, any Akt in the closed conformation should open up, resulting in a blue-shifted emission spectrum of the apo kinase. Titration of the iFLiK construct with IP₄, however, did not change the PyMPO fluorescence spectrum. Likewise, pre-incubation with the phosphoinositol did not have any effect on the assay curves with allosteric inhibitors. Taken together, these results suggest that the equilibrium of the recombinantly expressed Akt essentially lies at the open state already.

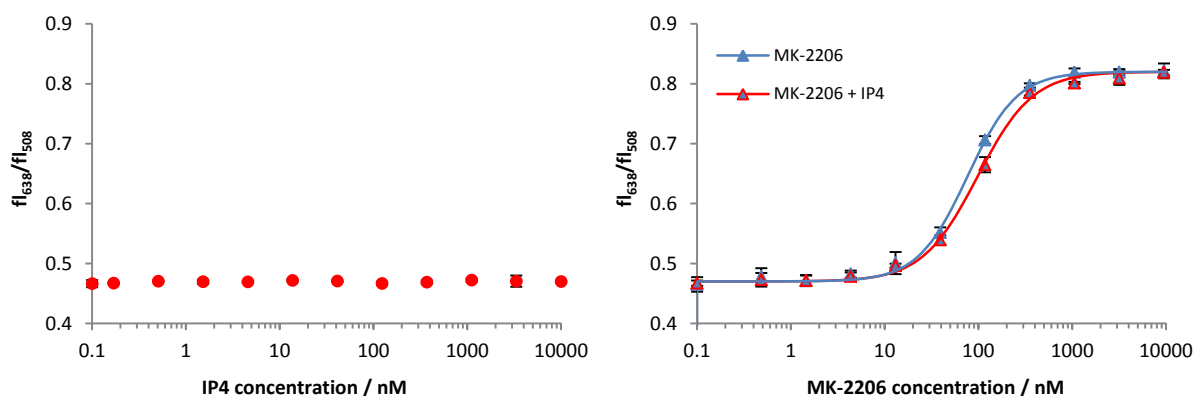


Figure 52 iFLiK response to the presence of the activator IP₄. Left: titration series of PyMPO-labelled Akt with IP₄. Right: MK-2206 dose-response curves with and without pre-incubation with 10 μ M IP₄.

On the other hand, the PH and kinase domain can only be close towards each other in the DFG-out conformation. To investigate whether a prior occupation of the ATP binding pocket has any influence on the binding of allosteric inhibitors, Akt was pre-incubated with 10 mM ATP and 100 μ M ATP-competitive inhibitors (GSK690693, CCT128930 and H-89) before adding MK-2206. Additionally, the apo protein was incubated in increasing concentrations of ATP up to 10 mM. Both experiments reveal that none of these ATP pocket binders have an effect on the assay readout or the binding of allosteric inhibitors, providing identical assay windows and K_d s. The only differences were observed for GSK690693, which already caused a slight bathochromic shift at 100 μ M (see Figure 44). The addition of MK-2206 produced the same end point, which was reached at slightly higher concentrations (K_d of GSK690693-preincubated MK-2206 measurement about 2.5 times higher than the control measurements and preincubation with the other ATP pocket binders). This observation could suggest a partial occupation of the inter-domain binding pocket by GSK690693. Further implication of this will be discussed at the end of this chapter.

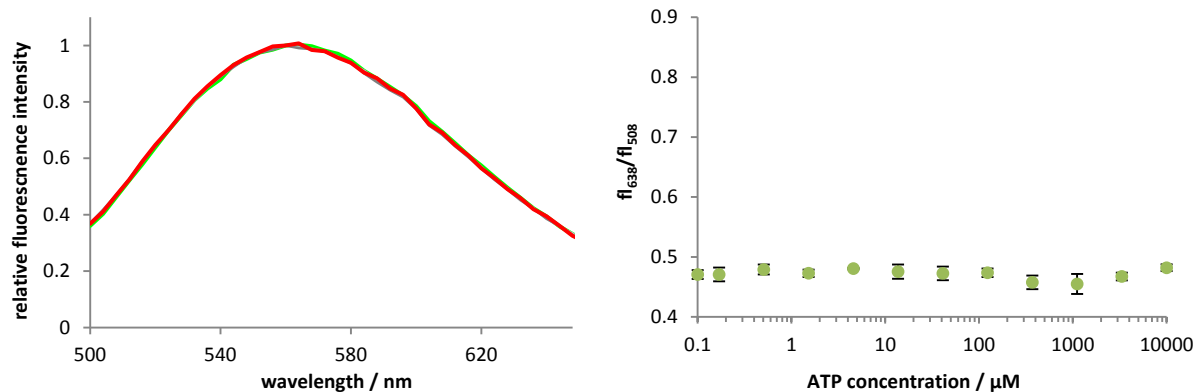


Figure 53 Response of PyMPO fluorescence in increasing ATP concentrations. Left: PyMPO emission spectra (red = apo; green = 10 mM ATP). Right: f_{638}/f_{508} ratio plotted against ATP concentration.

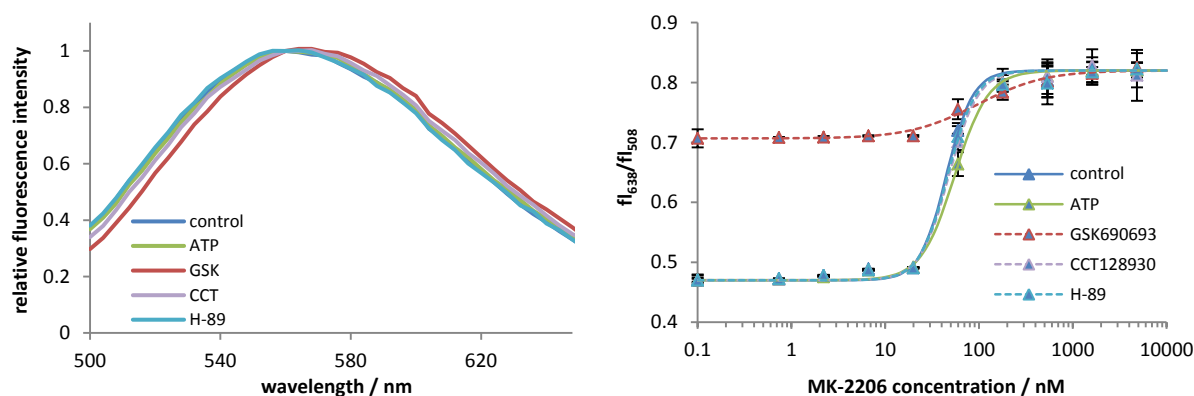


Figure 54 iFLiK assay response when pre-incubated with ATP or ATP-competitive inhibitors. Left: PyMPO emission spectra of pr-eincubated Akt before addition of MK-2206. Right: MK-2206 dose-response curves after 1 h pre-incubated Akt.

In their role as enzymes that have to dynamically catalyse phosphorylation reactions, kinases are rather unstable proteins. In fact, empirical data in our own group indicate that some kinases lose their activity after a few hours at RT, whereas others are stable for several days. In previous measurements, the recombinantly expressed Akt mutant displayed favourable stability, providing reliable iFLiK data even after 3 days at 4 °C. However, minute drifts in the PyMPO spectra causes slight decreases of the f_{638}/f_{508} ratios over time, which increase more when left at RT for longer time periods (Figure 55A). After 8 days at RT, the maxima of all curves in a dilution series have reached the same shape with an emission maximum at 543 nm, indicating that the protein is denatured and can no longer be distinguished between apo and bound form. To better understand the assay response towards the protein's state, apo and MK-2206-bound de92 fluorescence was compared under different conditions: a) aggregative denaturation by heating up hermetically to 50 °C for 5 h, b) dissociative denaturation by adding guanidinium chloride and c) standard treatment for comparison. While the standard measurement conformably provided different spectra for apo and bound protein (maximum at 563 nm and 572 nm, respectively), the wells subjected to thermal denaturation did not, both

showing an emission maximum at 543 nm, indicating their inability to distinguish ligand binding. Consistent with the linearisation of proteins known to be caused by the denaturant, the GndCl-treated spectra were lower in intensity, red-shifted to 582 nm and did not distinguish between apo and MK-2206 measurements. All spectra correctly reflected the expected polarity changes upon denaturation and confirmed that the allosteric inhibitor MK-2206 was not able to bind to the denatured Akt anymore. In conclusion, as the protein in iFLiK experiments eventually also reached a fluorescence maximum at 543 nm, we can assume that the protein has denatured by aggregation after 8 days at RT.

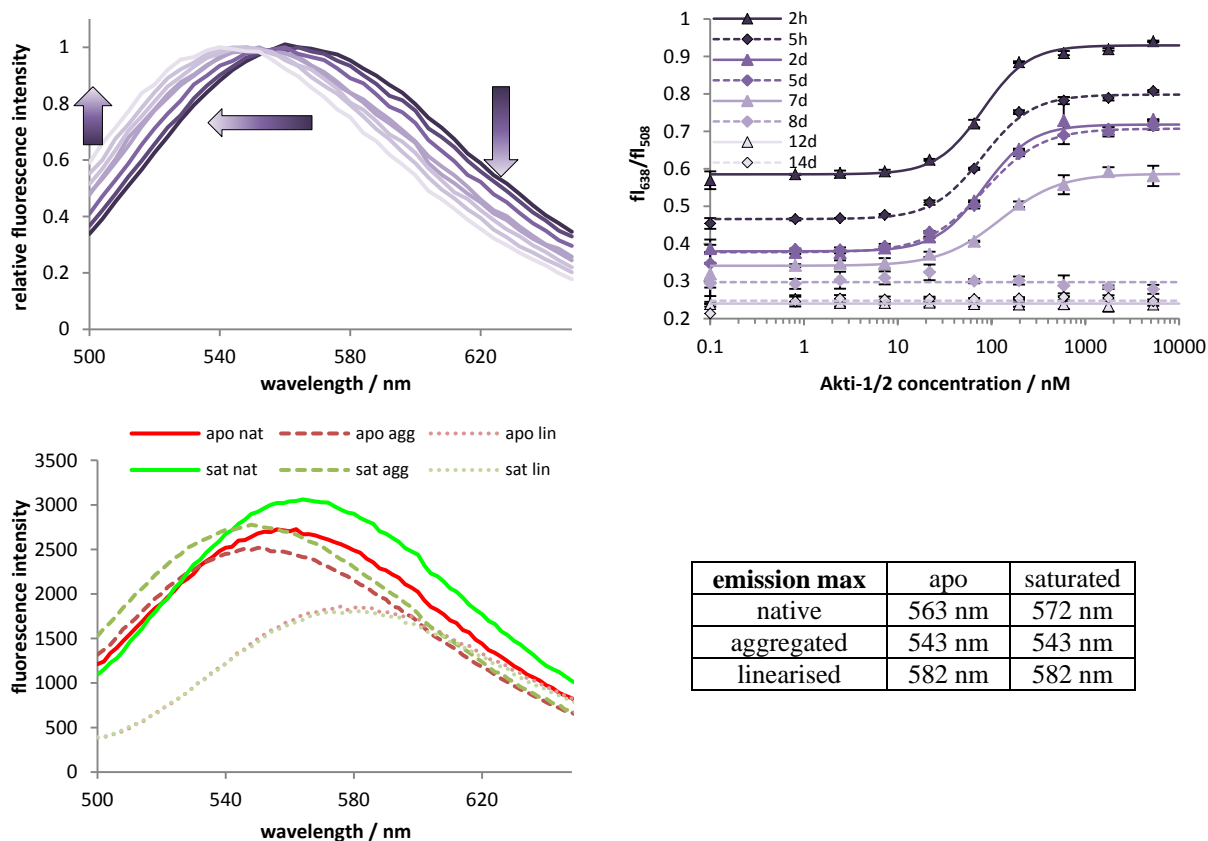


Figure 55 A) Hypsochromic emission shifts of PyMPO over long periods. B) Akti-1/2 dose-response curves over longer incubation periods at RT. f_{508}/f_{638} ratios drop over time, describing the denaturing process of the protein. C) iFLiK response to denaturing conditions (apo = apo Akt, sat = saturated with MK-2206, nat = natively folded, agg = aggregated by thermal denaturing, lin = linearised with GndCl).

After this extensive and careful assay optimisation, the iFLiK assay could now be used to determine binding affinities of all Akt inhibitors available in our lab. These include the allosteric commercially available MK-2206 and Akti-1/2, the synthesised **63a-g** and **64a-d**, as well as the ATP-competitive GSK690693, CCT128930 and H-89 (Figure 56). Intrinsic compound auto-fluorescence was accounted for by subtracting fluorescence intensities of the respective compound alone in buffer. All allosteric inhibitors provoked a bathochromic shift of the emission spectrum up to 16 nm, which allowed the determination of their K_{dS} (Table 10).

Mixtures of inhibitors with PyMPO-labelled glutathione or β -mercaptoethanol displayed no change in their fluorescence spectrum, confirming that the observed responses are specific to the conformational changes of Akt, and not due to interaction with the fluorophores alone. The SAR gained from the K_d s perfectly mirrors the IC_{50} s determined in the activity-based KinEASE assay (Table 5). Interestingly, weak ID inhibitors seem to level out earlier and to not reach the same end point as the potent inhibitors, maybe due to solubility issues. K_d values were obtained using equation (9) with the MK-2206 end point as upper asymptote. In comparison, the classic ATP-competitive Akt inhibitors had no effect on PyMPO fluorescence. Only at very high concentrations ($>100 \mu\text{M}$), some very potent ATP-competitive inhibitors show an erratic behaviour. The subnanomolar inhibitor GSK690693 for example started to produce a bathochromic PyMPO shift that resembles the shift caused by ID inhibitors. There are three explanations for this finding: 1) Occupation of the ATP binding site could be picked up by the PyMPO label. However, since the label is located at the PH domain, and this effect was not observed with other ATP-competitive Akt inhibitors, and only at high concentrations of GSK690693, this could not be substantiated by any rationale. 2) Direct interaction of GSK690693 with the fluorophore could cause a spectrum change. However, control experiments with the free PyMPO and GSK690693 alone showed that the inhibitor did not have any influence on the emission spectrum, refuting this hypothesis. This leaves 3) a conformational change caused by unspecific binding of GSK690693 to another part of the kinase once the ATP binding pocket is saturated with the inhibitor, which could include the allosteric binding pocket. Earlier experiments, in which preincubation of Akt with $100 \mu\text{M}$ GSK690693 decreased the binding affinity of MK-2206, might indicate in the same direction, further corroborating this hypothesis. To allow for an accurate interpretation of the data, this phenomenon will have to be investigated in more detail. In the status quo, however, this is pure speculation.

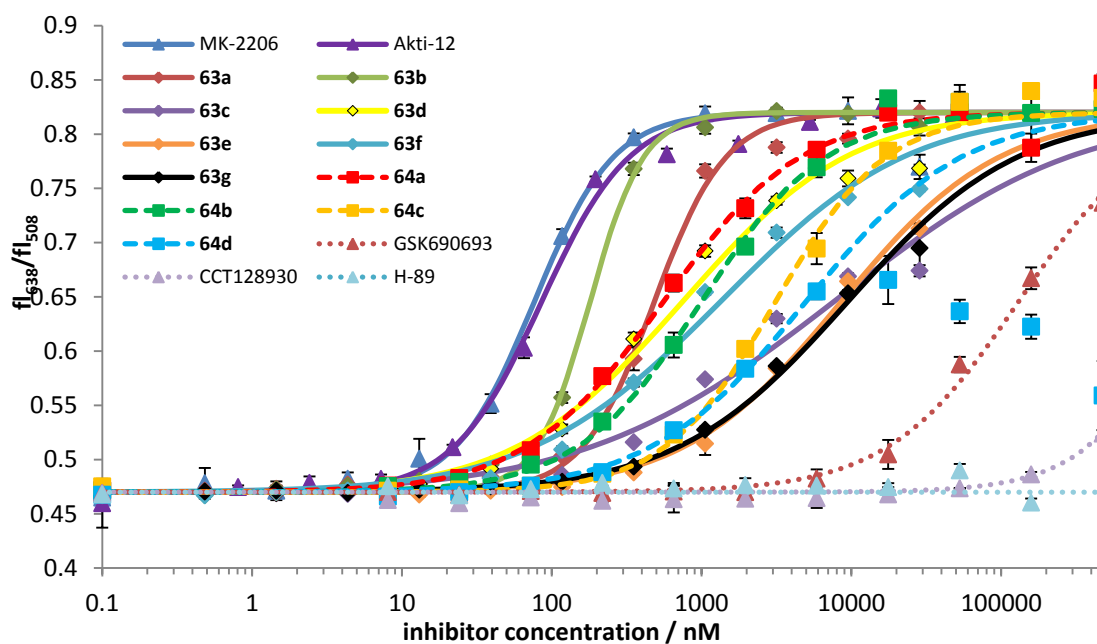


Figure 56 iFLiK assay response for allosteric and ATP-competitive Akt inhibitors.

Table 10 Binding affinities for allosteric and ATP-competitive Akt inhibitors determined with iFLiK. n.r. = no response up to 500 μ M.

Ligand	K_d / μ M
63a	0.41 ± 0.07
63b	0.15 ± 0.04
63c	6 ± 2
63d	0.9 ± 0.3
63e	7.2 ± 0.9
63f	1.1 ± 0.2
63g	8 ± 1
64a	0.43 ± 0.01
64b	1.2 ± 0.3
64c	2.6 ± 0.9
64d	18 ± 16
MK-2206	0.09 ± 0.01
Akti-1/2	0.08 ± 0.02
GSK690693	n.r.
CCT128930	n.r.
H-89	n.r.

In summary, the iFLiK assay has been successfully established. The optimal assay conditions were determined to be: incubation of inhibitors with 5% DMSO at RT for 2-3 h in 10 μ L of a 200 nM PyMPO-labelled Akt construct in a buffer of 50 mM HEPES, 200 mM NaCl, 0.01% Triton X-100, pH 7.4-7.6. iFLiK was proven to be very dependable, giving reproducible results even after a 3 day-incubation period at RT and with 2 year old proteins stored at -80 $^{\circ}$ C. Consistent and reproducible results could be repeatedly obtained with different batches of labellings and expressions. The ability of iFLiK to detect conformational changes of Akt induced by allosteric inhibitors was successfully demonstrated. ATP-competitive inhibitors do not facilitate the closed conformation and, therefore, were not detected by the iFLiK assay.

3.5.4 Validation with NanoTemper Assay

In order to validate the K_d values obtained with iFLiK, orthogonal assay systems were required. The NanoTemper assay was chosen, as it is based on an entirely different physical property: NanoTemper monitors the thermophoresis of proteins or ligands in a temperature gradient. This gradient of about 2-8 K is produced by an IR laser over a distance of 150 μm inside a capillary. Changes of their hydrodynamic properties such as hydration shells, charges, conformations or masses are reflected in an altered diffusion behaviour (see detailed description of the assay principle in chapter 0). To enable the selective tracking of the protein's movements, it needed to be fluorescently labelled. Examining the available excitation and emission filters, Alexa Fluor 568 and Atto 550 were chosen as fluorophores (Figure 57).

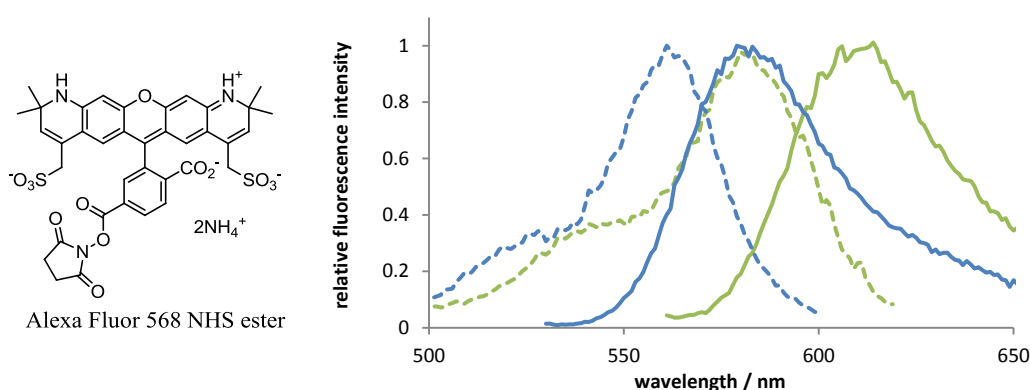


Figure 57 Structure and fluorescence spectra (solid lines = emission, dotted lines = excitation) of NHS ester conjugates of Alexa Fluor 568 (blue) and Atto 550 (green). The structure of Atto 550 is not publicly disclosed.

For an orthogonal labelling, the NanoTemper labels were attached to amino substituents *via* NHS ester conjugates. To this end, de92 was incubated with 5 eq Alexa Fluor 568 at pH 8.3 for 1 h at 4 $^{\circ}\text{C}$. The AF568-labelled protein was purified over a size exclusion column. To calculate the ratio of fluorophore:protein, the concentrations of fluorophore and protein were determined by photometric measurements at 595 nm (where only the fluorophore absorbs) and 280 nm (where both fluorophore and protein absorb) with equation (10). After determining the molar extinction coefficient for both species at 280 nm and 595 nm, the labelling ratio was determined to 3.7:1 (Figure 58).

$$c_{fl} = \frac{A_{595}}{\epsilon_{fl,595}} \quad c_p = \frac{A_{280} - c_{fl} \cdot \epsilon_{fl,280}}{\epsilon_{p,280}} \quad (10)$$

c_{fl} = fluorophore concentration

$\epsilon_{fl,595}$ = molar extinction coefficient of fluorophore at 595 nm

$\epsilon_{fl,280}$ = molar extinction coefficient of fluorophore at 280 nm

$\epsilon_{p,280}$ = molar extinction coefficient of protein at 280 nm

c_p = protein concentration

A_{595} = absorption at 595 nm

A_{280} = absorption at 280 nm

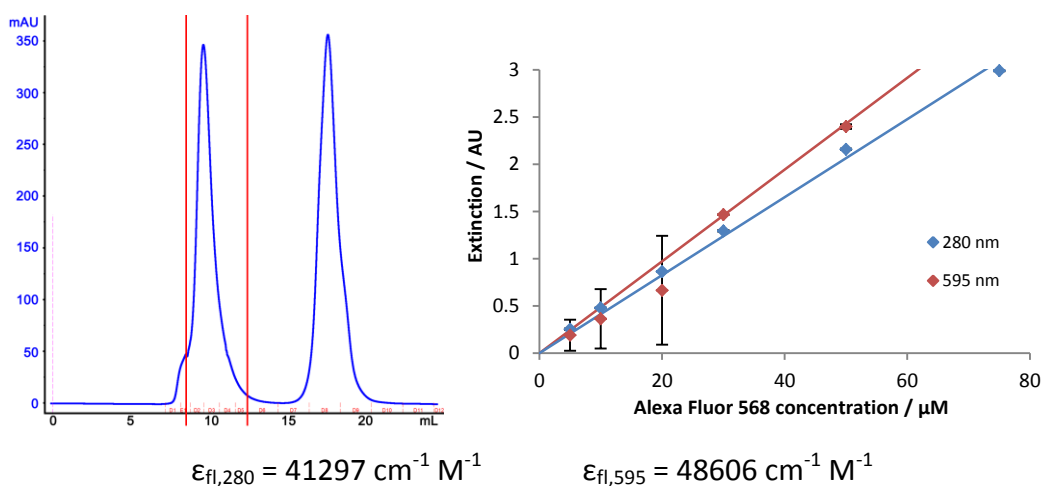


Figure 58 Left: Purification of AF568-labelled de92. Right: photometric calibration curves for determination of extinction coefficients and concentrations.

Due to extreme surface-to-volume ratios inside the capillaries used for NanoTemper, many proteins tend to aggregate on the inner tube surface. To investigate the stability of the protein solution in the capillaries, a 100 nM Akt solution was transferred into standard treated glass capillaries. A cross-section spatial scan across the capillary diameter revealed a bifurcated fluorescence spectrum, indicative for protein aggregation on the surface. Several alternatives were explored: 1) Change capillaries to glycosyl-coated hydrophilic capillaries or PEG-coated hydrophobic capillaries to modulate phase boundary-effects, 2) change detergent from 0.01% Triton X-100 from the iFLiK buffer to 0.05% of the stronger Tween-20 and 3) sharply centrifuge protein solution prior to capillary transfer to separate aggregated proteins by pelleting. However, neither of these measures nor any of these combinations improved protein stability (Figure 59).

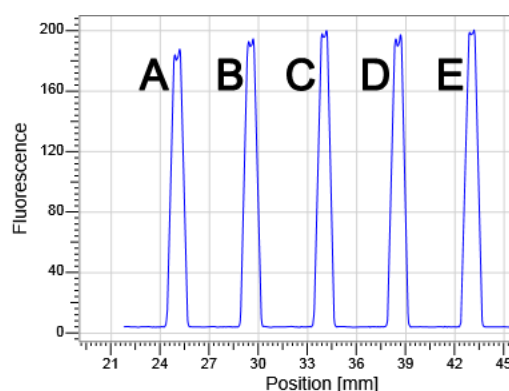


Figure 59 Capillary scans of AF568-labelled de92 in A-C) standard treated, D) hydrophilically coated and E) hydrophilically coated capillaries. A, B, D and E are in a buffer consisting of 50 mM HEPES, 200 mM NaCl, 0.01% Triton X-100, pH 7.4, whereas 0.05% Tween-20 was used as detergent in C. B represents the supernatant after centrifuging at 20,000 g for 10 min.

Interestingly, when incubating Akt with increasing concentrations of MK-2206, a stabilisation of the protein was observed (Figure 60). Since stabilisation of proteins by complexation with ligands is a well-known phenomenon, it supports the assumption that the bifurcated spectrum in the apo form is indeed owed to protein instability. Eventually, stable fluorescence signals could be obtained using enhanced gradient capillaries that have a smaller diameter and therefore reduce aggregations.

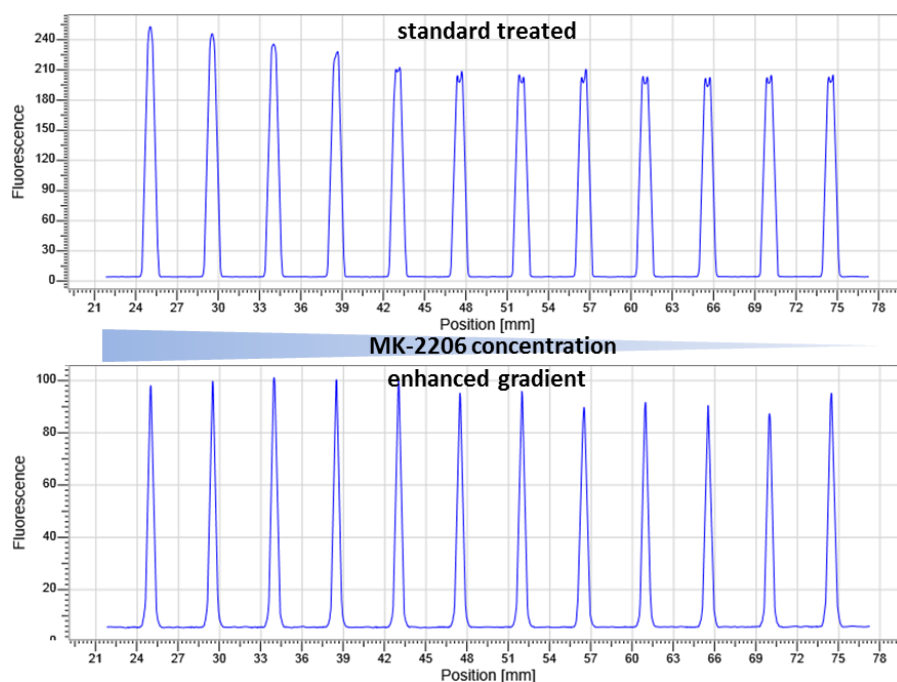


Figure 60 Capillary scan of AF568-labelled de92 incubated with dilution series of MK-2206 in standard treated (upper) and enhanced gradient (lower) capillaries.

As a proof of concept, labelled de92 was incubated with a dilution series of **63b** in both standard treated and enhanced gradient capillaries, and their thermophoresis upon temperature jump was monitored over time. In standard treated capillaries, the measurements were hampered by random (in some cases very substantial) fluctuations caused by protein aggregates. These problems did not occur in enhanced gradient capillaries, where a nice dose dependence could be ascertained.

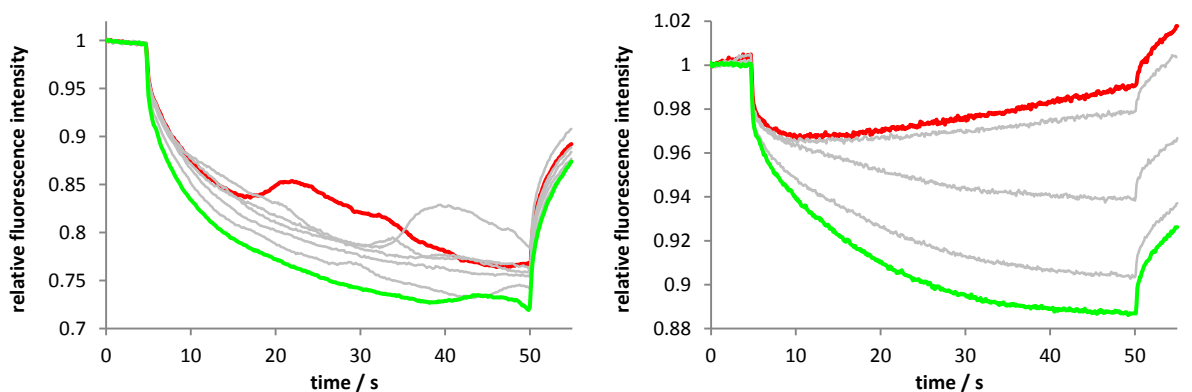


Figure 61 Thermophoretic curves for Akt-MK-2206 complexes in standard treated (left) and enhanced gradient capillaries (right). The red curves correspond to apo Akt, the green curves to saturated Akt.

Having established that a change in thermophoretic behaviour could indeed be observed for different concentrations of ligands, we set out to optimise the assay conditions. First, the effect of laser and LED intensity were examined. While increasing the LED brightness produced a stronger fluorescence, bleaching of the fluorophore was also accelerated. 90% LED power was determined as a good compromise for the relatively photon-stable Alexa Fluor 568, which still gave good signal intensities. On the other hand, increasing the IR laser power creates a steeper temperature gradient inside the capillary, but also promotes thermal degradation of the protein. However, no adverse effects could be observed for our kinase under even strong irradiation, so laser intensities were set to 100%. To determine the optimal assay conditions and readout, the assay was carried out for different thermophoresis durations, and the ratio of fluorescence intensities was calculated for different combinations of the respective end points to intensities at various time intervals (just before temperature jump, immediately after temperature jump, and about 3 seconds later when the system has adjusted to equilibrium at the new temperature). With these values, the Z' -factor and signal-to-noise ratios for the different permutations were inspected using 6 measurements each of apo and MK-2206-bound Akt. These experiments revealed that a longer thermophoresis time uniformly provided higher S/N ratios. While calculating fluorescence ratios immediately after the T-jump gives a higher S/N, the data is less reliable than when thermal equilibrium has ensued. In consequence, a sequence of 5 s equilibration, 45 s thermophoresis and 5 s back diffusion was programmed, and the ratio of fluorescence intensities at 45 s to 9 s was chosen as assay readout.

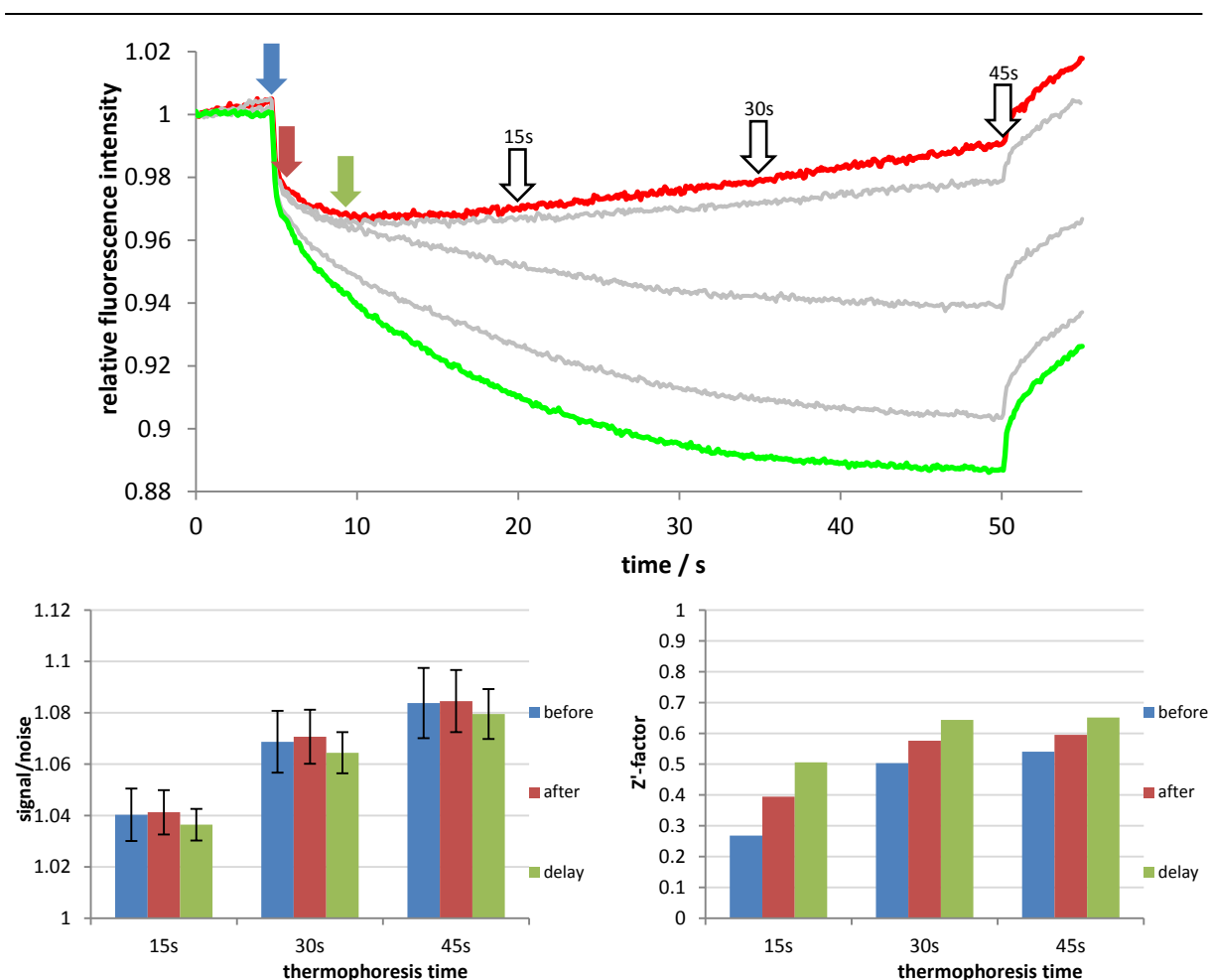


Figure 62 Determining optimal assay readout for NanoTemper assay. Calculated Z' -factors and signal-to-noise ratios for the various combinations depicted in the thermophoresis plot. Before refers to the time just before the temperature jump, after to the time immediate after the temperature jump, and delay to the time at which the system has adjusted to equilibrium at the new temperature.

In these configurations, the synthesised probes **63a-g**, and the references MK-2206 and GSK690693 were measured with NanoTemper, and the K_d values were calculated using the internal evaluation software with a 4-point Hill equation (11). Attempts to use the alternative K_d -driven equation (12) produced inapt fitting curves. Interestingly, re-measuring the inhibitors after 6 h still inside the capillaries at RT produced the same results, suggesting that the protein solution was now stable in the enhanced gradient capillaries. After obtaining K_d s with equation (11), mixtures of the same compounds incubated with Alexa Fluor 568 alone were recorded as a negative control. In accordance to expectations, no thermophoretic responses were observed, thereby ruling out those arise from direct interactions of the compounds with the fluorophore.

$$f(c) = \frac{c^H}{K_d + c^H} \quad (11)$$

c = ligand concentration

H = Hill coefficient

K_d = dissociation constant

$$f(c) = L + \frac{A(T + c + K_d - \sqrt{(T + c + K_d)^2 - 4T \cdot c})}{2T} \quad (12)$$

c = ligand concentration

L = lower asymptote

A = binding amplitude

T = protein concentration

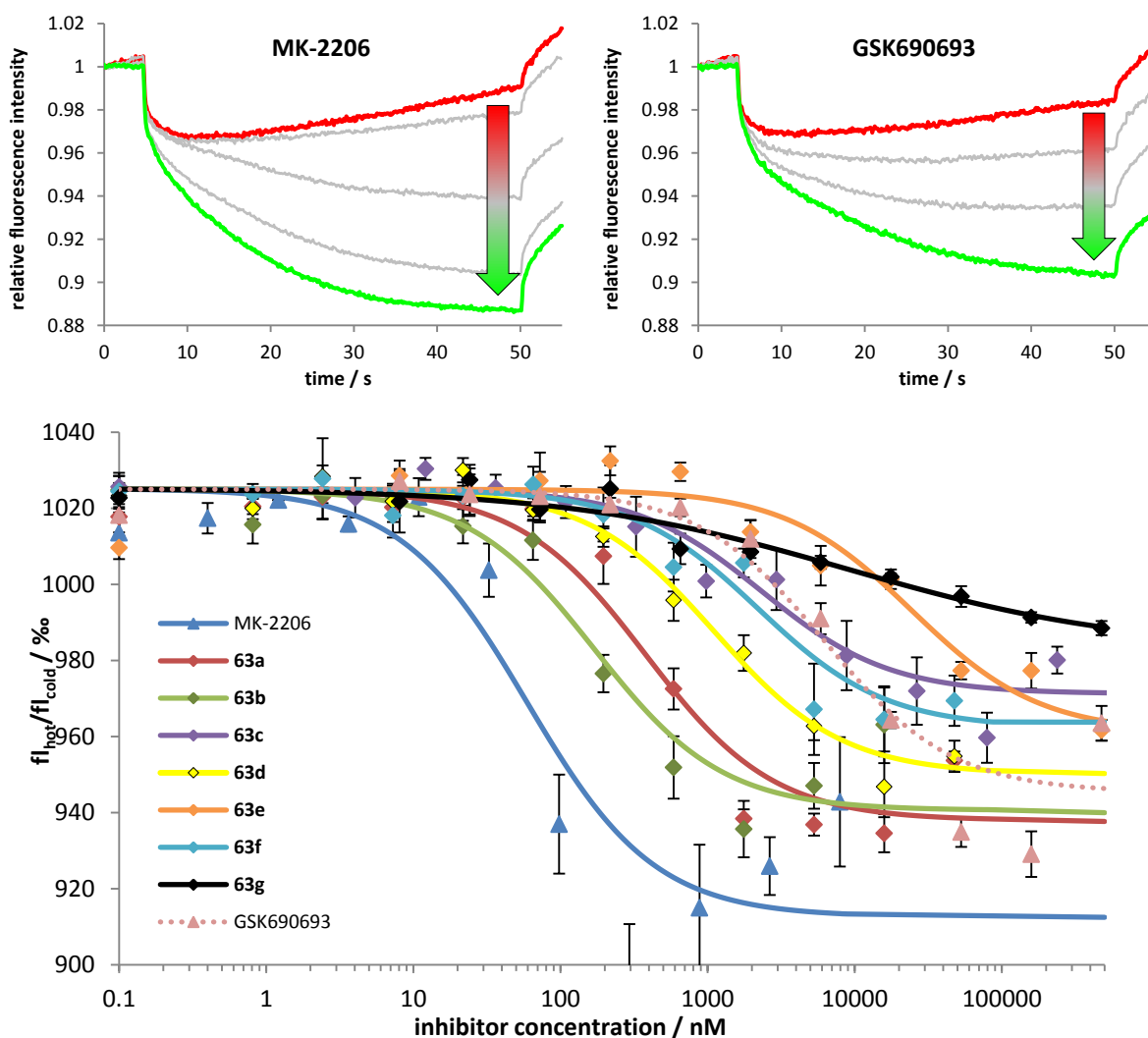


Figure 63 Upper: Exemplary thermophoretic plots of Akt with allosteric (MK-2206) and ATP-competitive inhibitors (GSK690693). Lower: Dose-response curves of allosteric and ATP-competitive Akt inhibitors measured with NanoTemper.

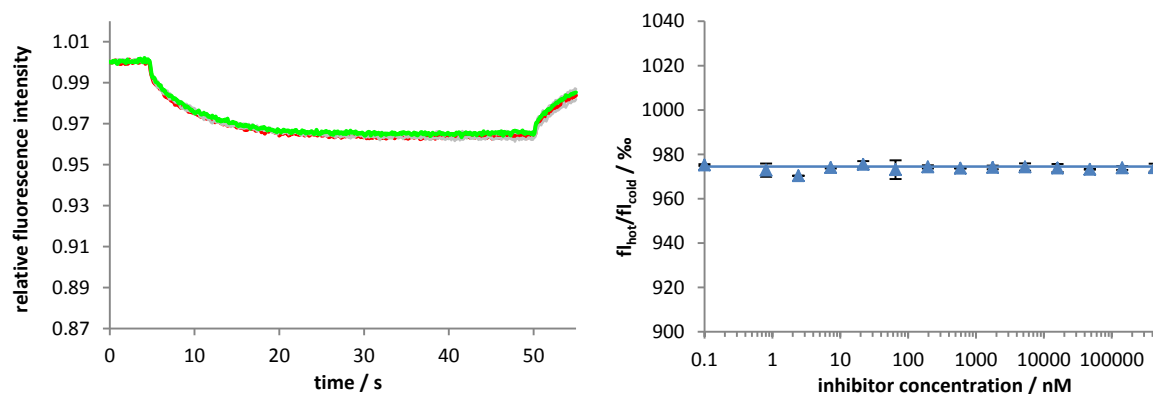


Figure 64 No thermophoretic response when Akt inhibitors were incubated with Alexa Fluor 568 alone.

To investigate the effect of the PyMPO labelling on the binding affinity of the inhibitors to Akt, all previously described NanoTemper experiments were repeated for de92 that is labelled with both Alexa Fluor 568 *via* amine groups and PyMPO *via* the Cys49 thiol group. For this, the previously AF568-labelled de92 was further incubated with PyMPO following the same protocol as for iFLiK experiments. As the results in Table 11 show, the dually labelled Akt exhibits near-identical binding affinities to allosteric as well as ATP-competitive inhibitors as the single-labelled Akt did. This indicates that PyMPO labelling of Akt *via* Cys49 does not significantly change affinity towards its inhibitors.

Table 11 Overview of K_d s for the single AF568-labelled and the dually AF568/PyMPO-labelled de92 measured with NanoTemper.

K_d / μM	AF568	AF568/PyMPO
63a	0.33 ± 0.09	0.41 ± 0.03
63b	0.18 ± 0.05	0.18 ± 0.05
63c	3.9 ± 0.8	3.6 ± 1.5
63d	1.3 ± 0.6	1.5 ± 1.0
63e	27 ± 10	31 ± 9
63f	2.1 ± 0.1	2.5 ± 0.9
63g	16 ± 8	13 ± 8
MK-2206	0.06 ± 0.01	0.06 ± 0.02
GSK690693	7.0 ± 2.1	5.9 ± 0.8

Since this dually labelled Akt also carried the PyMPO label at Cys49, it was reasonable to assume that conducting iFLiK experiments would still be possible by exciting PyMPO. A comparative excitation scan of the single- and dual-labelled protein shows a near-zero absorption of the AF568-labelled kinase at 440 nm, whereas the AF568/PyMPO-labelled kinase exhibited sufficiently high absorptions at this wavelength. Therefore, dilution series of allosteric and ATP-competitive Akt inhibitors were incubated with both constructs and their emission spectra recorded upon excitation at 440 nm. As anticipated, the single-labelled protein showed negligible fluorescence, confirming that Alexa Fluor 568 was not excited under these conditions. Remarkably, in the AF568/PyMPO labelled protein, instead of a

broad emission spectrum with a maximum around 560 nm that would be expected for PyMPO, a narrow emission around 606 nm characteristic for Alexa Fluor 568 was observed. With increasing inhibitor concentration, this spectrum was not red-shifted, but exhibited an increase in intensity by up to about 2 times (Figure 65). No increase occurred for the ATP-competitive GSK690693, suggesting that this effect is still iFLiK-specific.

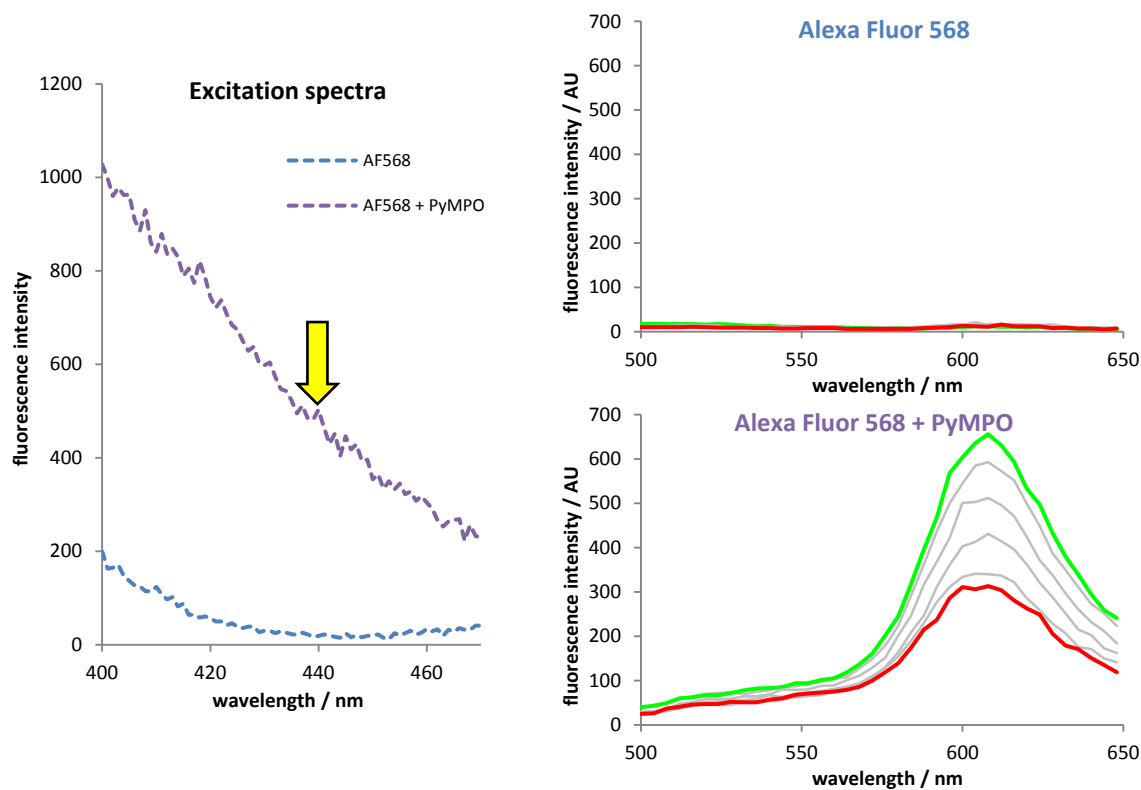


Figure 65 Left: Excitation spectra of AF568-labelled and AF568/PyMPO-labelled Akt. Right: Spectrum changes of these two differently labelled proteins (upper: Alexa Fluor 568; lower: Alexa Fluor 568 + PyMPO) when incubated with dilution series of the allosteric inhibitor **63b** upon excitation at 440 nm (red = apo; green = saturated).

The only species in this system absorbing at 440 nm is PyMPO, so the most plausible explanations were an extreme bathochromic shift of PyMPO or an energy transfer from PyMPO to Alexa Fluor 568. PyMPO emission is much broader in general and unable to reach these long wavelengths (even in the most polar solvent H₂O, the emission maximum is at 586 nm), rendering the first explanation highly unlikely. Considering the excitation spectrum of Alexa Fluor 568, however, a great spectral overlap with the PyMPO emission can be discerned. As the PyMPO spectrum is bathochromically shifted upon incubation with allosteric inhibitors in the iFLiK setup, this overlap is increased even more, which explains the signal increase observed in the dually labelled kinase (and the lack thereof upon incubation with ATP-competitive inhibitors).

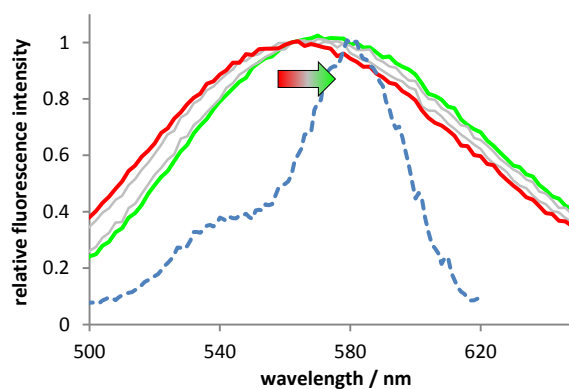


Figure 66 PyMPO emission (solid lines) and Alexa Fluor 568 excitation (dotted line) exhibit a high spectral overlap, which is even increased further upon bathochromic shift of the PyMPO spectrum when incubated with allosteric inhibitors (red = apo; green = saturated).

Using this signal increase for dose-response curves, sigmoidal curves were obtained for allosteric inhibitors, which were used to calculate the binding affinity analogous to the iFLiK experiments. Although very crude and subject to high fluctuations, a rough estimate for the K_d could be obtained, which seem to be higher by a factor of about 2-3. This might indicate that labelling with Alexa Fluor 568 slightly decreases the binding affinity of Akt to allosteric inhibitors.

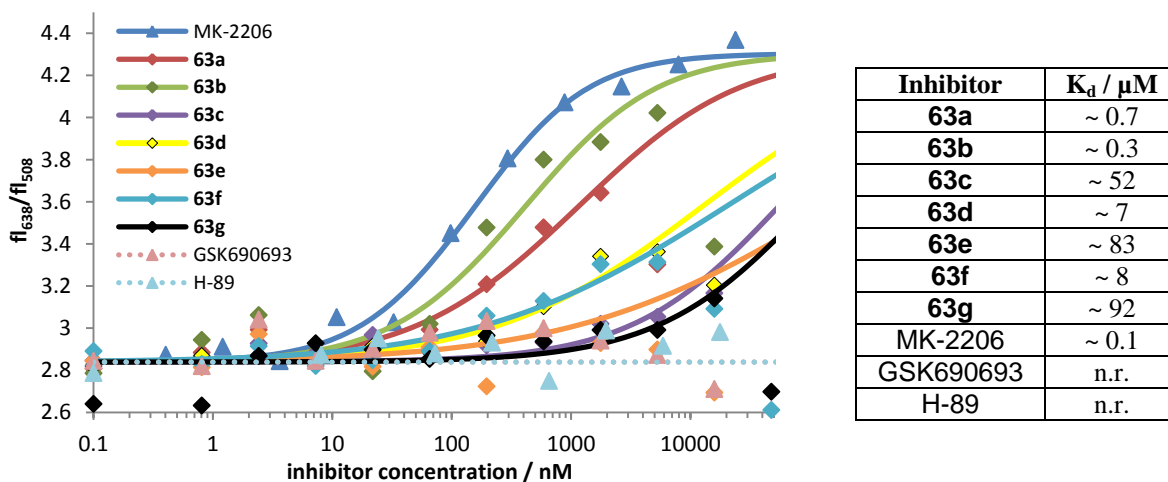


Figure 67 Dose-response curves of AF568/PyMPO-labelled de92 when incubated with allosteric and ATP-competitive Akt inhibitors, using 440 nm as excitation wavelength and fl_{638}/fl_{508} as assay readout, and their respective calculated K_d s. n.r. = no response up to 500 μM .

Interestingly, irradiating the dual-labelled Akt at 570 nm also produced a dose-dependent fluorescence increase of Alexa Fluor 568 specific to allosteric inhibitors, which cannot be observed in the single-labelled Akt (Figure 68). Although PyMPO does not absorb at this wavelength, this finding suggests that PyMPO has a role of some kind in this phenomenon. A more detailed investigation will be left for future work as this additional information did not impede the main purpose of NanoTemper to provide an orthogonal method to measure binding affinities of Akt.

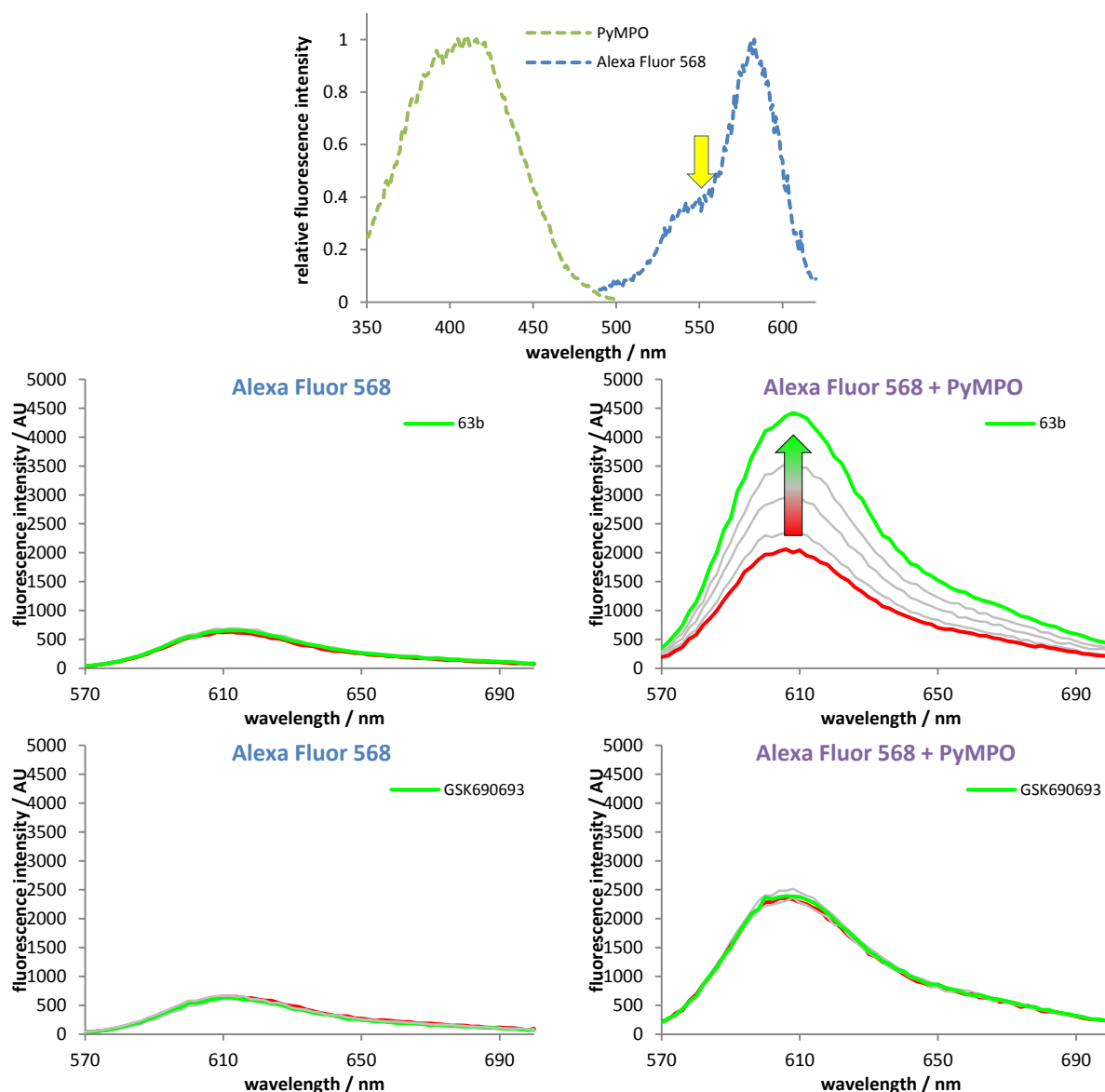


Figure 68 Top: Excitation spectra of PyMPO and Alexa Fluor 568. At an excitation at $\lambda = 550$ nm, PyMPO does not absorb. Middle & bottom: Fluorescence emission spectra of AF568-labelled (left) and AF568/PyMPO-labelled Akt (right) when incubated with of the allosteric **63b** (middle) and the ATP-competitive GSK690693 (bottom) at increasing concentrations (red = apo; green = saturated).

Comparing the binding affinities obtained with NanoTemper to the iFLiK results, both assays produce very similar results. Figure 69 nicely shows that the K_d values are almost identical for all allosteric inhibitors, except for low affinity ligands such as **63e** and **63g**, which seem to be evaluated differently by the two assay systems and deviate from each other. The higher K_d determined with NanoTemper is probably owed to the unspecific labelling with Alexa Fluor 568, which was shown to decrease the binding affinity of Akt to its inhibitors. Most importantly, while iFLiK distinguishes between allosteric and ATP-competitive, the NanoTemper assay does not.

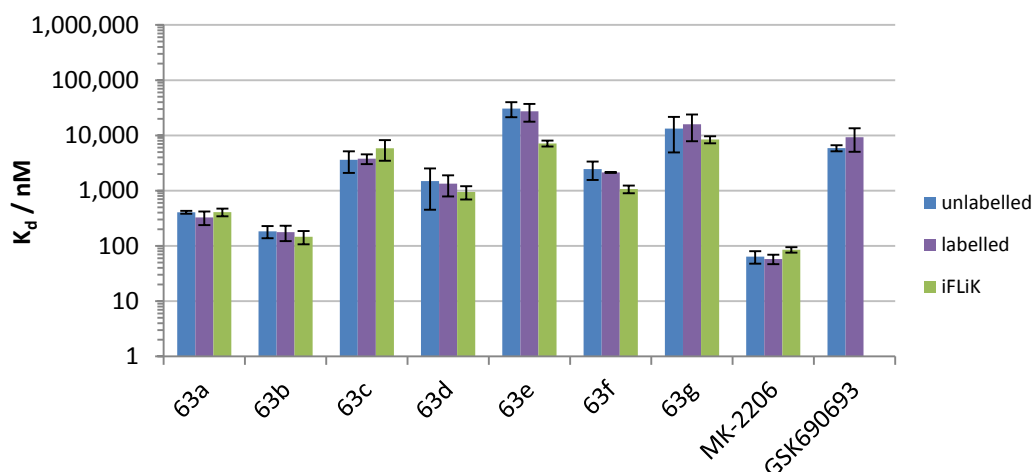


Figure 69 Comparison of K_d s obtained with NanoTemper for both proteins and with iFLiK for comparison.

Finally for the sake of completeness, the binding of the inhibitors to Akt1 wt was investigated by labelling commercially available Akt1 wt (purchased from Millipore) with Alexa Fluor 568. Since the commercial kinase has been activated by PDK1, its catalytic activity could be measured with the KinEASE assay before and after labelling with the fluorophore. The parallel experiments with different concentrations of the kinase show that Akt retained its catalytic activity after Alexa Fluor 568 labelling, but with a slightly lower activity (Figure 70): The concentration of half-maximal activity AC_{50} was reached at 55 pM for the unlabelled and 158 pM for the labelled enzyme. Like the binding affinity determined earlier, the potency of the AF568-labelled kinase was reduced by about 3-fold by the unspecific alkylation of amine residues.

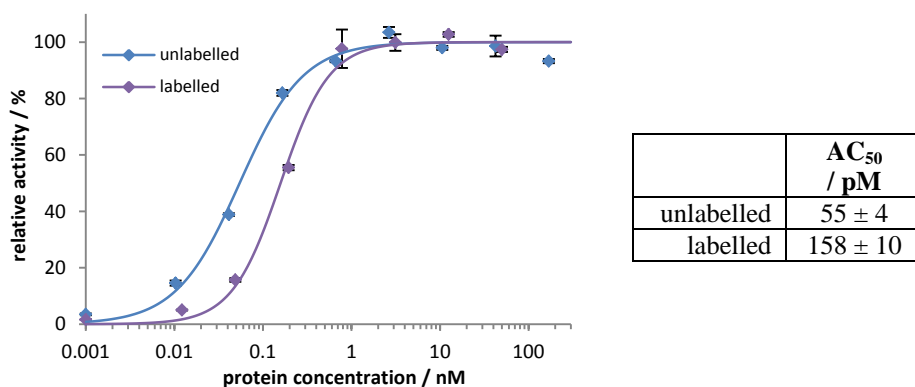


Figure 70 Akt1 wt still shows activity after labelling with Alexa Fluor 568 with a slightly increased AC_{50} .

Due to its high protein consumption, only a few experiments were possible with the commercially purchased kinase. These experiments, however, indicated that the activated kinase exhibited a higher affinity for ATP-competitive inhibitors than the inactive (K_d of GSK690693 was determined to 0.2 μM for the active and 5.9 μM for the inactive Akt), and show no response to allosteric inhibitors up to 500 μM . Preliminary, unpublished findings by the Zimmermann group obtained with Biacore reflect this phenomenon.¹⁸⁰ It is also well known that ATP-competitive inhibitors bind preferably into active conformations of kinases, whereas allosteric inhibitors have a stronger affinity towards the inactive form. For this reason, to enable a direct comparison between wt and the iFLiK mutant, the Akt1 wild type would have to be expressed under the same conditions as de92. This could be subjected in future works. Previous studies in our own group with other kinase, however, have shown that most Cys-to-Ser mutations of surface-exposed cysteines had little impact on the kinase activity or binding affinity compared to the wild type.^{153,181}

As an alternative fluorophore, Atto 550 was explored for its use with the NanoTemper assay. In analogy to the previous experiments with Alexa Fluor 568, de92 was incubated with 5 eq of the Atto 550 NHS ester at pH 8.3 for 1 h at 4 °C and purified over a size exclusion column. After calculating its molar extinction coefficients with equation (10) shown below to $\epsilon_{fl,280} = 13534 \text{ cm}^{-1} \text{ M}^{-1}$ and $\epsilon_{fl,595} = 4409 \text{ cm}^{-1} \text{ M}^{-1}$, the labelling ratio was determined to be 1.5:1. The Atto 550-labelled protein, too, did not aggregate in the enhanced gradient capillaries. However, when performing thermophoresis measurements with dilution series of the various Akt inhibitors, the assay exhibited a highly erratic behaviour (Figure 71): With increasing residence time in the capillary, the thermophoretic diffusion increased as well (i.e. the fluorescence intensity ratio hot/cold dropped), as it was discovered by measuring the same concentrations at different times. This effect was observed for all measured Akt inhibitors and was independent of the inhibitor's nature, mode of action or concentration. Like many Atto-Tec products, Atto 550 was now identified as a fluorophore unsuitable for NanoTemper.

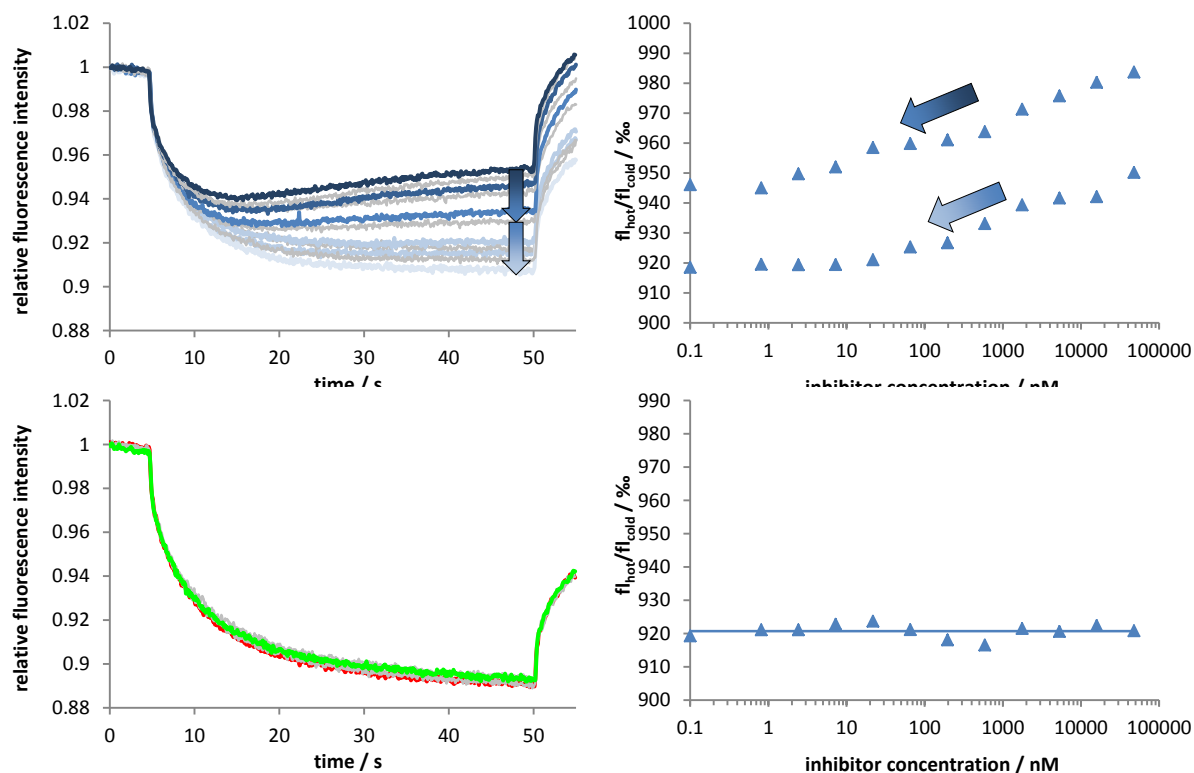


Figure 71 Thermophoresis curves and NanoTemper response of Atto 550-labelled de92 incubated with increasing concentrations of MK-2206. Upper: Capillaries with the same concentrations measured at different capillary residence times (darker blue = 1-12 min; lighter blue = 13-24 min) exhibit increased thermophoresis. Lower: Independent measurements after a capillary residence time of 30 min, no dose-dependent differences in thermophoresis were detectable.

In summary, the NanoTemper assay has been established for the Akt constructs used in this thesis. Except for low affinity ligands, K_d s obtained with iFLiK and NanoTemper exhibited a very good match, thereby validating the iFLiK assay as an eligible tool for determining binding affinities of Akt inhibitors. In contrast to iFLiK, however, NanoTemper cannot distinguish between allosteric and ATP-competitive inhibitors as it detects any binding event. By comparing two differently labelled constructs, it was shown that PyMPO labelling does not significantly alter binding affinity towards Akt inhibitors. On the other hand, AF568 labelling does slightly reduce activity and binding affinity. Data also indicated that allosteric inhibitors preferred the inactive, whereas ATP-competitive inhibitors favoured the active Akt enzyme.

3.5.5 Validation with Biacore Assay

As an additional orthogonal assay to validate the iFLiK results, the Biacore assay by GE Healthcare was explored for this purpose, which is based on the detection of changes on surfaces *via* laser-stimulated surface plasmon resonance. In the present case, the protein is immobilised on a gold-coated chip, and the mass increase upon binding of a ligand is

measured in real time by a change in the refractive index (for a detailed description of the assay, see chapter 1.4.3). A variety of methods for protein immobilisation and protocols for the detection of ligand binding to Akt have been tested, which are described in more detail in the appendix, chapter 0.

Even though the resultant protocol gave highly unreliable results, the synthesised probe compounds **63a-g**, MK-2206 and GSK690693 were measured nonetheless with this suboptimal protocol as a first proof of principle. Despite high fluctuations in the signal intensity, a dose-dependent change of the gold surface refraction could be detected upon inhibitor binding. Using the internal steady state thermodynamics model, the dissociation constants were calculated for all inhibitors with limited success. These rough preliminary results indicate that the K_{ds} determined with iFLiK and NanoTemper can be reproduced with Biacore, as the values are in a comparable range (Figure 72) and mirror the trends observed in the activity-based KinEASE assay (Table 5). However, while these were single results based on low quality data, the inhibitors do exhibit different binding affinities, so they can only be treated as a rough guide.

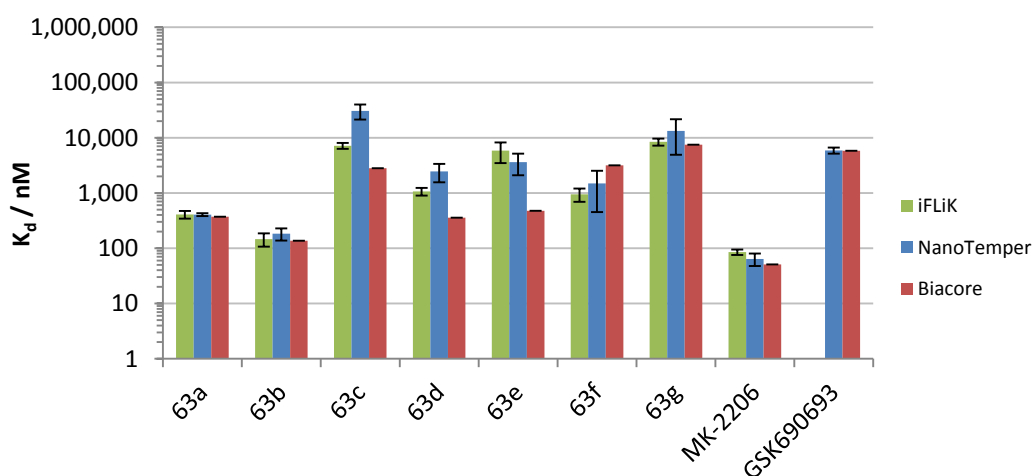


Figure 72 Comparison of dissociation constants determined with the different assay technologies.

Since experiments with the NanoTemper assay have already provided the required information, establishing the Biacore assay for Akt as an additional analytical method was eventually abandoned due to problems with the protein immobilisation, which is the most common bottleneck for establishing Biacore assays.

3.6 High-Throughput Screening

After establishing a proof of concept, optimising the protocol and validating the results with orthogonal assay systems, the iFLiK assay can now be used in the high-throughput screening of compound libraries to identify novel allosteric inhibitors of Akt.

3.6.1 Primary Screen of RL Library

The RL library is an in-house collection of compounds that were synthesised in the Rauh group over time for various projects or bought from commercial sources. Therefore, it is highly enriched in ATP-competitive kinase inhibitors specifically developed for various kinase families. As a preparation for larger libraries, this RL library was screened first to gather experience in setting up primary screens and interpreting the resulting data. This pilot screen will help in further optimising the protocols for using iFLiK in HTS campaigns. At a compound concentration of 10 μM , all 1099 inhibitors were incubated for 2 h each with 200 nM of PyMPO-labelled de92 and buffer in 384-well plates using several DMSO wells as negative and MK-2206 as positive controls. Fluorescence intensities at 508 nm and 638 nm when excited at 419 nm were recorded, the inhibitor-in-buffer signals subtracted as background correction, and the remaining f_{638}/f_{508} ratio calculated. Compounds that produced at least 25% of the positive control signal response in either direction were considered as hits.

In this 1-point primary screen, 25 compounds appeared as hits using this 25% cutoff (apart from the known allosteric Akt inhibitors), representing an initial hit rate of 2.27%. However, 12 of these compounds exhibited an intrinsic fluorescence of more than 50% of the PyMPO signal. It was therefore very likely that the detected changes in the f_{638}/f_{508} ratio purely arose from fluctuations in the compounds fluorescence. And indeed, when following up on these hits in dilution series iFLiK experiments, none of these strongly fluorescent molecules were able to provoke the expected dose-dependent bathochromic shift of PyMPO emission up to 500 μM . 7 of the other non-fluorescent hits in the primary screen at 10 μM exhibited a highly erratic behaviour in the follow-up and displayed no clear dose dependency. A closer look revealed that although their auto-fluorescence only became significant at higher concentrations, a low fluorescence at 10 μM had been the cause for the false hit. In addition, 4 compounds that gave a >25% response in the single 1-point measurement did not produce any response in the triplicate dilution series experiment, which is owed to random outliers unavoidable in single point measurements and can only be detected by repetition or multiple measurements.¹⁸²

Ultimately, 2 compounds evoked the expected dose-dependent bathochromic PyMPO emission shift. However, these compounds are K252a, a known broadband kinase inhibitor derived from staurosporine, and GSK690693, a known commercially available Akt inhibitor. Although both being not allosteric, this is consistent with the finding that only very potent ATP-competitive inhibitors seem to produce a slight PyMPO red-shift at high concentrations, as it was discussed in chapter 0. This still shows that ATP-competitive Akt inhibitors are not detected by iFLiK in general as they do not facilitate inter-domain interactions between the PH and kinase domain, which is corroborated by the fact that the less potent CCT128930 and H-89 (IC₅₀s of 29 nM and 2 μM, respectively) were not picked up in the primary screen. As a result, the actual validated hit rate in this screen is 0.18%. This is a pleasantly low value, as it indicates that iFLiK does not produce many random false positives.

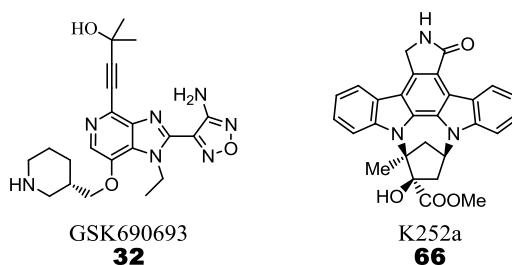


Figure 73 Validated hits found in the screen of the RL library with iFLiK.

For validation purposes, all 25 hits were tested for their inhibitory activity on Akt1 with the KinEASE assay. As expected, none of the fluorescent compounds were confirmed as actual Akt inhibitors, whereas the inhibition by K252a and GSK690693 could be shown. This means that the screen of the RL library with iFLiK produced a 0.18% validated hit rate with no false positives. However, intrinsic compound fluorescence presented the main limitation in identifying inhibitors with iFLiK. This screen has shown that compounds with an auto-fluorescence of 50% of the PyMPO signal can not be investigated with iFLiK. Furthermore, singlicate measurements were prone to give false positives, which however can be easily alleviated in subsequent dose dependency tests. The knowledge from this pilot screen can now be used to improve the future screen of larger libraries.

3.6.2 Primary Screen of Waldmann Library

Similar to the RL library, the Waldmann library is an in-house collection consisting both of compounds from commercial screening libraries and products and intermediates from past synthesis projects in the Waldmann group. It contains about 40,000 compounds and covers a greater chemical space than the RL library, including many natural products and their derivatives. Following the pilot screen of the Rauh group library, 10,680 compounds from this library were screened at 10 μM in 384-well plates, again using MK-2206 as positive and DMSO as negative controls.

As a lesson from the pilot screen, the emission intensities at 508 nm and 638 nm were maintained, but an additional excitation wavelength at 440 nm was added (Figure 74): In order to avoid intrinsic compound fluorescence, which is more likely at shorter wavelengths, irradiation at 75% of the excitation maximum (440 nm in the case of PyMPO) was considered a good compromise of signal intensity and interference by auto-fluorescence. However, compounds that do still fluoresce at 440 nm are more likely to emit at 508 nm due to their smaller Stokes shift than PyMPO. In this case, excitation at 419 nm will provide the signal with less background fluorescence. This and the greater signal intensity are the reasons for retaining 419 nm as excitation wavelength. Furthermore, comparing the results of the two wavelength channels, outliers from random systematic errors can be identified and excluded from the final hit list.

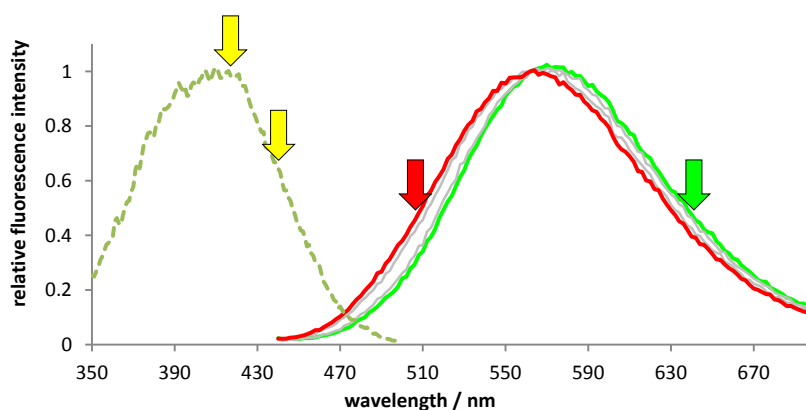


Figure 74 Schematic representation of assay strategy employed in the Waldmann library screen to handle compound fluorescence and to identify outliers. Excitation (dotted lines) at two different wavelengths (419 nm and 440 nm), record emission intensity (solid lines) at 508 nm (red = apo) and 638 nm (green = saturated).

With 10 μM of each compound in buffer alone as background correction, the $\text{fl}_{638}/\text{fl}_{508}$ ratio at each excitation wavelength was determined for every compound. A cutoff of more than 25% signal change of the MK-2206 control was employed, and the hits were categorised according to the following criteria:

- Promising: Hits that exhibited >25% binding on both channels.
- Interesting: Hits that exhibited >25% binding on either the 419 nm or 440 nm channel or <-25% binding on both channels.
- Questionable: Hits with borderline affinities on one channel only or an auto-fluorescence of 0-50% of the PyMPO signal.
- Artefact: Hits with an auto-fluorescence of more than 50% of the PyMPO signal.

Applying these selection filters, 215 compounds met these criteria, categorised into 13 promising, 11 interesting, 35 questionable and 156 artefacts. From experience gained in the pilot screen, the results categorised as questionable or artefacts should not be considered as hits and were therefore not further investigated. The remaining 24 compounds were picked for follow-up, representing a 0.22% hit rate for a 1-point screen. In triplicate dose-response measurements with iFLiK up to 50 μM , 13 out of these 24 hits from the primary screen were validated to produce a dose-dependent change in the $\text{fl}_{508}/\text{fl}_{638}$ ratio (Figure 75), which amounts to an actual hit rate of 0.12% and a false hit rate of 0.10% for the singlicate screen of the Waldmann library. This low value again demonstrates the selectivity of the iFLiK assay, as it did not pick up any random compounds. Also, the false hit rate was exquisitely low despite being a 1-point measurement.

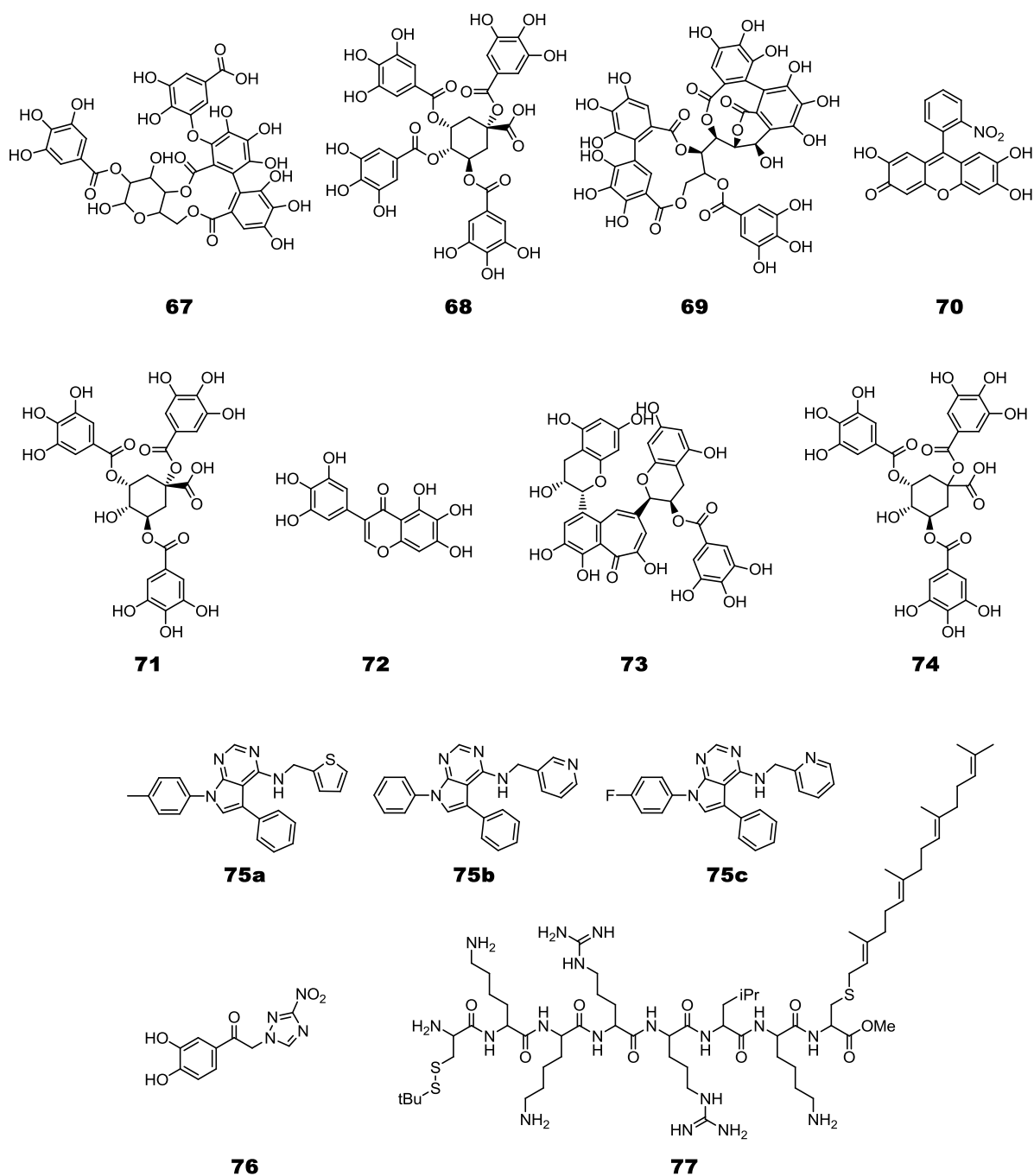


Figure 75 Validated hits from the primary screen of the Waldmann library with iFLiK.

While all these 13 compounds gave an increase in the fI_{508}/fI_{638} ratio, a differential response can be discerned at a closer look. While **75a-c** evoked a bathochromic shift of the PyMPO fluorescence spectrum and **77** a hypsochromic shift, the other compounds **67-74** and **76** primarily caused a reduction of the fluorescence intensity.

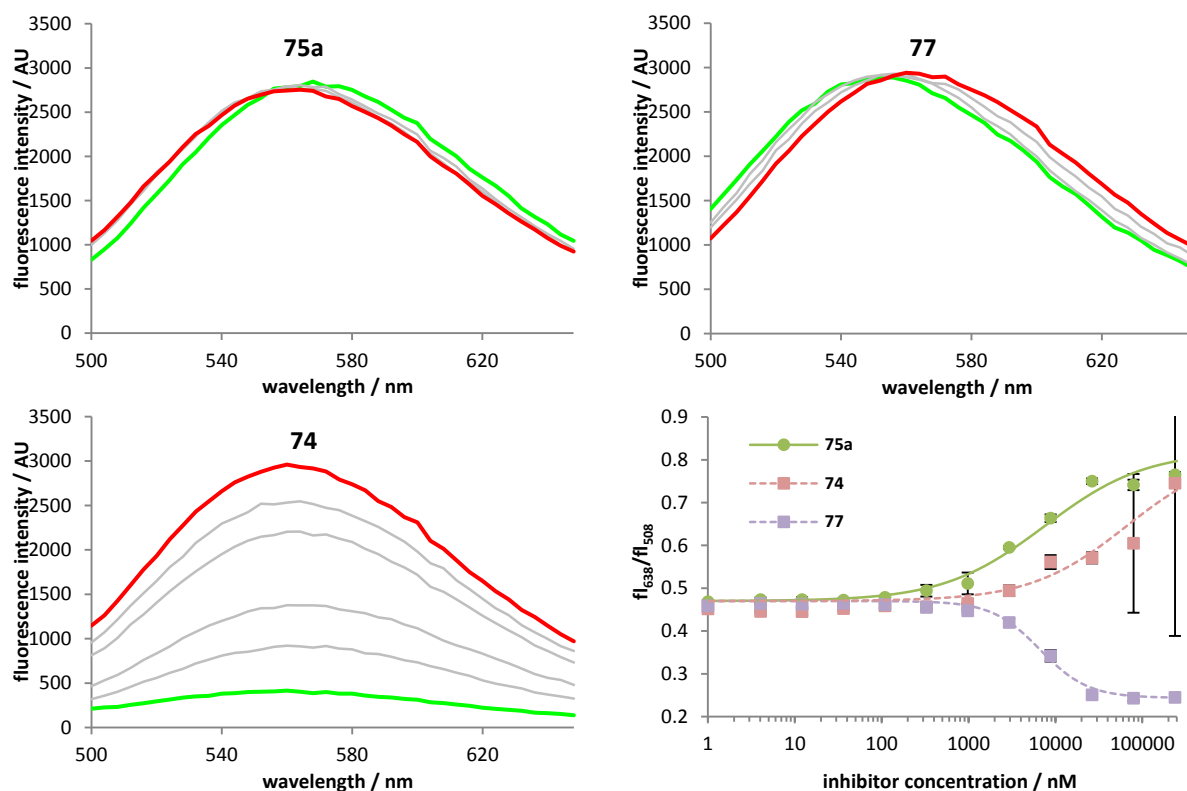


Figure 76 Different effects of hit compounds in dose dependency studies. While all hits produced an increase in the f_{508}/f_{638} ratio, **75a-c** effects a bathochromic shift of the PyMPO fluorescence, compounds like **67-74** mainly reduced the overall fluorescence intensity. The peptide derivative **77** induced a hypsochromic shift and hence a decrease in the f_{508}/f_{638} ratio.

In order to investigate their inhibitory activity, all 24 hits of the primary screen were measured against Akt1 and Δ PH-Akt1 with the KinEASE assay (Table 12). As expected, none of the false hits inhibited Akt, whereas 12 of the 13 validated hits from the screen indeed were active against the full length Akt1, demonstrating the high selectivity and reliability of the iFLiK assay. However, the compounds that quenched the PyMPO fluorescence in the iFLiK experiments (except **76**, which was inactive overall), as well as **77**, which produced a hypsochromic PyMPO spectrum shift, showed inhibition of Δ PH-Akt1 as well. Only the 3 compounds that solely provoked a bathochromic emission spectrum shift were selective for the full-length kinase, as would be expected for allosteric inhibitors.

Table 12 Biological activity of hits from the primary screen of the Waldmann library. Binding affinities were determined with iFLiK, inhibitory activity with KinEASE. Compounds in red cells were negative in the iFLiK follow-up (structures not shown), yellow had quenched PyMPO fluorescence, green provoked a hypsochromic shift of PyMPO emission, blue a bathochromic shift. n.r. = no response up to 500 μ M. n.i. = not inhibiting up to 200 μ M.

Compound	K_d / μ M	IC ₅₀ (Akt1) / μ M	IC ₅₀ (Δ PH-Akt1) / μ M
67	>500	9 \pm 1	3.3 \pm 0.1
68	>500	26 \pm 17	10 \pm 4
69	432 \pm 303	56 \pm 79	5 \pm 2
70	>500	4.9 \pm 0.9	3.4 \pm 0.6
71	>500	11 \pm 6	5 \pm 3
72	>500	7 \pm 6	5 \pm 3
73	>500	1.5 \pm 0.9	1.1 \pm 0.3
74	>500	11 \pm 4	5 \pm 3
75a	8 \pm 4	35 \pm 17	n.i.
75b	22 \pm 5	97 \pm 42	n.i.
75c	194 \pm 93	>200	n.i.
76	>500	-	-
77	9 \pm 1	37 \pm 22	9 \pm 7
hit 1	n.r.	n.i.	n.i.
hit 2	n.r.	n.i.	n.i.
hit 3	n.r.	n.i.	n.i.
hit 4	n.r.	n.i.	n.i.
hit 5	n.r.	n.i.	n.i.
hit 6	n.r.	n.i.	n.i.
hit 7	n.r.	n.i.	n.i.
hit 8	n.r.	n.i.	n.i.
hit 9	n.r.	n.i.	n.i.
hit 10	n.r.	n.i.	n.i.
hit 11	n.r.	n.i.	n.i.

The peptide derivative **77** produced a 5 nm blue-shift, which indicates a decrease in the polarity surrounding the PyMPO sensor (Figure 76). In our working model for the assay, such a decrease can be interpreted as an equilibrium shift of the kinase towards the open conformation. Since this peptide shows Akt inhibition regardless of the PH domain presence, it suggests an inhibition by occupying the substrate pocket, which is only accessible in the open conformation. Interestingly, the sequence of **77** (CKKRRLKC) does not resemble any of the known peptide inhibitors of Akt so far.^{56,183,184} However, this peptide will have to be further investigated in more detail for a more accurate statement about its mode of action.

Compounds **67-74** also showed inhibition of both Akt1 and Δ PH-Akt1 and a slight redshift of 2 nm, but most prominently reduced the intensity of PyMPO fluorescence by up to 75% (Figure 76). Such hydrophobic, aromatic, poly-hydroxylic compounds are known to facilitate protein aggregation and unfolding, and regularly appear in screening campaigns.¹⁸⁵⁻¹⁸⁷ Therefore, the fluorescence decrease could be attributed to contact quenching by intermolecular collisions with the protein molecules, due to a high local concentration in the

aggregates. Usually, such compounds are not followed up on, as their mode of action is very unspecific and they do not provide a clear SAR.

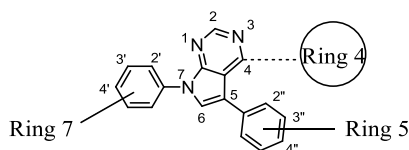


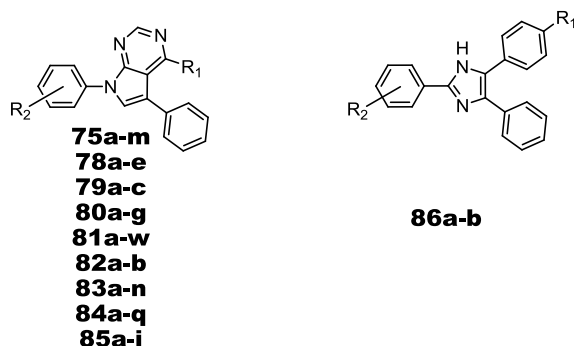
Figure 77 Nomenclature of the pyrrolo[2,3-*d*]pyrimidines found in this screen.

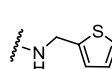
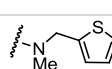
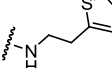
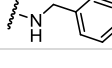
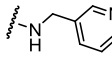
Only **75a-c** provoked a red-shift of the PyMPO emission spectrum by up to 8 nm and inhibited the full-length Akt but not the truncated kinase, suggesting an allosteric mode of action.

3.6.3 Secondary Screen

To further explore the binding of **75a-c**, another 88 commercially available compounds based on this pyrrolopyrimidine scaffold were ordered and tested with iFLiK and KinEASE (Table 13). Some of these compounds also showed an effect in the iFLiK assay and exhibited selective inhibitory activity on the full-length Akt1, displaying a wide range of K_d s determined with iFLiK and IC_{50} s determined with KinEASE, providing a distinct SAR.

Table 13 Structures and results of pyrrolopyrimidine inhibitors in binding (iFLiK) and activity (KinEASE) assays. n.r. = no response up to 500 μ M. n.i. = no inhibition up to 200 μ M.



Name	R ₁	R ₂	K_d / μ M	IC_{50} Akt1 / μ M	IC_{50} Δ PH-Akt1 / μ M
75d		H	2.2 ± 0.7	71 ± 30	n.i.
75e		3'-Me	99 ± 61	n.i.	n.i.
75h		3'-CF ₃	n.r.	n.i.	n.i.
75a		4'-Me	2.2 ± 0.5	196 ± 102	n.i.
75g		3'-Cl, 4'-Me	264 ± 284	1435 ± 132	n.i.
75i		H	n.r.	n.i.	n.i.
75j		4'-Cl	n.r.	n.i.	n.i.
75f		4'-Me	6 ± 4	2760 ± 4431	n.i.
75b		H	7.8 ± 0.7	160 ± 44	n.i.
75k		3'-Cl	n.r.	n.i.	n.i.
75l		4'-OMe	n.r.	n.i.	n.i.

Name	R ₁	R ₂	K _d / μM	IC ₅₀ Akt1 / μM	IC ₅₀ ΔPH-Akt1 / μM
75m		H	n.r.	n.i.	n.i.
75c		4'-F	20 ± 7	n.i.	n.i.
78a	OH	3'-Me	n.r.	n.i.	n.i.
78b		4'-Me	n.r.	n.i.	n.i.
78c		4'-OMe	n.r.	n.i.	n.i.
78d		4'-OEt	n.r.	n.i.	n.i.
78e		4'-F	n.r.	n.i.	n.i.
79a	SMe	4'-F	n.r.	n.i.	n.i.
79b	SEt	4'-OMe	n.r.	n.i.	n.i.
79c		4'-OEt	n.r.	n.i.	n.i.
80a	NHPr	4'-OEt	n.r.	n.i.	n.i.
80b	NHiPr	H	n.r.	n.i.	n.i.
80c		3'-CF ₃	n.r.	n.i.	n.i.
80d		4'-F	n.r.	n.i.	n.i.
80e		4'-Br	n.r.	n.i.	n.i.
80f	NEt ₂	H	n.r.	n.i.	n.i.
80g		4'-OMe	n.r.	n.i.	n.i.
81a		4'-OMe	n.r.	n.i.	n.i.
81b		4'-OEt	n.r.	n.i.	n.i.
81c		4'-F	n.r.	n.i.	n.i.
81d		4'-Cl	n.r.	n.i.	n.i.
81e		4'-OMe	n.r.	n.i.	n.i.
81f		4'-Br	n.r.	n.i.	n.i.
81g		H	n.r.	n.i.	n.i.
81h		H	n.r.	n.i.	n.i.
81i		4'-Br	n.r.	n.i.	n.i.
81j		4'-Me	n.r.	n.i.	n.i.
81k		4'-OEt	n.r.	n.i.	n.i.
81l		H	n.r.	n.i.	n.i.
81m		4'-OEt	n.r.	n.i.	n.i.
81n		4'-Cl	n.r.	n.i.	n.i.
81o		H	n.r.	n.i.	n.i.
81p		3'-Me	n.r.	n.i.	n.i.
81q		3'-CF ₃	n.r.	n.i.	n.i.
81r		4'-F	n.r.	n.i.	n.i.
81s		H	n.r.	n.i.	n.i.
81t		3'-CF ₃	n.r.	n.i.	n.i.
81u		3'-Cl, 4'-Me	n.r.	n.i.	n.i.
81v		4'-F	n.r.	n.i.	n.i.
81w		3'-CF ₃	n.r.	n.i.	n.i.
82a		4'-OEt	n.r.	n.i.	n.i.
82b		3'-F	n.r.	n.i.	n.i.
83a		H	n.r.	n.i.	n.i.
83b		3'-CF ₃	n.r.	n.i.	n.i.
83c		4'-Me	n.r.	n.i.	n.i.
83d		4'-OMe	n.r.	n.i.	n.i.
83e		4'-Cl	n.r.	n.i.	n.i.
83f		4'-OMe	n.r.	n.i.	n.i.

Name	R ₁	R ₂	K _d / μM	IC ₅₀ Akt1 / μM	IC ₅₀ ΔPH-Akt1 / μM
83g 83h 83i 83j 83k		H 3'-Me 3'-Cl, 4'-Me 4'-OMe 4'-OEt	n.r. n.r. n.r. n.r. n.r.	n.i. n.i. n.i. n.i. n.i.	n.i. n.i. n.i. n.i. n.i.
83l		4'-OMe	n.r.	n.i.	n.i.
83m		4'-Br	n.r.	n.i.	n.i.
83n		3'-Cl	n.r.	n.i.	n.i.
84a 84b		3'-Me 4'-OEt	n.r. n.r.	n.i. n.i.	n.i. n.i.
84c 84d		4'-F 4'-Br	n.r. n.r.	n.i. n.i.	n.i. n.i.
84e		3'-Me	n.r.	n.i.	n.i.
84f 84g		4'-OEt 4'-Br	n.r. n.r.	n.i. n.i.	n.i. n.i.
84h		4'-OEt	n.r.	n.i.	n.i.
84i 84j 84k		H 3'-CF ₃ 4'-OEt	n.r. n.r. n.r.	n.i. n.i. n.i.	n.i. n.i. n.i.
84l		4'-OEt	n.r.	n.i.	n.i.
84m 84n		4'-OMe 4'-Br	n.r. n.r.	n.i. n.i.	n.i. n.i.
84o 84p 84q		H 3'-CF ₃ 4'-Br	n.r. n.r. n.r.	n.i. n.i. n.i.	n.i. n.i. n.i.
85a		4'-OEt	n.r.	n.i.	n.i.
85b 85c		H 4'-OMe	n.r. n.r.	n.i. n.i.	n.i. n.i.
85d		4'-OMe	n.r.	n.i.	n.i.
85e 85f 85g 85h 85i		H 3'-Me 3'-CF ₃ 4'-OMe 4'-Br	n.r. n.r. n.r. n.r. n.r.	n.i. n.i. n.i. n.i. n.i.	n.i. n.i. n.i. n.i. n.i.
86a	Cl	4'-OH	14 ± 3	336 ± 111	n.i.
86b		3'-OH, 4'-OH	n.r.	n.i.	n.i.

Despite this amount of data, a few key facts can be established for the SAR. Most obviously, the substituent on the 4-position played a decisive role. It appears that an aromatic system is required at the 4-position, as no compound showed any affinity that featured simple small groups (like the **78**, **79** and **80** family), purely aliphatic chains (like the **81** and **82** family) or saturated carbo and heterocycles (like the **83** family) as R₁. Even very bulky, hydrophobic substituents of the **84** family do not seem to produce the desired activity. Not every aromatic group, however, seems to be eligible, as the missing efficacy of the **85** family testify. Apparently, while heterocycles are tolerated (thiophenes and pyridines were active), the aromatic ring must not be substituted (like in **85a-i**). Positioning of the heteroatom affects the efficacy (*meta* substitution of **75b** binds more strongly than *ortho*-substituted **75c**). Furthermore, both the free NH (the N-methylated **75i** completely lost activity compared to the fairly active **75d**) as well as the distance to the core scaffold (longer linker of **75j** abolishes activity) were identified as crucial parameters. Substitution in the *meta* position of ring 7 negatively affects their affinity (complete loss of activity in **75h** and **75k**, strong reduction in **75e** and **75g**). While a relatively small methyl group in ring 7 *para* position is well tolerated (affinities of **75d** and **75a** about equal), the methoxy substituent caused a loss of activity, perhaps due to its electron-donating nature (**75b** compared to **75l**), whereas the electron-withdrawing fluoro substituent restored an otherwise low affinity (**75c** compared to **75m**). Interestingly, the **86** family with a cropped down imidazole core instead of pyrrolopyrimidine also displayed an allosteric mode of action. Here, too, the *meta* substitution of the R₂ phenyl ring reduced their activity (**86b** compared to **86a**).

In order to understand this SAR, a knowledge of these pyrrolopyrimidines' binding mode is necessary. In the literature, some ATP-competitive Akt inhibitors with a pyrrolo[2,3-*d*]-pyrimidine scaffold and their binding mode are known, such as the commercially available CCT128930. However, X-ray crystal structures show that these inhibitors form hinge contacts to Glu228 and Ala230 *via* nitrogen atoms at the 1- and 7- position (PDB code 2V06).¹⁸⁸ An analogous binding mode is not possible for the **75** family due to their phenyl substituents at the 7- and 5-position. The preferred solution for elucidating their actual binding mode is co-crystallisation with Akt for an X-ray structural investigation. However, since the crystallisation has been unsuccessful so far (for a detailed description of the crystallisation experiments see chapter 3.7), a computational approach to calculate their binding modes was chosen by docking these structures into published full-length crystal structures of Akt (PDB codes 3O96 and 4EJN).^{76,131} Without imposing constraints for the modelling, which could bias the results computed by Glide, both crystal structures yielded the same two main binding modes

(Figure 78): Binding mode A resembles the conformation of Akti-1/2 in 3O96, with the phenyl group at the 7-position exerting π - π -interactions with Trp80, and the phenyl group at the 5-position occupying the binding pocket of Akti-1/2's phenyl groups. In this position, the N1 atom of the pyrrolopyrimidine might replace the N5 atom of Akti-1/2, which is known to be crucial for inhibitory activity for these allosteric inhibitors.¹⁷⁶ Presumably, this nitrogen atom forms hydrogen bonds to Gln79, Thr81, Thr82, Asp292 and Gly294, mediated by a complex network of water molecules, that can be seen in the co-crystal structure of Akt1 with **53**.¹³¹ In addition, the thiophene group of **75a**, **75d**, **75e** and **75g**, as well as the pyridine group of **75b** and **75c** could take the place of the Akti-1/2's piperidine group. In fact, this might explain the low efficacy of **75c** compared to **75b**, as the nitrogens in the *meta*-substituted pyridine overlap better than the *ortho*-substituted. In binding mode B, the pyrrolopyrimidines are oriented like the original ligand **53** in the crystal structure 4EJN. Their N7 phenyl substituents expel the water molecules close to the protein surface, leading to a favourable entropic contribution to the Gibbs free energy of binding. In this conformation, the thiophene/pyridine/phenyl substituents at the 4-position and the phenyl group at the 5-position occupy the original ligand's pyridine and phenyl position, respectively. Additionally, the exocyclic nitrogen atom at the 4-position might establish the aforementioned water network to the protein. Furthermore, the substituents of ring 4 in the **85** family would not fit into the inter-domain binding pocket in this orientation.

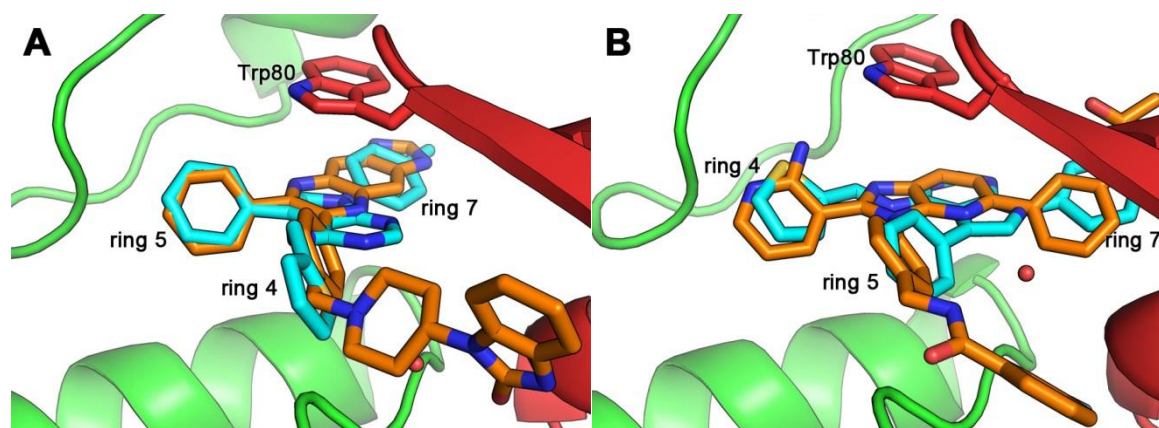


Figure 78 The two main binding modes for the pyrrolopyrimidines found in the screen (**75a** shown as an example in cyan sticks) as calculated by Glide. For reference in binding mode A (left) and B (right), the co-crystallised inhibitors Akti-1/2 from PDB entry 3O96 and **53** from PDB entry 4EJN are displayed as orange sticks, respectively.

In both binding modes, the lack of aromatic groups at the 4-position (like in the **78-84** family) would lead to a loss of affinity, as either one of the phenyl group pockets would not be occupied any more. Also, both are sensitive towards the nitrogen position of the ring 4 pyridine, as the *meta* nitrogen coincides well with the piperidine nitrogen of Akti-1/2 in mode A, and the SAR of **53** also showed a stronger activity of the pyridine moiety with a *meta* nitrogen in mode B. However, binding mode A cannot describe the retained affinity of **75f**, as its phenyl group is unable to form the water-mediated hydrogen bond to Gln79. Binding mode B can explain, why the **75i** shows no effect on Akt, since its additional methylene unit causes a misalignment of the thiophene group with the pyridine group of **53**. Furthermore, the loss of activity upon substitution of ring 4 is illustrated in mode B, whereas mode A can easily tolerate these substituents. On the other hand, only binding mode A can plausibly describe the binding affinity of the truncated imidazole derivative **86a**. However, neither of these binding modes can explain the dramatic decrease in affinity upon N-methylation (as in **75i**) or introduction of a *meta* substituent at ring 7 (as in **75e**, **75g**, **75h** and **75k**). Also, neither binding mode provides a rational explanation for the activity loss with the electron-donating methoxy group of **75l** or activity gain with the electron-withdrawing fluoro group of **75c**.

In summary, the 91 compounds in the secondary screen displayed a wide range of potency, in which the trends in the binding affinities (determined with iFLiK) mirrored the inhibitory activities (determined with KinEASE). A few key observations could be derived to formulate a preliminary SAR, but they were insufficient to provide conclusive evidence for one of the binding modes predicted by molecular modelling. A more focussed library of pyrrolo[2,3-*d*]-pyrimidines is hence required to further explore their SAR, develop a pharmacophore model and clarify their binding mode. As such specialised compounds are not commercially available, further work should revolve around synthesising more potent inhibitors based on the insights gained from the previously discussed SAR.

3.7 Crystallisation

A co-crystal structure of Akt with the newly discovered pyrrolopyrimidines would greatly improve our understanding of their binding mode. As the crystallisation of Akt has not been established in our lab, the protocol of the first published X-ray crystal structure of full length Akt with an ID inhibitor was adapted first with the Akt strong binders MK-2206 and **63b**. A small crystallisation screen was carried out on a 24-well plate, using the two constructs de91 and de92 incubated with 250 μ M of each inhibitor in the hanging drop method. The general reservoir buffer conditions (12.5 mM NaOAc, 25 mM sodium citrate) were varied from 19-24% PEG 2000 in a pH range from 5.0-5.6 and incubated at 20 $^{\circ}$ C. The crystal growth was checked regularly. However, even after 7 months, no crystals have grown for either inhibitor in either protein construct.

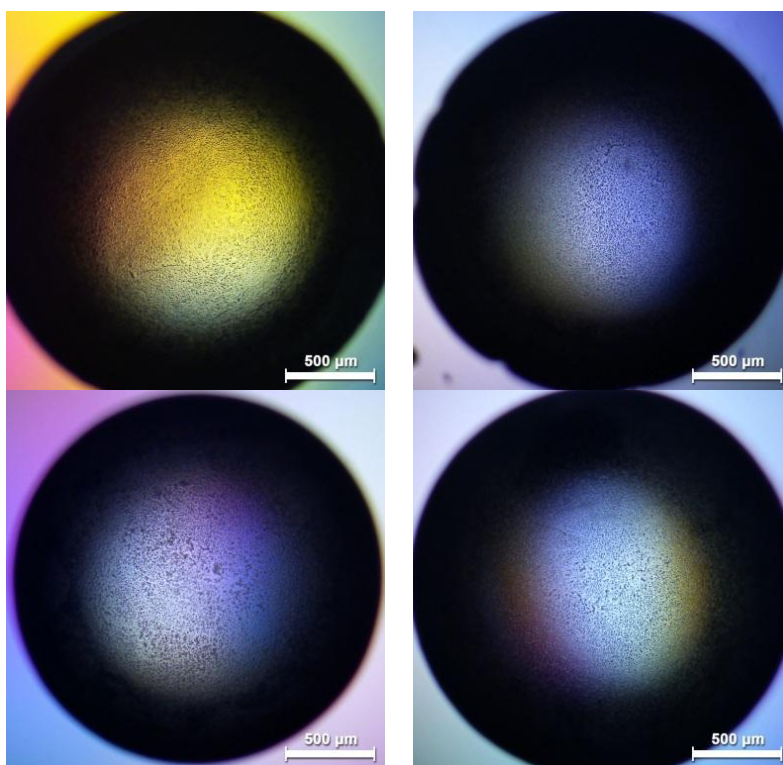


Figure 79 Representative pictures of hanging drops in the crystallisation screen with de91 (left) and de92 (right) co-crystallised with MK-2206 (upper) and **63b** (lower). Pictures were taken at a magnification of 4x after incubating for 7 months.

Wu *et al.* have reported that they were not able to obtain crystals of Akt with the full length protein, but only after cutting off all amino acids after Met446, which seemed to reduce flexibility.⁷⁶ In fact, the only two crystal structures published in the PDB so far both employed a construct consisting of the residues 1-446 of Akt1.¹³¹ Therefore, it was not surprising that the full-length de92 did not yield protein crystals. However, even the truncated construct de91, which comprises the residues 1-445, did not crystallise in the reported conditions. Apparently, the mutations introduced into de91 (E49C,C296S,C310S,C344S) have changed its crystallisation behaviour. Therefore, in order to obtain X-ray crystal structures with the expressed iFLiK constructs of Akt, a larger screen covering a wider range of buffer systems and conditions has to be implemented in future works.

Due to the unsuccessful crystallisation experiments, *in silico* molecular modelling has been chosen to elucidate the binding mode for the pyrrolopyrimidine hit compounds (discussed in chapter 3.6.3).

3.8 Summary and Conclusion

In summary, the iFLiK assay was successfully developed as a biochemical assay that can selectively detect the binding of allosteric Akt inhibitors and the resulting conformational changes by employing environmentally sensitive fluorophores (Figure 80).

Having studied the cellular, mutagenesis and X-ray data in the literature, it was decided to introduce the conformation sensor *via* an artificial cysteine at position Glu49, which is at the PH domain close to the domain interface, where conformational changes induced by allosteric inhibitors should be most perceptible. Three Akt constructs were created according to this structure-guided assay design, which were merged into a baculovirus in order to obtain the required proteins by insect cell expression and protein purification *via* FPLC. A series of fluorophores have been systematically tested for their applicability as biosensors. Nearly all of the selected fluorophores were able to report on the conformational changes of Akt when choosing the appropriate readouts, providing a proof of concept for the iFLiK assay. Using the solvatochromic PyMPO as fluorophore label, which reacts to the binding of ID inhibitors by a bathochromic shift of the emission spectrum, the assay has been optimised with respect to construct design, buffers, additives and reaction conditions. This extensive optimisation has resulted in an assay with excellent reproducibility and reliability, which was able to selectively detect allosteric Akt inhibitors and measure their binding affinities.

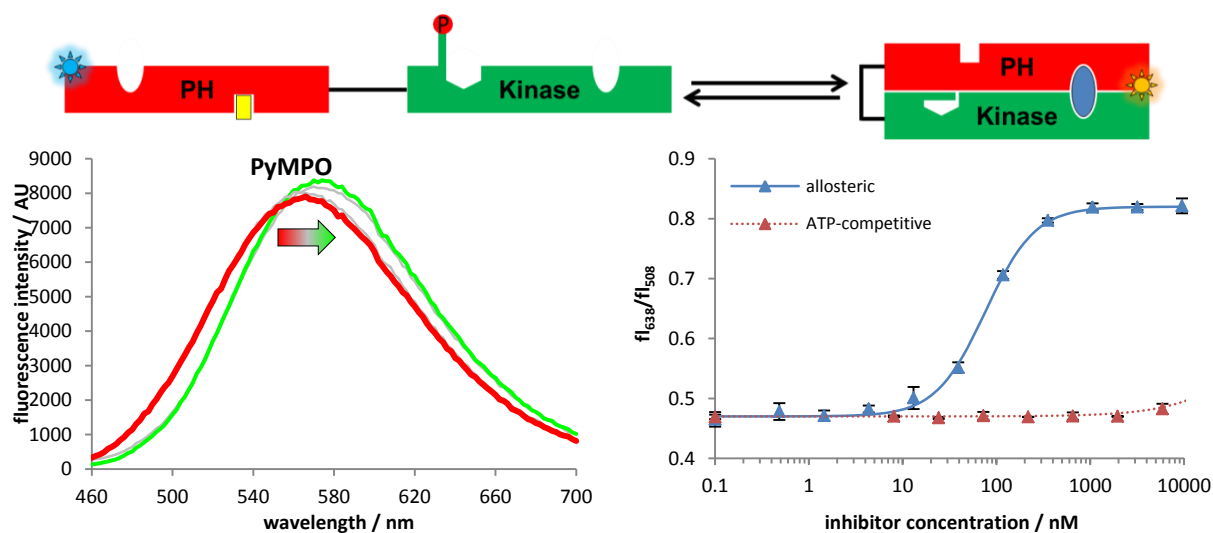
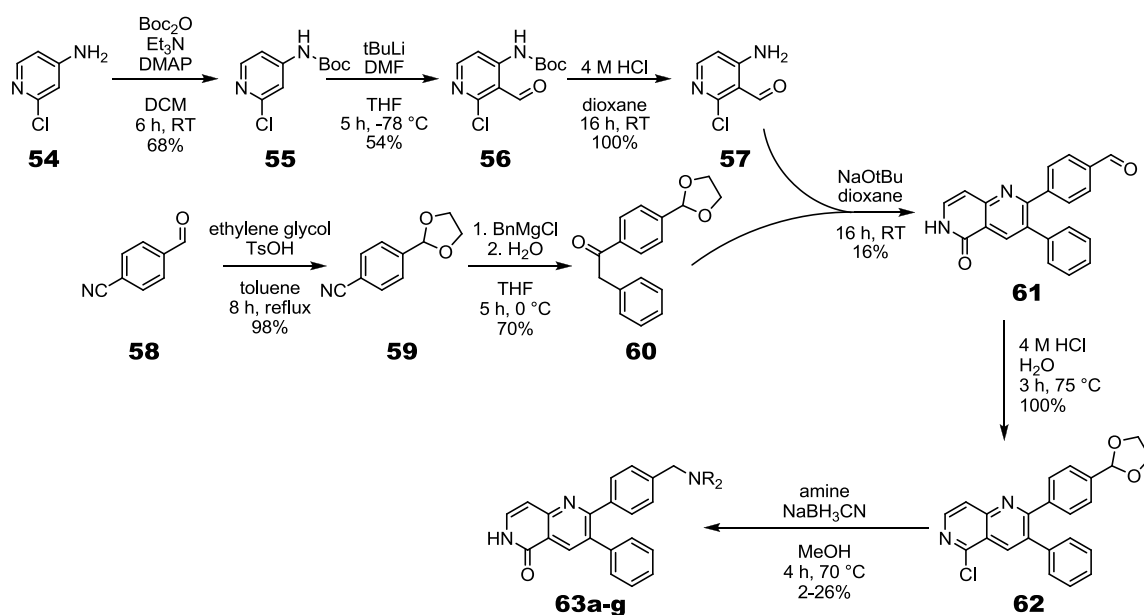


Figure 80 iFLiK assay principle: Top) Conformational changes induced by inter-domain inhibitors (blue circle) affect the environment around the PyMPO sensor (blue and orange star), leading to a bathochromic shift of the fluorescence emission (left). This can be quantified by calculating the intensity ratios at two different wavelengths left and right of the emission maximum and plotting a dose-response (right).

In the wake of developing the assay, a focussed library of naphthyridines based on known inter-domain inhibitors have been synthesised as probe compounds in the assay following

Scheme 7. After establishing the respective activity-based assays, these probes displayed nanomolar to low-micromolar activities *in vitro* as well as micromolar activities in human Akt-sensitive cell lines.



Scheme 7 Synthesis route for the preparation of 63a-g.

The dissociation constants produced by iFLiK could be verified with orthogonal assay systems based on completely different biophysical principles. The NanoTemper assay, which measures the thermophoretic behaviour of protein solutions, was successfully established and yielded comparable K_{d} s for both reference and synthesised Akt inhibitors. It also indicated that PyMPO labelling of the kinase does not significantly influence the binding of inhibitors. Although the Biacore assay, which detects ligand binding-correlated mass increases by surface plasmon resonance, could not be robustly established as an additional orthogonal assay, preliminary results seemed to give similar results to iFLiK and NanoTemper. In contrast to iFLiK, however, these commercial assays were not able to distinguish between allosteric and ATP-competitive inhibitors.

Following optimisation and validation of the iFLiK assay, it was employed in the screening of the RL and the Waldmann library. The primary screens displayed a hit rate of 0.12%, which is evidence for the high selectivity of iFLiK. A few compounds belonging to the family of pyrrolo[2,3-*d*]pyrimidines have been identified as hits from these screens, as they produced a dose-dependent bathochromic shift of the PyMPO emission spectrum. Their selective inhibitory effect on the full-length kinase over the kinase domain alone has been validated in activity-based assays, signifying the discovery of a novel class of allosteric Akt inhibitors which have not been described in the literature so far.

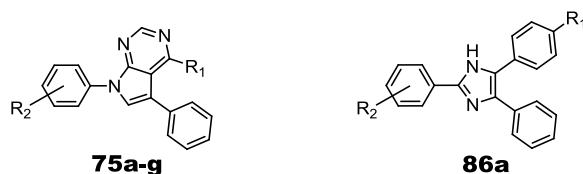


Figure 81 Compound class of pyrrolo[2,3-*d*]pyrimidines identified as novel allosteric Akt inhibitors in screening campaigns with the iFLiK assay.

In order to determine their binding mode, a structural examination by X-ray crystallography was attempted, but the crystallisation of Akt was unsuccessful. As an alternative, these pyrrolopyrimidines were docked into known crystal structures of Akt, yielding two plausible binding modes. To substantiate the actual binding orientation, their SAR was further explored by testing 91 of such derivatives in a secondary screen for their binding affinity with iFLiK and inhibitory activity with KinEASE. The following conclusions for the SAR could be drawn by studying the results of this follow-up study, supporting either of these two binding modes (for nomenclature of pyrrolopyrimidine substitution see Figure 77 on page 102, for their structures see Table 13 on page 102, for their binding mode see Figure 78 on page 106):

- Heterocycles are tolerated: thiophenes **75d**, **75e**, **75a** and **75g**, and pyridines **75b** and **75c** are active (binding mode B).
- Positioning of heteroatom important: *meta* substitution of **75b** binds more strongly than *ortho*-substituted **75c** (binding mode A & B).
- Aromatic group must not be substituted: **85a-i** are not active (binding mode B).
- Free NH at 4-position is crucial: methylated **75i** is not active (neither binding mode).
- Correct distance to the core scaffold: longer linker of **75j** abolishes activity (binding mode B).
- Substitution in the *meta* position of ring 7 negatively affects affinity: complete loss of activity in **75h** and **75k**, strong reduction in **75e** and **75g** (neither binding mode).
- Substitution in the *para* position of ring 7 is tolerated well in general: methylated **75a** is just as active as unsubstituted **75d** (binding mode A & B).
- Substitution in the *para* position of ring 7 with electron-donating or sterically more demanding groups causes a loss of activity: methoxy group in **75l** is not active in contrast to the unsubstituted **75b**, while the small electron-withdrawing fluoro group of **75c** restored affinity compared to **75m** (neither binding mode).

Although many findings seem to point towards binding mode B, the activity of **86a** can only be explained by binding mode A, so the actual binding mode still remains uncertain.

3.9 Future Work

In order to identify the actual binding mode of the pyrrolo[2,3-*d*]pyrimidines, additional experiments are necessary. By employing saturation transfer difference (STD) NMR spectroscopy, protein-bound ligands are measured with off-resonance irradiation. Ligand protons that are in contact with the protein receive a stronger enhancement than those exposed to the solvent. Therefore, STD NMR experiments can be used to determine which parts are interacting with the protein.^{189,190} Ultimately, crystallisation of the novel scaffolds would provide the best structural information on the binding mode. As a consequence, a screen covering a wide range of buffer systems and conditions should be carried out to establish a working crystallisation protocol for full-length Akt.

Due to the limited commercial availability of suitable pyrrolo[2,3-*d*]pyrimidines that fit well into the Akt inter-domain pocket, more sophisticated compounds based on the SAR determined in this thesis should be synthesised.

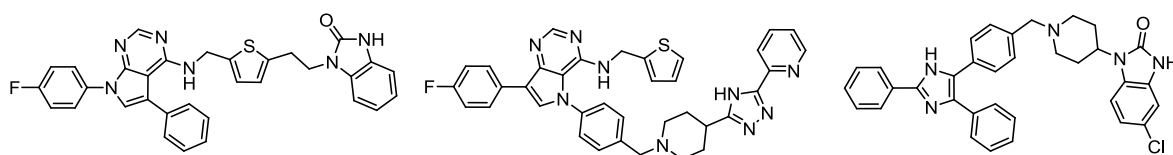


Figure 82 A few exemplary structures proposed for future pyrrolopyrimidine- and imidazole-based inhibitors.

Although the iFLiK assay was able to reliably identify novel Akt inhibitors from the Waldmann library screen, these hits are far from potent with their micromolar affinities. The main limitation to finding novel scaffolds is the chemical space covered in a compound library. With the encouraging results from screening the RL and Waldmann libraries, the HTS of much larger libraries can be approached, which should hopefully provide a more diverse set of hit structures.

For a more pronounced sensitivity of conformational changes, other labelling positions on both the PH and the kinase domain can be tested. Furthermore, previous work in the group has shown that the labelling position can decisively determine whether conformational changes can be detected by fluorophore sensors. The difference might be as much as one amino acid as have been demonstrated before.¹⁹¹ Even today, after analysing the successful and unsuccessful labelling positions in FLiK, FLiP and iFLiK experiments, there is no rationale that can guide the search for the optimal labelling position. Further mutagenesis studies with the FLiK, FLiP and iFLiK technology can help in understanding the factors that determine the conformational sensitivity.

Various publications and the screens in this thesis have demonstrated that the choice of compounds that can be investigated can be strongly limited by intrinsic compound fluorescence.¹⁸² However, fluorophores with long-wavelength excitations are nearly inevitably associated with low solvatochromism, attributable to their structure which predicates on an extensively conjugated π -electron system. In order to increase their sensitivity towards changes in their environment, their excitation dipole moment has to be increased. Therefore, more sensitive fluorophores have to be developed that can be used as cysteine-reactive sensors. A reactive variant of the solvatochromic anthradan could be such a solution, as it shows high sensitivity to polarity (emission maxima ranging from 490 nm to 610 nm in various solvents) and an excitation maximum of around 470 nm.¹⁹²

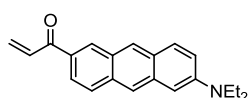


Figure 83 Proposed structure of an anthradan-derived solvatochromic fluorophore

4 Experimental

4.1 General Experimental

If not noted otherwise, all buffers were formulated with Milli-Q grade purified water.

For visualisation of protein structures, PyMol version 1.5.0.4 by Schrödinger was used. Data management was handled with Pipeline Pilot version 6.1 by Accelrys.

4.1.1 Instruments

Microtiter plate reader	Tecan Infinite M1000
NanoTemper	NanoTemper Monolith NT.115 G008
Biacore	Biacore T100
Centrifuges	Beckman Coulter Avanti J-25
	Beckman Coulter Avanti J-26
	Beckman Coulter JA-10
	Beckman Coulter JLA 8.1
	Eppendorf Centrifuge 5415 D
	Heraeus Multifuge 3 S-R
Gel electrophoresis	Bio-Rad Mini-PROTEAN 3 Cell
Incubator shaker	New Brunswick Scientific Innova 4430
Photometer	Eppendorf Biophotometer
FPLC	ÄKTA Purifier
Preparative HPLC	Agilent 1200 series

4.1.2 Materials and Consumables

Crystallisation plates	Qiagen EasyXtal 24-well
384-well plate	Greiner Bio One 384 Well Small Volume HiBase Polystyrene
	Greiner Bio One 384 Well Polystyrene Microplates solid bottom

Pipette tips	Starlab TipOne system
Desalting Columns	Thermo Scientific Protein Desalting Spin Columns 7 kDa
Insect cell medium	Invitrogen Gibco Sf-900 III SFM
Biacore chips	Biacore CM5 Biacore NTA
HPLC columns	Macherey-Nagel Nucleodur C18 Gravity 5 µm 21/125 Macherey-Nagel VP50/21
FPLC columns	GE Healthcare Superdex HiLoad 200 16/600 pg GE Healthcare Superdex 75 10/300 GL

4.2 Protein Production

4.2.1 Expression

construct de92:

Human Akt1 (residues 1-480) containing the mutations E49C, C296S, C310S and C344S was codon-usage optimised for insect cell expression and synthesised synthetically (Genart AG). The amino acid and nucleotide sequence are shown below with artificial mutation sites underlined and coloured blue.

Mutated amino acid sequence (artificial mutations are marked blue and underlined):

```
MSDVAIVKEG WLHKRGEYIK TWRPRYFLLK NDGTFIGYKE RPQDVDQRCA
PLNDFSVAQC QLMKTERPRP NTFIIRCLQW TTVIERTFHV ETPEEREEWT
TAIQTVADGL KKQEEEEEMDF RSGSPSDNSG AEEMEVSLAK PKHRVTMNEF
EYLKLLGKGT FGKVILVKEK ATGRYYAMKI LKKEVIVAKD EVAHTLTENR
VLQNSRHPFL TALKYSFQTH DRLCFVMEYA NGGELFFHLS RERVFSEDRA
RFYGAEIVSA LDYLHSEKNV VYRDLKLENL MLDKDGHIKI TDFGLSKEGI
KDGATMKTFS GTPEYLAPEV LEDNDYGRAV DWWGLGVVMY EMMSGRLPFY
NQDHEKLFEL ILMEEIRFPR TLGPEAKSLL SGLLKKDPKQ RLGGGSEDAK
EIMQHRFFAG IVWQHVEYKK LSPPFKPQVT SETDTRYFDE EFTAQMIIITIT
PPDQDDSMEC VDSERRPHFP QFSYSASGTA
```

Mutated nucleotide sequence:

```
1 atgagcgacg tggctattgt gaaggagggt tggctgcaca aacgagggga gtacatcaag
```

```

61 acctggcggc cacgctactt cctcctcaag aatgatggca cttcattgg ctacaaggag
121 cggccgcagg atgtggacca acgttgcgct cccctcaaca acttctctgt ggcgcagtgc
181 cagctgatga agacggagcg gccccggccc aacaccttca tcatccgctg cctgcagtgg
241 accactgtca tcgaacgcac cttccatgtg gagactcctg aggagcggga ggagtggaca
301 accgccatcc agactgtggc tgacggcctc aagaagcagg aggaggagga gatggacttc
361 cggtcgggct caccagtgca caactcaggg gctgaagaga tggaggtgtc cctggccaag
421 cccaagcacc gcgtagccat gaacgagttt gactacctga agctgctggg caagggcact
481 ttcggcaagg tgatcctggt gaaggagaag gccacaggcc gctactacgc catgaagatc
541 ctcaagaagg aagtcatcgt ggccaaggac gaggtggccc acacactcac cgagaaccgc
601 gtccctgcaga actccaggca ccccttcctc acagccctga agtactcttt ccagaccac
661 gaccgcctct gctttgtcat ggagtacgcc aacggggggcg agctgttctt ccacctgtcc
721 cgggagcgtg tgttctccga ggaccgggcc cgcttctatg gcgctgagat tgtgtcagcc
781 ctggactacc tgcactcgga gaagaacgtg gtgtaccggg acctcaagct ggagaacctc
841 atgctggaca aggacgggca cattaagatc acagacttgc ggctgagcaa ggaggggatc
901 aaggacggtg ccacatgaa gacctttagc ggcacacctg agtacctggc ccccgaggtg
961 ctggaggaca atgactacgg ccgtgcagtg gactgggtggg ggctgggctg ggtcatgtac
1021 gagatgatgaa_gcggtcgcct gcccttctac aaccaggacc atgagaagct ttttgagctc
1081 atccctcatgg aggagatccg cttcccgcgc acgcttggtc ccgaggccaa gtccttgctt
1141 tcagggctgc tcaagaagga cccaagcag aggcttggcg ggggctccga ggacgccaa
1201 gagatcatgc agcatcgctt ctttgccggt atcgtgtggc agcacgtgta cgagaagaag
1261 ctacagccac ctttcaagcc ccaggtcacg tcggagactg acaccaggta ttttgatgag
1321 gagtacacgg ccagatgat caccatcaca ccacctgacc aagatgacag catggagtgc
1381 gtggacacgc agcgcaggcc ccaactcccc cagttctcct actcggccag cggcacggcc
1441 tga

```

construct pHT1023:

Human Akt1 (residues 1-480) containing the mutations E49C, C296S, C310S, C344S and C460S was codon-usage optimised for insect cell expression and synthesised synthetically (Geneart AG). The amino acid and nucleotide sequence are shown below with artificial mutation sites underlined.

Mutated amino acid sequence (artificial mutations are marked blue and underlined):

```

MSDVAIVKEG WLHKRGEYIK TWRPRYFLK NDGTFIGYKE RPQDVDQRCA
PLNNFSVAQC QLMKTERPRP NTFIIRCLQW TTVIERTFHV ETPEEREWEW
TAIQTVADGL KKQEEEEEMDF RSGSPSDNSG AEEMEVSLAK PKHRVTMNEF
EYLKLLGKGT FGKVILVKEK ATGRYYAMKI LKKEVIVAKD EVAHTLTENR
VLQNSRHPFL TALKYSFQTH DRLCFVMEYA NGGELFFHLS RERVFSEDRA
RFYGAEIVSA LDYLVHSEKNV VYRDLKLENL MLDKDGHKI TDFGLSKEGI
KDGATMKTFS GTPEYLAPEV LEDNDYGRAV DWWGLGVVMY EMMSGRLPFY
NQDHEKLFEL ILMEEIRFPR TLGPEAKSL SGLLKKDPKQ RLGGGSEDAK

```

EIMQHRFFAG IVWQHVEYK LSPPFKPQVT SETDTRYFDE EFTAQMITIT
PPDQDDSMES VDSERRPHFP QFSYSASGTA

Mutated nucleotide sequence:

1 atgagcgacg tggctattgt gaaggagggt tggctgcaca aacgagggga gtacatcaag
61 acctggcggc cacgctactt cctcctcaag aatgatggca ccttcattgg ctacaaggag
121 cggccgcagg atgtggacca acgttgcgct cccctcaaca acttctctgt ggcgcagtgc
181 cagctgatga agacggagcg gccccggccc aacaccttca tcatccgctg cctgcagtgg
241 accactgtca tcgaacgcac cttccatgtg gagactcctg aggagcggga ggagtggaca
301 accgcatcc agactgtggc tgacggcctc aagaagcagg aggaggagga gatggacttc
361 cggtcgggct caccagtgca caactcaggg gctgaagaga tggaggtgtc cctggccaag
421 cccaagcacc gcgtgacat gaacgagttt gagtacctga agctgctggg caagggcact
481 ttggcaagg tgatcctggt gaaggagaag gccacaggcc gctactacgc catgaagatc
541 ctcaagaagg aagtcacgt ggccaaggac gaggtggccc acacactcac cgagaaccgc
601 gtcctgcaga actccaggca ccccttctc acagccctga agtactcttt ccagaccac
661 gaccgcctct gctttgtcat ggagtagcc aacgggggcg agctgttctt ccacctgtcc
721 cgggagcgtg tgttctccga ggaccggcc cgcttctatg gcgctgagat tgtgtcagcc
781 ctggactacc tgactcggga gaagaacgtg gtgtaccggg acctcaagct ggagaacctc
841 atgctggaca aggacgggca cattaagatc acagacttgc ggctgagcaa ggaggggatc
901 aaggacggtg ccacatgaa gacctttagc ggcacacctg agtacctggc ccccgaggtg
961 ctggaggaca atgactacgg ccgtgcagtg gactggtggg ggctgggctg ggtcatgtac
1021 gagatgatga a_gcggtcgct gcccttctac aaccaggacc atgagaagct ttttgagctc
1081 atcctcatgg aggagatccg cttcccgcgc acgcttggtc ccgaggccaa gtccttgctt
1141 tcagggtgc tcaagaagga cccaagcag aggcttggcg ggggctccga ggacgccaag
1201 gagatcatgc agcatcgctt ctttgccggt atcgtgtggc agcacgtgta cgagaagaag
1261 ctgagccac cttcaagcc ccaggtcacg tcggagactg acaccaggta ttttgatgag
1321 gagttcacgg ccagatgat caccatcaca ccacctgacc aagatgacag catggagagc
1381 gtggacagcg agcgcaggcc ccacttcccc cagttctcct actcggccag cggcacggcc
1441 tga

construct de91:

Human Akt1 (residues 1-446) containing the mutations E49C, C296S, C310S and C344S was codon-usage optimised for insect cell expression and synthesised synthetically (Genart AG). The amino acid and nucleotide sequence are shown below with artificial mutation sites underlined.

Mutated amino acid sequence (artificial mutations are marked blue and underlined):

MSDVAIVKEG WLHKRGEYIK TWRPRYFLLK NDGTFIGYKE RPQDVDQRCA
PLNDFSVAQC QLMKTERPRP NTFIIRCLQW TTVIERTFHV ETPEEREWEW
TAIQTVADGL KKQEEEEEMDF RSGSPDNSG AEEMEVSLAK PKHRVTMNEF
EYLKLLGKGT FGKVILVKEK ATGRYYAMKI LKKEVIVAKD EVAHTLTENR

VLQNSRHPFL TALKYSFQTH DRLCFVMEYA NGGELFFHLS RERVFSEDRA
RFYGAEIVSA LDYLVHSEKNV VYRDLKLENL MLDKDGHKI TDFGLSKEGI
KDGATMKTFS GTPEYLAPEV LEDNDYGRAV DWWGLGVVMY EMMSGRLPFY
NQDHEKLFEL ILMEEIRFPR TLGPEAKSL L SGLLKKDPKQ RLGGSSEDAK
EIMQHRFFAG IVWQHVEKK LSPPFKPQVT SETDTRYFDE EFTAQM

Mutated nucleotide sequence:

1 atgagcgacg tggctattgt gaaggagggt tggctgcaca aacgagggga gtacatcaag
61 acctggcggc cacgctactt cctcctcaag aatgatggca cttcattgg ctacaaggag
121 cggccgcagg atgtggacca acgttgcgct cccctcaaca acttctctgt ggcgcagtgc
181 cagctgatga agacggagcg gccccggccc aacacctca tcatccgctg cctgcagtgg
241 accactgtca tcgaacgcac cttccatgtg gagactcctg aggagcggga ggagtggaca
301 accgccatcc agactgtggc tgacggcctc aagaagcagg aggaggagga gatggacttc
361 cggtcgggct caccagtga caactcaggg gctgaagaga tggaggtgtc cctggccaag
421 cccaagcacc gcgtgaccat gaacgagttt gactacctga agctgctggg caagggcact
481 ttcggcaagg tgatcctggt gaaggagaag gccacaggcc gctactacgc catgaagatc
541 ctcaagaagg aagtcatcgt ggccaaggac gaggtggccc acacactcac cgagaaccgc
601 gtcctgcaga actccaggca ccccttctc acagccctga agtactcttt ccagaccac
661 gaccgcctct gctttgtcat ggagtacgcc aacgggggcg agctgttctt ccacctgtcc
721 cgggagcgtg tgttctccga ggaccgggcc cgcttctatg gcgctgagat tgtgtcagcc
781 ctggactacc tgcactcggga gaagaacgtg gtgtaccggg acctcaagct ggagaacctc
841 atgctggaca aggacgggca cattaagatc acagacttcg ggctgagcaa ggaggggatc
901 aaggacggtg ccaccatgaa gacctttagc ggcacacctg agtacctggc ccccgagggtg
961 ctggaggaca atgactacgg ccgtgcagtg gactggtggg ggctgggctg ggtcatgtac
1021 gagatgatgaa_gcggtcgcct gcccttctac aaccaggacc atgagaagct ttttgagctc
1081 atcctcatgg aggagatccg cttcccgcgc acgcttggtc ccgaggcaa gtccttgctt
1141 tcagggctgc tcaagaagga cccaagcag aggcttggcg ggggctccga ggacgccaag
1201 gagatcatgc agcatcgctt ctttgccggt atcgtgtggc agcacgtgta cgagaagaag
1261 ctacagccac cttcaagcc ccaggtcacg tcggagactg acaccaggta ttttgatgag
1321 gagttcacgg cccagatg

The gene retained a His₆-tag at the N-terminus followed by a TEV protease cleavage site. The Akt1 constructs were cloned into a pREN4427-HIS-DEST vector and introduced into a baculovirus with the BacMagic Kit (Calbiochem) in Sf21 cells (Invitrogen). The virus was amplified by infecting TriEx Sf9 cells (Millipore) at an MOI = 0.01 and incubating for 5 d at 28 °C in an incubator shaker.

The virus titer was determined with the BacPAK Baculovirus Rapid Titer Kit (Clontech) according to protocols: TriEx Sf9 cells (Millipore) were seeded at $6.5 \cdot 10^4$ cells/well into a sterile 96-well plate and incubated at 27 °C for 1 h. After aspirating the medium, 25 μ L of virus dilution series of each virus were added at final dilutions of 10^{-3} , 10^{-4} and 10^{-5} and

incubated for 1 h at RT. The inoculum was aspirated, and 50 μ L of the provided methyl cellulose overlay was added and incubated at 27 °C for 46 h. Afterwards, the cells were fixated with a 4% paraformaldehyde solution for 10 min at RT. The solution was removed and the wells washed 3x 5 min with 200 μ L PBS + 0.05% Tween-20. After pre-incubation with 50 μ L normal goat serum, 25 μ L diluted mouse anti-gp64 antibody was incubated at 37 °C for 25 min, washed 2x 5 min with 200 μ L PBS + 0.05% Tween-20. Subsequently, 50 μ L diluted goat anti-mouse/HRP conjugate were added, incubated at 37 °C for 25 min and washed 3x 5min with 200 μ L PBS + 0.05% Tween-20. The infection was visualised by addition of 50 μ L Blue Peroxidase substrate and developed for 10 min. Stained cells were counted to calculate the virus titer.

All Akt1 constructs were expressed in stably transfected *Spodoptera frugiperda* TriEx Sf9 cells (Millipore) at 28 °C. de92 (His₆-TEV-(2-480) E49C,C296S,C310S,C344S): MOI = 3 and incubation time = 48 h. pHT1023 (His₆-TEV-(2-480) E49C,C296S,C310S,C344S, C460S): MOI = 0.5 and incubation time = 72 h. de91 (His₆-TEV-(2-446) E49C,C296S, C310S,C344S): MOI = 0.3 and incubation time = 72 h. Cells were harvested by centrifugation with 2000 g at 4 °C for 10 min and removal of the medium.

4.2.2 Purification

Lysis buffer: 50 mM Tris, 500 mM NaCl, 10% v/v glycerol, 1 mM DTT, 5 mM MgCl₂, 0.1% Triton X-100, cOmplete EDTA-free Protease inhibitor cocktail, 10 U/L Benzoase, pH 8.0 at 4 °C.

Ni²⁺ affinity chromatography buffer: 50 mM Tris, 500 mM NaCl, 0-500 mM imidazole, 10% glycerol, 1 mM DTT, pH 8.0 at 4 °C.

Size exclusion buffer: 50 mM HEPES, 200 mM NaCl, 10% glycerol, 6 ppm Triton X-100, pH 7.3 at 4 °C.

Ni-NTA affinity chromatography

The His-tagged protein was enriched from the TriEx Sf9 cell lysate in lysis buffer on a 3 mL nickel-affinity column (Qiagen) at 1 mL/min and washed with 0 mM imidazole Ni-NTA buffer. The protein was eluted stepwise with 20 mM, 50 mM and 100 mM imidazole, then in a buffer gradient up to 500 mM imidazole.

Size exclusion chromatography

The protein was further purified on a Superdex HiLoad 200 16/600 pg column (GE Healthcare) using the size exclusion buffer and concentrated to approximately 50 μ M. All

purification steps were performed at 4 °C, and the final protein was flash frozen in liquid nitrogen and stored at -80 °C.

4.3 Biochemical Assays

4.3.1 KinEASE

Akt1 wt

Kinase buffer: 50 mM HEPES, 5 mM MgCl₂, 0.1 mM Na₃VO₄, 0.02% (w/v) NaN₃, 0.01% (w/v) BSA, 1 mM DTT, 0.01% Triton X-100, pH 7.0.

Start solution: 1 μM STK substrate 3, 200 μM ATP, 50 mM HEPES, 5 mM MgCl₂, 0.1 mM Na₃VO₄, 0.02% (w/v) NaN₃, 0.01% (w/v) BSA, 1 mM DTT, 0.01% Triton X-100, pH 7.0.

Stop solution: 50 mM HEPES, 0.1% (w/v) BSA, 800 mM KF, 20 mM EDTA, 31.25 nM XL665, diluted STK antibody, pH 7.0.

An inhibitor dilution series was created by diluting an 8% DMSO inhibitor solution in kinase buffer into 8% DMSO in kinase buffer. 2.5 μL of each inhibitor dilution were added in duplicates into 5 μL of a 240 pM kinase solution (Akt1 wt from Millipore, Lot # D8MN034U-L) in a 384-well plate and pre-incubated in a dark wet chamber for 1 h at RT. To start the reaction, 2.5 μL of the start solution were added to each well and incubated in a dark wet chamber for 45 min at RT. To stop the reaction, 10 μL of the stop solution were added to each well and incubated in a dark wet chamber for 1 h at RT. Each well was excited at 317 nm and emission was measured at 620 nm and 665 nm with a 60 μs delay. The fl₆₆₅/fl₆₂₀ ratio was used as assay readout.

Akt2 wt

Kinase buffer: 50 mM HEPES, 5 mM MgCl₂, 0.1 mM Na₃VO₄, 0.02% (w/v) NaN₃, 0.01% (w/v) BSA, 1 mM DTT, 0.01% Triton X-100, pH 7.0.

Start solution: 1.2 μM STK substrate 3, 260 μM ATP, 50 mM HEPES, 5 mM MgCl₂, 0.1 mM Na₃VO₄, 0.02% (w/v) NaN₃, 0.01% (w/v) BSA, 1 mM DTT, 0.01% Triton X-100, pH 7.0.

Stop solution: 50 mM HEPES, 0.1% (w/v) BSA, 800 mM KF, 20 mM EDTA, 37.5 nM XL665, diluted STK antibody, pH 7.0.

An inhibitor dilution series was created by diluting an 8% DMSO inhibitor solution in kinase buffer into 8% DMSO in kinase buffer. 2.5 μL of each inhibitor dilution were added in duplicates into 5 μL of a 1.02 nM kinase solution (Akt2 wt from Invitrogen, Lot # PV3184_28770N) in a 384-well plate and pre-incubated in a dark wet chamber for 1 h at RT. To start the reaction, 2.5 μL of the start solution were added to each well and incubated in a

dark wet chamber for 17 min at RT. To stop the reaction, 10 μ L of the stop solution were added to each well and incubated in a dark wet chamber for 1 h at RT. Each well was excited at 317 nm and emission was measured at 620 nm and 665 nm with a 60 μ s delay. The f_{665}/f_{620} ratio was used as assay readout.

Δ PH-Akt1

Kinase buffer: 50 mM HEPES, 5 mM $MgCl_2$, 0.1 mM Na_3VO_4 , 0.02% (w/v) NaN_3 , 0.01% (w/v) BSA, 1 mM DTT, 0.01% Triton X-100, pH 7.0.

Start solution: 1.2 μ M STK substrate 3, 260 μ M ATP, 50 mM HEPES, 5 mM $MgCl_2$, 0.1 mM Na_3VO_4 , 0.02% (w/v) NaN_3 , 0.01% (w/v) BSA, 1 mM DTT, 0.01% Triton X-100, pH 7.0.

Stop solution: 50 mM HEPES, 0.1% (w/v) BSA, 800 mM KF, 20 mM EDTA, 37.5 nM XL665, diluted STK antibody, pH 7.0.

An inhibitor dilution series was created by diluting an 8% DMSO inhibitor solution in kinase buffer into 8% DMSO in kinase buffer. 2.5 μ L of each inhibitor dilution were added in duplicates into 5 μ L of a 120 pM kinase solution (Δ PH-Akt1 wt from Millipore, Lot # 1600485-E) in a 384-well plate and pre-incubated in a dark wet chamber for 1 h at RT. To start the reaction, 2.5 μ L of the start solution were added to each well and incubated in a dark wet chamber for 20 min at RT. To stop the reaction, 10 μ L of the stop solution were added to each well and incubated in a dark wet chamber for 1 h at RT. Each well was excited at 317 nm and emission was measured at 620 nm and 665 nm with a 60 μ s delay. The f_{665}/f_{620} ratio was used as assay readout.

4.3.2 iFLiK

Labelling

Labelling buffer: 50 mM HEPES, 200 mM NaCl, 10% glycerol, pH 7.3 @ 4 $^{\circ}$ C.

The protein was dissolved in labelling buffer to a resulting concentration of 2 mg/mL. 0.9 equivalents of 10 mM PyMPO in DMF were dissolved in an equal volume of labelling buffer. Both solutions were mixed and incubated in the dark at 4 $^{\circ}$ C over night. The labelled protein was purified by concentrating and passing over a gel filtration column (Superdex 75 10/300 GL by GE Healthcare). The purified protein was shock-frozen in liquid nitrogen and stored at -80 $^{\circ}$ C.

Optimisation

All experiments for the assay optimisation were either determined with end-point measurements (according to “Z’-factors and signal-to-noise ratios”) or with dose-dependency (according to “Measuring K_d ”) in variations of the parameter to be investigated.

Z’-factors and signal-to-noise ratios

iFLiK buffer: 50 mM HEPES, 200 mM NaCl, 0.01% Triton-X 100, pH 7.4.

If not noted otherwise, 200 nM of the PyMPO labelled protein was incubated with 5 μ M MK-2206 and DMSO, each in hexuplicates. After 2 h incubation, each well was excited at 419 nm and 440 nm, and emission was measured at 638 nm and 508 nm. Background-corrected intensity ratios f_{638}/f_{508} nm was used as assay readout.

Primary screen

iFLiK buffer: 50 mM HEPES, 200 mM NaCl, 0.01% Triton-X 100, pH 7.4.

0.5 μ L of each inhibitor were added at 21x final concentration into 10 μ L of a 200 nM labelled protein solution in a 384-well plate and into 10 μ L of buffer as background correction. After shaking at 1500 rpm for 30 s, all solutions were incubated in a dark wet chamber for 2 h at RT. Each well was excited at 419 nm and 440 nm, and emission was measured at 638 nm and 508 nm. Background-corrected intensity ratio f_{638}/f_{508} nm was used as assay readout, with a cutoff of 25% of maximum binding of MK-2206 as positive control.

Measuring K_d

iFLiK buffer: 50 mM HEPES, 200 mM NaCl, 0.01% Triton-X 100, pH 7.4.

An inhibitor dilution series was created by diluting an DMSO inhibitor solution into wet DMSO. 0.5 μ L of each inhibitor dilution was added in triplicates into 10 μ L of a 200 nM labelled protein solution in a 384-well plate and into 10 μ L of buffer in quadruplicates as background correction. After shaking at 1500 rpm for 30 s, all solutions were incubated in a dark wet chamber for 2 h at RT. Each well was excited at 419 nm and emission was measured at 638 nm and 508 nm. Each background data point was averaged for subtraction, and background-corrected intensity ratios f_{638}/f_{508} nm were used as assay readout.

4.3.3 NanoTemper

Labelling

Labelling buffer: 50 mM HEPES, 200 mM NaCl, 10% glycerol, pH 8.3 @ 4 °C.

Storage buffer: 50 mM HEPES, 200 mM NaCl, 10% glycerol, pH 7.3 @ 4 °C.

The protein was dissolved in labelling buffer to a resulting concentration of 40 μM . 3 equivalents of 10 mM Alexa Fluor 568 maleimide in DMF were added, mixed and incubated in the dark at 4 $^{\circ}\text{C}$ for 1 h. The labelled protein was purified over a gel filtration column (Superdex 75 10/300 GL by GE Healthcare) into the storage buffer, shock-frozen with liquid nitrogen and stored at -80 $^{\circ}\text{C}$.

Measuring K_d

NanoTemper buffer: 50 mM HEPES, 200 mM NaCl, 0.05% Tween-20, pH 7.4.

An inhibitor dilution series were created by diluting an DMSO inhibitor solution into wet DMSO. 0.5 μL of each inhibitor dilution was added into 10 μL of a 100 nM labelled protein solution in a 384-well plate. All solutions were incubated for 2 h at RT. The solutions were transferred into enhanced gradient standard treated NanoTemper capillaries and analysed using green excitation and emission filters. Excite capillaries at 25 $^{\circ}\text{C}$ with 90% LED power for 5 s, track thermophoresis for 45 s at 100% laser intensity, track back-diffusion for 5 s. Fluorescence intensities were measured at 8-9 s and 49-50 s, and intensity ratios of hot/cold were used as assay readout.

4.3.4 Biacore

Biacore buffer: 50 mM Tris, 200 mM NaCl, 5 mM MgCl_2 , 0.05% Tween-20, 2% DMSO, pH 7.5.

Washing solution was passed at 10 $\mu\text{L}/\text{min}$. Solvent correction was calculated using 1.4%, 1.6%, 1.8%, 2.0%, 2.2%, 2.4%, 2.6% and 2.8% DMSO in Biacore buffer and extrapolated with the evaluation software to 5000 RU. Each assay cycle consisted of the following steps: The NTA chip was conditioned with a 500 μM NiCl_2 solution at 10 $\mu\text{L}/\text{min}$ for 45 s and stabilised for 20 s. A 20 $\mu\text{g}/\text{mL}$ protein solution in Biacore buffer was passed over the chip at 10 $\mu\text{L}/\text{min}$ for 2 min for immobilisation. After stabilising the signal for 1 min, the ligand solution was passed at 10 $\mu\text{L}/\text{min}$ for a contact time of 2 min and dissociation time of 4 min with Biacore buffer, followed by 30 s stabilisation. The chip surface was regenerated with 350 mM EDTA for 45 s and a 3 min stabilisation period. All steps except the NiCl_2 immobilisation were conducted in parallel and used as background subtraction. Kinetic fits were conducted with the evaluation software and single site kinetics, or with a steady state affinity model.

4.3.5 Tryptic Digest

Dialysis buffer: 40 mM Tris, 200 mM NaCl, pH 8.

Reaction buffer: 50 mM NH_4HCO_3 , pH 8.

DTT stock: 200 mM DTT, 100 mM NH₄HCO₃, pH 8.

IAA stock: 1 M iodoacetamide, 100 mM NH₄HCO₃, pH 8.

Separately, unlabelled and labelled de92 (1.5 nmol) were dialysed in dialysis buffer, desalted with Pierce columns and lyophilised. After resuspension in 100 µL reaction buffer, the disulphide bridges were reduced by incubating with 5 µL of DTT stock for 10 min at 95 °C. Free thiol groups were capped with 4 µL of IAA stock at RT for 1 h in the dark and subsequently quenched with 20 µL DTT stock. Both samples were incubated with proteomics grade trypsin (60 pmol by Sigma) overnight at 37 °C, frozen in liquid nitrogen and lyophilised. The lyophilised powder was then resuspended in 40 µL of a water:MeCN 1:1 + 0.2% formic acid solution for analysis *via* MS.

4.3.6 Mass Spectrometry

5 µL of the digested sample was injected onto an Atlantis dC 18 HPLC column (Waters, column dimensions: 2.1x150 mm, 3 µm particle size). The separations were carried out using a series 1100 HPLC-system (Agilent, system consisting of binary pump, thermostated autosampler, and diode array detector) coupled on-line to a LTQ XL linear ion trap (Thermo Electron Corporation) using the standard electrospray ionisation source. For the HPLC separation a flow rate of 200 µL/min and a linear gradient starting with 100% solvent A / 0% solvent B for 5 min and increasing to 40% solvent A / 60% solvent B in 55 min was used, followed by a linear gradient increasing to 20% Solvent A / 80% solvent B in 10 min. After that the column was washed with 20% solvent A / 80% solvent B for 5 min and re-equilibrated to starting conditions for additional 10 min (solvent A: water containing 0.1% formic acid, solvent B: acetonitril containing 0.1% formic acid). For mass spectrometric detection the electrospray ionisation was carried out in positive ionisation mode using a source voltage of 4.5 kV. The capillary voltage was set to 46 V, the capillary temperature to 275 °C, and the tube lens voltage to 160 V. Spectra were acquired in triple play mode. First a full mass spectrum with a mass-to-charge range from 200 to 2000 was acquired, followed by a zoom scan of the most intense ion with a minimum signal intensity of 10 000 and a MS/MS spectrum using collision induced fragmentation for all at least doubly charged ions. For CID fragmentation the isolation width was set to 2 and the normalised collision energy to 35%. The AGC target was set to 30000 for full scan spectra, to 1000 for zoom scans, and to 10000 for MS/MS spectra. After performing one MS/MS spectrum the parent mass was set onto an exclusion list for 180 s.

4.4 Cellular Experiments

NCI-H441 and BT-474 were provided from the American Type Culture Collection (ATCC). Both cell lines were maintained in RPMI-1640 Medium with L-Glutamine (PAA) supplemented with 10% fetal calf serum (PAA) and 1% penicillin-streptomycin (Gibco) in a humidified incubator with 5% CO₂ at 37 °C. Inhibitors were dissolved in DMSO at a stock concentration of 10 mM and stored at -20 °C. Compound treatment was carried out using serial dilutions 16 hours after plating. The viability was assessed in 96-well plates starting from 3000 cells/well. 96 hours after compound treatment, the cellular ATP content was determined (CellTiter.Glo, Promega). Luminiscence was measured with an Infinite200 Pro microplate reader (Tecan). All experiments were performed in triplicates at 3 independent time points.

4.5 Protein Crystallisation

Constructs de91 and de92 were transferred into the storage buffer (25 mM Tris, 100 mM NaCl, 10% glycerol, 5 mM DTT, pH 7.5) *via* gel filtration chromatography and concentrated to approximately 10 mg/mL. Crystals were grown by the vapor diffusion method. Both constructs were adjusted to 4.7 mg/mL and incubated with both MK-2206 and ZF176 at 250 µM. Hanging drops were set up in the presence of 50% precipitant, consisting of 12.5 mM NaOAc, 37.5 mM sodium citrate, 21% PEG 2000, pH 5.2 at 20 °C. Pictures were taken on an Olympus DT21 with a Plan 4x/0.10 air lens.

4.6 Molecular Docking

Molecular docking experiments were conducted with the Maestro software version 9.1.207 and Glide version 5.6 by Schrödinger. The crystal structure of the full length Akt1 co-crystallised with Akti-1/2 (PDB code 3O96) was used as template for molecular docking. After pre-processing by adding hydrogens, correcting bond lengths and angles, severing bonds to metal atoms and removing water molecules with the protein preparation wizard, a binding pocket of a volume of 20 Å around the original ligand was calculated without any constraints for the receptor grid with Glide, allowing for full rotation of tyrosine, threonine and serine residues. Conformers of the ligands were generated with ConfGen Standard using the OPLS_2005 force field. Tautomers and protonation states at pH 5-9 were calculated with Epik. The thusly prepared ligands were docked flexibly with Glide at a van der Waals radius cutoff of 0.8 and partial charge cutoff 0.15 with standard precision. 50 poses per ligand were

calculated after post-docking minimisation and 10 poses retained for final results. Scoring was computed according to GlideScore, nonplanar conformations were penalised.

4.7 Compound Synthesis

Commercially available solvents and reagents were obtained from Sigma-Aldrich, Alfa Aesar, ABCR Chemicals, Acros Organics, Maxbridge, Fluka, Riedel-de H en, Lancaster or Carl Roth and used without further purification unless noted otherwise. Brine refers to a saturated NaCl solution in water. For ultrasonic treatment of suspensions, a VWR Ultrasonic Cleaner was employed.

¹H-NMR and ¹³C-NMR spectra were recorded at ambient temperature on a Bruker DRX-400 operating at 400 MHz, Bruker DRX-500 operating at 500 MHz, Bruker DRX-600 operating at 600 MHz and Varian Mercury 400 operating at 400 MHz, with tetramethylsilane as an internal standard. Chemical shifts (δ) are expressed in ppm, referenced to an internal tetramethyl silane standard for ¹H-NMR and relative to solvent for ¹³C-NMR. Abbreviations for NMR data: s = singlet; d = doublet; t = triplet; q = quartet; sept = septet; m = multiplet; br s = broad signal. *J* values are given in Hz. NMR raw data were evaluated with MestreNova 6.0.5604 by Mestrelab.

ESI-MS spectra were recorded on a LTQ XL linear ion trap (Thermo Electron Corporation), high resolution ESI-MS spectra were recorded on a LTQ Orbitrap by Thermo Electron. Detected ion masses (*m/z*) are expressed in Th.

Analytical thin layer chromatography (TLC) was performed using commercially available aluminium backed plates coated with Merck Kieselgel 60 F₂₅₄ 0.20 mm (ALUGRAM® sil G/UV₂₅₄) and visualised under ultra-violet light at 254 nm, or by staining with iodine, potassium permanganate, vanillin, ninhydrin or cerium molybdate solution. If not noted otherwise, varying mixtures of ethyl acetate and PE or methanol and dichloromethane were used as eluents. Flash column chromatography was carried out using J. T. Baker silica gel (particle size: 0.040-0.060 mm).

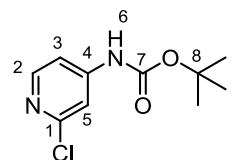
4.7.1 *tert*-Butyl 2-chloropyridin-4-ylcarbamate (55)

2-Chloropyridin-4-amine (409.0 mg, 3.181 mmol), Et₃N (884 μ L, 6.362 mmol) and DMAP (116.6 mg, 0.9543 mmol) were dissolved in 25 mL DCM and degassed for 20 min with argon. Boc anhydride (416.6 mg, 1.909 mmol) were added to the reaction and stirred for 24 h at RT. The RM was quenched with 100 mL of a saturated aqueous NH₄Cl solution and extracted

with 3x50 mL EtOAc. The combined organic phases were washed with 50 mL saturated NaHCO₃ and brine, dried over MgSO₄, and evaporated to yield orange crystals. The crude product was purified by flash column chromatography (PE:EtOAc = 3:1) to afford a white solid (241.7 mg, 0.946 mmol, 49.8%).

LR-MS [M+H]⁺ = calculated 229.07, found 228.80 (-0.12%)

¹H-NMR (500 MHz, CDCl₃): δ = 8.21 (1H, d, *J* = 6, H-2), 7.52 (1H, s, H-5), 7.19 (1H, d, *J* = 6, H-3), 6.97 (1H, br s, H-6), 1.54 (9H, s, H-9) ppm.



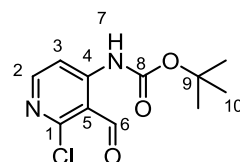
¹³C-NMR (125 MHz, CDCl₃): δ = 152.84 (C-4), 151.95 (C-7), 150.31 (C-2), 148.18 (C-1), 112.48 (C-5), 111.71 (C-3), 82.62 (C-8), 28.55 (C-9) ppm.

4.7.2 *tert*-Butyl 2-chloro-3-formylpyridin-4-ylcarbamate (56)

The following steps were carried out in an argon atmosphere: A solution of *tert*-butyl 2-chloropyridin-4-ylcarbamate (203.7 mg, 0.891 mmol) was dissolved in 10 mL of dry THF, cooled to -78 °C and degassed. A 1.7 M solution of *tert*-butyl lithium in pentane (1.5 mL, 2.55 mmol) was added dropwise. The reaction was stirred for two hours before dry DMF (0.25 mL, 3.25 mmol) was added. The reaction was allowed to slowly warm to room temperature over a 12 h period. The reaction mixture was quenched with 6 mL of a 3 M HCl solution and extracted with 3x20 mL Et₂O. The combined ether layers were washed with saturated NaHCO₃ and brine, dried over MgSO₄, filtered and evaporated under reduced pressure. The resulting orange solid was purified with flash column chromatography (PE:EtOAc = 5:1), affording a white solid (123.1 mg, 0.480 mmol, 53.8%).

LR-MS [M+H]⁺ = calculated 256.06, found 256.72 (+0.26%)

¹H-NMR (400 MHz, CDCl₃): δ = 11.00 (1H, br s, H-7), 11.52 (1H, d, *J* = 1, H-6), 8.38 (1H, dd, *J* = 6 and 1, H-3), 8.31 (1H, dd, *J* = 6 and 1, H-2), 1.54 (9H, s, H-10) ppm.



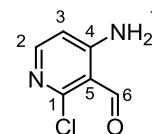
¹³C-NMR (100 MHz, CDCl₃): δ = 194.32 (C-6), 156.7 (C-1), 154.01 (C-2), 151.92 (C-4), 151.03 (C-8), 113.24 (C-5), 112.43 (C-3), 82.94 (C-9), 28.30 (C-10) ppm.

4.7.3 2-Chloro-3-formylpyridin-4-amine (57)

tert-Butyl 2-chloro-3-formylpyridin-4-ylcarbamate (51.0 mg, 0.199 mmol) was dissolved in 5 mL of a dioxanic HCl solution and stirred for 4 h at RT. The RM was evaporated under reduced pressure and dried in *vacuo*, affording an offset white solid in quantitative yields.

LR-MS $[M+H]^+$ = calculated 157.02, found 157.02 (+0.00%)

$^1\text{H-NMR}$ (400 MHz, MeOD): δ = 10.39 (1H, d, J = 1, H-6), 7.82 (1H, d, J = 6, H-2), 6.68 (1H, dd, J = 6 and 1, H-3) ppm.



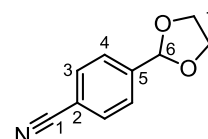
4.7.4 4-(1,3-Dioxolan-2-yl)benzonitrile (59)

4-Cyanobenzaldehyde (131.2 mg, 1 mmol), ethylene glycol (248.3 mg, 4 mmol) and catalytic amounts of tosylic acid were dissolved in toluene and refluxed for 8 h with a fitted Dean Stark. The RM was cooled to RT, washed with 2x20 mL saturated NaHCO_3 solution and 20 mL brine. The combined aqueous layers were extracted with 2x20 mL EtOAc. The combined organic layers were evaporated *in vacuo*. The solid residue was triturated in *n*-hexane, yielding 700 mg of a white solid.

LR-MS $[M+H]^+$ = calculated 176.07, not ionisable

$^1\text{H-NMR}$ (400 MHz, CDCl_3): δ = 7.69 (2H, d, J = 8, H-3), 7.60 (2H, d, J = 8, H-4), 5.86 (1H, s, H-6), 4.14-4.05 (4H, m, H-7) ppm.

$^{13}\text{C-NMR}$ (100 MHz, CDCl_3): δ = 143.48 (C-5), 132.62 (C-3), 127.58 (C-4), 119.01 (C-1), 113.27 (C-2), 102.83 (C-6), 65.85 (C-7) ppm.



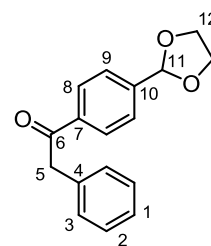
4.7.5 1-(4-(1,3-Dioxolan-2-yl)phenyl)-2-phenylethanone (60)

4-(1,3-Dioxolan-2-yl)benzonitrile (787.6 mg, 4.496 mmol) was dissolved in anhydrous THF (25 mL), cooled down to 0 °C and degassed with argon. A 2 M solution of benzyl magnesium chloride (8.0 mL, 16.0 mmol) was added slowly. After 1 h the mixture was warmed to room temperature and stirred for 4 h. The RM was quenched with saturated NH_4Cl and extracted with 3x30 mL EtOAc. The combined organic layers were dried over MgSO_4 , filtered and concentrated. The resulting yellow oil was purified by flash column chromatography (5:1 EtOAc:PE), affording a yellow solid (1.102 g, 4.107 mmol, 91.4%).

LR-MS $[M+H]^+$ = calculated 269.12, found 269.05 (-0.03%)

$^1\text{H-NMR}$ (400 MHz, CDCl_3): δ = 8.02 (2H, d, J = 8, H-9), 7.56 (2H, d, J = 9, H-3), 7.31 (2H, dd, J = 9 and 5, H-2), 7.28-7.22 (3H, m, H-1, H-8), 5.84 (1H, s, H-11), 4.28 (2H, s, H-5), 4.16-3.98 (4H, m, H-12) ppm.

$^{13}\text{C-NMR}$ (100 MHz, CDCl_3): δ = 197.69 (C-6), 143.35 (C-10), 137.50 (C-4), 134.79 (C-7), 129.83 (C-3), 129.16 (C-2), 129.10 (C-8), 127.33 (C-1), 127.12 (C-6), 103.31 (C-11), 65.81 (C-12), 46.06 (C-5) ppm.

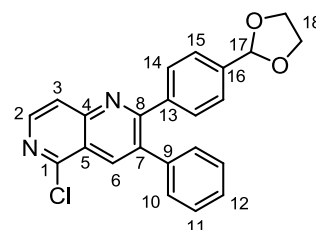


4.7.6 2-(4-(1,3-Dioxolan-2-yl)phenyl)-5-chloro-3-phenyl-1,6-naphthyridine (61)

2-Chloro-3-formylpyridin-4-aminium chloride (93.5 mg, 0.484 mmol), 1-(4-(1,3-dioxolan-2-yl)phenyl)-2-phenylethanone (131.1 mg, 0.489 mmol), sodium *tert*-butoxide (117.3 mg, 1.221 mmol) were dissolved in 20 mL dry dioxane. The reaction vessel was filled with an argon atmosphere and fitted with a drying tube, and the RM and stirred for 3 h at RT. The RM was evaporated under reduced pressure. The resulting yellow solid was washed with saturated NaHCO_3 solution, water and Et_2O , and dried azeotropically with toluene, affording a slightly yellow solid (29.4 mg, 0.076 mmol, 15.6%).

LR-MS $[\text{M}+\text{H}]^+$ = calculated 389.11, found 389.15 (+0.01%)

$^1\text{H-NMR}$ (400 MHz, CDCl_3): δ = 8.58 (1H, s, H-6), 8.51 (1H, d, J = 6, H-2), 7.93 (1H, d, J = 6, H-3), 7.50 (2H, d, J = 8, H-15), 7.42 (2H, d, J = 8, H-14), 7.38-7.31 (3H, m, H-4, H-12), 7.31-7.24 (2H, m, H-11), 5.82 (1H, s, H-17), 4.18-3.95 (4H, m, H-18) ppm.



$^{13}\text{C-NMR}$ (100 MHz, CDCl_3): δ = 151.17 (C-8), 145.55 (C-2), 140.11 (C-1), 139.04 (C-9), 138.91 (C-7), 137.47 (C-4), 136.29 (C-6), 135.44 (C-16), 135.34 (C-13), 130.32 (C-15), 129.85 (C-11), 128.87 (C-10), 128.23 (C-12), 126.52 (C-14), 122.45 (C-3), 122.06 (C-5), 103.52 (C-17), 65.48 (C-18) ppm.

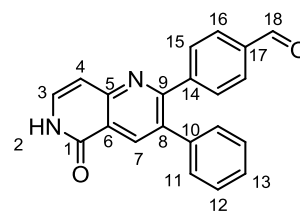
4.7.7 4-(5-Oxo-3-phenyl-5,6-dihydro-1,6-naphthyridin-2-yl)benzaldehyde (62)

2-(4-(1,3-Dioxolan-2-yl)phenyl)-5-chloro-3-phenyl-1,6-naphthyridine (15.97 mg, 0.041 mmol) and 3 mL conc. hydrochloric acid were mixed and stirred at 90 °C for 3 h. The RM was frozen in liquid nitrogen and lyophilised.

LR-MS $[\text{M}+\text{H}]^+$ = calculated 327.12, found 327.17 (+0.02%)

HR-MS $[\text{M}+\text{H}]^+$ = calculated 327.11280, found 327.11290 (+0.28940 ppm)

¹H-NMR (400 MHz, CDCl₃): δ = 10.03 (1H, s, H-18), 9.10 (1H, s, H-7), 9.00 (1H, br s, H-2), 8.20 (1H, d, *J* = 5, H-3), 7.83 (2H, d, *J* = 8, H-15), 7.65 (2H, d, *J* = 8, H-16), 7.56 (1H, d, *J* = 5, H-4), 7.40-7.31 (3H, m, H-11, H-13), 7.31-7.26 (2H, m, H-12) ppm.



¹³C-NMR (100 MHz, *d*₆-DMSO): δ = 193.48 (C-18), 162.56 (C-1), 160.72 (C-5), 153.57 (C-7), 145.83 (C-9), 139.07 (C-8), 137.75 (C-17), 136.27 (C-3), 134.60 (C-10), 134.46 (C-14), 131.18 (C-16), 130.14 (C-12), 129.61 (C-15), 129.22 (C-11), 128.35 (C-13), 121.40 (C-6), 106.43 (C-4) ppm.

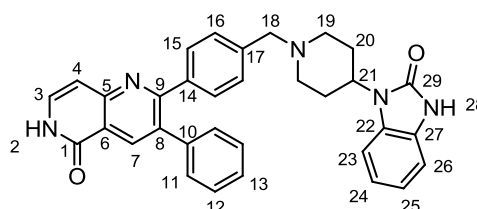
4.7.8 2-(4-((4-(2-Oxo-2,3-dihydro-1*H*-benzo[*d*]imidazol-1-yl)piperidin-1-yl)methyl)-phenyl)-3-phenyl-1,6-naphthyridin-5(6*H*)-one (63a)

4-(5-Hydroxy-3-phenyl-1,6-naphthyridin-2-yl)benzaldehyde (482 mg, 1.3 mmol) and 1-(piperidin-4-yl)-1*H*-benzo[*d*]imidazol-2(3*H*)-one (201.2 mg, 0.926 mmol) were dissolved in 30 mL dry MeOH and stirred for 4 h at 75 °C. Then NaBH₃CN (63.2 mg, 0.972 mmol) was added at RT and reacted over night. The reaction mixture was evaporated under reduced pressure. The residue was purified by preparative HPLC (H₂O/MeCN + 5 mM NH₄OAc), affording a yellow solid (14.5 mg, 0.028 mmol, 2.2%).

LR-MS [M+H]⁺ = calculated 528.24, found 528.18 (-0.01%)

HR-MS [M+H]⁺ = calculated 528.23940, found 528.23958 (+0.34695 ppm)

¹H-NMR (400 MHz, CDCl₃): δ = 8.40 (1H, s, H-2), 7.51 (1H, d, *J* = 5, H-3), 7.46-7.40 (2H, m, H-7, H-28), 7.38-7.32 (5H, m, H-11, H-13, H-16), 7.29-7.23 (5H, m, H-15, H-12, H-26), 7.00-6.96 (3H, m,



H-23, H-24, H-25), 6.70 (1H, d, *J* = 5, H-4), 4.20-4.10 (1H, m, H-21), 3.53 (2H, s, H-18), 2.93 (2H, d, *J* = 10, H-19), 2.42-2.31 (2H, m, H-20), 2.14-2.06 (2H, m, H-19), 1.64 (2H, d, *J* = 11, H-20) ppm.

¹³C-NMR (100 MHz, CDCl₃): δ = 162.88 (C-1), 162.05 (C-5), 154.57 (C-29), 153.76 (C-9), 139.87 (C-10), 139.77 (C-8), 138.97 (C-17), 137.64 (C-7), 134.56 (C-14), 134.40 (C-3), 130.50 (C-16), 130.22 (C-12), 130.02 (C-22), 129.28 (C-11), 129.05 (C-15), 128.32 (C-13), 129.16 (C-23), 127.40 (C-27), 121.23 (C-25), 121.06 (C-6), 109.67 (C-24), 109.56 (C-26), 106.77 (C-4), 62.31 (C-18), 53.42 (C-19), 50.97 (C-21), 29.51 (C-20) ppm.

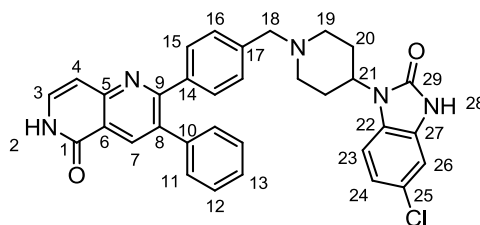
4.7.9 2-(4-((4-(5-Chloro-2-oxo-2,3-dihydro-1H-benzo[d]imidazol-1-yl)piperidin-1-yl)-methyl)phenyl)-3-phenyl-1,6-naphthyridin-5(6H)-one (63b)

4-(5-Hydroxy-3-phenyl-1,6-naphthyridin-2-yl)benzaldehyde hydrochloride (14.03 mg, 0.039 mmol) and 4-chloro-1-(piperidin-4-yl)-1H-benzo[d]imidazol-2(3H)-one (213.95 mg, 0.850 mmol) were dissolved in 10 mL dry MeOH and stirred for 4 h at 75 °C. Then NaBH₃CN (55 mg, 0.85 mmol) was added at RT and reacted over night. The reaction mixture was evaporated under reduced pressure. The residue was purified by preparative HPLC (H₂O/MeCN + 5 mM NH₄OAc), affording a yellow powder (5.5 mg, 0.010 mmol, 26%).

LR-MS [M+H]⁺ = calculated 562.20, found 562.14 (-0.01%)

HR-MS [M+H]⁺ = calculated 562.20043, found 562.19992 (-0.90344 ppm), calculated 564.19748, found 564.19707 (-0.72365 ppm)

¹H-NMR (500 MHz, *d*₆-DMSO): δ = 8.40 (1H, s, H-7), 7.51 (1H, d, *J* = 7 Hz, H-3), 7.36-7.31 (5H, m, H-11, H-13, H-16), 7.28-7.23 (5H, m, H-12, H-15, H-26), 7.03-7.01 (2H, m, H-23, H-24), 6.69 (1H, d, *J* = 7 Hz, H-4), 3.53 (2H, s, H-18), 2.92 (2H, d,



J = 11 Hz, H-19), 2.38-2.27 (2H, m, H-20), 2.09 (2H, t, *J* = 11 Hz, H-19), 1.65 (2H, dd, *J* = 12 and 2 Hz, H-20) ppm.

¹³C-NMR (125 MHz, *d*₆-DMSO): δ = 162.87 (C-1), 162.04 (C-5), 154.61 (C-29), 153.78 (C-9), 139.89 (C-10), 139.78 (C-8), 138.99 (C-17), 137.66 (C-7), 134.55 (C-3), 134.44 (C-14), 130.55 (C-22), 130.52 (C-16), 130.46 (C-27), 130.23 (C-12), 129.29 (C-11), 129.04 (C-15), 128.32 (C-13), 125.55 (C-25), 121.08 (C-24), 120.83 (C-6), 110.67 (C-26), 109.55 (C-23), 106.74 (C-4), 62.30 (C-18), 53.37 (C-19), 51.19 (C-21), 29.46 (C-20) ppm.

4.7.10 2-(4-((3,4-Dihydroisoquinolin-2(1H)-yl)methyl)phenyl)-3-phenyl-1,6-naphthyridin-5(6H)-one (63c)

4-(5-Hydroxy-3-phenyl-1,6-naphthyridin-2-yl)benzaldehyde hydrochloride (14.03 mg, 0.039 mmol) and 1,2,3,4-tetrahydroisoquinoline (88 μL, 0.7 mmol) were dissolved in 10 mL dry MeOH and stirred for 4 h at 75 °C. Then NaBH₃CN (45.4 mg, 0.7 mmol) was added at RT and reacted over night. The reaction mixture was evaporated under reduced pressure. The residue was purified by preparative HPLC (H₂O/MeCN + 5 mM NH₄OAc), affording a yellow powder (0.9 mg, 0.002 mmol, 5%).

LR-MS $[M+H]^+$ = calculated 444.20, found 444.02 (-0.04%)

HR-MS $[M+H]^+$ = calculated 444.20704, found 444.20647 (-1.28506 ppm)

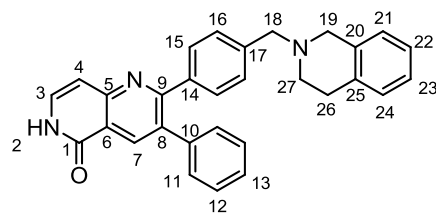
$^1\text{H-NMR}$ (500 MHz, d_6 -DMSO): δ = 8.40 (1H, s, H-7),

7.50 (1H, d, J = 7 Hz, H-3), 7.36-7.32 (5H, m, H-11,

H-13, H-16), 7.30-7.24 (5H, m, H-12, H-15, H-21), 7.11-

7.08 (2H, m, H-24, H-23), 7.01-6.99 (1H, m, H-22), 6.70

(1H, d, J = 6 Hz, H-4), 3.65 (2H, s, H-18), 3.52 (2H, s, H-19), 2.82 (2H, s, H-26), 2.67 (2H, s, H-27) ppm.



$^{13}\text{C-NMR}$ (125 MHz, d_6 -DMSO): δ = 162.42 (C-1), 161.60 (C-5), 153.33 (C-9), 139.22 (C-10), 138.63 (C-8), 137.38 (C-7), 135.10 (C-17), 134.52 (C-25), 133.85 (C-20), 130.56 (C-16), 130.24 (C-12), 129.31 (C-24), 129.26 (C-15), 129.04 (C-11), 128.57 (C-14), 128.30 (C-13), 127.17 (C-21), 126.83 (C-23), 126.33 (C-22), 134.08 (C-3), 120.61 (C-6), 106.39 (C-4), 61.97 (C-18), 55.94 (C-19), 50.72 (C-27), 29.13 (C-26) ppm.

4.7.11 Methyl 1-(4-(5-oxo-3-phenyl-5,6-dihydro-1,6-naphthyridin-2-yl)benzyl)piperidine-4-carboxylate (63d)

4-(5-Hydroxy-3-phenyl-1,6-naphthyridin-2-yl)benzaldehyde hydrochloride (14.03 mg, 0.039 mmol) and methyl piperidine-4-carboxylate (94.6 μL , 0.7 mmol) were dissolved in 10 mL dry MeOH and stirred for 4 h at 75 $^\circ\text{C}$. Then NaBH_3CN (45.4 mg, 0.7 mmol) was added at RT and reacted over night. The reaction mixture was evaporated under reduced pressure. The residue was purified by preparative HPLC ($\text{H}_2\text{O}/\text{MeCN}$ + 5 mM NH_4OAc), affording a yellow powder (4.1 mg, 0.009 mmol, 23%).

LR-MS $[M+H]^+$ = calculated 454.21, found 454.06 (-0.03%)

HR-MS $[M+H]^+$ = calculated 454.21252, found 454.21183 (-1.52357 ppm)

$^1\text{H-NMR}$ (600 MHz, d_6 -DMSO): δ = 8.38 (1H, d, J = 1,

H-7), 7.50 (1H, d, J = 7, H-3), 7.34-7.29 (5H, m, H-11,

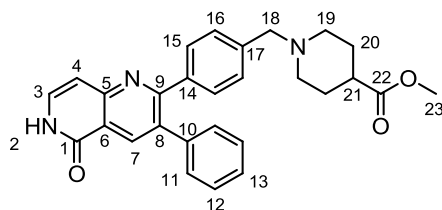
H-13, H-16), 7.25-7.22 (2H, m, H-12), 7.20 (2H, d,

J = 8, H-15), 6.68 (1H, dd, J = 7 and 1, H-4), 3.59 (2H,

s, H-23), 3.43 (2H, s, H-18), 3.22 (1H, s, H-23), 2.71 (2H, dt, J = 11 and 4, H-19), 2.30 (1H,

tt, J = 11 and 4, H-21), 1.97 (2H, dt, J = 11 and 2, H-19), 1.78 (2H, dd, J = 13 and 3, H-20),

1.55 (2H, ddd, J = 15, 12 and 4, H-20) ppm.



¹³C-NMR (150 MHz, *d*₆-DMSO): δ = 175.50 (C-22), 162.67 (C-1), 161.84 (C-5), 153.59 (C-9), 139.70 (C-10), 139.48 (C-8), 138.76 (C-17), 137.44 (C-7), 134.35 (C-3), 134.24 (C-14), 130.28 (C-16), 130.03 (C-12), 129.07 (C-15), 128.85 (C-13), 128.11 (C-11), 120.90 (C-6), 106.53 (C-4), 62.48 (C-18), 52.84 (C-19), 52.05 (C-23), 40.61 (C-21), 28.66 (C-20) ppm.

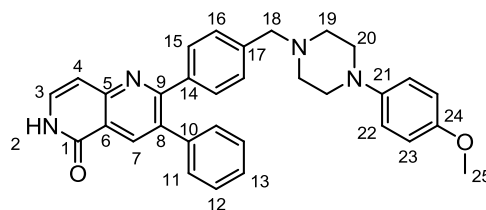
4.7.12 2-(4-((4-(4-Methoxyphenyl)piperazin-1-yl)methyl)phenyl)-3-phenyl-1,6-naphthyridin-5(6*H*)-one (63e)

4-(5-Hydroxy-3-phenyl-1,6-naphthyridin-2-yl)benzaldehyde hydrochloride (14.03 mg, 0.039 mmol) and 1-(4-methoxyphenyl)piperazine (139.62 mg, 0.726 mmol) were dissolved in 10 mL dry MeOH and stirred for 4 h at 75 °C. Then NaBH₃CN (45.4 mg, 0.7 mmol) was added at RT and reacted over night. The reaction mixture was evaporated under reduced pressure. The residue was purified by preparative HPLC (H₂O/MeCN + 5 mM NH₄OAc), affording a yellow powder (0.9 mg, 0.002 mmol, 5%).

LR-MS [M+H]⁺ = calculated 503.24, found 503.09 (-0.03%)

HR-MS [M+H]⁺ = calculated 503.24415, found 503.24320 (-1.88644 ppm)

¹H-NMR (500 MHz, *d*₆-DMSO): δ = 8.40 (1H, s, H-7), 7.51 (2H, d, *J* = 7 Hz, H-3), 7.38-7.31 (5H, m, H-11, H-13, H-16), 7.28-7.23 (4H, m, H-12, H-15), 6.88 (2H, d, *J* = 9 Hz, H-22), 6.81 (2H, d, *J* = 9 Hz,



H-23), 6.70 (2H, d, *J* = 7 Hz, H-4), 3.68 (3H, s, H-25), 3.52 (2H, s, H-18), 3.01 (4H, br s, H-20), 2.49 (4H, br s, H-19) ppm.

¹³C-NMR (125 MHz, *d*₆-DMSO): δ = 162.86 (C-1), 153.74 (C-5), 153.60 (C-24), 146.31 (C-21), 141.52 (C-9), 139.39 (C-10), 139.34 (C-8), 139.31 (C-17), 137.25 (C-7), 134.00 (C-3), 130.16 (C-16), 129.93 (C-12), 129.27 (C-14), 129.18 (C-6), 128.94 (C-15), 128.90 (C-11), 128.04 (C-13), 106.27 (C-4), 61.85 (C-18), 55.63 (C-25), 53.07 (C-19), 50.00 (C-20) ppm.

4.7.13 3-Phenyl-2-(4-((4-(pyrimidin-2-yl)piperazin-1-yl)methyl)phenyl)-1,6-naphthyridin-5(6*H*)-one (63f)

4-(5-Oxo-3-phenyl-5,6-dihydro-1,6-naphthyridin-2-yl)benzaldehyde hydrochloride (14.03 mg, 0.039 mmol) and 2-(piperazin-1-yl)pyrimidine (107.4 μL, 0.7 mmol) were dissolved in 5 mL dry MeOH and stirred for 4 h at 75 °C. Then NaBH₃CN (45.4 mg,

0.7 mmol) was added at RT and reacted over night. The reaction mixture was evaporated under reduced pressure. The residue was purified by preparative HPLC (H₂O/MeCN + 5 mM NH₄OAc), affording a yellow powder (2 mg, 0.004 mmol, 10%).

LR-MS [M+H]⁺ = calculated 475.22, found 475.09 (-0.03%)

HR-MS [M+H]⁺ = calculated 475.22409, found 475.22335 (-1.55503 ppm)

¹H-NMR (500 MHz, *d*₆-DMSO): δ = 8.40 (1H, s, H-7),

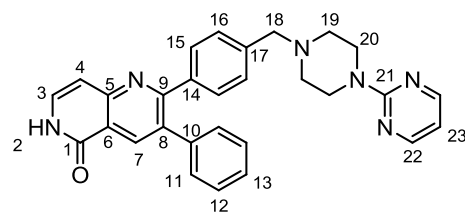
8.35 (2H, d, *J* = 5 Hz, H-22), 7.51 (1H, d, *J* = 7 Hz,

H-3), 7.36-7.31 (5H, m, H-11, H-13, H-16), 7.28-7.24

(4H, m, H-12, H-15), 6.70 (1H, d, *J* = 7 Hz, H-4), 6.62

(1H, t, *J* = 5 Hz, H-23), 3.73 (4H, br s, H-20), 3.52 (2H, s, H-18), 2.41 (4H, br s, H-19) ppm.

¹³C-NMR (125 MHz, *d*₆-DMSO): δ = 162.84 (C-1), 162.02 (C-21), 158.75 (C-22), 153.76 (C-5), 151.09 (C-9), 139.84 (C-10), 139.24 (C-8), 139.07 (C-17), 137.63 (C-7), 134.56 (C-14), 134.38 (C-3), 130.51 (C-16), 130.23 (C-12), 129.27 (C-11), 129.21 (C-15), 128.31 (C-13), 121.09 (C-6), 110.93 (C-23), 106.75 (C-4), 62.47 (C-18), 53.20 (C-19), 44.13 (C-20) ppm.



4.7.14 3-Phenyl-2-(4-((4-(tetrahydrofuran-2-carbonyl)piperazin-1-yl)methyl)phenyl)-1,6-naphthyridin-5(6H)-one (63g)

4-(5-Hydroxy-3-phenyl-1,6-naphthyridin-2-yl)benzaldehyde hydrochloride (14.03 mg, 0.039 mmol) and piperazin-1-yl(tetrahydrofuran-2-yl)methanone (131.69 mg, 0.719 mmol) were dissolved in 10 mL dry MeOH and stirred for 4 h at 75 °C. Then NaBH₃CN (45.4 mg, 0.7 mmol) was added at RT and reacted over night. The reaction mixture was evaporated under reduced pressure. The residue was purified by preparative HPLC (H₂O/MeCN + 5 mM NH₄OAc), affording a yellow powder (0.8 mg, 0.002 mmol, 5%).

LR-MS [M+H]⁺ = calculated 495.24, found 495.09 (-0.03%)

HR-MS [M+H]⁺ = calculated 495.23907, found 495.23827 (-1.60462 ppm)

¹H-NMR (500 MHz, *d*₆-DMSO): δ = 8.39 (1H, s,

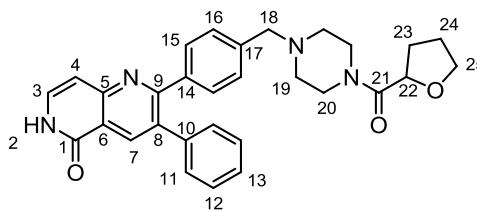
H-7), 7.50 (1H, d, *J* = 7 Hz, H-3), 7.34-7.31 (5H, m,

H-11, H-13, H-16), 7.26-7.22 (4H, m, H-12, H-15),

6.70 (1H, d, *J* = 7 Hz, H-4), 4.64 (1H, t, *J* = 6 Hz,

H-22), 3.79-3.70 (2H, m, H-25), 3.50 (2H, s, H-18), 3.49-3.46 (4H, m, H-20), 2.38-2.28 (4H,

m, H-19), 2.02-1.97 (2H, m, H-23), 1.84-1.79 (2H, m, H-24) ppm.



^{13}C -NMR (125 MHz, d_6 -DMSO): δ = 162.86 (C-1), 162.09 (C-21), 153.85 (C-5), 153.79 (C-9), 139.85 (C-10), 139.11 (C-8), 139.07 (C-17), 137.18 (C-7), 134.01 (C-3), 130.43 (C-14), 130.15 (C-16), 129.88 (C-12), 129.19 (C-6), 128.90 (C-13), 128.83 (C-11), 128.00 (C-15), 106.38 (C-4), 75.29 (C-22), 68.60 (C-25), 61.85 (C-18), 52.77 (C-19), 45.17 (C-29), 28.46 (C-23), 25.61 (C-24) ppm.

5 Appendix

5.1 Establishing the KinEASE Assay

The activity of a particular preparation batch determines the kinase concentration required for a stable and representative assay. To determine this value, the assay was performed at increasing kinase concentrations in duplicates and quenched after a incubation time of 30 min. The relative activity was determined from the f_{l665}/f_{l620} ratio and then plotted logarithmically against the kinase concentration as shown in Figure 84. The optimal kinase concentration would be as high as possible but still in the linear range. This was found to be 0.12 nM for Akt1, 0.51 nM for Akt2, and 0.06 nM for Δ PH-Akt1.

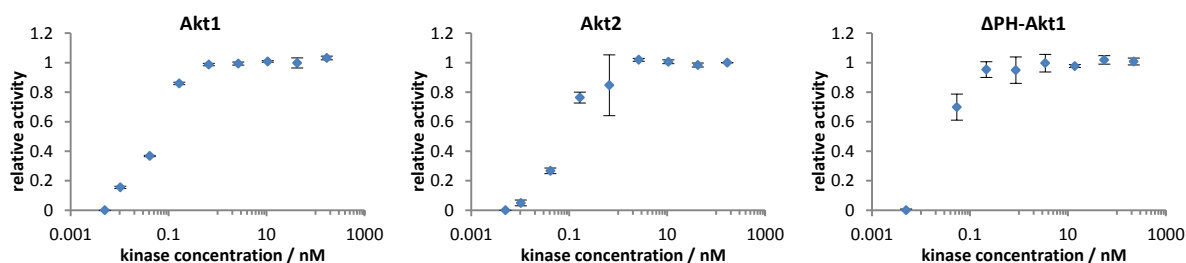


Figure 84 Determination of kinase activity for Akt1, Akt2 and Δ PH-Akt1. The relative activity is plotted logarithmically against the kinase concentration in the assay.

In the next step, the optimal incubation time for the assay had to be determined by starting the phosphorylation reaction with the addition of ATP and substrate, and quenching the reaction with EDTA at different incubation times. Again, Figure 85 shows the relative activity plotted against the incubation time. The optimal incubation times were determined to be 45 min for Akt1, 17 min for Akt2, and 20 min for Δ PH-Akt1.

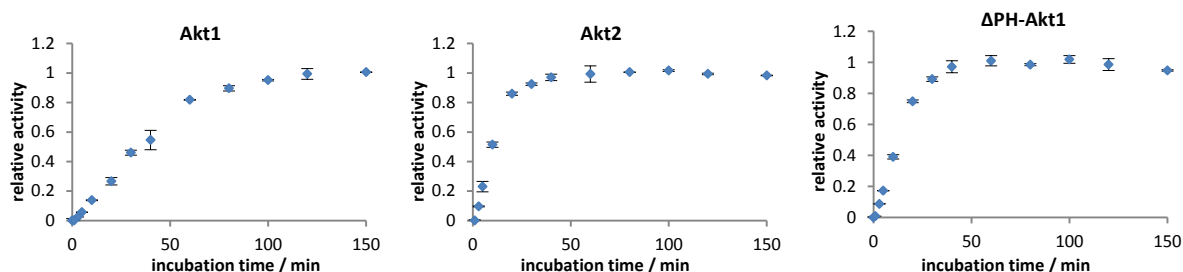


Figure 85 Determination of kinase phosphorylation kinetics for Akt1, Akt2 and Δ PH-Akt1. The relative activity is plotted against incubation time.

According to the Michaelis-Menten kinetics, an assay running with a reactant concentration far below the enzyme's K_m (i.e. $[R] \ll K_m$ with $[R]$ being the reactant concentration) is highly sensitive to fluctuations in its concentration.¹⁹³ In the case of ATP, however, a high concentration would compete with the binding of ATP-competitive inhibitors, thereby unnecessarily increasing the observed IC_{50} . In order to obtain comparable results across different assays, the convention for kinases is to operate at an ATP concentration of $ATP-K_m$, which represents a good compromise of the above mentioned considerations. To this end, the assay was run with saturating amounts of substrate and a dilution series of ATP. All results were determined in duplicates and repeated in three independent experiments

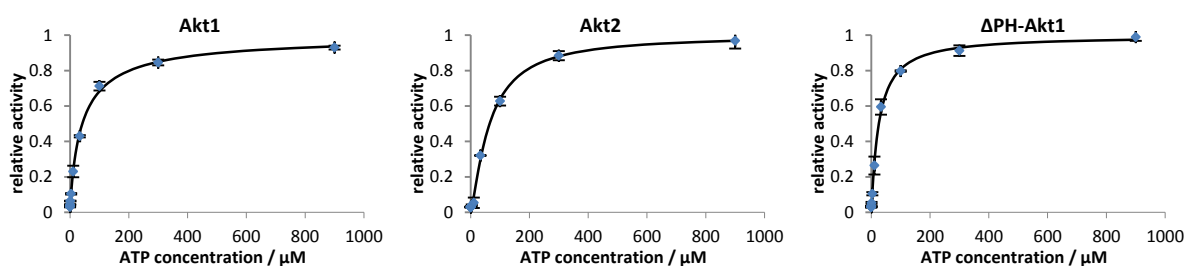


Figure 86 Michaelis-Menten curves of the phosphorylation reaction catalysed by Akt1, Akt2 and Δ PH-Akt1 in dependence of ATP. The relative activity is plotted against the ATP concentration, a representative curve was selected out of 3 independent experiments.

The same procedure was repeated for the artificial STK3 substrate peptide, which is able to be phosphorylated by all three kinases. In these experiments, saturating amounts of ATP were provided while measuring a dilution series of STK3 in duplicates. Since the substrate to fluorophore ratio needs to be kept at 8:1, the reactions were quenched with a dilution series of the stop solution as well. Here, too, three independent measurements were conducted for each kinase (Table 14). The experiments for Δ PH-Akt1 were executed by Patrik Wolle under my supervision.

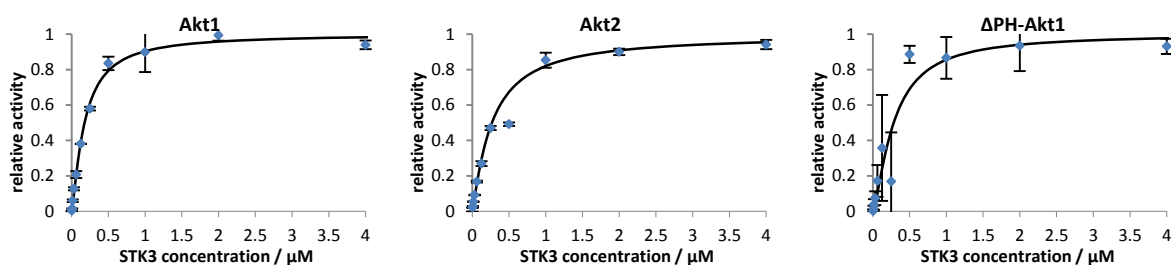


Figure 87 Michaelis-Menten curves of the phosphorylation reaction catalysed by Akt1, Akt2 and Δ PH-Akt1 in dependence of the artificial substrate peptide. The relative activity is plotted against the ATP concentration, a representative curve was selected out of 3 independent experiments.

The kinetic parameters were calculated according to the Michaelis-Menten model by fitting the experimental data using equation (13). The thusly determined and derived parameters are summarised in Table 14. No significant differences between the three constructs were found for the apparent K_m of ATP and STK3. There is no previously published data for the STK3- K_m , but the ATP- K_m matched with the literature results.¹⁹⁴ Unsurprisingly, the apparent turnover number k_{cat} of Δ PH-Akt1 was much higher than Akt1 and Akt2, as this constructs harboured the activating mutation S473D.

$$f(c) = \frac{V_{max} \cdot c^n}{c^n + K_m^n} \quad (13)$$

c = substrate concentration

V_{max} = maximum reaction velocity

K_m = Michaelis constant

n = slope factor

Table 14 Summary of the determined parameters in the Michaelis-Menten model.

		Akt1	Akt2	Δ PH-Akt1
ATP	$v_{max} / \text{nM s}^{-1}$	0.57 ± 0.05	1.60 ± 0.05	1.16 ± 0.02
	$K_m / \mu\text{M}$	43 ± 6	64 ± 6	28 ± 4
	k_{cat} / s^{-1}	4.8 ± 0.4	3.2 ± 0.1	20.8 ± 0.4
	$k_{cat}/K_m = \text{s}^{-1} \mu\text{M}^{-1}$	0.113 ± 0.018	0.050 ± 0.005	0.752 ± 0.097
STK3	$v_{max} / \text{nM s}^{-1}$	0.44 ± 0.02	1.16 ± 0.03	1.33 ± 0.08
	$K_m / \mu\text{M}$	0.15 ± 0.03	0.26 ± 0.03	0.30 ± 0.02
	k_{cat} / s^{-1}	3.7 ± 0.2	2.3 ± 0.1	24.0 ± 1.4
	$k_{cat}/K_m = \text{s}^{-1} \mu\text{M}^{-1}$	25 ± 5	11 ± 3	81 ± 8

5.2 Establishing the Biacore Assay

In a first attempt, the CM5 chip was used, which possesses a carboxymethylated dextran matrix on the gold surface for an irreversible, undirected immobilisation of the protein *via* its NH₂- and SH-groups. For optimal enrichment of the protein on the negatively charged surface, buffers at 3 different pHs below the pI of Akt were tested (3.5, 4.0 and 4.5). The refractogram in a pH scouting experiment (no addition of the coupling reagent EDC and hence no nucleophilic substitution on the carboxymethyl matrix) reports increasing levels of immobilisation with decreasing pH (Figure 88). However, the immobilised protein could not be removed by washing with a basic solution, indicating unspecific interactions with the surface due to aggregation. A test run was carried out by immobilising de92 at pH 4.5 onto the CM5 chip and passing increasing concentrations of MK-2206 over the thusly prepared chip produced highly irregular signals without dose dependency, confirming the denaturation of the kinase.

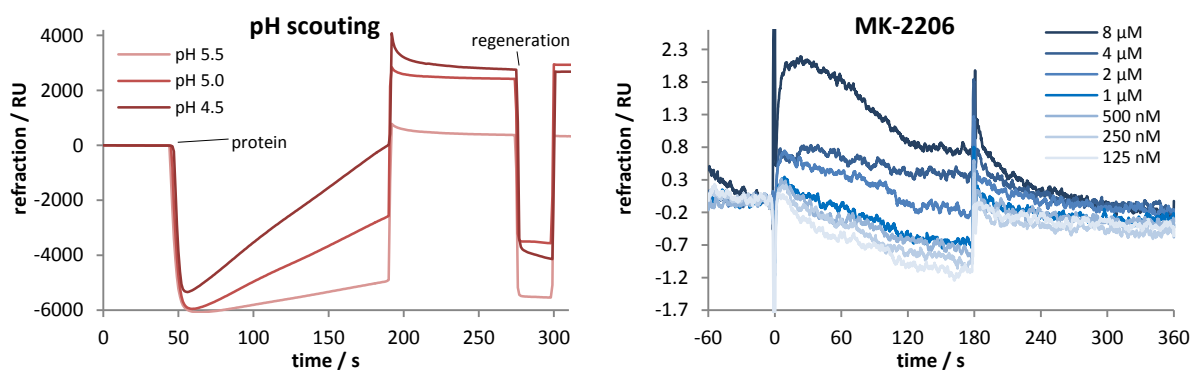


Figure 88 Left: Refractogram of Akt immobilisation onto a CM5 chip *via* pH scouting. Right: Refractogram of de92-immobilised CM5 chip with increasing concentrations of MK-2206.

To circumvent this problem, a reversible immobilisation on an NTA-modified carboxymethylated dextran matrix *via* the protein's His-Tag was chosen. After conditioning the NTA chip with NiCl₂, Akt could be successfully immobilised on the gold surface in the standard iFLiK buffer, producing an intensity increase of 676 RU. This immobilisation level could not be improved by increasing the pH from 7.4 to 8.0 to deprotonate the His-Tag. After immobilisation, it became obvious that the protein was not stably immobilised by the Ni²⁺ complexation, as the refraction signal continuously dropped within minutes. Attempts to measure MK-2206 by sequentially incubating with higher concentrations of the allosteric inhibitor failed, as protein levels continued to fall during each subsequent concentration step (Figure 89).

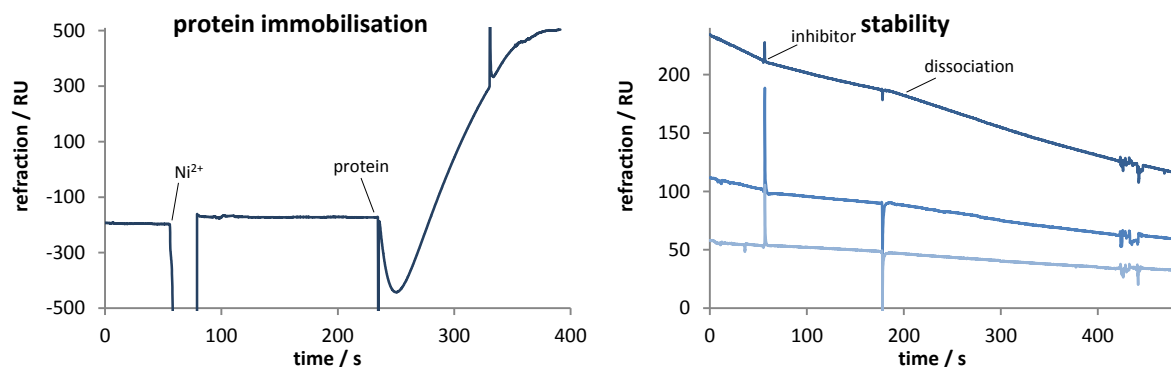


Figure 89 Refractogram of de92 protein immobilisation onto NTA chip *via* its His₆-tag after conditioning with NiCl₂ (left) and stability of immobilisation levels to repeated buffer injections (right).

In order to compensate this bleeding of Akt, each inhibitor concentration as well as several DMSO blanks were measured with a freshly immobilised protein carpet. If the enzyme was washed away at the same rate in each measurement, a background subtraction of the DMSO blank should provide stable baselines. However, the protein dissociation was not uniform in every step, so refraction signals produced by the binding of inhibitors was very instable. As the signal did not drop to starting levels after decomplexation of the protein and Ni²⁺ with imidazole and EDTA, it was suspected that some protein still remained on the NTA surface, preventing fresh protein from binding in the next step. Therefore, additional washing steps with GndCl, SDS and DMSO were included in the method to remove protein residues from the surface under these harsh conditions. However, these reagents had an even worse influence on the signal stability. Especially the surfactant SDS exhibited a remarkable persistency, corrupted the measurements and could only be removed from the system by washing for several hours. Studies by Nordin *et al.* have shown that Tris-based buffers produced more stable signals than HEPES, which was used in our experiments so far.¹⁹⁵ Indeed, when replacing HEPES with Tris, the Biacore assay produced slightly more consistent signals.

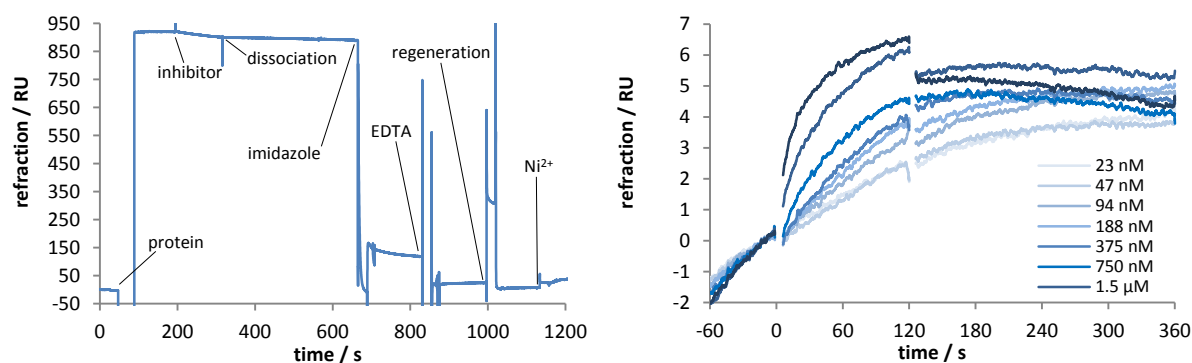


Figure 90 Left: Refractogram displaying the individual stages of each cycle with fresh immobilisation of de92 on NTA chips prior to applying the sample. Right: Dose-dependent increase of refraction changes upon treatment with Akt inhibitors.

5.3 NMR Spectra

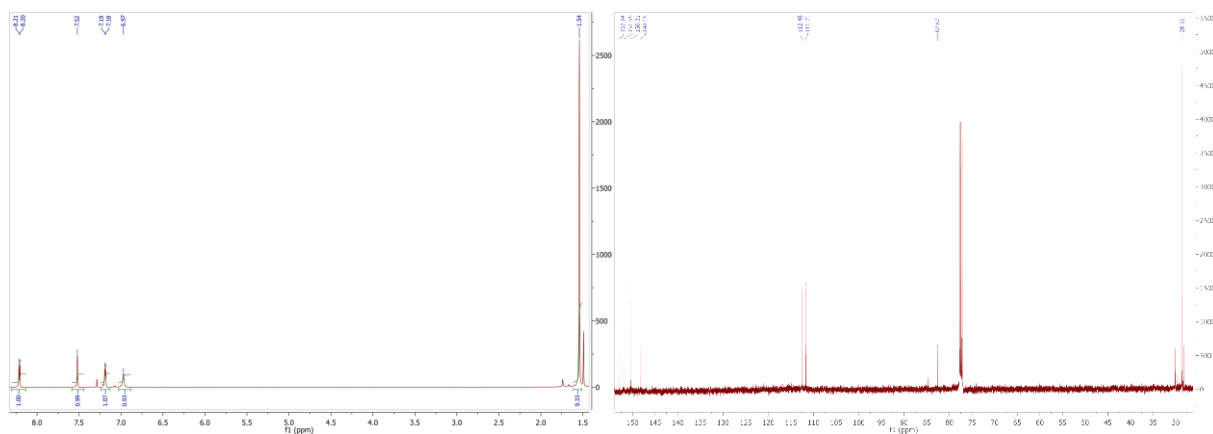


Figure 91 ^1H - (left) and ^{13}C -NMR spectra (right) of **55**.

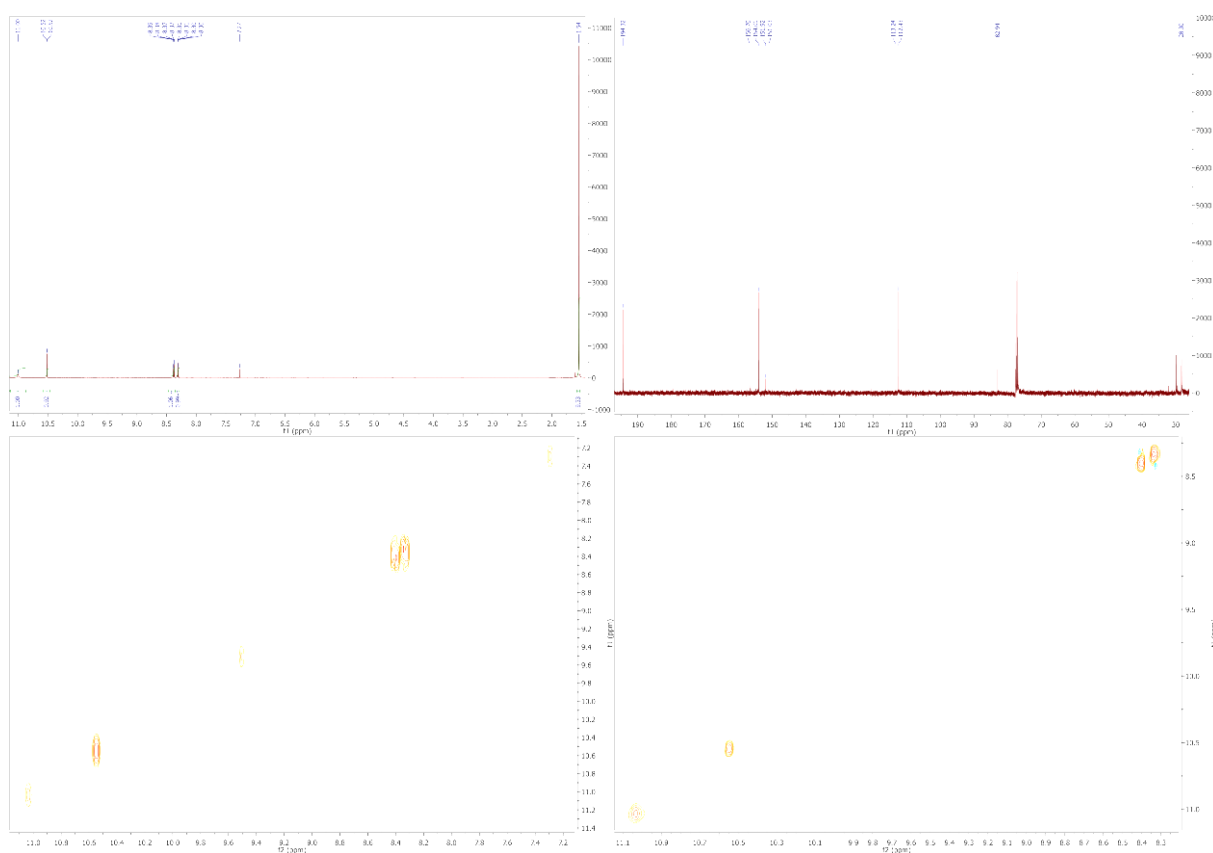


Figure 92 ^1H - (upper left), ^{13}C - (upper right), ^1H -COSY- (lower left) and ^1H -NOESY-NMR spectra (lower right) of **56**.

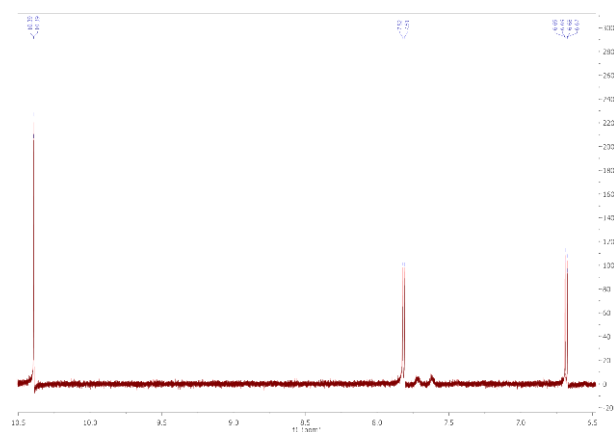


Figure 93 ^1H -NMR spectrum of **57**.

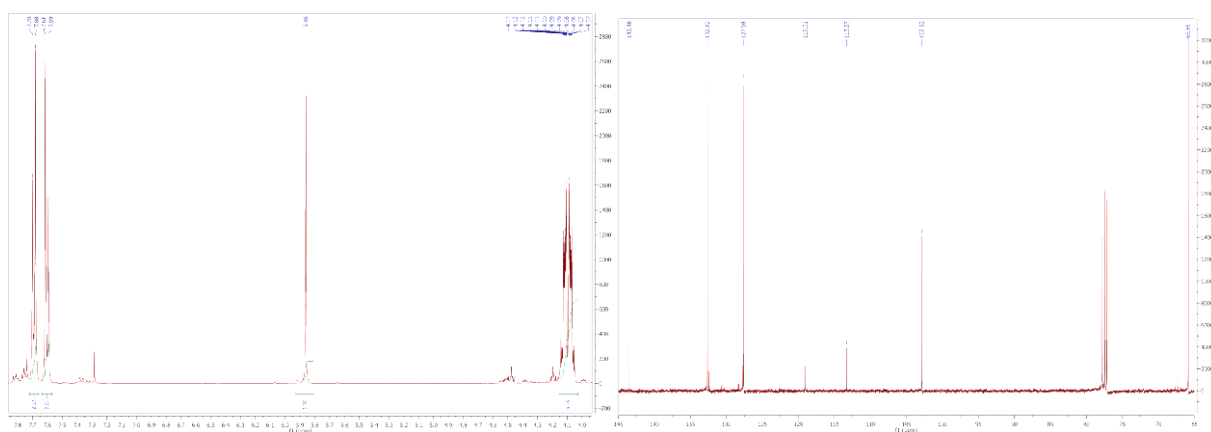


Figure 94 ^1H - (left) and ^{13}C -NMR spectra (right) of **59**.

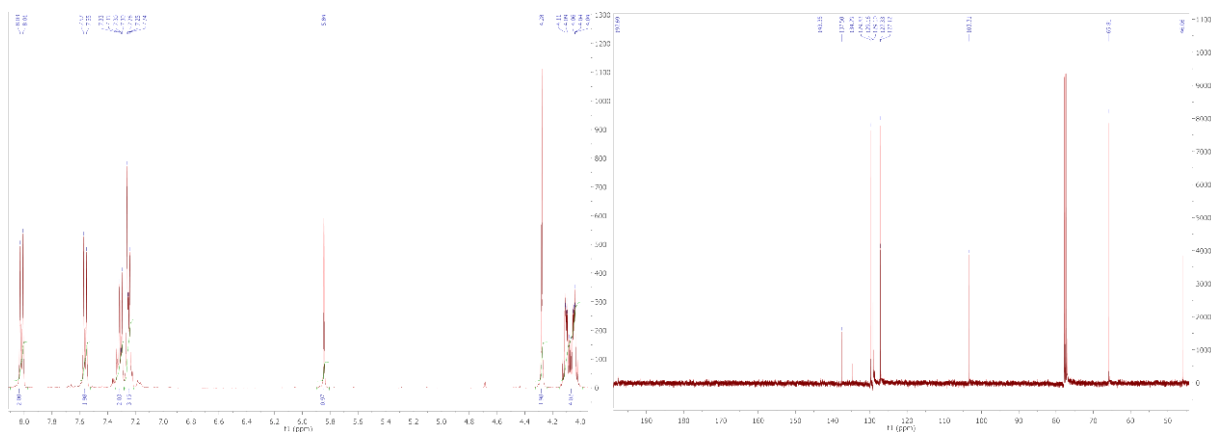


Figure 95 ^1H - (left) and ^{13}C -NMR spectra (right) of **60**.

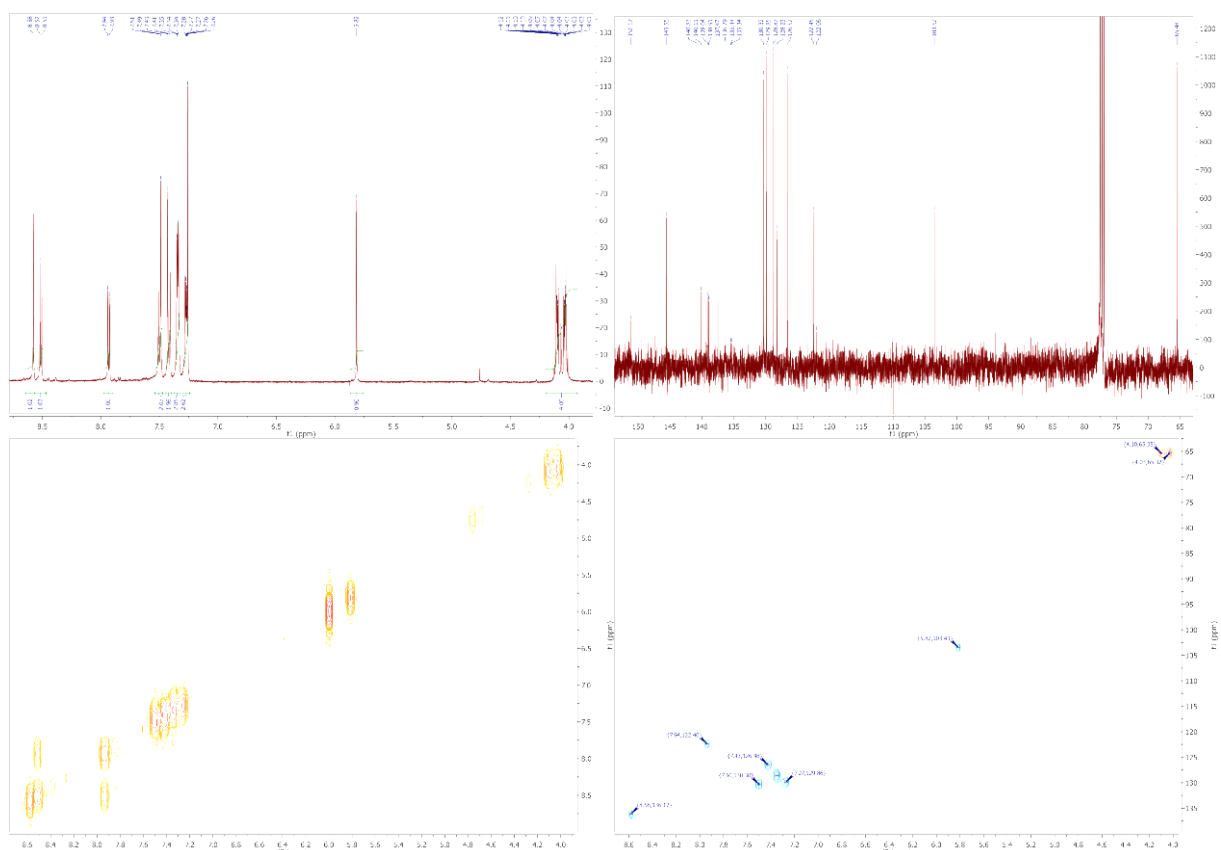


Figure 96 ^1H - (upper left), ^{13}C - (upper right), ^1H -COSY- (lower left) and ^1H - ^{13}C -HSQC-NMR spectra (lower right) of **61**.

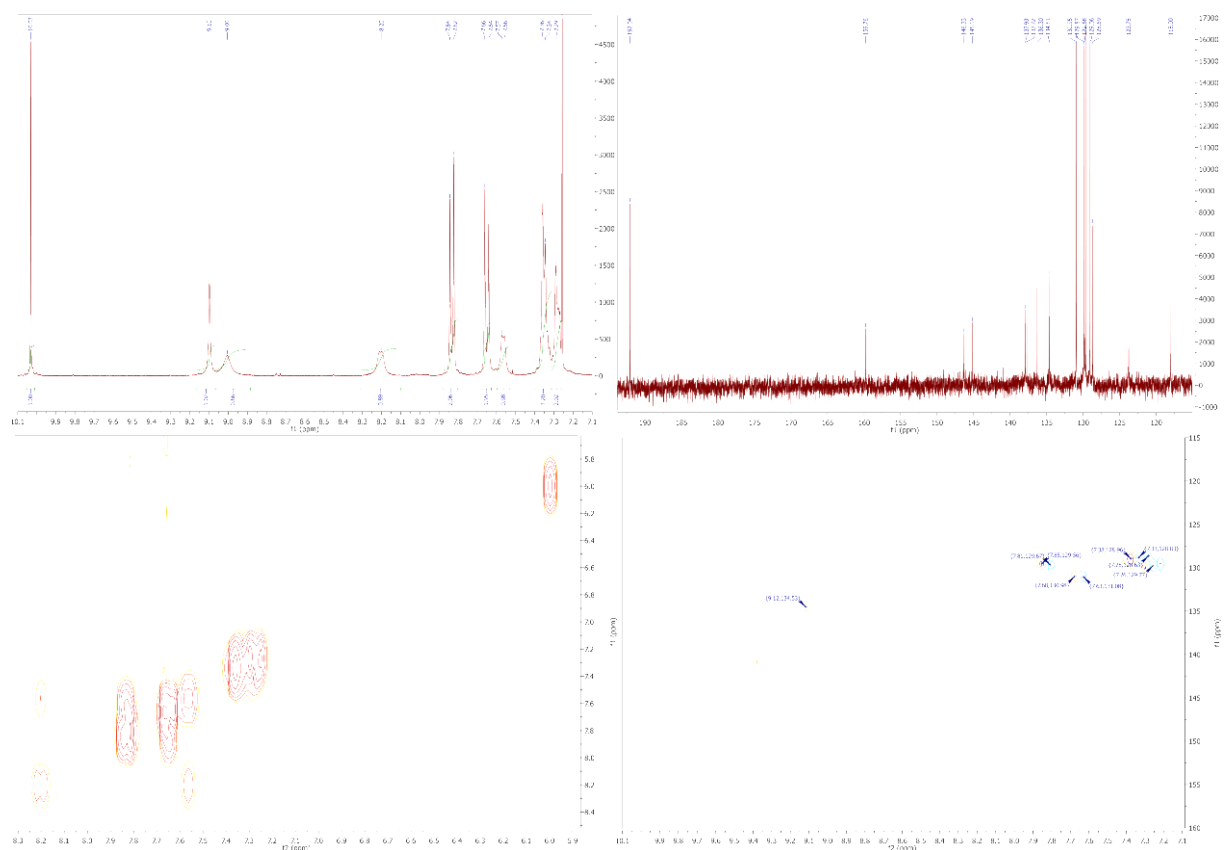


Figure 97 ^1H - (upper left), ^{13}C - (upper right), ^1H -COSY- (lower left) and ^1H - ^{13}C -HSQC-NMR spectra (lower right) of **62**.

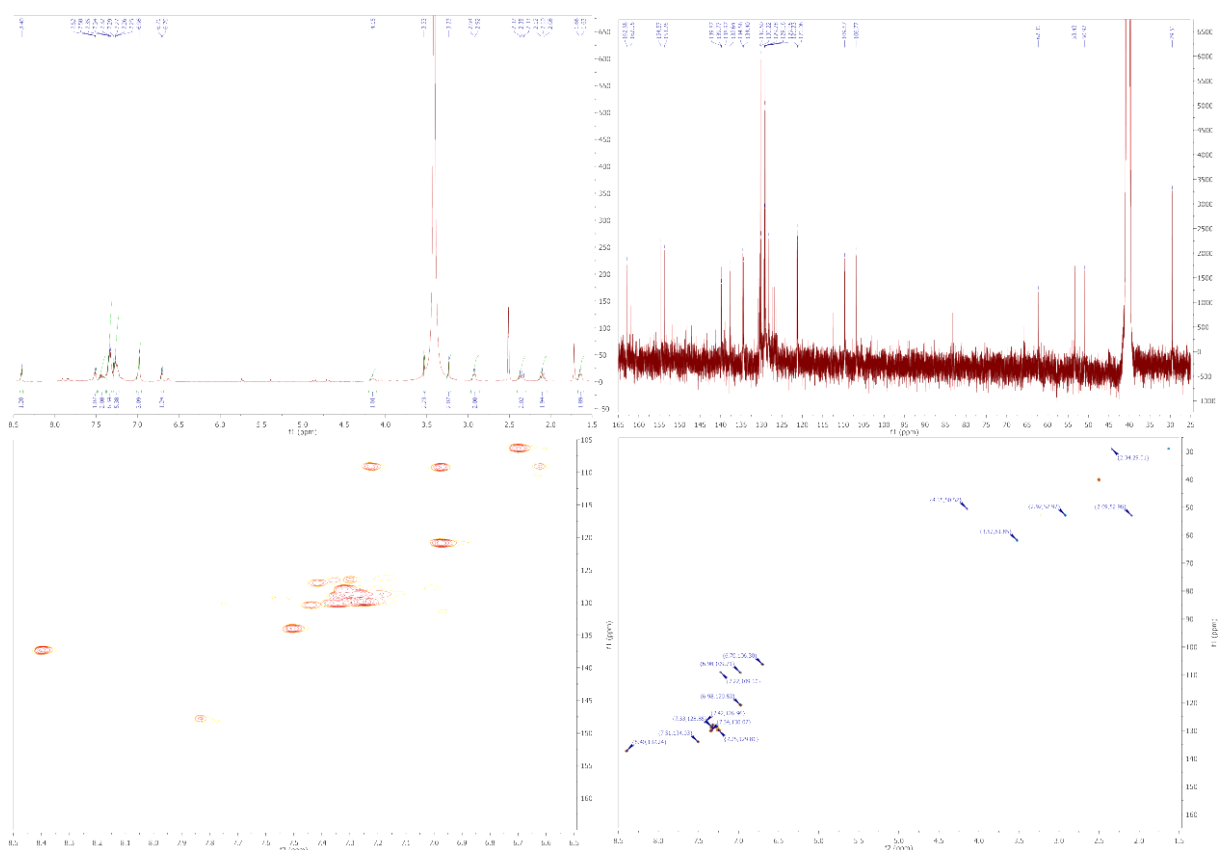


Figure 98 ^1H - (upper left), ^{13}C - (upper right), ^1H -COSY- (lower left) and ^1H - ^{13}C -HSQC-NMR spectra (lower right) of **63a**.

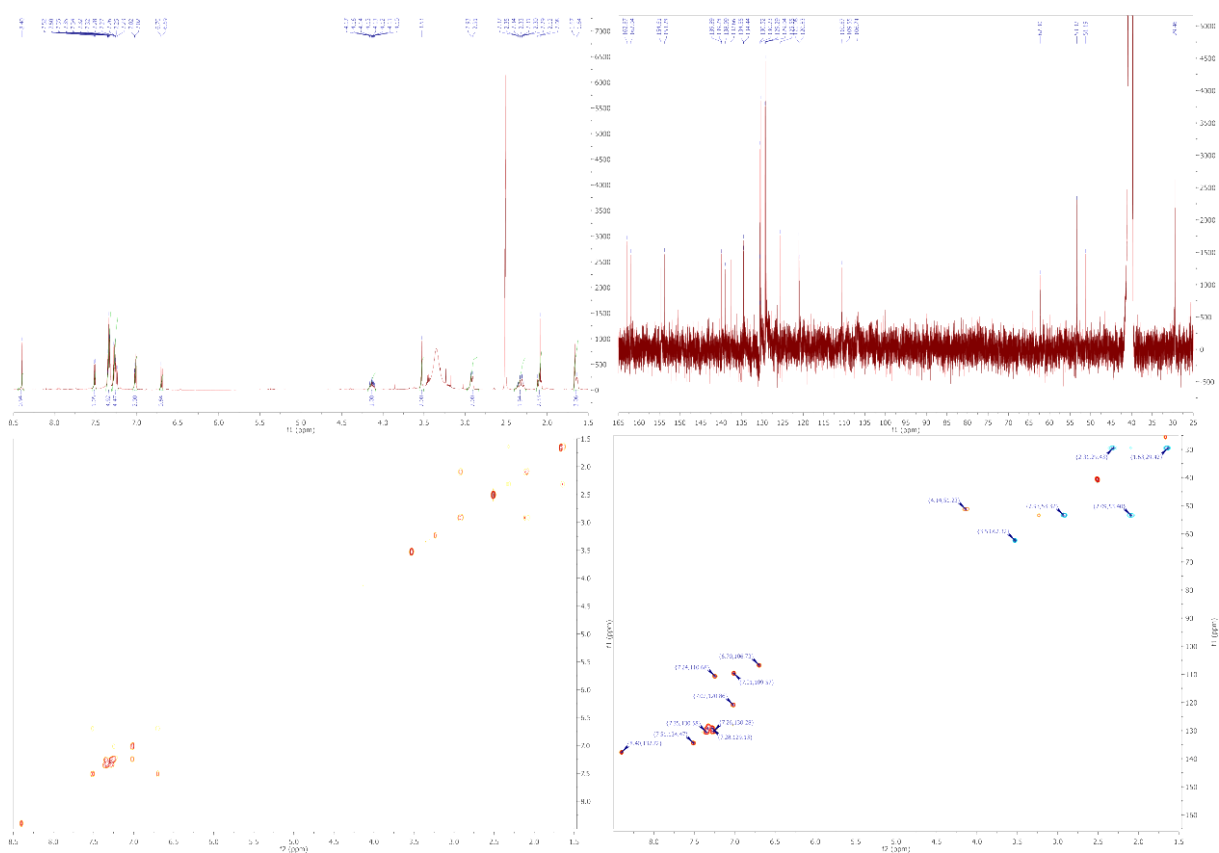


Figure 99 ^1H - (upper left), ^{13}C - (upper right), ^1H -COSY- (lower left) and ^1H - ^{13}C -HSQC-NMR spectra (lower right) of **63b**.

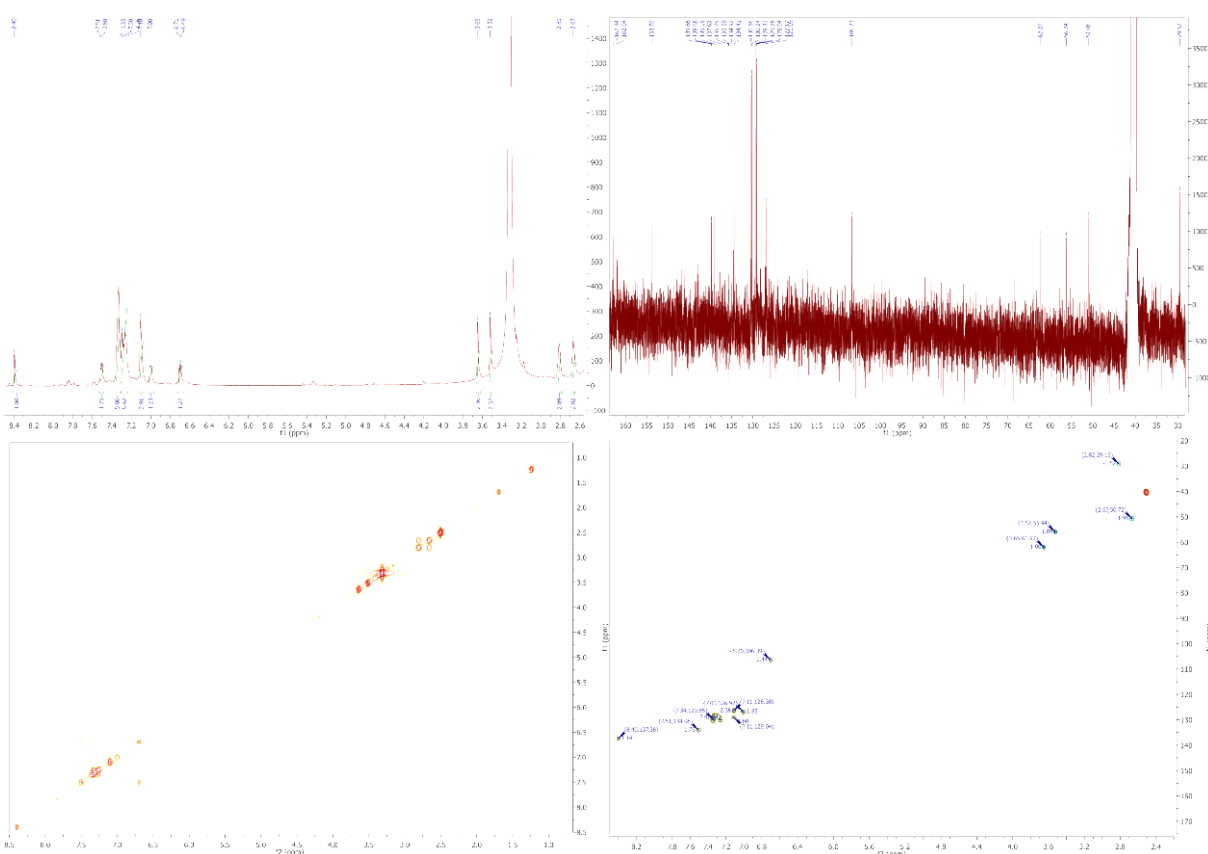


Figure 100 ^1H - (upper left), ^{13}C - (upper right), ^1H -COSY- (lower left) and ^1H - ^{13}C -HSQC-NMR spectra (lower right) of **63c**.

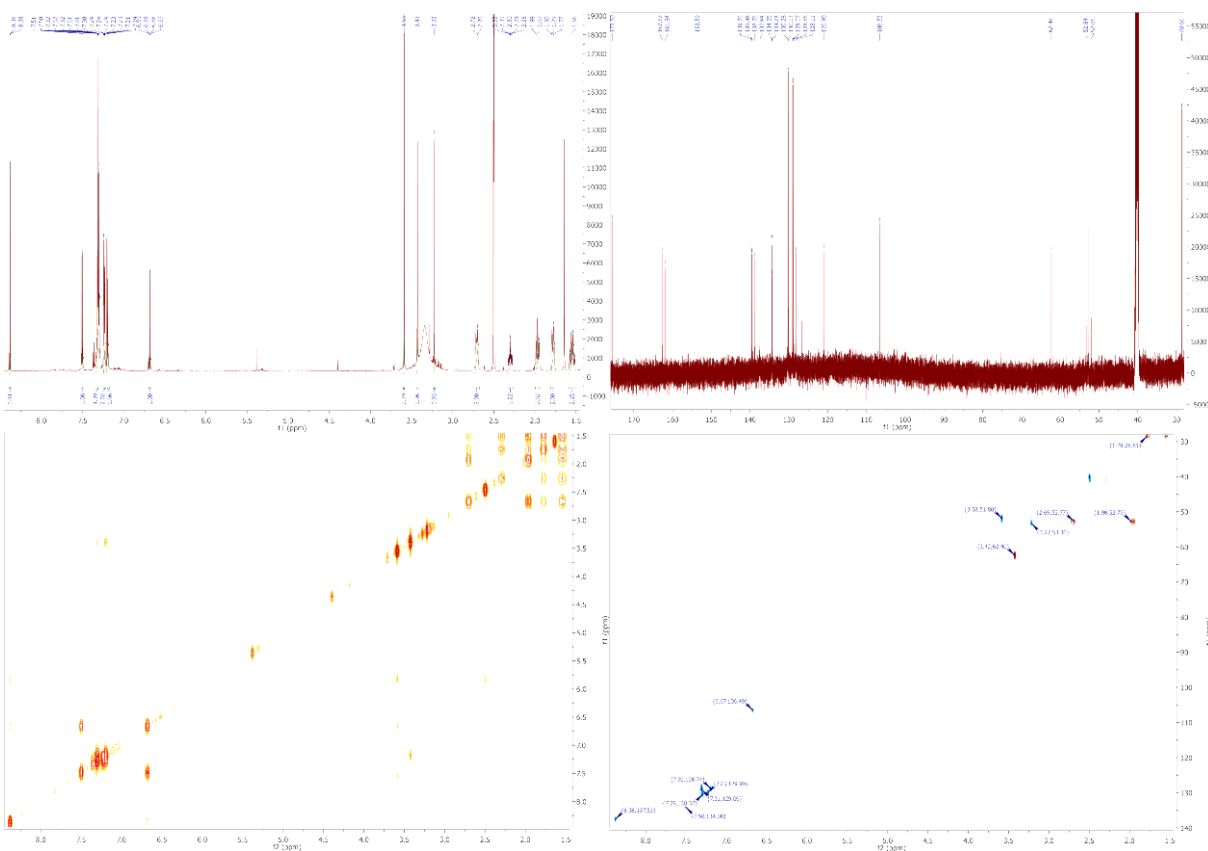


Figure 101 ^1H - (upper left), ^{13}C - (upper right), ^1H -COSY- (lower left) and ^1H - ^{13}C -HSQC-NMR spectra (lower right) of **63d**.

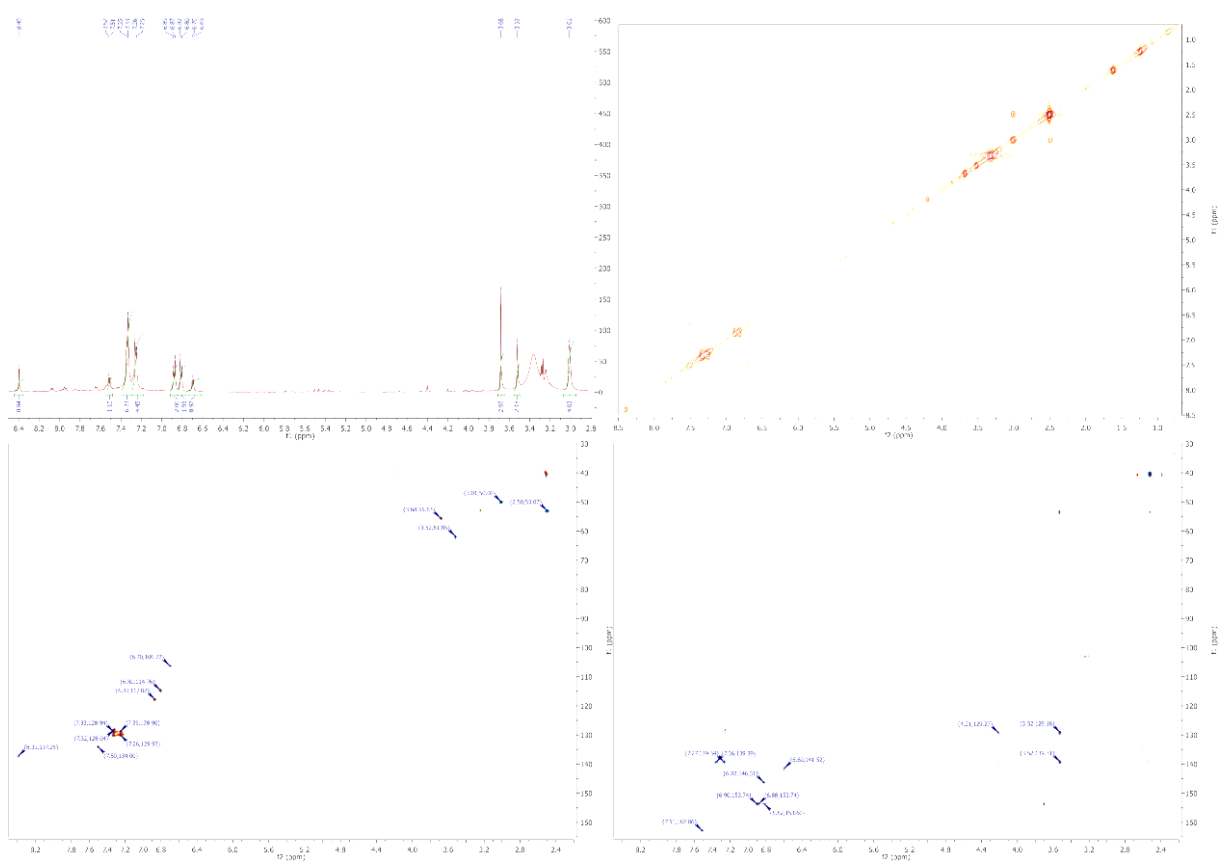


Figure 102 ^1H - (upper left), ^1H -COSY- (upper right), ^1H - ^{13}C -HSQC- (lower left) and ^1H - ^{13}C -HMBC-NMR spectra (lower right) of **63e**.

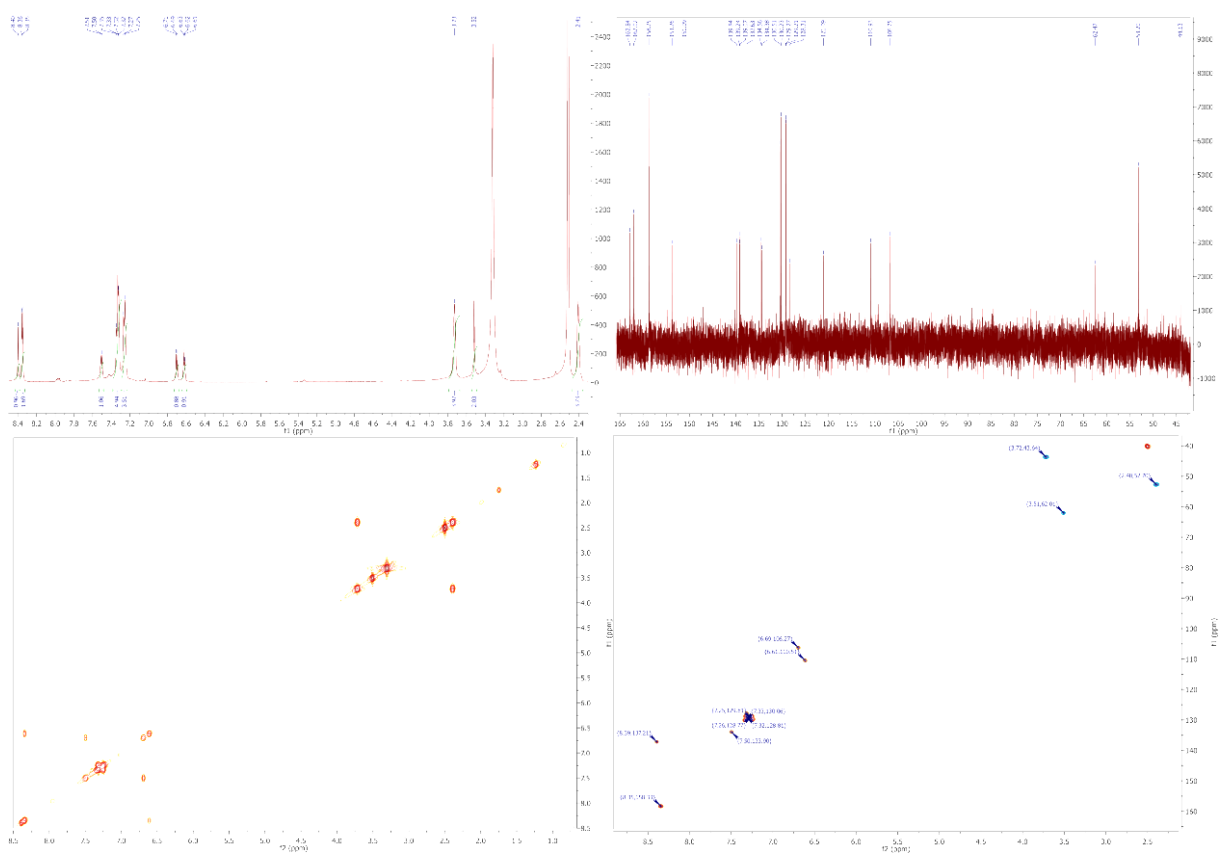


Figure 103 ^1H - (upper left), ^{13}C - (upper right), ^1H -COSY- (lower left) and ^1H - ^{13}C -HSQC-NMR spectra (lower right) of **63f**.

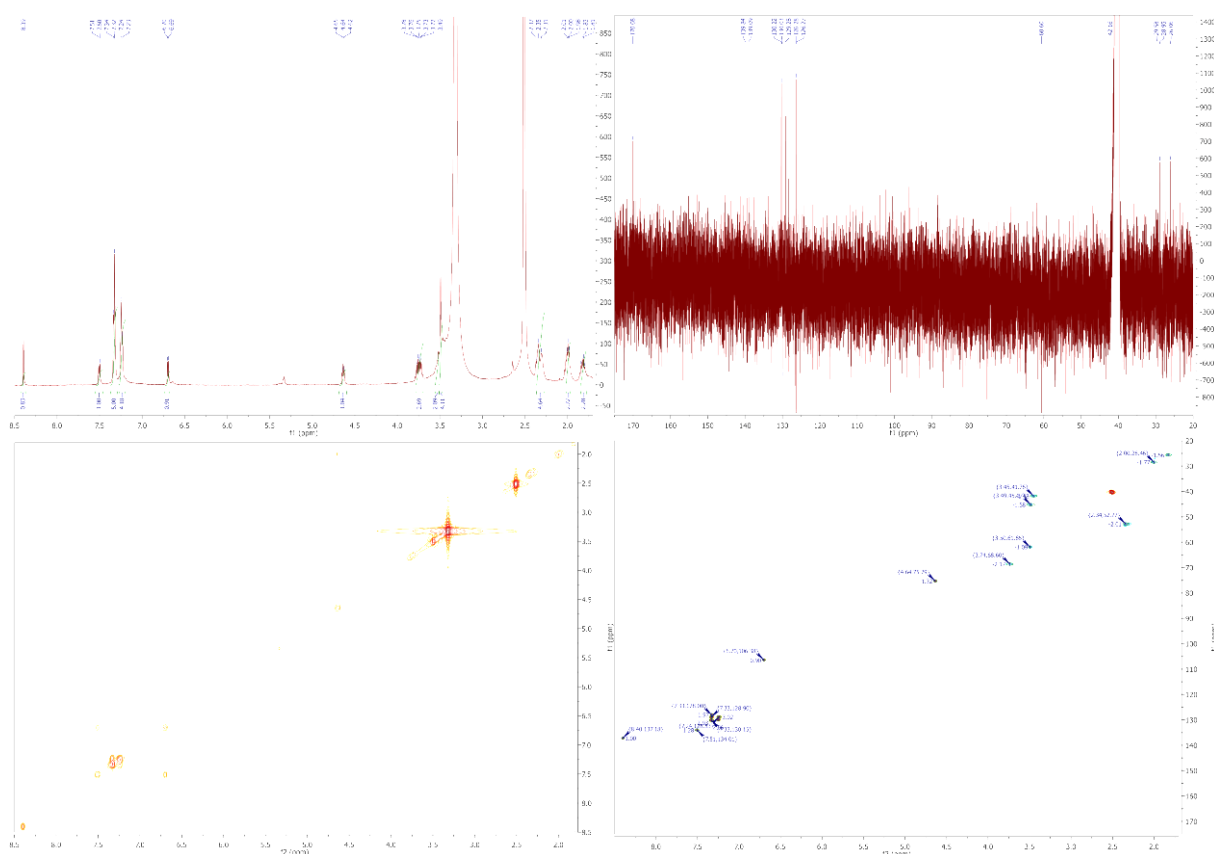


Figure 104 ^1H - (upper left), ^{13}C - (upper right), ^1H -COSY- (lower left) and ^1H - ^{13}C -HSQC-NMR spectra (lower right) of **63g**.

Table of References

- 1 A. Jemal, R. Siegel, E. Ward, Y. Hao, J. Xu, T. Murray & M. J. Thun. Cancer statistics, 2008. *CA Cancer J. Clin.*, **2008**, *58*, 71-96.
- 2 World Health Organization. *GLOBOCAN 2008*, <<http://globocan.iarc.fr/factsheets/populations/factsheet.asp?uno=900>> (**2008**).
- 3 Deutsches Krebsforschungszentrum. *Die fünf häufigsten Krebstodesursachen in Deutschland*, <<http://www.dkfz.de/de/krebsatlas/download/h5cam.pdf>> (**2013**).
- 4 D. Hanahan & R. A. Weinberg. Hallmarks of cancer: the next generation. *Cell*, **2011**, *144*, 646-674.
- 5 D. G. Savage & K. H. Antman. Imatinib mesylate – a new oral targeted therapy. *New Engl. J. Med.*, **2002**, *346*, 683-693.
- 6 M. Rabiller, M. Getlik, S. Klüter, A. Richters, S. Tückmantel, J. R. Simard & D. Rauh. Proteus in the world of proteins: conformational changes in protein kinases. *Arch. Pharm. (Weinheim, Ger.)*, **2010**, *343*, 193-206.
- 7 K. Yoshida, K. Komatsu, H.-G. Wang & D. Kufe. c-Abl Tyrosine Kinase Regulates the Human Rad9 Checkpoint Protein in Response to DNA Damage. *Mol. Cell. Biol.*, **2002**, *22*, 3292-3300.
- 8 S. Faderl, M. Talpaz, Z. Estrov & H. M. Kantarjian. Chronic Myelogenous Leukemia: Biology and Therapy. *Ann. Intern. Med.*, **1999**, *131*, 207-219.
- 9 C. L. Sawyers. Chronic Myeloid Leukemia. *New Engl. J. Med.*, **1999**, *340*, 1330-1340.
- 10 Y. Q. Gosser, J. Zheng, M. Overduin, B. J. Mayer & D. Cowburn. The solution structure of Abl SH3, and its relationship to SH2 in the SH(32) construct. *Structure*, **1995**, *3*, 1075-1086.
- 11 H. Pluk, K. Dorey & G. Superti-Furga. Autoinhibition of c-Abl. *Cell*, **2002**, *108*, 247-259.
- 12 B. Nagar, O. Hantschel, M. A. Young, K. Scheffzek, D. Veach, W. Bornmann, B. Clarkson, G. Superti-Furga & J. Kuriyan. Structural Basis for the Autoinhibition of c-Abl Tyrosine Kinase. *Cell*, **2003**, *112*, 859-871.

-
- 13 O. Hantschel, B. Nagar, S. Guettler, J. Kretzschmar, K. Dorey, J. Kuriyan & G. Superti-Furga. A Myristoyl/Phosphotyrosine Switch Regulates c-Abl. *Cell*, **2003**, *112*, 845-857.
 - 14 W. D. Bradley & A. J. Koleske. Regulation of cell migration and morphogenesis by Abl-family kinases: emerging mechanisms and physiological contexts. *J. Cell Sci.*, **2009**, *122*, 3441-3454.
 - 15 A. Mora, D. Komander, D. M. F. van Aalten & D. R. Alessi. PDK1, the master regulator of AGC kinase signal transduction. *Semin. Cell Dev. Biol.*, **2004**, *15*, 161-170.
 - 16 D. R. Alessi, S. R. James, C. P. Downes, A. B. Holmes, P. R. J. Gaffney, C. B. Reese & P. Cohen. Characterization of a 3-phosphoinositide-dependent protein kinase which phosphorylates and activates protein kinase Ba. *Curr. Biol.*, **1997**, *7*, 261-269.
 - 17 J. R. Bayascas, N. R. Leslie, R. Parsons, S. Fleming & D. R. Alessi. Hypomorphic Mutation of PDK1 Suppresses Tumorigenesis in PTEN^{+/-} Mice. *Curr. Biol.*, **2005**, *15*, 1839-1846.
 - 18 D. R. Alessi, M. Deak, A. Casamayor, F. B. Caudwell, N. Morrice, D. G. Norman, P. Gaffney, C. B. Reese, C. N. MacDougall, D. Harbison, A. Ashworth & M. Bownes. 3-Phosphoinositide-dependent protein kinase-1 (PDK1): structural and functional homology with the *Drosophila* DSTPK61 kinase. *Curr. Biol.*, **1997**, *7*, 776-789.
 - 19 R. M. Biondi, P. C. F. Cheung, A. Casamayor, M. Deak, R. A. Currie & D. R. Alessi. Identification of a pocket in the PDK1 kinase domain that interacts with PIF and the C-terminal residues of PKA. *EMBO J.*, **2000**, *19*, 979-988.
 - 20 R. M. Biondi, A. Kieloch, R. A. Currie, M. Deak & D. R. Alessi. The PIF-binding pocket in PDK1 is essential for activation of S6K and SGK, but not PKB. *EMBO J.*, **2001**, *20*, 4380-4390.
 - 21 A. Balendran, A. Casamayor, M. Deak, A. Paterson, P. Gaffney, R. Currie, C. P. Downes & D. R. Alessi. PDK1 acquires PDK2 activity in the presence of a synthetic peptide derived from the carboxyl terminus of PRK2. *Curr. Biol.*, **1999**, *9*, 393-404.
 - 22 Y. T. Ip & R. J. Davis. Signal transduction by the c-Jun N-terminal kinase (JNK) — from inflammation to development. *Curr. Opin. Cell Biol.*, **1998**, *10*, 205-219.

-
- 23 R. J. Davis. Signal Transduction by the JNK Group of MAP Kinases. *Cell*, **2000**, *103*, 239-252.
- 24 A. J. Whitmarsh, J. Cavanagh, C. Tournier, J. Yasuda & R. J. Davis. A Mammalian Scaffold Complex That Selectively Mediates MAP Kinase Activation. *Science*, **1998**, *281*, 1671-1674.
- 25 M. Dickens, J. S. Rogers, J. Cavanagh, A. Raitano, Z. Xia, J. R. Halpern, M. E. Greenberg, C. L. Sawyers & R. J. Davis. A Cytoplasmic Inhibitor of the JNK Signal Transduction Pathway. *Science*, **1997**, *277*, 693-696.
- 26 Y.-S. Heo, S.-K. Kim, C. I. Seo, Y. K. Kim, B.-J. Sung, H. S. Lee, J. I. Lee, S.-Y. Park, J. H. Kim, K. Y. Hwang, Y.-L. Hyun, Y. H. Jeon, S. Ro, J. M. Cho, T. G. Lee & C.-H. Yang. Structural basis for the selective inhibition of JNK1 by the scaffolding protein JIP1 and SP600125. *EMBO J.*, **2004**, *23*, 2185-2195.
- 27 C. Yan, T. Kaoud, S. Lee, K. N. Dalby & P. Ren. Understanding the Specificity of a Docking Interaction between JNK1 and the Scaffolding Protein JIP1. *J. Phys. Chem.*, **2011**, *115*, 1491-1502.
- 28 P. Liu, T. E. Cleveland 4th, S. Bouyain, P. O. Byrne, P. A. Longo & D. J. Leahy. A single ligand is sufficient to activate EGFR dimers. *Proc. Natl. Acad. Sci. USA*, **2012**, *109*, 10861-10866.
- 29 C. Bähr & B. Groner. The insulin like growth factor-1 receptor (IGF-1R) as a drug target: novel approaches to cancer therapy. *Growth Hormone & IGF Research*, **2004**, *14*, 287-295.
- 30 H. Kato, T. N. Faria, B. Stannard, C. T. Roberts, Jr. & D. LeRoith. Role of tyrosine kinase activity in signal transduction by the insulin-like growth factor-I (IGF-I) receptor. Characterization of kinase-deficient IGF-I receptors and the action of an IGF-I-mimetic antibody (alpha IR-3). *J. Biol. Chem.*, **1993**, *268*, 2655-2661.
- 31 P. Delafontaine, Y.-H. Song & Y. Li. Expression, Regulation, and Function of IGF-1, IGF-1R, and IGF-1 Binding Proteins in Blood Vessels. *Arteriosclerosis, Thrombosis and Vascular Biology*, **2004**, *24*, 435-444.
- 32 U. Galderisi, F. P. Jori & A. Giordano. Cell cycle regulation and neural differentiation. *Oncogene*, **2003**, *22*, 5208-5219.

-
- 33 P. D. Jeffrey, A. A. Russo, K. Polyak, E. Gibbs, J. Hurwitz, J. Massagué & N. P. Pavletich. Mechanism of CDK activation revealed by the structure of a cyclinA-CDK2 complex. *Nature*, **2002**, *376*, 313-320.
- 34 A. A. Russo, P. D. Jeffrey, A. K. Patten, J. Massagué & N. P. Pavletich. Crystal structure of the p27Kip1 cyclin-dependent-kinase inhibitor bound to the cyclin A-Cdk2 complex. *Nature*, **1996**, *382*, 325-331.
- 35 Q. Yang & K.-L. Guan. Expanding mTOR signaling. *Cell Res.*, **2007**, *17*, 666-681.
- 36 J. Choi, J. Chen, S. L. Schreiber & J. Clardy. Structure of the FKBP12-Rapamycin Complex Interacting with Binding Domain of Human FRAP. *Science*, **1996**, *273*, 239-242.
- 37 K. Yonezawa, C. Tokunaga, N. Oshiro & K.-i. Yoshino. Raptor, a binding partner of target of rapamycin. *Biochem. Biophys. Res. Commun.*, **2004**, *313*, 437-441.
- 38 A. C. Dar & K. M. Shokat. The Evolution of Protein Kinase Inhibitors from Antagonists to Agonists of Cellular Signaling. *Annu. Rev. Biochem.*, **2011**, *80*, 769-795.
- 39 M. L. Sos, S. Fischer, R. Ullrich, M. Peifer, J. M. Heuckmann, M. Koker, S. Heynck, I. Stückrath, J. Weiss, F. Fischer, K. Michel, A. Goel, L. Regales, K. A. Politi, S. Perera, M. Getlik, L. C. Heukamp, S. Ansén, T. Zander, R. Beroukhim, H. Kashkar, K. M. Shokat, W. R. Sellers, D. Rauh, C. Orr, K. P. Hoeflich, L. Friedman, K.-K. Wong, W. Pao & R. K. Thomas. Identifying genotype-dependent efficacy of single and combined PI3K- and MAPK-pathway inhibition in cancer. *Proc. Natl. Acad. Sci.*, **2009**, *106*, 18351-18356.
- 40 J. Zheng, D. R. Knighton, L. F. T. Eyck, R. Karlsson, N. Xuong, S. S. Taylor & J. M. Sowadski. Crystal structure of the catalytic subunit of cAMP-dependent protein kinase complexed with magnesium-ATP and peptide inhibitor. *Biochemistry*, **1993**, *32*, 2154-2161.
- 41 S. W. Cowan-Jacob, H. Mobitz & D. Fabbro. Structural biology contributions to tyrosine kinase drug discovery. *Curr. Opin. Cell Biol.*, **2009**, *21*, 280-287.
- 42 R. A. Copeland. Conformational adaptation in drug-target interactions and residence time. *Future Med. Chem.*, **2011**, *3*, 1491-1501.

-
- 43 L. Palmieri & G. Rastelli. α C helix displacement as a general approach for allosteric modulation of protein kinases. *Drug Disc. Today*, **2012**, *18*, 407-414.
- 44 B. J. Druker & N. B. Lydon. Lessons learned from the development of an abl tyrosine kinase inhibitor for chronic myelogenous leukemia. *J. Clin. Invest.*, **2000**, *105*, 3-7.
- 45 Z. A. Knight, H. Lin & K. M. Shokat. Targeting the cancer kinome through polypharmacology. *Nat. Rev. Cancer*, **2010**, *10*, 130-137.
- 46 Z. Fang, C. Grütter & D. Rauh. Strategies for the Selective Regulation of Kinases with Allosteric Modulators: Exploiting Exclusive Structural Features. *ACS Chem. Biol.*, **2013**, *8*, 58-70.
- 47 F. J. Adrián, Q. Ding, T. Sim, A. Velentza, C. Sloan, Y. Liu, G. Zhang, W. Hur, S. Ding, P. Manley, J. Mestan, D. Fabbro & N. S. Gray. Allosteric inhibitors of Bcr-abl-dependent cell proliferation. *Nat. Chem. Biol.*, **2006**, *2*, 95-102.
- 48 Y. Choi, M. A. Seeliger, S. B. Panjarian, H. Kim, X. Deng, T. Sim, B. Couch, A. J. Koleske, T. E. Smithgall & N. S. Gray. N-Myristoylated c-Abl Tyrosine Kinase Localizes to the Endoplasmic Reticulum upon Binding to an Allosteric Inhibitor. *J. Biol. Chem.*, **2009**, *284*, 29005-29014.
- 49 J. Zhang, F. J. Adrián, W. Jahnke, S. W. Cowan-Jacob, A. G. Li, R. E. Iacob, T. Sim, J. Powers, C. Dierks, F. Sun, G.-R. Guo, Q. Ding, B. Okram, Y. Choi, A. Wojciechowski, X. Deng, G. Liu, G. Fendrich, A. Strauss, N. Vajpai, S. Grzesiek, T. Tuntland, Y. Liu, B. Bursulaya, M. Azam, P. W. Manley, J. R. Engen, G. Q. Daley, M. Warmuth & N. S. Gray. Targeting Bcr-Abl by combining allosteric with ATP-binding-site inhibitors. *Nature*, **2010**, *463*, 501-506.
- 50 A. Converso, T. Hartingh, R. M. Garbaccio, E. Tasber, K. Rickert, M. E. Fraley, Y. Yan, C. Kreatsoulas, S. Stirdivant, B. Drakas, E. S. Walsh, K. Hamilton, C. A. Buser, X. Mao, M. T. Abrams, S. C. Beck, W. Tao, R. Lobell, L. Sepp-Lorenzino, J. Zugay-Murphy, V. Sardana, S. K. Munshi, S. M. Jezequel-Sur, P. D. Zuck & G. D. Hartman. Development of thioquinazolinones, allosteric Chk1 kinase inhibitors. *Bioorg. Med. Chem. Lett.*, **2009**, *19*, 1240-1244.
- 51 D. Vanderpool, T. O. Johnson, C. Ping, S. Bergqvist, G. Alton, S. Phonephaly, E. Rui, C. Luo, Y.-L. Deng, S. Grant, T. Quenzer, S. Margosiak, J. Register, E. Brown & J. Ermolieff. Characterization of the CHK1 Allosteric Inhibitor Binding Site. *Biochemistry*, **2009**, *48*, 9823-9830.
-

-
- 52 D. J. Owen, M. E. M. Noble, E. F. Garman, A. C. Papageorgiou & L. N. Johnson. Two structures of the catalytic domain of phosphorylase kinase: an active protein kinase complexed with substrate analogue and product. *Structure*, **1995**, *3*, 467.
- 53 P. F. Jones, T. Jakubowicz, F. J. Pitossi, F. Maurer & B. A. Hemmings. Molecular cloning and identification of a serine/threonine protein kinase of the second-messenger subfamily. *Proc. Natl. Acad. Sci.*, **1991**, *88*, 4171-4175.
- 54 K. Du & M. Montminy. CREB Is a Regulatory Target for the Protein Kinase Akt/PKB. *J. Biol. Chem.*, **1998**, *273*, 32377-32379.
- 55 P. C. van Weeren, K. M. T. de Bruyn, A. M. M. de Vries-Smits, J. van Lint & B. M. T. Burgering. Essential Role for Protein Kinase B (PKB) in Insulin-induced Glycogen Synthase Kinase 3 Inactivation. *J. Biol. Chem.*, **1998**, *273*, 13150-13156.
- 56 J. Q. Cheng, C. W. Lindsley, G. Z. Cheng, H. Yang & S. V. Nicosia. The Akt/PKB pathway: molecular target for cancer drug discovery. *Oncogene*, **2005**, *24*, 7482-7492.
- 57 Z. Chang, Q. Zhang, Q. Feng, J. Xu, T. Teng, Q. Luan, C. Shan, Y. Hu, B. A. Hemmings, X. Gao & Z. Yang. Deletion of Akt1 causes heart defects and abnormal cardiomyocyte proliferation. *Dev. Biol.*, **2010**, *347*, 384-391.
- 58 W. S. Chen, P.-Z. Xu, K. Gottlob, M.-L. Chen, K. Sokol, T. Shiyanova, I. Roninson, W. Weng, R. Suzuki, K. Tobe, T. Kadowaki & N. Hay. Growth retardation and increased apoptosis in mice with homozygous disruption of the akt1 gene. *Genes Dev.*, **2001**, *15*, 2203-2208.
- 59 H. Cho, J. Mu, J. K. Kim, J. L. Thorvaldsen, Q. Chu, E. B. C. III, K. H. Kaestner, M. S. Bartolomei, G. I. Shulman & M. J. Birnbaum. Insulin Resistance and a Diabetes Mellitus-Like Syndrome in Mice Lacking the Protein Kinase Akt2 (PKB β). *Science*, **2001**, *292*, 1728-1731.
- 60 R. M. Easton, H. Cho, K. Roovers, D. W. Shineman, M. Mizrahi, M. S. Forman, V. M.-Y. Lee, M. Szabolcs, R. d. Jong, T. Oltersdorf, T. Ludwig, A. Efstratiadis & M. J. Birnbaum. Role for Akt3/Protein Kinase B in Attainment of Normal Brain Size. *Mol. Cell. Biochem.*, **2005**, *25*, 1869-1878.
- 61 O. Tschopp, Z.-Z. Yang, D. Brodbeck, B. A. Dummler, M. Hemmings-Mieszczak, T. Watanabe, T. Michaelis, J. Frahm & B. A. Hemmings. Essential role of protein kinase B γ (PKB γ /Akt3) in postnatal brain development but not in glucose homeostasis. *Development (Cambridge, UK)*, **2005**, *132*, 2943-2954.
-

-
- 62 J. R. Testa & A. Bellacosa. AKT plays a central role in tumorigenesis. *Proc. Natl. Acad. Sci.*, **2001**, 98, 10983-10985.
- 63 J. Á. Fresno Vara, E. Casado, J. d. Castro, P. Cejas, C. Belda-Iniesta & M. González-Barón. PI3K/Akt signalling pathway and cancer. *Cancer Treat. Rev.*, **2004**, 30, 193-204.
- 64 K. Nakatani, D. A. Thompson, A. Barthel, H. Sakaue, W. Liu, R. J. Weigel & R. A. Roth. Up-regulation of Akt3 in Estrogen Receptor-deficient Breast Cancers and Androgen-independent Prostate Cancer Lines. *J. Biol. Chem.*, **1999**, 274, 21528-21532.
- 65 J. Q. Cheng, B. Rugger, W. M. Klein, G. Sonoda, D. A. Altomare, D. K. Watson & J. R. Testa. Amplification of AKT2 in human pancreatic cells and inhibition of AKT2 expression and tumorigenicity by antisense RNA. *Proc. Natl. Acad. Sci.*, **1996**, 93, 3636-3641.
- 66 S. P. Staal. Molecular cloning of the akt oncogene and its human homologues AKT1 and AKT2: amplification of AKT1 in a primary human gastric adenocarcinoma. *Proc. Natl. Acad. Sci.*, **1987**, 84, 5034-5037.
- 67 P. Dhawan, A. B. Singh, D. L. Ellis & A. Richmond. Constitutive Activation of Akt/Protein Kinase B in Melanoma Leads to Up-Regulation of Nuclear Factor- κ B and Tumor Progression. *Cancer Res.*, **2002**, 62, 7335-7342.
- 68 V. Vasko, M. Saji, E. Hardy, M. Kruhlak, A. Larin, V. Savchenko, M. Miyakawa, O. Isozaki, H. Murakami, T. Tsushima, K. Burman, C. De Micco & M. Ringel. Akt activation and localisation correlate with tumour invasion and oncogene expression in thyroid cancer. *J. Med. Genet.*, **2004**, 41, 161-170.
- 69 J. Xu, J.-Y. Zhou, W.-Z. Wei & G. S. Wu. Activation of the Akt Survival Pathway Contributes to TRAIL Resistance in Cancer Cells. *PLoS One*, **2010**, 5, e10226.
- 70 X. Zhang, N. Tang, T. J. Hadden & A. K. Rishi. Akt, FoxO and regulation of apoptosis. *Biochim. Biophys. Acta*, **2011**, 1813, 1978-1986.
- 71 I. Eke, U. Koch, S. Hehlhans, V. Sandfort, F. Stanchi, D. Zips, M. Baumann, A. Shevchenko, C. Pilarsky, M. Haase, G. B. Baretton, V. Calleja, B. Larijani, R. Fässler & N. Cordes. PINCH1 regulates Akt1 activation and enhances radioresistance by inhibiting PP1 α . *J. Clin. Invest.*, **2010**, 120, 2516-2527.
-

-
- 72 M. Falasca. PI3K/Akt Signalling Pathway Specific Inhibitors: A Novel Strategy to Sensitize Cancer Cells to Anti-Cancer Drugs. *Curr. Pharm. Des.*, **2010**, *16*, 1410-1416.
- 73 N. Xu, N. Hegarat, E. J. Black, M. T. Scott, H. Hochegger & D. A. Gillespie. Akt/PKB suppresses DNA damage processing and checkpoint activation in late G2. *J. Cell Biol.*, **2010**, *190*, 297-305.
- 74 R. J. Haslam, H. B. Koide & B. A. Hemmings. Pleckstrin domain homology. *Nature*, **1993**, *363*, 309-310.
- 75 V. Calleja, D. Alcor, M. Laguerre, J. Park, B. Vojnovic, B. A. Hemmings, J. Downward, P. J. Parker & B. Larijani. Intramolecular and Intermolecular Interactions of Protein Kinase B Define Its Activation In Vivo. *PLoS Biology*, **2007**, *5*, 780-791.
- 76 W.-I. Wu, W. C. Voegtli, H. L. Sturgis, F. P. Dizon, G. P. A. Vigers & B. J. Brandhuber. Crystal Structure of Human AKT1 with an Allosteric Inhibitor Reveals a New Mode of Kinase Inhibition. *PLoS One*, **2010**, *5*, e12913.
- 77 J.-i. Okano, I. Gaslightwala, M. J. Birnbaum, A. K. Rustgi & H. Nakagawa. Akt/Protein Kinase B Isoforms Are Differentially Regulated by Epidermal Growth Factor Stimulation. *J. Biol. Chem.*, **2000**, *275*, 30934-30942.
- 78 M. Pozuelo-Rubio, N. R. Leslie, J. Murphy & C. MacKintosh. Mechanism of Activation of PKB/Akt by the Protein Phosphatase Inhibitor Calyculin A. *Cell Biochem. Biophys.*, **2010**, *58*, 147-156.
- 79 Q. Li. Recent progress in the discovery of Akt inhibitors as anticancer agents. *Expert Opin. Ther. Patents*, **2007**, *17*, 1077-1130.
- 80 V. Calleja, M. Laguerre, P. J. Parker & B. Larijani. Role of a Novel PH-Kinase Domain Interface in PKB/Akt Regulation: Structural Mechanism for Allosteric Inhibition. *PLoS Biology*, **2009**, *7*, 189-200.
- 81 V. Calleja, M. Laguerre & B. Larijani. 3-D structure and dynamics of protein kinase B — new mechanism for the allosteric regulation of an AGC kinase. *J. Chem. Biol.*, **2009**, *2*, 11-25.
- 82 J. Yang, P. Cron, V. Thompson, V. M. Good, D. Hess, B. A. Hemmings & D. Barford. Molecular Mechanism for the Regulation of Protein Kinase B/Akt by Hydrophobic Motif Phosphorylation. *Mol. Cell*, **2002**, *9*, 1227-1240.

-
- 83 E. E. Vincent, D. J. E. Elder, E. C. Thomas, L. Phillips, C. Morgan, J. Pawade, M. Sohail, M. T. May, M. R. Hetzel & J. M. Tavaré. Akt phosphorylation on Thr308 but not on Ser473 correlates with Akt protein kinase activity in human non-small cell lung cancer. *Br. J. Cancer*, **2011**, *104*, 1755-1761.
- 84 B. T. Chua, D. Gallego-Ortega, A. R. d. Molina, A. Ullrich, J. C. Lacal & J. Downward. Regulation of Akt(ser473)phosphorylation by Choline kinase in breast carcinoma cells. *Mol. Cancer*, **2009**, *8*, 131.
- 85 D. D. Sarbassov, D. A. Guertin, S. M. Ali & D. M. Sabatini. Phosphorylation and Regulation of Akt/PKB by the Rictor-mTOR Complex. *Science*, **2005**, *307*, 1098-1101.
- 86 J. Feng, J. Park, P. Cron, D. Hess & B. A. Hemmings. Identification of a PKB/Akt Hydrophobic Motif Ser-473 Kinase as DNA-dependent Protein Kinase. *J. Biol. Chem.*, **2004**, *279*, 41189-41196.
- 87 S. Persad, S. Attwell, V. Gray, N. Mawji, J. T. Deng, D. Leung, J. Yan, J. Sanghera, M. P. Walsh & S. Dedhar. Regulation of Protein Kinase B/Akt-Serine 473 Phosphorylation by Integrin-linked Kinase. *J. Biol. Chem.*, **2001**, *276*, 27462-27469.
- 88 M. J. Rane, P. Y. Coxon, D. W. Powell, R. Webster, J. B. Klein, W. Pierce, P. Ping & K. R. McLeish. p38 Kinase-dependent MAPKAPK-2 Activation Functions as 3-Phosphoinositide-dependent Kinase-2 for Akt in Human Neutrophils. *J. Biol. Chem.*, **2001**, *276*, 3517-3523.
- 89 L. Q. Dong & F. Liu. PDK2: the missing piece in the receptor tyrosine kinase signaling pathway puzzle. *Am. J. Physiol. Endocrinol. Metab.*, **2005**, *289*, E187-E196.
- 90 Y.-H. Ou, M. Torres, R. Ram, E. Formstecher, C. Roland, T. Cheng, R. Brekken, R. Wurz, A. Tasker, T. Polverino, S.-L. Tan & M. A. White. TBK1 Directly Engages Akt/PKB Survival Signaling to Support Oncogenic Transformation. *Mol. Cell*, **2011**, *41*, 458-470.
- 91 X. Xie, D. Zhang, B. Zhao, M.-K. Lu, M. You, G. Condorelli, C.-Y. Wang & K.-L. Guan. I κ B kinase ϵ and TANK-binding kinase 1 activate AKT by direct phosphorylation. *Proc. Natl. Acad. Sci.*, **2011**, *108*, 6474-6479.
- 92 K. Lin, J. Lin, W.-I. Wu, J. Ballard, B. B. Lee, S. L. Gloor, G. P. A. Vigers, T. H. Morales, L. S. Friedman, N. Skelton & B. J. Brandhuber. An ATP-Site On-Off Switch That Restricts Phosphatase Accessibility of Akt. *Sci. Signal.*, **2012**, *5*, ra37.
-

-
- 93 S. J. Humphrey & D. E. James. Uncaging Akt. *Sci. Signal.*, **2012**, *5*, pe20.
- 94 R. H. Insall & O. D. Weiner. PIP3, PIP2, and cell movement--similar messages, different meanings? *Dev. Cell*, **2001**, *1*, 743-747.
- 95 H. Yoshizaki, N. Mochizuki, Y. Gotoh & M. Matsuda. Akt-PDK1 Complex Mediates Epidermal Growth Factor-induced Membrane Protrusion through Ral Activation. *Mol. Biol. Cell.*, **2007**, *18*, 119-128.
- 96 S. A. J. Rosen, P. R. J. Gaffney, B. Spiess & I. R. Gould. Understanding the relative affinity and specificity of the pleckstrin homology domain of protein kinase B for inositol phosphates. *Phys. Chem. Chem. Phys.*, **2011**, *14*, 929-936.
- 97 J. D. Carpten, A. L. Faber, C. Horn, G. P. Donoho, S. L. Briggs, C. M. Robbins, G. Hostetter, S. Boguslawski, T. Y. Moses, S. Savage, M. Uhlik, A. Lin, J. Du, Y.-W. Qian, D. J. Zeckner, G. Tucker-Kellogg, J. Touchman, K. Patel, S. Mousses, M. Bittner, R. Schevitz, M.-H. T. Lai, K. L. Blanchard & J. E. Thomas. A transforming mutation in the pleckstrin homology domain of AKT1 in cancer. *Nature*, **2007**, *448*, 439-444.
- 98 C. Parikh, V. Janakiraman, W.-I. Wu, C. K. Foo, N. M. Kljavin, S. Chaudhuri, E. Stawiski, B. Lee, J. Lin, H. Li, M. N. Lorenzo, W. Yuan, J. Guillory, M. Jackson, J. Rondon, Y. Franke, K. K. Bowman, M. Sagolla, J. Stinson, T. D. Wu, J. Wu, D. Stokoe, H. M. Stern, B. J. Brandhuber, K. Lin, N. J. Skelton & S. Seshagiri. Disruption of PH-kinase domain interactions leads to oncogenic activation of AKT in human cancers. *Proc. Natl. Acad. Sci.*, **2012**, *109*, 19368-19373.
- 99 G. S. Loving, M. Sainlos & B. Imperiali. Monitoring protein interactions and dynamics with solvatochromic fluorophores. *Trends Biotech.*, **2010**, *28*, 73-83.
- 100 H. Reuveni, N. Livnah, T. Geiger, S. Klein, O. Ohne, I. Cohen, M. Benhar, G. Gellerman & A. Levitzki. Toward a PKB inhibitor: modification of a selective PKA inhibitor by rational design. *Biochemistry*, **2002**, *41*, 10304-10314.
- 101 C. B. Breitenlechner, T. Wegge, L. Berillon, K. Graul, K. Marzenell, W.-G. Friebe, U. Thomas, R. Schumacher, R. Huber, R. A. Engh & B. Masjost. Structure-based optimization of novel azepane derivatives as PKB inhibitors. *J. Med. Chem.*, **2004**, *47*, 1375-1390.
- 102 J. F. Blake, N. C. Kallan, D. Xiao, R. Xu, J. R. Bencsik, N. J. Skelton, K. L. Spencer, I. S. Mitchell, R. D. Woessner, S. L. Gloor, T. Risom, S. D. Gross, M. Martinson, T.

-
- H. Morales, G. P. A. Vigers & B. J. Brandhuber. Discovery of pyrrolopyrimidine inhibitors of Akt. *Bioorg. Med. Chem. Lett.*, **2010**, *20*, 5607-5612.
- 103 J. R. Bencsik, D. Xiao, J. F. Blake, N. C. Kallan, I. S. Mitchell, K. L. Spencer, R. Xu, S. L. Gloor, M. Martinson, T. Risom, R. D. Woessner, F. Dizon, W.-I. Wu, G. P. A. Vigers, B. J. Brandhuber, N. J. Skelton, W. W. Prior & L. J. Murray. Discovery of dihydrothieno- and dihydrofuopyrimidines as potent pan Akt inhibitors. *Bioorg. Med. Chem. Lett.*, **2010**, *20*, 7037-7041.
- 104 Y. Luo, A. R. Shoemaker, X. Liu, K. W. Woods, S. A. Thomas, R. de Jong, E. K. Han, T. Li, V. S. Stoll, J. A. Powlas, A. Oleksijew, M. J. Mitten, Y. Shi, R. Guan, T. P. McGonigal, V. Klinghofer, E. F. Johnson, J. D. Levenson, J. J. Bouska, M. Mamo, R. A. Smith, E. E. Gramling-Evans, B. A. Zinker, A. K. Mika, P. T. Nguyen, T. Oltersdorf, S. H. Rosenberg, Q. Li & V. L. Giranda. Potent and selective inhibitors of Akt kinases slow the progress of tumors in vivo. *Mol. Cancer Ther.*, **2005**, *4*, 977-986.
- 105 T. G. Davies, M. L. Verdonk, B. Graham, S. Saalau-Bethell, C. C. F. Hamlett, T. McHardy, I. Collins, M. D. Garrett, P. Workman, S. J. Woodhead, H. Jhoti & D. Barford. A Structural Comparison of Inhibitor Binding to PKB, PKA and PKA-PKB Chimera. *J. Mol. Biol.*, **2007**, *367*, 882-894.
- 106 D. A. Heerding, N. Rhodes, J. D. Leber, T. J. Clark, R. M. Keenan, L. V. Lafrance, M. Li, I. G. Safonov, D. T. Takata, J. W. Venslavsky, D. S. Yamashita, A. E. Choudhry, R. A. Copeland, Z. Lai, M. D. Schaber, P. J. Tummino, S. L. Strum, E. R. Wood, D. R. Duckett, D. Eberwein, V. B. Knick, T. J. Lansing, R. T. McConnell, S. Zhang, E. A. Minthorn, N. O. Concha, G. L. Warren & R. Kumar. Identification of 4-(2-(4-Amino-1,2,5-oxadiazol-3-yl)-1-ethyl-7-(((3S)-3-piperidinylmethyl)oxy))-1H-imidazo[4,5-c]pyridin-4-yl)-2-methyl-3-butyn-2-ol (GSK690693), a Novel Inhibitor of AKT Kinase. *J. Med. Chem.*, **2008**, *51*, 5663-5679.
- 107 T. McHardy, J. J. Caldwell, K.-M. Cheung, L. J. Hunter, K. Taylor, M. Rowlands, R. Ruddle, A. Henley, A. d. H. Brandon, M. Valenti, T. G. Davies, L. Fazal, L. Seavers, F. I. Raynaud, S. A. Eccles, G. W. Aherne, M. D. Garrett & I. Collins. Discovery of 4-Amino-1-(7H-pyrrolo[2,3-d]pyrimidin-4-yl)piperidine-4-carboxamides As Selective, Orally Active Inhibitors of Protein Kinase B (Akt). *J. Med. Chem.*, **2010**, *53*, 2239-2249.
- 108 J. F. Blake, R. Xu, J. R. Bencsik, D. Xiao, N. C. Kallan, S. Schlachter, I. S. Mitchell, K. L. Spencer, A. L. Banka, E. M. Wallace, S. L. Gloor, M. Martinson, R. D.
-

-
- Woessner, G. P. Vigers, B. J. Brandhuber, J. Liang, B. S. Safina, J. Li, B. Zhang, C. Chabot, S. Do, L. Lee, J. Oeh, S. Sampath, B. B. Lee, K. Lin, B. M. Liederer & N. Skelton. Discovery and Preclinical Pharmacology of a Selective ATP-competitive Akt Inhibitor (GDC-0068) for the Treatment of Human Tumors. *J. Med. Chem.*, **2012**, *55*, 8110-8127.
- 109 A. R. Katritzky, S. Ozcana & E. Todadze. Synthesis and fluorescence of the new environment-sensitive fluorophore 6-chloro-2,3-naphthalimide derivative. *Org. Biomol. Chem.*, **2010**, *8*, 1296-1300.
- 110 E. J. Meuillet, D. Mahadevan, H. Vankayalapati, M. Berggren, R. Williams, A. Coon, A. P. Kozikowski & G. Powis. Specific Inhibition of the Akt1 Pleckstrin Homology Domain by D-3-Deoxy-Phosphatidyl-myo-Inositol Analogues. *Mol. Cancer Ther.*, **2003**, *2*, 389-399.
- 111 A. M. Ahad, S. Zuohe, L. Du-Cuny, S. A. Moses, L. L. Zhou, S. Zhang, G. Powis, E. J. Meuillet & E. A. Mash. Development of sulfonamide AKT PH domain inhibitors. *Bioorg. Med. Chem.*, **2011**, *19*, 2046-2054.
- 112 G. Loving & B. Imperiali. A Versatile Amino Acid Analogue of the Solvatochromic Fluorophore 4-N,N-Dimethylamino-1,8-naphthalimide: A Powerful Tool for the Study of Dynamic Protein Interactions. *J. Am. Chem. Soc.*, **2008**, *130*, 13630-13638.
- 113 S. S. Castillo, J. Brognard, P. A. Petukhov, C. Zhang, J. Tsurutani, C. A. Granville, M. Li, M. Jung, K. A. West, J. G. Gills, A. P. Kozikowski & P. A. Dennis. Preferential Inhibition of Akt and Killing of Akt-Dependent Cancer Cells by Rationally Designed Phosphatidylinositol Ether Lipid Analogues. *Cancer Res.*, **2004**, *64*, 2782-2792.
- 114 S. B. Kondapaka, S. S. Singh, G. P. Dasmahapatra, E. A. Sausville & K. K. Roy. Perifosine, a novel alkylphospholipid, inhibits protein kinase B activation. *Mol. Cancer Ther.*, **2003**, *2*, 1093-1103.
- 115 C. C. Kumar & V. Madison. AKT crystal structure and AKT-specific inhibitors. *Oncogene*, **2005**, *24*, 7493-7501.
- 116 H. Jo, P.-K. Lo, Y. Li, F. Loison, S. Green, J. Wang, L. E. Silberstein, K. Ye, H. Chen & H. R. Luo. Deactivation of Akt by a small molecule inhibitor targeting pleckstrin homology domain and facilitating Akt ubiquitination. *Proc. Natl. Acad. Sci.*, **2011**, *108*, 6486-6491.

-
- 117 W.-L. Yang, C.-Y. Wu, J. Wu & H.-K. Lin. Regulation of Akt signaling activation by ubiquitination. *Cell Cycle*, **2010**, 9, 486-497.
- 118 L. Toral-Barza, W.-G. Zhang, X. Huang, L. A. McDonald, E. J. Salaski, L. R. Barbieri, W.-D. Ding, G. Krishnamurthy, Y. B. Hu, J. Lucas, V. S. Bernan, P. Cai, J. I. Levin, T. S. Mansour, J. J. Gibbons, R. T. Abraham & K. Yu. Discovery of lactoquinomycin and related pyranonaphthoquinones as potent and allosteric inhibitors of AKT/PKB: mechanistic involvement of AKT catalytic activation loop cysteines. *Mol. Cancer Ther.*, **2007**, 6, 3028-3038.
- 119 E. J. Salaski, G. Krishnamurthy, W.-D. Ding, K. Yu, S. S. Insaf, C. Eid, J. Shim, J. I. Levin, K. Tabei, L. Toral-Barza, W.-G. Zhang, L. A. McDonald, E. Honores, C. Hanna, A. Yamashita, B. Johnson, Z. Li, L. Laakso, D. Powell & T. S. Mansour. Pyranonaphthoquinone Lactones: A New Class of AKT Selective Kinase Inhibitors Alkylate a Regulatory Loop Cysteine. *J. Med. Chem.*, **2009**, 52, 2181-2184.
- 120 C. W. Lindsley, Z. Zhao, W. H. Leister, R. G. Robinson, S. F. Barnett, D. Defeo-Jones, R. E. Jones, G. D. Hartman, J. R. Huff, H. E. Huber & M. E. Duggan. Allosteric Akt (PKB) inhibitors: discovery and SAR of isozyme selective inhibitors. *Bioorg. Med. Chem. Lett.*, **2005**, 15, 761-764.
- 121 S. F. Barnett, M. T. Bilodeau & C. W. Lindsley. The Akt/PKB Family of Protein Kinases: A Review of Small Molecule Inhibitors and Progress Towards Target Validation. *Curr. Top. Med. Chem.*, **2005**, 5, 109-125.
- 122 M. T. Bilodeau, A. E. Balitza, J. M. Hoffman, P. J. Manley, S. F. Barnett, D. Defeo-Jones, K. Haskell, R. E. Jones, K. Leander, R. G. Robinson, A. M. Smith, H. E. Huber & G. D. Hartman. Allosteric inhibitors of Akt1 and Akt2: A naphthyridinone with efficacy in an A2780 tumor xenograft model. *Bioorg. Med. Chem. Lett.*, **2008**, 18, 3178-3182.
- 123 J. C. Hartnett, S. F. Barnett, M. T. Bilodeau, D. Defeo-Jones, G. D. Hartman, H. E. Huber, R. E. Jones, A. M. Kral, R. G. Robinson & Z. Wu. Optimization of 2,3,5-trisubstituted pyridine derivatives as potent allosteric Akt1 and Akt2 inhibitors. *Bioorg. Med. Chem. Lett.*, **2008**, 18, 2194-2197.
- 124 Z. Wu, J. C. Hartnett, L. A. Neilson, R. G. Robinson, S. Fu, S. F. Barnett, D. Defeo-Jones, R. E. Jones, A. M. Kral, H. E. Huber, G. D. Hartman & M. T. Bilodeau.
-

-
- Development of Pyridopyrimidines as Potent Akt1/2 Inhibitors. *Bioorg. Med. Chem. Lett.*, **2008**, *18*, 1274-1279.
- 125 T. Siu, Y. Li, J. Nagasawa, J. Liang, L. Tehrani, P. Chua, R. E. Jones, D. Defeo-Jones, S. F. Barnett & R. G. Robinson. The design and synthesis of potent and cell-active allosteric dual Akt 1 and 2 inhibitors devoid of hERG activity. *Bioorg. Med. Chem. Lett.*, **2008**, *18*, 4191-4194.
- 126 J. Kawakami, M. Duncton, D. Sherman, H.-Y. He, A. Kiselyov & B. Pytowski. PKB Inhibitors as Anti-Tumor Agents, international patent *WO 2005/007099 A2* (**2005**).
- 127 J. G. Kettle, S. Brown, C. Crafter, B. Davies, P. Dudley, G. Fairley, P. Faulder, S. Fillery, H. Greenwood, J. Hawkins, M. James, K. Johnson, C. Lane, M. Pass, J. Pink, H. Plant & S. Cosulich. Diverse Heterocyclic Scaffolds as Allosteric Inhibitors of AKT. *J. Med. Chem.*, **2011**, *55*, 1261-1273.
- 128 C. J. Green, O. Göransson, G. S. Kular, N. R. Leslie, A. Gray, D. R. Alessi, K. Sakamoto & H. S. Hundal. Use of Akt Inhibitor and a Drug-resistant Mutant Validates a Critical Role for Protein Kinase B/Akt in the Insulin-dependent Regulation of Glucose and System A Amino Acid Uptake. *J. Chem. Biol.*, **2008**, *283*, 27653-27667.
- 129 T. Siu, J. Liang, J. Arruda, Y. Li, R. E. Jones, D. Defeo-Jones, S. F. Barnett & R. G. Robinson. Discovery of potent and cell-active allosteric dual Akt 1 and 2 inhibitors. *Bioorg. Med. Chem. Lett.*, **2008**, *18*, 4186-4190.
- 130 A. Okamoto, K. Tainaka, T. Unzai & I. Saito. Synthesis and fluorescence properties of dimethylaminonaphthalene–deoxyuridine conjugates as polarity-sensitive probes. *Tetrahedron*, **2007**, *63*, 3465-3470.
- 131 M. A. Ashwell, J.-M. Lapierre, C. Brassard, K. Bresciano, C. Bull, S. Cornell-Kennon, S. Eathiraj, D. S. France, T. Hall, J. Hill, E. Kelleher, S. Khanapurkar, D. Kizer, S. Koerner, J. Link, Y. Liu, S. Makhija, M. Moussa, N. Namdev, K. Nguyen, R. Nicewonger, R. Palma, J. Szwaya, M. Tandon, U. Uppalapati, D. Vensel, L. P. Volak, E. Volckova, N. Westlund, H. Wu, R.-Y. Yang & T. C. K. Chan. Discovery and Optimization of a Series of 3-(3-Phenyl-3H-imidazo[4,5-b]pyridin-2-yl)pyridin-2-amines: Orally Bioavailable, Selective, and Potent ATP-Independent Akt Inhibitors. *J. Med. Chem.*, **2012**, *55*, 5291-5310.
- 132 D. DeFeo-Jones, S. F. Barnett, S. Fu, P. J. Hancock, K. M. Haskell, K. R. Leander, E. McAvoy, R. G. Robinson, M. E. Duggan, C. W. Lindsley, Z. Zhao, H. E. Huber & R.

-
- E. Jones. Tumor cell sensitization to apoptotic stimuli by selective inhibition of specific Akt/PKB family members. *Mol. Cancer Ther.*, **2005**, *4*, 271-279.
- 133 A. W. Tolcher, T. A. Yap, I. Fearen, A. Taylor, C. Carpenter, A. T. Brunetto, M. Beeram, K. Papadopoulos, L. Yan & J. de Bono. A phase I study of MK-2206, an oral potent allosteric Akt inhibitor (Akti), in patients (pts) with advanced solid tumor (ST). *J. Clin. Oncol.*, **2009**, *27*, 3503.
- 134 Y. Cheng, X. Ren, Y. Zhang, R. Patel, A. Sharma, H. Wu, G. P. Robertson, L. Yan, E. H. Rubin & J.-M. Yang. eEF-2 Kinase Dictates Crosstalk between Autophagy and Apoptosis Induced by Akt Inhibition, thereby Modulating Cytotoxicity of Novel Akt Inhibitor MK-2206. *Cancer Res.*, **2011**, *71*, 2654-2663.
- 135 H. Hirai, H. Sootome, Y. Nakatsuru, K. Miyama, S. Taguchi, K. Tsujioka, Y. Ueno, H. Hatch, P. K. Majumder, B.-S. Pan & H. Kotani. MK-2206, an Allosteric Akt Inhibitor, Enhances Antitumor Efficacy by Standard Chemotherapeutic Agents or Molecular Targeted Drugs In vitro and In vivo. *Mol. Cancer Ther.*, **2010**, *9*, OF1-12.
- 136 B. B. Y. Ma, V. W. Y. Lui, C. W. C. Hui, C. P. Y. Lau, C.-H. Wong, E. P. Hui, M. H. Ng, S. W. Tsao, Y. Li & A. T. C. Chan. Preclinical evaluation of the AKT inhibitor MK-2206 in nasopharyngeal carcinoma cell lines. *Invest. New Drugs*, **2012**, *in press*.
- 137 J. R. Lakowicz. *Principles of Fluorescence Spectroscopy*, Third Edition (Springer Science + Business Media, LLC, **2006**).
- 138 S. Ohkuma & B. Poole. Fluorescence probe measurement of the intralysosomal pH in living cells and the perturbation of pH by various agents. *Proc. Natl. Acad. Sci. USA*, **1978**, *75*, 3327-3331.
- 139 J. Biwersi, B. Tulk & A. S. Verkman. Long-wavelength chloride-sensitive fluorescent indicators. *Anal. Biochem.*, **1994**, *219*, 139-143.
- 140 E. Lippert. Spektroskopische Bestimmung des Dipolmomentes aromatischer Verbindungen im ersten angeregten Singulettzustand. *Z. Elektrochem.*, **1957**, *61*, 962-975.
- 141 A. N. Perov. Energy of intermediate pair interactions as a characteristic of their nature: theory of the solvato(fluoro)chromism of three-component solutions. *Opt. Spectrosc.*, **1980**, *49*, 371-374.

-
- 142 T. Förster. Zwischenmolekulare Energiewanderung und Fluoreszenz. *Ann. Phys.*, **1948**, 437, 55-75.
- 143 J. R. Lakowicz, I. Gryczynski, H. C. Cheung, C.-K. Wang, M. L. Johnson & N. Joshi. Distance distributions in proteins recovered by using frequency-domain fluorometry. Applications to troponin I and its complex with troponin C. *Biochemistry*, **1988**, 27, 9149-9160.
- 144 J.-H. Zhang, T. D. Y. Chung & K. R. Oldenburg. A Simple Statistical Parameter for Use in Evaluation and Validation of High Throughput Screening Assays. *J. Biomol. Screen.*, **1999**, 4, 67-73.
- 145 *Radioactive in vitro kinase assays*, <http://www.perkinelmer.de/Resources/TechnicalResources/ApplicationSupportKnowledgebase/radiometric/invitro_kinase.xhtml> (**2013**).
- 146 C. B. Carlson, M. B. Robers, K. W. Vogel & T. Machleidt. Development of LanthaScreen cellular assays for key components within the PI3K/AKT/mTOR pathway. *J. Biomol. Screen.*, **2009**, 14, 121-132.
- 147 *Adapta™ Universal Kinase Assay*, <<http://www.invitrogen.com/adapta>> (**2013**).
- 148 M. D. Shults & B. Imperiali. Versatile fluorescence probes of protein kinase activity. *J. Am. Chem. Soc.*, **2003**, 125, 14248-14249.
- 149 *Z'-LYTE™ Kinase Assay*, <<http://www.invitrogen.com/z-lyte>> (**2013**).
- 150 G. Mathis. HTRF(R) Technology. *J. Biomol. Screen.*, **1999**, 4, 309-314.
- 151 C. Drexler. HTRF® KinEASET™: a new solution for screening serine-threonine kinases. *Nat. Methods*, **2006**, 3, i-ii.
- 152 O. Prat, E. Lopez & G. Mathis. Europium(III) cryptate: a fluorescent label for the detection of DNA hybrids on solid support. *Anal. Biochem.*, **1991**, 195, 283-289.
- 153 J. R. Simard, M. Getlik, C. Grütter, V. Pawar, S. Wulfert, M. Rabiller & D. Rauh. Development of a Fluorescent-Tagged Kinase Assay System for the Detection and Characterization of Allosteric Kinase Inhibitors. *J. Am. Chem. Soc.*, **2009**, 131, 13286-13296.
- 154 J. R. Simard, M. Getlik, C. Grütter, R. Schneider, S. Wulfert & D. Rauh. Fluorophore Labeling of the Glycine-Rich Loop as a Method of Identifying Inhibitors That Bind to Active and Inactive Kinase Conformations. *J. Am. Chem. Soc.*, **2010**, 132, 4152-4160.

-
- 155 M. Getlik, J. R. Simard, M. Termathe, C. Grütter, M. Rabiller, W. A. L. v. Otterlo & D. Rauh. Fluorophore Labeled Kinase Detects Ligands That Bind within the MAPK Insert of p38 α Kinase. *PLoS One*, **2012**, 7, e39713.
- 156 R. Schneider, C. Becker, J. R. Simard, M. Getlik, N. Bohlke, P. Janning & D. Rauh. Direct Binding Assay for the Detection of Type IV Allosteric Inhibitors of Abl. *J. Am. Chem. Soc.*, **2012**, 134, 9138-9141.
- 157 R. Schneider, C. Beumer, J. R. Simard, C. Grütter & D. Rauh. Selective Detection of Allosteric Phosphatase Inhibitors. *J. Am. Chem. Soc.*, **2013**, 135, 6838-6841.
- 158 S. Duhr & D. Braun. Why molecules move along a temperature gradient. *Proc. Natl. Acad. Sci.*, **2006**, 103, 19678-15682.
- 159 C. J. Wienken, P. Baaske, U. Rothbauer, D. Braun & S. Duhr. Protein-binding assays in biological liquids using microscale thermophoresis. *Nat. Commun.*, **2010**, 1, 100.
- 160 S. Zeng, K.-T. Yong, I. Roy, X.-Q. Dinh, X. Yu & F. Luan. A Review on Functionalized Gold Nanoparticles for Biosensing Applications. *Plasmonics*, **2011**, 6, 491-506.
- 161 K. Andersson, R. Karlsson, S. Löfås, G. Franklin & M. D. Hämmäläinen. Label-free kinetic binding data as a decisive element in drug discovery. *Expert Opin. Drug Discov.*, **2006**, 1, 439-446.
- 162 M. I. Davis, J. P. Hunt, S. Herrgard, P. Ciceri, L. M. Wodicka, G. Pallares, M. Hocker, D. K. Treiber & P. P. Zarrinkar. Comprehensive analysis of kinase inhibitor selectivity. *Nat. Biotechnol.*, **2011**, 29, 1046-1051.
- 163 G. Casiraghi, G. Casnati, G. Puglia, G. Sartori & G. Terenghi. Selective reactions between phenols and formaldehyde. A novel route to salicylaldehydes. *J. Chem. Soc., Perkin Trans. 1*, **1980**, 1862-1865.
- 164 J. Marco-Contelles, E. Prez-Mayoral, A. Samadi, M. do Carmo Carreiras & E. Soriano. Recent Advances in the Friedländer Reaction. *Chem. Rev.*, **2009**, 109, 2652-2671.
- 165 K. Hirose, H. Takeshima & M. Iino. Fluorescent indicators for inositol 1,4,5-trisphosphate based on bioconjugates of pleckstrin homology domain and fluorescent dyes. *Anal. Commun.*, **1999**, 36, 175-177.

-
- 166 C.-S. Jia, Z. Zhang, S.-J. Tu & G.-W. Wang. Rapid and efficient synthesis of poly-substituted quinolines assisted by p-toluene sulphonic acid under solvent-free conditions: comparative study of microwave irradiation versus conventional heating. *Org. Biomol. Chem.*, **2006**, *4*, 104-110.
- 167 J. M. Arruda, B. T. Campbell, N. D. P. Cosford, J. M. Hoffman, E. H. Hu, M. E. Layton, Y. Li, J. Liang, K. J. Rodzinak, T. Siu, B. A. Stearns & L. R. Tehrani. Preparation of naphthyridine derivatives as inhibitors of Akt activity, international patent (**2006**).
- 168 J. Wu, H.-G. Xia & K. Gao. Molecular iodine: a highly efficient catalyst in the synthesis of quinolines via Friedländer annulation. *Org. Biomol. Chem.*, **2006**, *4*, 126-129.
- 169 R. Varala, R. Enugala & S. R. Adapa. Efficient and Rapid Friedlander Synthesis of Functionalized Quinolines Catalyzed by Neodymium(III) Nitrate Hexahydrate. *Synthesis*, **2006**, 3825-3830.
- 170 M. K. Kuimova, G. Yahioglu, J. A. Levitt & K. Suhling. Molecular Rotor Measures Viscosity of Live Cells via Fluorescence Lifetime Imaging. *J. Am. Chem. Soc.*, **2008**, *130*, 6672-6673.
- 171 Q.-B. She, S. Chandarlapaty, Q. Ye, J. Lobo, K. M. Haskell, K. R. Leander, D. DeFeo-Jones, H. E. Huber & N. Rosen. Breast Tumor Cells with PI3K Mutation or HER2 Amplification Are Selectively Addicted to Akt Signaling. *PLoS One*, **2008**, *3*, e3065.
- 172 S. R. Datta, A. Brunet & M. E. Greenberg. Cellular survival: a play in three Akts. *Genes Dev.*, **1999**, *13*, 2905-2927.
- 173 D. R. Alessi, M. Andjelkovic, B. Caudwell, P. Cron, N. Morrice, P. Cohen & B. A. Hemmings. Mechanism of activation of protein kinase B by insulin and IGF-1. *EMBO J.*, **1996**, *15*, 6541-6551.
- 174 N. Dephoure, C. Zhou, J. Villen, S. A. Beausoleil, C. E. Bakalarski, S. J. Elledge & S. P. Gygi. A quantitative atlas of mitotic phosphorylation. *Proc. Natl. Acad. Sci.*, **2008**, *105*, 10762-10767.
- 175 J. V. Olsen, B. Blagoev, F. Gnad, B. Macek, C. Kumar, P. Mortensen & M. Mann. Global, in vivo, and site-specific phosphorylation dynamics in signaling networks. *Cell*, **2006**, *127*, 635-648.
-

-
- 176 F. Moreno, M. Cortijo & J. González-Jiménez. Interaction of Acrylodan with Human Serum Albumin. A Fluorescence Spectroscopic Study. *Photochem. Photobiol.*, **1999**, *70*, 695-700.
- 177 J. Kalia & R. T. Raines. Catalysis of imido group hydrolysis in a maleimide conjugate. *Bioorg. Med. Chem. Lett.*, **2007**, *17*, 6286-6289.
- 178 B. Lovitt, E. C. Vanderporten, Z. Sheng, H. Zhu, J. Drummond & Y. Liu. Differential effects of divalent manganese and magnesium on the kinase activity of leucine-rich repeat kinase 2 (LRRK2). *Biochemistry*, **2010**, *49*, 3092-3100.
- 179 N. Rhodes, D. A. Heerding, D. R. Duckett, D. J. Eberwein, V. B. Knick, T. J. Lansing, R. T. McConnell, T. M. Gilmer, S.-Y. Zhang, K. Robell, J. A. Kahana, R. S. Geske, E. V. Klymenova, A. E. Choudhry, Z. Lai, J. D. Leber, E. A. Minthorn, S. L. Strum, E. R. Wood, P. S. Huang, R. A. Copeland & R. Kumar. Characterization of an Akt Kinase Inhibitor with Potent Pharmacodynamic and Antitumor Activity. *Cancer Res.*, **2008**, *68*, 2366-2374.
- 180 B. Zimmermann, 2012, pers. comm.
- 181 J. R. Simard, S. Klüter, Christian Grütter, M. Getlik, M. Rabiller, H. B. Rode & D. Rauh. A new screening assay for allosteric inhibitors of cSrc. *Nat. Chem. Biol.*, **2009**, *5*, 394-396.
- 182 R. Schneider, A. Gohla, J. R. Simard, D. B. Yadav, Z. Fang, W. A. L. van Otterlo & D. Rauh. Overcoming compound fluorescence in the FLiK screening assay with red-shifted fluorophores. *J. Am. Chem. Soc.*, **2013**, *135*.
- 183 M. Hiromura, F. Okada, T. Obata, D. Auguin, T. Shibata, C. Roumestand & M. Noguchi. Inhibition of Akt Kinase Activity by a Peptide Spanning the A Strand of the Proto-oncogene TCL1. *J. Biol. Chem.*, **2004**, *279*, 53407-53418.
- 184 Y. Tal-Gan, M. Hurevich, S. Klein, A. Ben-Shimon, D. Rosenthal, C. Hazan, D. E. Shalev, M. Y. Niv, A. Levitzki & C. Gilon. Backbone-Cyclic Peptide Inhibitors of Protein Kinase B (PKB/Akt). *J. Med. Chem.*, **2011**, *54*, 5154-5164.
- 185 S. L. McGovern, E. Caselli, N. Grigorieff & B. K. Shoichet. A Common Mechanism Underlying Promiscuous Inhibitors from Virtual and High-Throughput Screening. *J. Med. Chem.*, **2002**, *45*, 1712-1722.
-

-
- 186 S. L. McGovern & B. K. Shoichet. Kinase Inhibitors: Not Just for Kinases Anymore. *J. Med. Chem.*, **2003**, *46*, 1478-1483.
- 187 K. E. D. Coan, D. A. Maltby, A. L. Burlingame & B. K. Shoichet. Promiscuous Aggregate-Based Inhibitors Promote Enzyme Unfolding. *J. Med. Chem.*, **2009**, *52*, 2067-2075.
- 188 J. J. Caldwell, T. G. Davies, A. Donald, T. McHardy, M. G. Rowlands, G. W. Aherne, L. K. Hunter, K. Taylor, R. Ruddle, F. I. Raynaud, M. Verdonk, P. Workman, M. D. Garrett & I. Collins. Identification of 4-(4-aminopiperidin-1-yl)-7H-pyrrolo[2,3-d]pyrimidines as selective inhibitors of protein kinase B through fragment elaboration. *J. Med. Chem.*, **2008**, *51*, 2147-2157.
- 189 M. Mayer & B. Meyer. Characterization of Ligand Binding by Saturation Transfer Difference NMR Spectroscopy. *Angew. Chem.*, **1999**, *38*, 1784-1788.
- 190 O. Korb, H. M. Moller & T. E. Exner. NMR-guided molecular docking of a protein-peptide complex based on ant colony optimization. *ChemMedChem*, **2010**, *5*, 1001-1006.
- 191 C. Becker. *Optimierung und Anwendung eines Assays zur Detektion allosterischer Kinaseinhibitoren*, Master in Chemical Biology thesis, **2011**, Technische Universität Dortmund.
- 192 Z. Lu, S. J. Lord, H. Wang, W. E. Moerner & R. J. Twieg. Long-Wavelength Analogue of PRODAN: Synthesis and Properties of Anthradan, a Fluorophore with a 2,6-Donor–Acceptor Anthracene Structure. *J. Org. Chem.*, **2006**, *71*, 9651-9657.
- 193 R. Eisenthal & M. J. Danson. *Enzyme Assays: A Practical Approach, 2nd Edition*, (Oxford University Press, **2002**).
- 194 X. Zhang, S. Zhang, H. Yamane, R. Wahl, A. Ali, J. A. Lofgren & R. L. Kendall. Kinetic Mechanism of AKT/PKB Enzyme Family. *J. Biol. Chem.*, **2006**, *281*, 13949-13956.
- 195 H. Nordin, M. Jungnelius, R. Karlsson & O. P. Karlsson. Kinetic studies of small molecule interactions with protein kinases using biosensor technology. *Anal. Biochem.*, **2005**, *340*, 359-368.